UNIVERSITÉ DE MONTRÉAL

MICROSTRUCTURE AND GROWTH KINETICS OF NICKEL SILICIDE ULTRA-THIN FILMS SYNTHESIZED BY SOLID-STATE REACTIONS

CÉDRIK COIA
DÉPARTEMENT DE GÉNIE PHYSIQUE
ÉCOLE POLYTECHNIQUE DE MONTRÉAL

THÈSE PRÉSENTÉE EN VUE DE L'OBTENTION DU DIPLÔME DE
PHILOSOPHIÆ DOCTOR (Ph.D.)
(GÉNIE PHYSIQUE)
DÉCEMBRE 2008

© Cédrik Coia, 2008.

Library and Archives Canada

Published Heritage Branch

395 Wellington Street
Ottawa ON K1A 0N4
Canada

Bibliothèque et Archives Canada

Direction du Patrimoine de l'édition

395, rue Wellington
Ottawa ON K1A 0N4
Canada

Your file Votre référence
ISBN: 978-0-494-48884-3
Our file Notre référence
ISBN: 978-0-494-48884-3

NOTICE:
The author has granted a non-exclusive license allowing Library and Archives Canada to reproduce, publish, archive, preserve, conserve, communicate to the public by telecommunication or on the Internet, loan, distribute and sell theses worldwide, for commercial or non-commercial purposes, in microform, paper, electronic and/or any other formats.

The author retains copyright ownership and moral rights in this thesis. Neither the thesis nor substantial extracts from it may be printed or otherwise reproduced without the author's permission.

AVIS:
L'auteur a accordé une licence non exclusive permettant à la Bibliothèque et Archives Canada de reproduire, publier, archiver, sauvegarder, conserver, transmettre au public par télécommunication ou par l'Internet, prêter, distribuer et vendre des thèses partout dans le monde, à des fins commerciales ou autres, sur support microforme, papier, électronique et/ou autres formats.

L'auteur conserve la propriété du droit d'auteur et des droits moraux qui protège cette thèse. Ni la thèse ni des extraits substantiels de celle-ci ne doivent être imprimés ou autrement reproduits sans son autorisation.

In compliance with the Canadian Privacy Act some supporting forms may have been removed from this thesis.

While these forms may be included in the document page count, their removal does not represent any loss of content from the thesis.

Conformément à la loi canadienne sur la protection de la vie privée, quelques formulaires secondaires ont été enlevés de cette thèse.

Bien que ces formulaires aient inclus dans la pagination, il n'y aura aucun contenu manquant.

Canada

UNIVERSITÉ DE MONTRÉAL

ÉCOLE POLYTECHNIQUE DE MONTRÉAL

Cette thèse intitulée :

MICROSTRUCTURE AND GROWTH KINETICS OF NICKEL SILICIDE ULTRA-THIN FILMS SYNTHESIZED BY SOLID-STATE REACTIONS

présentée par : COIA Cédrik
en vue de l'obtention du diplôme de : Philosophiæ Doctor
a été dûment acceptée par le jury d'examen constitué de :

M. MARTINU Ludvik, Ph.D., président
M. DESJARDINS Patrick, Ph.D., membre et directeur de recherche
M. LAVOIE Christian, Ph.D., membre et co-directeur de recherche
M. TURENNE Sylvain, Ph.D., membre
M. MANGELINCK Dominique, Ph.D., membre

À ma mère, pour son dévouement et tous les sacrifices qu'elle a faits pour moi.

À mon père et à mon oncle Antoine, qui m'ont intéressés aux sciences et aux technologies et qui ont eu la patience de répondre aux mille et une questions d'un jeune garçon curieux.

ACKNOWLEDGEMENTS / REMERCIEMENTS

Mes premiers remerciements vont sans aucun doute à mes parents Anna et Hubert. Sans leur soutien indéfectible, mes études universitaires, surtout aux cycles supérieurs auraient certainement été plus difficiles voire impossibles. Je les remercie d'avoir fait de mon éducation une priorité et d'y avoir investi tant d'énergie. Je leur serai éternellement reconnaissant de tous les sacrifices qu'ils ont fait pour moi. J'ose espérer que je saurai offrir à mes enfants un cadre et un support comparables à ceux dont j'ai moi-même pu bénéficier. Le défi qui m'attend est grand!

I am deeply indebted to my advisors Patrick Desjardins and Christian Lavoie for allowing me to join their team and being so patient with me. While undertaking a Ph.D. was certainly a challenge for me, I can safely state that training me has been a greater challenge for them, especially for the written communications aspect. I look up to them for their scientific rigor and I hope it is reflected in this thesis. They have spared no effort to build an environment whereby I could learn and develop myself as a scientist and engineer and I have learned so much thanks to them. I am especially grateful to them for creating two internship opportunities at IBM and allowing me to interrupt my Ph.D. to leave and get a valuable industrial experience. I also which to thank Dr. Lavoie for his highly appreciated hospitability on the many occasions I went to Yorktown to work or to connect before to go to Brookhaven National Laboratory.

I wish to thank IBM Research and two exceptional managers, James Harper and Kenneth Rodbell, for working into facilitating, building and maintaining the research collaboration between Dr. Lavoie and prof. Desjardins' group. This collaboration grants Prof. Desjardins' students with an access to IBM's facilities in Yorktown and at the Synchrotron of the Brookhaven National Laboratory, and to a stimulating research environment. It gives an incredible added value to the training of students and should serve as a model.

I wish to thank the members of the jury, professors Dominique Mangelinck, Ludvik Martinu, and Sylvain Turenne for accepting to evaluate my thesis. I especially thank them for accepting to read such a big thesis on a rather short notice.

Je souhaite également remercier Lyne Denommé, pour ses conseils concernant la mise en page et la présentation de ce document, ainsi que le personnel du service d'impression et de reprographie de Polytechnique, plus particulièrement Roger et Jean-Claude, pour leur diligence et la qualité du service qu'ils m'ont offert.

None of the work presented in this thesis would have been possible without the help of Roy Carruthers at IBM Yorktown, who has deposited the countless thin films I have studied. I also wish to thank Jean Jordan Sweet for her indispensable and much appreciated help at beam line X20 of the National Synchrotron Light Source. Working with her was such a pleasure. I have appreciated her scientific knowledge and technical skills as much as her kind, friendly and welcoming personality. I would like to thank Sadanand Deshpande, my manager at IBM East Fishkill, for facilitating my integration to his team, Lynne Gignac for allowing me to be one of the very few interns to use her transmission electron microscope, and Steve Cohen for allowing me and helping me to use his electrical probing stations.

Our collaboration with the group of Pr. Christophe Detavernier in Ghent has been instrumental to the success of this project and I wish to thank them for sharing some of their results with us. Without their contribution, our understanding of both Ni-Si and general solid state reactions would have been far less complete, at least in my opinion.

I wish to thank Philippe Plamondon and Jean-Philippe Masse from the Centre de caractérisation microscopique des matériaux (CM^2) for their help with the transmission electron microscopy. I thank Andrew Kellock (IBM research, Almaden) and Suzie

Poulin respectively for the RBS and the SIMS measurements. I also want to thank professors Sjoerd Roorda and François Schiettekatte from Université de Montréal respectively for letting me use a differential scanning calorimetry system and for useful advices concerning the analysis of Rutherford backscattering spectra.

Au delà du défi académique qu'il a représenté, mon doctorat aura été une épreuve morale au cours de laquelle j'ai pu compter sur le support de beaucoup de gens dans mon entourage. Je remercie ma femme Nathalie pour avoir patiemment attendu toutes ces années que je sorte enfin de l'école et surtout pour s'être occupé si bien de notre petit Émile au cours de la dernière année. Mes études ont certainement été une épreuve pour elle aussi et ma réussite lui appartient en partie. Je remercie également mes amis et collègues du B-552 et du P-4047: Carla Aguirre, Jean-Nicolas Beaudry, Carolyne Dion, Louis Forest et Martin Tremblay pour leurs encouragements et leur compagnie toujours agréable. Je remercie Simon Gaudet pour certaines discussions qui ont joué un rôle clé dans ma compréhension des réactions en phase solide. Finalement un merci tout spécial à ma comparse Annie Lévesque avec qui j'ai partagé les hauts et les bas de la vie au doc et hors-doc. Je n'oublirai jamais son support inestimable lors des interminables séances de préparation d'échantillons de microscopie électronique à transmission dans les sombres et sinistres locaux du bunker.

Je remercie également tous mes amis proches dont les encouragements et souvent la simple présence m'ont toujours été d'un grand réconfort: Jonathan, Jean-Claude, Katia, Éric, Geneviève, Marc, Jacynthe, Éric, Audrey, Patrick. Leur amitié m'est chère et j'espère pouvoir les garder près de moi le plus longtemps possible.

I also thank all my colleagues at IBM who became friends, Christian Lavoie, Ahmet Ozcan, Cyril Cabral, Anna Topol, Cev Noyan, Maurice McGlashan-Powell, Jean Jordan-Sweet, Nicholas Fuller, Katia Babich. Working with them was not only a

pleasure, but an honor. I want to thank especially Cyril Cabral for his mentoring and for allowing me to have an affordable place to live while I was an intern at IBM Yorktown.

Finally, I want to pay a tribute to the late François d'Heurle who has been an inspiration and such a nice person to work and interact with. I thank him for writing so many interesting and rigorous papers. I wish he was still with us as my Ph.D. finally comes to an end.

RÉSUMÉ

Depuis plus de 30 ans, les études portant sur les réactions entre couches minces de Ni de moins de 500 nm et substrats de Si n'ont révélé la formation que de trois composés, soit δ-Ni_2Si, NiSi et $NiSi_2$, alors que le diagramme des phases à l'équilibre du système Ni-Si pouvait laisser présager la formation d'au moins trois autres. Cette séquence à trois composés a cependant été remise en question récemment par des mesures de diffraction des rayons X synchrotron *in situ* pendant recuit. En effet, celles-ci ont révélé la formation de plus d'un composé supplémentaire lors de la réaction de couches de 10nm de Ni avec leur substrat de Si, suggérant que les réactions Ni-Si ne sont pas aussi bien comprises que ce à quoi on pourrait s'attendre d'un système étudié depuis si longtemps. En plus de revêtir un intérêt fondamental en science des matériaux, l'existence d'étapes supplémentaires dans le système de réaction Ni-Si peut avoir un impact important en microélectronique. En effet, les problèmes de matériaux reliés au procédé de mise en forme des siliciures rencontrés par le passé avec les métallurgies de contact à base de Ti et de Co ont mis en évidence l'importance capitale de comprendre les détails fondamentaux des réactions en phase solide menant à la formation du composé de basse résistivité.

Le but de ce projet de doctorat était de développer une compréhension fondamentale détaillée des réactions qui mènent à la formation du NiSi. Nous avons donc revisité les réactions entre couches minces de Ni et substrats de Si à l'aide notamment d'une technique de diffraction des rayons-X synchrotron *in situ* pendant recuit qui permet de détecter les composés qui se forment alors que les réactions se déroulent et ce avec une résolution temporelle inégalée. Bien que la XRD *in situ* soit un outil particulièrement puissant, la force du travail expérimental présenté dans cette thèse repose sur le nombre et la complémentarité des autres techniques que nous avons utilisées telles que la microscopie électronique à transmission, la spectroscopie de rétrodiffusion Rutherford (RBS) et la spectrométrie de masse des ions secondaires (SIMS).

Nous montrons que les réactions en phase solide entre les substrats de Si et les couches minces de Ni avec une épaisseur initiale comprise entre 4 et 500nm sont considérablement plus complexes que ce qu'il était communément accepté auparavant. Nous observons jusqu'à trois composés, soit θ-Ni_2Si, $Ni_{31}Si_{12}$ et Ni_3Si_2, en plus des trois énoncés plus haut et dont la formation a lieu avant celle du NiSi. Ces composés ont tous la particularité de co-exister latéralement (c.a.d. dans la même couche) avec δ-Ni_2Si et/ou NiSi alors qu'on s'attend à une co-existence de type couche-par-couche dans les réactions en couches minces. Malgré sa métastabilité aux températures inférieures à 825 °C, le composé non-stœchiométrique θ-Ni_2Si est présent dans tous les échantillons que nous avons étudiés et se forme systématiquement à la même température (300 ± 10 °C) nonobstant l'épaisseur intiale de la couche de Ni. Sa formation rapide est favorisée par un héritage de texture du δ-Ni_2Si, qui se fait d'ailleurs complètement consommer dans les échantillons avec moins de 10 nm de Ni au départ. La disparition du θ-Ni_2Si, qui est également très rapide, résulte à la fois en la formation de NiSi et en un surprenant retour partiel du δ-Ni_2Si préalablement consommé. La séquence de formation n'est donc pas monotone en composition contrairement à ce qui est attendu dans les réactions en phase solide.

Le $Ni_{31}Si_{12}$ n'est observé que dans des échantillons où du Ni non-réagi est encore disponible à des températures supérieures à 350 °C lors de recuits en mode rampe avec des taux de chauffage de 3 $°Cs^{-1}$. À l'instar du θ-Ni_2Si, la formation du $Ni_{31}Si_{12}$ consomme du δ-Ni_2Si, ce qui laisse supposer que les joints de grains du δ-Ni_2Si favorisent de manière générale la germination des nouveaux composés que nous observons. Bien que l'on observe des grains de Ni_3Si_2 co-exister latéralement avec θ-Ni_2Si et NiSi dans les échantillons avec 100nm de Ni, le Ni_3Si_2 ne développe de manière importante que s'il reste du δ-Ni_2Si non-réagi à des températures supérieures à 600 °C.

À travers l'étude des effets de *i)* l'alliage du Ni avec du Pt et du Co ainsi que de *ii)* l'implantation d'impuretés dans le Si (B, P, As, F et N) sur les réactions Ni-Si, nous avons pu déterminer que la germination joue un rôle limitant dans la croissance du composé métastable θ-Ni_2Si. Nous avons également vérifié l'importance du gabarit offert par les grains de δ-Ni_2Si qui favorise considérablement cette germination. Les résultats des réactions entre couches de Ni et substrats de Si amorphe ou amorphisés par l'implantation révèlent par contre que la germination du θ-Ni_2Si ne dépend pas de la possibilité d'une épitaxie avec le Si. Les dopants CMOS activés, tout comme les impurtées d'alliage, ont pour effet de retarder la formation des siliciures riches en Ni. A haute concentration, les impuretés d'alliage suppriment même la formation de θ-Ni_2Si, possiblement en raison d'une solubilité limitée dans ce composé. Au contraire, les impuretés implantées dans le Si sans recuit de recristallisation subséquent ont pour effet de stabiliser le θ-Ni_2Si en partie grâce à la présence d'une interface amorphe au début de la réaction. Cette stabilisation est particulièrement importante dans les échantillons implantés avec du fluor en raison *i)* d'une ségrégation des atomes d'impuerté dans les joints de grains, où ils forment des liens Si-F et Ni-F, mais également *ii)* d'une solubilité possiblement grande dans le θ-Ni_2Si où les atomes de fluor occuperaient les sites lacunaires. L'étude du développement des contraintes dans les échantillons où le θ-Ni_2Si est stabilisé révèle que sa disparition n'est pas causée par une accumulation de contrainte. En fait, nos données suggèrent que c'est la germination du NiSi, jusqu'alors gênée par l'existence de gradients de concentration à l'interface, qui cause la disparition du θ-Ni_2Si. La croissance du monosiliciure qui peut se faire rapidement en absorbant les lacunes des régions de θ-Ni_2Si non-transformées, causerait un enrichissement effectif en Ni de ces régions favorisant ensuite le retour vers la structure orthorhombique plus stable du δ-Ni_2Si. Ces transformations rapides sont en fait facilitées par une parenté entre les structures cristallines du NiSi, du δ-Ni_2Si et du θ-Ni_2Si.

L'étude quantitative de la cinétique de croissance du θ-Ni_2Si lors de la réaction entre des couches de 10 nm de Ni et leur substrat de Si (001) nous a permis de révéler l'existence de deux stades de croissance distincts. Nous proposons un modèle unique qui décrit les deux stades en unifiant un processus de germination-croissance 2D à l'interface siliciure/Si suivie d'une croissance non-planaire contrôlée par la diffusion au cours de laquelle le θ-Ni_2Si pénètre dans les joints de grains du δ-Ni_2Si surjacent. Malgré un accord remarquable entre les simulations prédites par ce modèle et les données expérimentales, nous montrons également qu'on ne peut exclure la possibilité que le deuxième stade de croissance consiste en un épaississement unidimensionnel d'une couche continue, contrôlé par la diffusion et au cours duquel la composition du θ-Ni_2Si (qui est non-stœchiométrique) change. Lorsque le Si est implanté avec de fortes doses de F, le premier stade de croissance observé pour le cas non dopé est supprimé, cependant un troisième stade apparaît et correspond à la croissance du θ-Ni_2Si en l'absence de Ni et de δ-Ni_2Si, donc apparemment de toute source externe d'atomes de Ni. Nous décrivons ce troisième stade à l'aide d'un modèle d'épaississement unidimensionnel d'une couche continue contrôlé par la diffusion qui inclut une composition et un coefficient de diffusion variables, tel que clairement suggéré par les données expérimentales.

La consommation du θ-Ni_2Si, tant dans les échantillons avec Si non-dopé qu'implanté au fluor, est bien décrite par un modèle d'Avrami avec un exposant de 2, ce qui suggère une réaction contrôlée par la germination en deux dimensions.

Les énergies d'activations que nous obtenons pour les premier et deuxième stades de croissance du θ-Ni_2Si ainsi que pour sa consommation sont respectivement de 1.17 ± 0.5, 2.55 ± 0.5 et 1.65 ± 0.5 eV et augmentent toutes avec l'implantation au fluor.

Les résultats présentés dans cette thèse montrent que grâce à des techniques qui permettent de suivre la réaction avec une résolution temporelle inégalée, nous avons observé la compétition cinétique que se livrent les différents composés dans les premiers stades de leur croissance dans les réactions en phase solide. Cette compétition était prédite depuis longtemps par plusieurs modèles de réaction en phase solide, mais pas encore observée à notre connaissance. Nous montrons également que cette compétition peut mener à une co-existence latérale de plusieurs composés dans une même couche alors que la plupart des modèles de réaction en phase solide présument ou nécessitent une co-existence en strates continues. Finalement, nous montrons que la combinaison de *(i)* l'existence de gradients de concentration interfaciaux, *(ii)* la similarité des structures cristallines de δ-Ni_2Si, NiSi et θ-Ni_2Si ainsi que *(iii)* la capacité de ce composé non-stœchiométrique à contenir des lacunes ainsi qu'à germer dans un gradient de concentration mène à un mécanisme de réaction très particulier qui résulte notamment une succession non-séquentielle de composés. Nos résultats revêtent ainsi un intérêt important en science fondamentale des matériaux en plus d'un intérêt technologique de par leur pertinence à l'égard du procédé SALICIDE utilisé en technologie CMOS pour mettre en œuvre les contacts à base de siliciures.

ABSTRACT

Ni monosilicide, synthesized through the thermally induced solid-state reaction of Ni thin films with the silicon substrate, is used as a low-resistance contact material in the complementary metal oxide semiconductor (CMOS) technology. For more than 30 years, that reaction has been reported to consist in the successive formation of δ-Ni_2Si, NiSi and $NiSi_2$. This surprisingly simple compound formation sequence – given the complexity of the Ni-Si equilibrium phase diagram – has recently been challenged by *in situ* x-ray diffraction experiments which revealed the formation of at least one additional compound before the appearance of NiSi. From a technological point of view, it is crucial to better understand the details of the silicidation reaction in order to optimize and control the fabrication process and to obtain the desired device performance. From a materials science perspective, Ni-Si solid-state reactions constitute a model system for investigating this peculiar behavior.

The objective of the thesis is to develop a detailed fundamental understanding of the thermally induced solid-state reactions that lead to the formation of the NiSi. We use *in situ* synchrotron x-ray diffraction as well as wafer curvature measurements to monitor reactions as they occur during the annealing treatment. These analyses are complemented by *ex situ* transmission electron microscopy, Rutherford backscattering spectroscopy, and secondary ions mass spectroscopy.

The solid-state reactions between 4 to 500 nm-thick Ni films and Si (001) are considerably more complex than previously believed. In addition to the commonly observed phases listed above, we observe the formation of three additional compounds – θ-Ni_2Si, $Ni_{31}Si_{12}$ and Ni_3Si_2 – before the complete transformation of the reacted film into NiSi. These compounds are found to co-exist laterally (within the same layer) with δ-Ni_2Si and/or NiSi. The metastable compound θ-Ni_2Si, which formation results from texture inheritance and rapid growth through vacancy diffusion, is present in all samples

and forms at the same temperature (300±10 °C) regardless of the initial Ni thickness. Indeed, this compound forms rapidly during ramps anneals, apparently consuming all the δ-Ni_2Si for initial Ni films thickness of up to 10 nm. Its disappearance is also rapid and is correlated to both the growth of NiSi and to a surprising return of the orthorhombic δ-Ni_2Si. The formation sequence is therefore not monotonic in composition in contrast to what is usually expected in solid-state reactions. $Ni_{31}Si_{12}$ is observed only in samples where unreacted Ni is still available at temperatures above 350 °C during ramp-type anneals of 3 °C s^{-1}. Like θ-Ni_2Si, its formation consumes the δ-Ni_2Si, which suggests that grain boundaries in δ-Ni_2Si generally favor the nucleation of the newly observed compounds. Although some Ni_3Si_2 grains are found to co-exist with θ-Ni_2Si and NiSi in samples with 100nm Ni, the presence of unreacted δ-Ni_2Si at temperatures above 600 °C is required to observe a significant development of this compound.

An investigation of the effect of alloying elements (Pt and Co) and impurities (B, P, As, F, N) on the Ni-Si reactions enables us to determine that nucleation plays a limiting role in the growth of metastable θ-Ni_2Si and that the template provided by δ-Ni_2Si is crucial in promoting this nucleation. Furthermore, reactions with amorphized and amorphous substrates indicate that the possibility of epitaxy with the Si substrate is not a necessary condition for θ-Ni_2Si to form. Activated CMOS dopants and alloying impurities delay the growth of all Ni-rich compounds and eventually suppress the formation of θ-Ni_2Si possibly because of a limited solubility. Impurities implanted without subsequent re-crystallization anneals stabilize the compound partly through the presence of an amorphous interface, at least at the beginning of the reaction. The stabilization effect is enhanced by segregation of F to grain boundaries, where it can form strong Si-F and Ni-F bonds, and by a possibly large solubility in θ-Ni_2Si in which the F atoms would most likely occupy the vacancy sites of this relatively open structure. A study of the stress development in samples where the θ-Ni_2Si is stabilized revealed

that its consumption is not triggered by the accumulation of stress. In fact our data suggest that the consumption of θ-Ni_2Si is most likely triggered by the nucleation of NiSi, previously hindered by interfacial concentration gradients, which grows rapidly by absorbing vacancies until they are sufficiently depleted so as to favor a return towards the more stable δ-

A quantitative investigation of the growth kinetics of θ-Ni_2Si on undoped Si(001) reveals two distinct stages which are well described by a model incorporating 2D nucleation-controlled growth at the silicide/Si interface and the non-planar diffusion-controlled penetration of θ-Ni_2Si in the overlying δ-Ni_2Si grains. Despite the very good fit of the model to our data, we cannot rule out the possibility that the second stage consists of a 1D diffusion-controlled planar growth during which the composition of the non-stoichiometric θ-Ni_2Si changes. In F-doped samples, the second stage corresponds to a 1D diffusion-controlled growth in the absence of δ-Ni_2Si and Ni, suggesting a possible compositional change during growth. In both the undoped and F-implanted samples, the θ-Ni_2Si consumption kinetics is well described by an Avrami model with an exponent of 2, indicating a two-dimensional in-plane reaction geometry. The low activation energy of the Avrami constant (1.7 eV) supports the hypothesis that vacancy diffusion play an important role in the process.

The results presented in this thesis show that thanks to the use of powerful *in situ* monitoring techniques we have observed the kinetic competition between different growing compounds in the early stages of their growth. This competition has been predicted by many growth models, yet to our knowledge it has not been observed so far. We also have shown that this competition can lead to the lateral co-existence of several compounds in the same layer whereas most solid-state reaction models assume or require a layer-by-layer co-existence scheme. Finally, we show that the combination of (i) strong interfacial concentration gradients, (ii) structural similarities between δ-Ni_2Si,

NiSi and θ-Ni_2Si, and (iii) the ability of the latter to sustain vacancies and to nucleate in concentration gradients lead to a very peculiar reaction pathway, which results in a striking non-sequential succession of compounds. Our results therefore bear an important interest on the fundamental material science point of view in addition to the technological points of view given their pertinence for the SALICIDE process used to implement the Ni-Si contact metallurgy in the CMOS technology.

CONDENSÉ EN FRANCAIS

Le monosiliciure de nickel est un matériau utilisé en microélectronique pour réduire la résistance des contacts dans les circuits intégrés de type métal-oxyde-semi-conducteur (CMOS). Dans le cadre de cette application, il est synthétisé par la réaction en phase solide, induite par le chauffage, entre une couche mince de nickel et un substrat de silicium sur lequel elle est déposée. Depuis plus de 30 ans, les études portant sur les réactions entre couches minces de Ni de moins de 500 nm et substrats de Si n'ont révélé la formation que de trois composés, soit δ-Ni_2Si, NiSi et $NiSi_2$, alors que le diagramme des phases à l'équilibre du système Ni-Si pouvait laisser présager la formation d'au moins trois autres. Cette séquence à trois composés a cependant été remise en question récemment par des mesures de diffraction des rayons X synchrotron *in situ* pendant recuit. En effet, celles-ci ont révélé la formation de plus d'un composé supplémentaire lors de la réaction de couches de 10nm de Ni avec leur substrat de Si, suggérant que les réactions Ni-Si ne sont pas aussi bien comprises que ce à quoi on pourrait s'attendre d'un système étudié depuis si longtemps. En plus de revêtir un intérêt fondamental en science des matériaux, l'existence d'étapes supplémentaires dans le système de réaction Ni-Si peut avoir un impact important en microélectronique. En effet, les problèmes de matériaux reliés au procédé de mise en forme des siliciures rencontrés par le passé avec les métallurgies de contact à base de Ti et de Co ont mis en évidence l'importance capitale de comprendre les détails fondamentaux des réactions en phase solide menant à la formation du composé de basse résistivité.

Le but de ce projet de doctorat était de développer une compréhension fondamentale détaillée des réactions qui mènent à la formation du NiSi. Nous avons donc revisité les réactions entre couches minces de Ni et substrats de Si à l'aide notamment d'une technique de diffraction des rayons-X synchrotron *in situ* pendant recuit qui permet de détecter les composés qui se forment alors que les réactions se déroulent et ce avec une résolution temporelle inégalée. Bien que la XRD *in situ* soit un

outil particulièrement puissant, la force du travail expérimental présenté dans cette thèse repose sur le nombre et la complémentarité des autres techniques que nous avons utilisées pour étudier *i)* l'évolution des contraintes pendant la réaction, *ii)* la microstructure et la distribution spatiale des composés dans des échantillons de couches minces recuits à différents stades ainsi que *iii)* la redistribution des impuretés suite à la réaction. Nous avons ainsi combiné des mesures de rayon de courbure des échantillons acquises *in situ* pendant recuit, de la microscopie électronique à transmission, de la spectrométrie de rétro-diffusion Rutherford ainsi que de la spectrométrie de masse des ions secondaires aux mesures de XRD *in situ.*

Nos expériences ont été principalement conçues de manière à identifier les composés supplémentaires qui se forment et de comprendre les phénomènes thermodynamiques et cinétiques qui sont en jeux lors de leur formation. Nous avons notamment étudié les réactions Ni-Si par XRD *in situ* tout en couvrant une vaste gamme d'épaisseurs initiales de Ni afin de comprendre pourquoi ces composés n'ont pas été observés plus tôt. Nous avons également étudié l'effet d'impuretés alliées au Ni (Pt et Co) et implantées dans le Si (B, P, F, N, Si) de manière à modifier l'énergétique des réactions et d'en observer l'impact sur la formation des composés. Finalement, nous avons étudié la cinétique de croissance du θ-Ni_2Si, un composé supplémentaire dont nous avons observé la formation avant celle du NiSi, tant sur substrats de Si purs qu'implantés avec du fluor.

Une revue sommaire de la littérature scientifique portant sur les réactions en phase solide en général révèle que dans les couples de diffusion massifs, où l'approvisionnement en réactifs est infini, tous les composés permis à la température du recuit par le diagramme des phases à l'équilibre pertinent sont observés sous forme de strates à l'interface entre les deux matériaux de départ. Dans les réactions impliquant des couches minces, l'approvisionnement limité d'un ou des deux matériaux de départ fait en sorte que les différents composés apparaissent généralement un par un, en séquence.

Dans cette séquence, les composés se succèdent en ordre de teneur décroissante en atomes de l'espèce mobile la plus rapide (soit le Ni dans les cas des siliciures de nickel). Selon la nature des phénomènes cinétiques qui limitent la croissance, certains composés peuvent être absents de la séquence de formation ou ne commenceront à se former que lorsque les composés déjà formés ont atteint une épaisseur critique minimale.

Une revue exhaustive de l'abondante littérature scientifique publiée sur le système Ni-Si nous révèle que la séquence à trois composés, δ-Ni_2Si, NiSi et $NiSi_2$, est systématiquement observée dans toutes les réactions impliquant des couches minces de Ni et des substrats massifs de Si, et ce, quelle que soit la nature et l'orientation cristalline de ces derniers. δ-Ni_2Si est ainsi le seul composé dont la formation soit observée avant celle du NiSi. Les composés tels que Ni_3Si, $Ni_{31}Si_{12}$ et Ni_3Si_2 ne sont observés que dans les couples de diffusion massifs recuits à haute températures pendant de longues périodes ou dans les réactions de couches minces de Si sur substrats de Ni massifs. Trois études rapportent la formation d'un composé NiSi stabilisé dans une structure cristalline hexagonale par une relation d'épitaxie avec le Si. Cependant, on ne trouve aucune mention de la formation de composés dits "haute température" tels que la phase θ-Ni_2Si dans les réactions en phase solide en couches minces.

Parmi la vaste gamme d'impuretés dont l'effet sur les réactions Ni-Si a été étudié, on note particulièrement le platine et le cobalt qui, lorsqu'introduites dans la réaction sous forme d'alliage avec le Ni, ont respectivement pour effet de défavoriser et de favoriser la germination du $NiSi_2$. Ce résultat s'explique par la similarité des structures cristallines de NiSi et PtSi ainsi que de $NiSi_2$ et $CoSi_2$ qui résultent en un effet d'entropie de mélange, stabilisant tantôt le NiSi, tantôt le $NiSi_2$. On note également le fluor qui est reconnu pour son effet inhibiteur de la dégradation thermique du NiSi ainsi que pour sa tendance à s'attacher aux défauts dans les joints de grains des siliciures.

Nos premiers efforts de recherche se sont concentrés sur l'identification des composés supplémentaires observés. Grâce à la combinaison de mesures XRD *in situ*, de figure de pôle de diffraction ainsi que de diffraction des électrons en faisceau convergeant, nous avons réussi à identifier un premier composé supplémentaire comme étant le composé haute-température θ-Ni_2Si. Ce composé non-stœchiométrique se forme avant le NiSi en consommant du δ-Ni_2Si a des températures auxquelles le diagramme d'équilibre Ni-Si suggère qu'il est métastable. La présence d'un pic de diffraction autour de 27° suggère l'existence de lacunes ordonnées sur le sous-réseau de Ni et une composition intermédiaire à celles de δ-Ni_2Si et NiSi. En effet, normalement interdit par la structure hexagonale du θ-Ni_2Si, ce pic correspond à une périodicité égale au double de celle des plans 110. Pour toutes les épaisseurs initiales de la couche de Ni comprises entre 4 et 500 nm, on observe la formation du θ-Ni_2Si systématiquement à la même température (310°C) lors d'expériences de recuits en rampe à 3°C/s. Ce résultat suggère que la germination joue un rôle clé dans la formation du composé qui est d'ailleurs rapide et brève. En effet, sitôt formé, le θ-Ni_2Si se fait consommer par la formation du NiSi qui est accompagnée d'un retour surprenant du δ-Ni_2Si préalablement consommé. Ainsi au lieu de suivre une séquence continue en terme de composition comme on s'y attendrait en réactions en couches minces, le système passe du θ-Ni_2Si vers un composé plus riche en Ni.

L'analyse de la structure cristalline du θ-Ni_2Si révèle qu'elle est parente avec celles du δ-Ni_2Si et du NiSi. Nous montrons que cette particularité joue un rôle important tant dans la formation du θ-Ni_2Si que dans sa consommation. En fait, Gaudet *et al.* ont montré que les composantes de texture que l'on observe pour δ-Ni_2Si et θ-Ni_2Si sont équivalentes. Par ailleurs, Hodaj *et al.* ont montré que la germination du NiSi à l'interface δ-Ni_2Si/Si pouvait être gênée par des gradients de concentration. Nous proposons donc que la formation du θ-Ni_2Si s'explique par la combinaison de *i)* sa

faculté de germer facilement dans un gradient de concentration (étant un composé non-stœchiométrique), *ii)* la difficulté pour NiSi d'en faire autant et *iii)* un effet de gabarit offert par les grains de δ-Ni_2Si, qui résulte en une très faible énergie d'interface associée à la germination. Selon le diagramme d'équilibre, la présence de NiSi devrait rendre le θ-Ni_2Si instable. Ainsi, une fois que le NiSi a pu germer, vraisemblablement à partir du θ-Ni_2Si, ce dernier disparaît rapidement. Nous expliquons le retour du δ-Ni_2Si par le fait que le NiSi pompe les lacunes présentes dans les régions de θ-Ni_2Si non-transformées en croissant, enrichissant de manière effective ces dernières en Ni. Ces régions ainsi enrichies en Ni peuvent ensuite se retransformer facilement en δ-Ni_2Si, grâce à la parenté des structures cristallines.

En plus du θ-Ni_2Si, notre étude a révélé la formation du $Ni_{31}Si_{12}$ et du Ni_3Si_2 dans des échantillons où il reste du Ni non-réagi à des températures supérieures à 373 et 600 °C respectivement. Ceci se produit dans les échantillons avec au moins 100 et 500 nm de Ni au départ. La formation du $Ni_{31}Si_{12}$ consomme elle aussi du δ-Ni_2Si qui est restitué en partie lors de son départ. La formation du Ni_3Si_2 est quant à elle observée lorsque la couche de δ-Ni_2Si est presqu'entièrement consommée par la formation du NiSi au cours d'une réaction qui consomme tant du δ-Ni_2Si que du NiSi.

Une étude détaillée de la microstructure par microscopie électronique à transmission (MET) s'est concentrée sur les échantillons avec 10 et 100 nm de Ni au départ. Les échantillons ont été recuits et trempés au moment où soit le θ-Ni_2Si ou le $Ni_{31}Si_{12}$ sont au maximum de leur développement selon la XRD *in situ*. On observe dans les deux cas une surprenante co-existence, tantôt de grains de θ-Ni_2Si tantôt de grains de $Ni_{31}Si_{12}$, avec des grains de δ-Ni_2Si dans une même couche. Selon la compréhension actuelle des réactions en couches minces, on s'attendait plutôt à observer une co-existence de type couche-par-couche. Cette coexistence latérale de plusieurs composés

semble être encore plus importante dans les échantillons avec 100 nm de Ni. En effet, on observe dans les échantillons recuits jusqu'au développement maximal du θ-Ni_2Si des grains de θ-Ni_2Si, de Ni_3Si_2 ainsi que de NiSi dans la même couche. Grâce à la technique de XRD *in situ* nous avons pu préparer des échantillons où nous sommes capables d'observer la compétition cinétique que se livrent les différents composés capables de germer et que θ-Ni_2Si semble gagner. Cette compétition a été prédite par plusieurs modèles de réaction en phase solide, mais jamais observée directement.

La microstructure et la localisation des grains de $Ni_{31}Si_{12}$ laisse suggérer que leur germination a eu lieu dans les joints de grains la couche de δ-Ni_2Si, probablement en raison d'un afflux local important d'atomes de Ni. Ceci est en accord avec le fait que le Ni est reconnu comme l'espèce la plus mobile dans les siliciures de Ni. Le retour du δ-Ni_2Si lors de la consommation du $Ni_{31}Si_{12}$ s'explique cette fois-ci par une mobilité des atomes de Si qui devient importante alors que la température avoisine les 400 °C dans les recuits en rampe que nous avons utilisés. Leur afflux croissant provenant du substrat vient ainsi appauvrir en Ni les régions occupées par $Ni_{31}Si_{12}$, les forçant à se transformer en δ-Ni_2Si.

Cette première étape de recherche nous a donc permis de mettre en évidence non seulement la formation d'un plus grand nombre de composés que ce qui était habituellement rapporté dans le système Ni-Si, mais surtout d'observer des phénomènes très particuliers de réaction en phase solide, soit la co-existence latérale de plusieurs composés dans une même couche ainsi que des épisodes de formation non-séquentielle. La figure présentée à la page suivante compare de manière schématique la séquence de réaction traditionnellement rapportée dans la littérature (a) avec celle que nous observons dans les échantillons avec des couches de Ni d'épaisseur respectivement inférieure (b) et supérieure (c) à 100 nm. Alors que ces résultats sont d'une importance capitale pour la microélectronique, le θ-Ni_2Si et le $Ni_{31}Si_{12}$ se formant avant le NiSi, ils

revêtent également un intérêt fondamental très important pour le domaine des réactions en phase solide. En fait, nous montrons que plusieurs phénomènes importants se produisent à une échelle de temps qui échappe aux techniques traditionnelles d'investigation des réactions en phase solide.

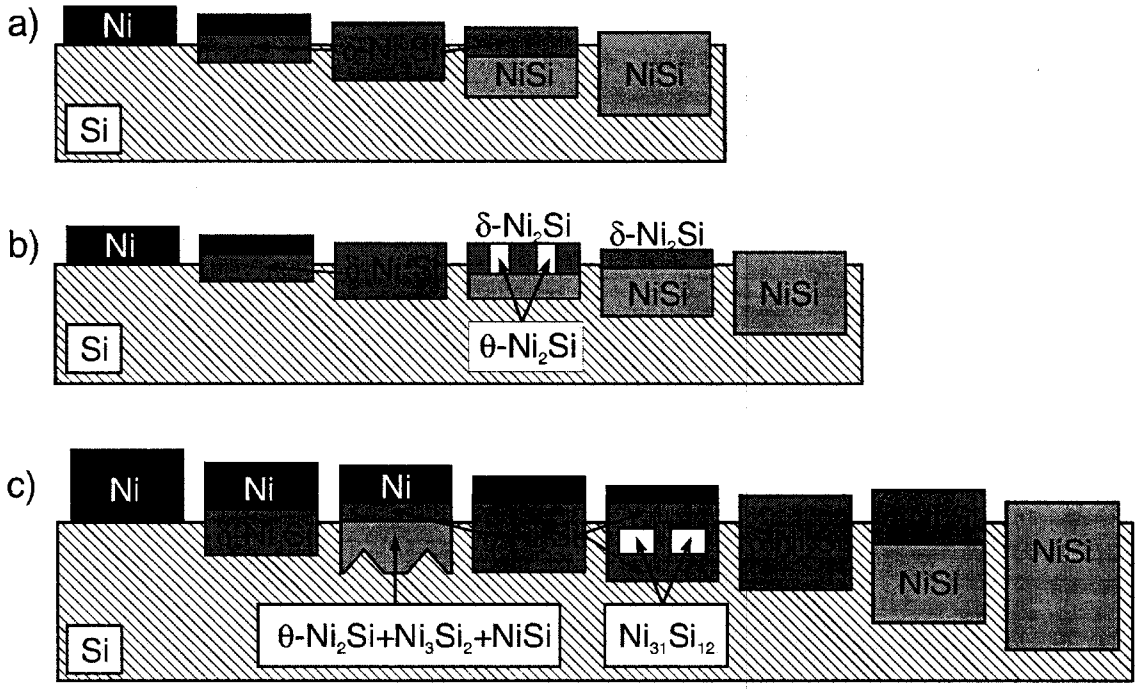

Figure C- 1: Comparaison des séquences de réaction a) traditionnellement rapportée avec celles que nous observons dans les échantillons avec b) moins de 100 nm et c) 100 nm de Ni et plus .

Afin de comprendre plus à fond les aspects énergétiques des réactions Ni-Si, nous avons étudié l'effet des impuretés alliées au Ni (Pt et Co) et implantées dans le Si (B, P, F, Si, N) sur les réactions. Nous observons que le platine et le cobalt, qui ont respectivement pour effet de favoriser et défavoriser la formation du NiSi, gênent tous deux la formation du θ-Ni_2Si. En effet, alors que celle-ci est supprimée dès l'addition de 5% de Pt, 15% de Co sont nécessaires pour parvenir à un résultat similaire. Nous déduisons de l'effet du platine que, tel que présumé plus tôt, la formation du NiSi joue effectivement un rôle déstabilisateur à l'endroit du θ-Ni_2Si. Cependant, nous suggérons

que c'est plutôt en raison d'une solubilité limitée dans le θ-Ni_2Si que le Co gêne la formation du composé.

De manière générale, la présence d'impuretés implantées dans le Si retarde la réaction, quoique la formation du NiSi soit complétée plus tôt en présence de phosphore. Cela dit, aucune des impurtés implantées ne supprime la formation du θ-Ni_2Si. Au contraire l'ajout de fluor stabilise de manière remarquable le composé, lui permettant d'exister sur une plus grande plage de température lors des recuits en rampe. Bien entendu, les concentrations d'impuretés atteintes lors de l'implantation dépassent difficilement les 2-3% comparativement aux 15% atteints avec les alliages. Quoiqu'il en soit, en plus de stabiliser le θ-Ni_2Si, le fluor supprime le retour du δ-Ni_2Si lors du départ du θ-Ni_2Si. Ce phénomène est attribuable en partie à la température plus élevée à laquelle la consommation du θ-Ni_2Si a lieu, mais également au fluor qui peuple les lacunes présentes sur le sous-réseau de Ni dans le composé non-stœchiométrique. Il bloque ainsi le mécanisme par lequel le NiSi peut pomper les lacunes et promouvoir la formation du δ-Ni_2Si. Cet effet du fluor nous a d'ailleurs permis d'identifier la signature du mécanisme de retour du δ-Ni_2Si dans les mesures de contrainte *in situ*. En effet, le départ de lacunes d'une région composée de θ-Ni_2Si doit s'accompagner d'une diminution de volume, qui se traduit par un mise en tension de l'empilement de couches minces. Ce phénomène donne lieu à un pic dans la courbe de contrainte en fonction du temps qui, à l'instar du retour du δ-Ni_2Si, est graduellement supprimé par une dose croissante de fluor.

Deux études complémentaires au cours desquelles les substrats de Si étaient soit amorphes soit implantés avec du Si (donc amorphisés) ou du N ont révélé des résultats similaires à ceux obtenus avec le fluor. Ceci indique donc que l'effet du fluor est à la fois chimique et physique et que la présence d'une interface de réaction amorphe, du moins au début de la réaction, contribue de manière importante à stabiliser le θ-Ni_2Si.

Cette deuxième étape de recherche nous a donc permis de vérifier l'hypothèse selon laquelle la germination du NiSi est la cause la plus probable du départ du θ-Ni_2Si en plus de confirmer le rôle important des lacunes dans la consommation du composé. Nous avons également démontré que la possibilité d'épitaxie avec le Si n'était pas nécessaire pour promouvoir la formation du θ-Ni_2Si, une condition souvent rapportée dans la littérature relative aux réactions en couches minces pour expliquer la stabilisation de composés métastables.

La formation du θ-Ni_2Si dans les couches ultra-minces étant particulièrement pertinente pour la microélectronique contemporaine, nous avons mis l'emphase, au cours d'une troisième étape de recherche, sur la cinétique de croissance de ce composé dans des échantillons avec 10 nm de Ni au départ. Nous avons observé que la formation du θ-Ni_2Si se produit en deux étapes claires et distinctes, surtout lors de recuits isothermes. Nous avons modélisé ces deux étapes avec succès en nous inspirant d'un modèle publié pour expliquer la croissance du δ-Ni_2Si sur substrats de Si amorphe. Le modèle original a été modifié de manière à permettre la coexistence latérale entre le θ-Ni_2Si et le δ-Ni_2Si. Nous avons donc modélisé le premier stade de formation comme une croissance contrôlée par la germination dans une interface amorphe. Ce premier stade fait ensuite place à un deuxième au cours duquel le θ-Ni_2Si pénètre dans les joints de grains du δ-Ni_2Si à travers un processus contrôlé par la diffusion du Ni. Nous avons modélisé ce phénomène à l'aide d'hémisphères dont la base est en contact avec la couche ayant germé dans le premier stade et dont le rayon croit avec la racine carrée du temps. Bien que ce modèle présente un accord remarquable avec les données expérimentales, nous ne pouvons exclure que le deuxième stade consiste en réalité en un épaississement unidimensionnel d'une couche continue, limité par la diffusion du Ni et avec une composition et un coefficient de diffusion qui varient en cours de réaction. Cela dit, ce dernier mécanisme n'est pas compatible avec une co-existence latérale du θ-

Ni_2Si et du δ-Ni_2Si telle que nous l'avons observée par microscopie électronique à transmission.

L'analyse de la cinétique de la consommation du θ-Ni_2Si nous indique que le processus est vraisemblablement limité par la germination et qu'il se produit dans une géométrie plane (bidimensinonelle). Les énergies d'activation obtenues pour les premier et deuxième stades de croissance ainsi que le stade de décomposition sont respectivement de 1.17 ± 0.5, 2.55 ± 0.5 et 1.65 ± 0.5 eV. Ces valeurs indiquent que le taux de réaction dans le deuxième stade de croissance devrait accélérer plus rapidement avec des changements de temperature que dans les deux autres stades. Cette conclusion s'accorde tout à fait avec nos résultats selon lesquels une quantité croissante de θ-Ni_2Si se forme dans les recuits isothermes effectués à plus haute température.

Pour terminer, nous avons étudié la cinétique de croissance du θ-Ni_2Si en présence de fluor de manière à comprendre plus à fond l'effet de cette impureté. Nous avons observé que le premier stade de germination se fait graduellement supprimer par une dose d'implantation croissante. Cependant, nous observons un troisième stade de croissance, surtout dans les échantillons implantés avec la plus forte dose. Ce troisième stade correspond à une croissance alors qu'il ne reste plus de δ-Ni_2Si ni de Ni. La formation du θ-Ni_2Si a donc lieu en l'absence de toute source externe d'atomes de Ni, un phénomène que nous avons modélisé comme un épaississement unidimensionnel d'une couche continue, limité par la diffusion du Ni et au cours duquel le coefficient de diffusion du Ni diminue alors que la teneur en Ni du θ-Ni_2Si diminue. En effet, une fois que le δ-Ni_2Si est complètement consommé par le θ-Ni_2Si, ce dernier devrait être présent sous forme d'une couche continue, ce que nos mesures de MET sur des échantillons implantés au fluor ont confirmé. Bien que nous n'ayons pas tenu compte explicitement de l'incorporation de fluor sur les sites lacunaires, cet effet est implicitement inclus dans la manière dont nous avons modélisé la variation de la composition et du coefficient de

diffusion. La variation de composition a été simulée par une variation du facteur de structure servant à calculer l'intensité diffractée et nous avons imposé une diminution du coefficient de diffusion malgré une diminution de l'occupation des sites lacunaires par le Ni. Par ailleurs, l'augmentation des énergies d'activation associés tant aux différents stades de croissance qu'à la consommation du θ-Ni_2Si corrobore l'hypothèse selon laquelle le fluor se greffe aux sites lacunaires, ralentissant et gênant la diffusion du Ni. Finalement, malgré la suppression du retour du δ-Ni_2Si et une augmentation de l'énergie d'activation, la cinétique de consommation du θ-Ni_2Si ne change pas de mode suite à une implantation de fluor. L'analyse indique encore un processus bidimensionnel contrôlé par la germination.

Cette troisième et dernière étape de recherche nous a permis de modéliser la croissance du θ-Ni_2Si, de proposer une explication pour la co-existence latérale entre le θ-Ni_2Si et le δ-Ni_2Si et de confirmer l'hypothèse selon laquelle la germination joue un rôle important dans la croissance du θ-Ni_2Si. De plus, l'effet du fluor sur les énergies d'activation confirme l'hypothèse selon laquelle les atomes de F se greffent aux sites lacunaires, influençant ainsi le chemin de réaction de la consommation.

Au cours de ce projet de doctorat, nous avons démontré à l'aide de techniques de caractérisation *in situ* qu'il pouvait exister des phénomènes importants qui échappent aux techniques traditionnelles d'investigation des réactions en phase solide. Notre étude s'est limitée aux systèmes en couches minces, mais ces conclusions peuvent également s'appliquer aux systèmes massifs. Nous avons non seulement mis en évidence la formation d'un nombre plus grand de composés pendant les réactions Ni-Si, mais surtout la manière dont plusieurs facteurs peuvent se combiner pour engendrer des comportements qui a priori bouleversent la compréhension commune des réactions en phase solide. Ainsi, on observe la formation du θ-Ni_2Si et un curieux retour du δ-Ni_2Si lors de sa consommation en raison de *i)* l'existence de gradients de concentration à

l'interface δ-Ni_2Si/Si qui gênent la germination du NiSi, *ii)* la similarité entre les structures cristallines du δ-Ni_2S, du NiSi et du θ-Ni_2Si qui permettent des effets de gabarits favorisant les transitions d'une structure à l'autre, *iii)* la faculté du θ-Ni_2Si à porter des lacunes et à germer dans un gradient de concentration étant donnée sa nature non-stœchiométrique et *iv)* la nature métastable de ce composé. Également, on observe la formation du $Ni_{31}Si_{12}$ et un second retour du δ-Ni_2Si en raison *i)* d'une compétition entre la cinétique de croissance des deux composés, *ii)* de la forte diffusion du Ni dans les joints de grains du δ-Ni_2Si et *iii)* d'une interruption abrupte de l'apport en Ni.

Au delà de leur impact sur la science des réactions en phase solide, les résultats de ce projet sont susceptibles de susciter un grand intérêt dans l'industrie de la microélectronique. En effet, le processus d'intégration de la métallurgie de contact à base de Ni à la technologie CMOS a été jalonné de plusieurs écueils. Outre les problèmes de stabilité thermique du NiSi, qui a la fâcheuse tendance à agglomérer à haute température, divers problèmes relatifs à la réaction en phase solide ont été rencontrés. Pour des raisons de confidentialité nous ne discutons pas les détails de ces problèmes dans le document. Cependant, il est intéressant de constater que l'alliage du platine au nickel, introduit par plusieurs compagnies dans l'industrie pour améliorer la stabilité thermique du NiSi, a également réglé plusieurs de ces problèmes. Or nous avons montré dans cette thèse que le platine avait pour effet de supprimer la formation du θ-Ni_2Si. Il est donc de l'avis du candidat que la formation du θ-Ni_2Si n'était pas étrangères aux problèmes mentionnés et que la compréhension amenée par la recherche que nous avons menée profitera directement à l'industrie de la microélectronique.

Ce projet de doctorat ouvre la porte à un vaste champ d'études. Entre autres, on connaît peu de chose sur les propriétés physiques de base du θ-Ni_2Si et leur dépendance à la composition. Il apparaît ainsi important de caractériser plus à fond les propriétés de ce composé. Également, le formalisme utilisé pour modéliser la croissance du θ-Ni_2Si a

été emprunté à une étude des réactions Ni-Si par calorimétrie différentielle à balayage (DSC). Cette technique permet une mesure directe de l'énergie échangée lors des réactions. Il serait donc particulièrement intéressant de revisiter les réactions Ni-Si par DSC à la lumière des informations supplémentaires que cette thèse apporte et notamment de voir si l'on peut déterminer l'ampleur des énergies impliquées dans la formation et la consommation du θ-Ni_2Si. Par ailleurs, plusieurs mesures de figure de pôle faites par notre groupe ont révélé la présence d'une couche fortement texturée à l'interface siliciure/Si dans les échantillons où le θ-Ni_2Si est présent. Cette couche dont le signal de diffraction est plus fort sur les échantillons implantés au fluor n'a à ce jour pas encore été identifiée (tant en composition qu'en structure cristalline). Il serait intéressant de vérifier si elle existe également lorsque la réaction a lieu sur Si amorphe et si c'est le cas, d'étudier la manière dont elle influence la réaction.

Sur le plan plus technologique, l'existence de lacunes mobiles proche du front de réaction a été une source de problème importante pour la métallurgie de contact à base de Co. Il serait intéressant de vérifier à quel point les lacunes, même en présence de Pt, sont susceptibles d'être à l'origine des problèmes mentionnés plus haut dans la synthèse du NiSi par réaction en phase solide dans les dispositifs microfabriqués.

Finalement, dans une perspective plus générale, il se fait de plus en plus de recherche sur les métamatériaux ou les matériaux nano-composites où le silicium est combiné à d'autres matériaux pour former des structures complexes aux propriétés particulières. On retrouve dans ces métamatériaux plusieurs interfaces, par exemple dans les systèmes de nanoparticules encastrées dans une matrice, où des siliciures sont susceptibles de se former et d'influencer les propriétés tant électriques que mécaniques des assemblages. La technique de diffraction des rayons-X *in situ* que nous avons présentée dans cette thèse pourrait être utilisée avantageusement pour étudier la formation et les caractéristiques de ces interfaces et ainsi développer des stratégies permettant d'optimiser leur propriétés.

TABLE OF CONTENT

DEDICATION ..... **IV**

ACKNOWLEDGEMENTS / REMERCIEMENTS ..... **V**

RÉSUMÉ ..... **IX**

ABSTRACT ..... **XIV**

CONDENSÉ EN FRANCAIS ..... **XVIII**

TABLE OF CONTENT ..... **XXXI**

LIST OF TABLES ..... **XXXIV**

LIST OF FIGURES ..... **XXXV**

LIST OF ACRONYMES AND ABBREVIATIONS ..... **XLVIII**

LIST OF SYMBOLS ..... **L**

Chapter 1 : INTRODUCTION **1**

1.1 TECHNOLOGICAL IMPORTANCE OF SILICIDES 1
1.2 SCALING ISSUES WITH SILICIDE PROCESSES 4
1.3 OBJECTIVES OF THE THESIS 9
1.4 STRUCTURE OF THE DOCUMENT 10

Chapter 2 : Thin-film solid-state reactions in the Ni-Si system **11**

2.1 BACKGROUND: FORMATION OF NEW COMPOUNDS FROM THE REACTION OF TWO ADJACENT SOLID PHASES 11
2.1.1 Diffusion in the solid-state *11*
2.1.2 Nucleation of a new crystalline compound in the intermixed region *16*
2.1.3 Selection of the first phase and phase formation sequence *19*
2.2 SOME IMPORTANT THIN FILM GROWTH KINETICS MODELS 23
2.2.1 The treatment of Johnson-Mehl-Avrami (JMA) for Nucleation-controlled growth *24*
2.2.2 The linear-parabolic growth model of Gösele and Tu *29*
2.2.3 Simultaneous growth of several compound layers *32*
2.2.4 Kissinger's analysis *36*

Chapter 3 : Formation of Ni silicides by solid-state reaction between Ni and Si: literature review **38**

3.1 FORMATION OF THE FIRST COMPOUND AND COMPOUND SEQUENCE 39
3.2 MOBILE SPECIES AND GROWTH KINETICS 47
3.3 INFLUENCE OF IMPURITIES 50
3.3.1 Impurities deposited as interlayers: Ti, Ge, and SiO_2 ..... *50*
3.3.2 Co-deposited impurities : Pt and Co *53*
3.3.3 Implanted impurities *57*
3.3.4 Effect of common implanted CMOS doping impurities : arsenic, boron and phosphorous *60*
3.3.5 Effect of BF_2^+ and fluorine *63*
3.4 CONCLUSION OF THE LITERATURE REVIEW 65

Chapter 4 : Experimental Techniques **68**

4.1 SAMPLE PREPARATION 68
4.2 IN SITU REAL TIME X-RAY DIFFRACTION 69
4.2.1 Principles and concepts *69*
4.2.2 Experimental setup *71*
4.2.3 Calibrations and assumptions *78*

4.2.4 Measurement of growth kinetics by X-ray diffraction *80*
4.3 TRANSMISSION ELECTRON MICROSCOPY 84
4.4 COMPLEMENTARY TECHNIQUES 87
4.4.1 Rutherford backscattering spectroscopy (RBS) *87*
4.4.2 Time-of-flight Secondary Ion Mass Spectroscopy (TOF-SIMS) *89*

Chapter 5 : Non-sequential formation and lateral co-existence of compounds during solid-state reactions in the Ni-Si system 92

5.1 INTRODUCTION 92
5.2 EXPERIMENTAL PROCEDURE 95
5.3 RESULTS 99
5.3.1 Compound sequence and microstructure in 10-nm-thick Ni/Si(001) samples *99*
5.3.2 Compound sequence and microstructure in 100-nm-thick Ni/Si(001) samples *109*
5.4 DISCUSSION 128
5.4.1 Lateral co-existence of compounds and nucleation in grain boundaries *128*
5.4.2 Non-sequential formation of compounds *130*
5.5 CONCLUSION 142

Chapter 6 : Effects of Ni-alloying, implanted impurities, and substrate crystallinity 144

6.1 INTRODUCTION 144
6.2 EXPERIMENTAL PROCEDURE 145
6.2.1 Implantation *145*
6.2.2 Metal and alloy deposition *146*
6.2.3 In situ XRD during annealing *147*
6.2.4 Ex situ analyses *149*
6.3 RESULTS 150
6.3.1 A. Effect of alloying *150*
6.3.2 Effect of CMOS dopants *154*
6.3.3 Effect of F, Si and N implantation *157*
6.3.4 Formation on amorphous Si substrates *166*
6.4 DISCUSSION 168
6.4.1 Effect of alloying impurities *168*
6.4.2 Effect of CMOS doping impurities and microstructure *170*
6.4.3 Effect of F, Si and N implantations and stress *170*
6.5 CONCLUSION 173

Chapter 7 : Growth kinetics of θ-Ni_2Si on undoped and F-implanted Si (001) substrates 174

7.1 INTRODUCTION 174
7.2 EXPERIMENTAL PROCEDURES 175
7.2.1 Sample preparation *175*
7.2.2 In situ XRD during annealing *175*
7.2.3 Kinetics analyses and extraction of the integrated diffracted intensities *177*
7.3 RESULTS: 181
7.3.1 Undoped Si *181*
7.3.2 F- implanted Si(001) *190*
7.4 ANALYSIS AND DISCUSSION 198
7.4.1 Growth kinetics of θ-Ni_2Si on Undoped c-Si (001): The Coffey-Clevenger-Barmak-Rudeman-Thompson model *198*
7.4.2 Analysis of the θ-Ni_2Si growth kinetics using the CCBRT model *203*
7.4.3 Analysis of the θ-Ni_2Si growth kinetics using a modified CCBRT model *209*
7.4.4 1D-diffusion-controlled growth with non-constant diffusion coefficient. *220*

7.4.5 Effect of fluorine on the θ-Ni_2Si growth kinetics *227*
7.4.6 Consumption of θ-Ni_2Si *231*
7.4.7 Activation energies *233*
7.5 CONCLUSION 234

Chapter 8 : Conclusion, general discussion, and perspectives 235

8.1 SUMMARY OF THE RESULTS 235
8.2 CURRENT UNDERSTANDING OF SOLID STATE REACTIONS 238
8.3 TECHNOLOGICAL IMPACT OF θ-NI_2SI 240
8.4 PERSPECTIVES 241

REFERENCES 244

LIST OF TABLES

Table 3-1: Composition and crystal structures of selected Ni-Si compounds 40

Table 4-1: X-ray attenuation lengths in some Ni silicides..... 82

Table 5-1: Silicide layer thicknesses (nm) determined by TEM (Figure 5.11) and RBS. 117

Table 6-1: Implanted concentrations as a function of dose determined using the implantation range simulated with TRIM® and assuming a Si density of 4.99_10^{22} at. cm^{-3} 147

Table 7-1: Isothermal annealing parameters. Duration (min) and temperature of the reaction. 176

Table 7-2: Temperatures of maximum θ-Ni_2Si growth and consumption rates for the Kissinger's analysis of the reactions on undoped Si(001). 188

Table 7-3: Time to half-rise during the 1st growth stage on undoped Si(001). 203

Table 7-4: List of parameters for the fits of the CCBRT model to the experimental growth data. 206

Table 7-5: List of parameters for the fits of the modified CCBRT model to the experimental growth data. 215

Table 7-6: Atomic positions in the θ-Ni_2Si unit cell for the calculation of the structure factor F_{hkl} 223

LIST OF FIGURES

Figure 1.1: Cross-sectional transmission electron micrograph of four contemporary CMOS transistors. Structures marked with a white "X" extend over long distances perpendicular to the plane of the page. 1

Figure 1.2: Illustration of the silicide synthesis by thin-film solid-state reaction. Cross-sectional view. 2

Figure 1.3: Self-aligned silicide solid-state sythesis in a typical CMOS integrated circuit fabrication process. 3

Figure 1.4: Co-Si equilibrium phase diagram. 4

Figure 1.5: a) Reaction of two semi-infinite solid slabs. b) Reaction between a thin film and a thick substrate. The compositions of the compounds are arbitrary however the figure suggests that i/j>m/n>x/y The chronological order of appearance of the compounds is also arbitrary. 5

Figure 1.6: Schematic illustration of the effect of low stable nuclei density on the silicide synthesis in small dimension features. As the silicided structures get smaller, conversion to C54 $TiSi_2$ is prevented in nucleus-free regions. The reaction process is viewed from the top. 6

Figure 1.7: Schematic illustration of the formation process of CoSi. Si diffuses through the growing layer and reacts with Co_2Si to form CoSi. Vacancies left in the Si coalescence into voids at the silicide/Si interface. 7

Figure 1.8: Nickel-Silicon equilibrium phase diagram. 8

Figure 2.1: Diffusion at the interface between two elemental materials. The concentration gradients are arbitrarily drawn as linear although it may not be the case. 12

Figure 2.2: Schematic molar Gibbs free-energy diagrams of a A-B binary system showing the origin of the gradients in the chemical potentials. 14

Figure 2.3: Schematic molar free-energy diagram illustrating the driving force for compound formation the intermixed region. 15

Figure 2.4: Schematic diagram of the nucleation barrier arising from the existence of an interface energy 17

Figure 2.5: EHF diagram and phase diagram for the Ni-Si system. (Taken from Ref. [13]) 21

Figure 2.6: a) 2D view of nucleation in a matrix of uniform composition, b) Impingement of nuclei. 25

Figure 2.7: Treatment of the impigement between growing nuclei. The extended transformed volume fraction includes the shaded area while the effective volume fraction excludes it. 27

Figure 2.8: Concentration gradients across a layer growing at the interface between two solid phases. (From reference 25.) 30

Figure 2.9: Concentration gradients across two layers growing at the interface between two solid phases. (From reference 25) 34

Figure 2.10: Growth regime diagrams for a) the general case and the cases where b) diffusion is limiting in both phases, c) interface reaction is limiting in both phases and d) diffusion and interface reaction are respectively limiting in $A_{\gamma}B$ and $A_{\beta}B$. From reference 25. 35

Figure 3.1: The Ni-Si phase diagram 39

Figure 3.2: a) bulk and b) Lateral diffusion couples. 44

Figure 3.3: Summary of the formation of Ni silicides, actual figure 5 of Tu *et al.* (Reference 63). 46

Figure 4.1: Diffraction at an angle 2θ from crystallographic planes spaced by a distance d. 70

Figure 4.2: a) Each grain of a polycrystalline sample is an individual crystal. Diffraction occurs whenever a hkl planes familiy satisfies the Bragg's law, i.e. that the bisector b is perpendicular to the planes. a) Diffraction from a polycrystalline sample yields several diffracted beams with fixed angle incident beam. 71

Figure 4.3: Schematic bird's eye view of a synchrotron. Arrows indicate the position of end stations. 73

Figure 4.4: Schematic diagram of the *in situ* annealing chamber. 76

Figure 4.5: a) Typical *in situ* x-ray diffraction result obtained during the annealing of a 100nm Ni layer on a Si (001) substrate along with b) the corresponding resistance and light scattering traces for two different length scales..... 77

Figure 4.6: Diagram of the flat versus curved detector. The data from the detector's controller provides a measure of intensity versus S..... 79

Figure 4.7: Evolution of the temperature correction factor as a function of temperature for Ni and Si. (Calculations made with the analytical form associated to cubic materials)..... 84

Figure 4.8: Process flow of TEM specimen preparation. 85

Figure 4.9: Schematic diagram of the energy spectrum of ions (m_1, Z1, E_0) scattered from a sample composed of a substrate (m_2, Z_2) and a surface film (m_3,Z_3) of thickness d. 89

Figure 4.10: Schematics of the SIMS technique. 90

Figure 5.1: XRD intensity contour maps ($\lambda = 0.1797$ nm) plotted as a function of annealing temperature T_a during a thermal ramp at 3 °C s^{-1} in purified He for a 10-nm-thick Ni layer deposited on c-Si(001) for three different 14° wide 2θ windows centered at (a) 27°, (b) 42°, and (c) 55°. (d) Resistance and light-scattering signals measured in situ during the same annealing experiments. LS 0.5 μm and LS 5 μm correspond to the light scattering intensity signals measured at angles selected to probe surface roughness variations for in-plane correlation lengths of 0.5 and 5 μm, respectively. 100

Figure 5.2: XRD intensities, integrated over angular ranges indicated in Fig. 1, as a function of annealing temperature during a thermal ramp at 3 °C s^{-1} in purified He for a 10-nm-thick Ni layer deposited on c-Si(001). Curve 1 is for δ-Ni_2Si (013)/(211), curve 3 for δ-Ni_2Si(020), curves 2 and 5 for θ-Ni_2Si, curve 4 for NiSi(011)/(002). 102

Figure 5.3: Pole figures from a 10-nm-thick Ni layer deposited on c-Si(001) annealed at 3 °C s^{-1} in purified He up to 325 °C (dashed line 2 in Fig. 1) and then quenched. (a) is for d = 0.191 nm and (b) is for d = 0.203 nm..... 104

Figure 5.4: (a) XRD intensity contour map (λ = 0.1797 nm) plotted as a function of annealing time t_a during an isothermal anneal at T_a = 260 °C for a 10-nm-thick Ni layer deposited on undoped SOI (001). (b) XRD intensities, integrated over the angular ranges indicated in (a), vs t_a for δ-Ni_2Si(013)/(211), θ-Ni_2Si, and δ-Ni_2Si(020)..... 105

Figure 5.5: Bright-field XTEM micrograph from a 10-nm-thick Ni layer on SOI (001) substrate isothermally annealed at T_a = 260 °C for t_a = 700 s (see dashed line in Figure 5.4). The image was recorded with the electron beam parallel to the [011] direction of the top Si slab of the SOI substrate. 107

Figure 5.6: Higher-magnification bright-field XTEM micrographs (a)-(c) together with convergent beam electron diffraction (CBED) patterns acquired in the location indicated by white circles (d)-(f) taken in different areas of the sample shown in Figure 5.5. Micrographs were recorded with the electron beam parallel to the zone axes for the CBED patterns..... 108

Figure 5.7: a) Schematic representation of the traditionally reported reaction sequence compared with b) the sequence we observed during the reactions between 10nm Ni layers and Si (001) substrates during both ramp-type and isothermal anneals..... 109

Figure 5.8: XRD intensity contour maps (λ = 0.1797 nm) plotted as a function of annealing temperature T_a during a thermal ramp at 3 °C s^{-1} in purified He for a 100-nm-thick Ni layer deposited on c-Si(001) for three different 14° wide 2θ windows centered at (a) 29°, (b) 42°, and (c) 55°. (d) Resistance and light-scattering signals measured in situ during the same annealing experiments..... 111

Figure 5.9: XRD intensities, integrated over angular ranges indicated in Fig. 7, as a function of annealing temperature during a thermal ramp at 3 °C s^{-1} in

purified He for a 10-nm-thick Ni layer deposited on c-Si(001). Curve 1 is for δ-Ni_2Si (301)/(121), curve 2 for δ-Ni_2Si (002), curve 3 for θ-Ni_2Si, curve 4 for NiSi (011)/(002), and curve 5 for NiSi (111)/(102)..... 112

Figure 5.10: (a) Bending force and (b) XRD intensity with the detector centered at 2θ = 55°C as a function of temperature acquired *in situ* during a 0.3 °C s^{-1} ramp anneal for a 100-nm-thick Ni layer on c-Si(001). Dashed lines indicate quench temperatures for the XTEM investigations presented in Figure 5.11..... 113

Figure 5.11: Bright field XTEM micrographs from 100-nm-thick Ni layers on c-Si(001): (a) as deposited and quenched at T_a values of (b) 295, (c) 310, (d) 330, (e) 355, (f) 373, (g) 400, and (h) 600 °C – as indicated by dashed lines in Figure 5.10– following a 0.3 °C s^{-1} ramp anneal. All images were recorded with the electron beam parallel to the [011] direction of the Si substrate. 115

Figure 5.12: (a) Bright-field XTEM micrograph together with (b)-(d) CBED patterns taken at locations indicated in (a) from a 100-nm-thick Ni layer annealed at 0.3 °C s^{-1} up to 310 °C. The XTEM image and the corresponding CBED patterns were acquired in a region of the TEM specimen that was thinned such as the top part of the layer stack visible in Figure 5.11 (c) was removed..... 118

Figure 5.13: (a) Bright-field XTEM micrograph together with (b) a corresponding CBED pattern taken at the location indicated in (a) from a 100-nm-thick Ni layer annealed at 0.3 °C s^{-1} up to 373 °C..... 120

Figure 5.14: Glancing angle RBS spectra from as deposited 100-nm-thick Ni layers on c-Si(001) and subjected to a 0.3 °C s^{-1} ramp anneal: (a) as-deposited and annealed at T_a = 295, 310, and 330 °C, (b) annealed at T_a = 355, 373, 400, and 600 °C. Solid lines correspond to RUMP simulations summarized in Table 5-1..... 122

Figure 5.15: a) Schematic representation of the traditionally reported reaction sequence compared with b) the sequence we observed during the reactions between 100nm Ni layers and Si (001) substrates during ramp-type anneals. 123

Figure 5.16: XRD intensity contour maps ($\lambda = 0.1797$ nm) plotted as a function of annealing temperature T_a during thermal ramps at 3 °C s^{-1} in purified He for (a) 4, (b) 6, (c) 10, (d) 15, (e) 30, (f) 50, (g) 100, and (h) 500 nm-thick Ni films on c-Si(001). The detector is centered at $2\theta = 55°$. 125

Figure 5.17: Ratio of the integrated θ-Ni_2Si(110) and Ni(111) peak intensities ($I_{\theta\text{-}Ni2Si}/I_{Ni}$) (▩) together with the θ-Ni_2Si formation (■) and dissolution (●) temperature as a function of initial Ni film thickness. These temperatures were taken as the local minimum and maximum of the derivative of the integrated intensity under the θ-Ni_2Si (110) peak with respect to temperature. The error bar represent uncertainties of 5 °C on temperatures and 5% on intensities..... 126

Figure 5.18 : a) Unit cell of the hexagonal θ-Ni_2Si crystal structure and (b) corresponding calculated diffraction curve for $\lambda = 0.1797$ nm. 132

Figure 5.19 : θ-Ni_2Si supercells consisting of 2x2x2 unit cells with vacancies arbitrarily ordered on the inner Ni sublattice to obtain compositions of (a) Ni_3Si_2 and (b) Ni_7Si_4. (c) corresponding calculated diffraction curves for $\lambda = 0.1797$ nm..... 134

Figure 5.20:Projection of the (θ)-Ni_2Si unit cell perpendicular to [001] direction (left) compared to the θ-Ni_2Si projection perpendicular to [110] direction (right) demonstrating the close match between the d-spacings for the δ-Ni_2Si (020) and θ-Ni_2Si (110) planes. The two darker shades of grey identify Ni atoms and the lighter shade of grey identifies Si atoms..... 136

Figure 6.1: a)-d) XRD intensity contour maps ($\lambda = 0.1797$ nm) plotted as a function of annealing temperature T_a during thermal ramps at 3 °C s^{-1} in purified He for

10-nm-thick Ni(Pt)-Alloy layers deposited on c-Si(001) with Pt content ranging from 0 to 15 %. e) Corresponding *in situ* resistance data normalized to the maximum value reached during Ni-rich silicide formation..... 152

Figure 6.2: a)-d) XRD intensity contour maps ($\lambda = 0.1797$ nm) plotted as a function of annealing temperature T_a during thermal ramps at 3 °C s^{-1} in purified He for 10-nm-thick Ni(Co)-Alloy layers deposited on c-Si(001) with Co content ranging from 0 to 15%. e) Corresponding *in situ* resistance data normalized to the maximum value reached during Ni-rich silicide formation..... 153

Figure 6.3: XRD intensity contour maps ($\lambda = 0.1797$ nm) plotted as a function of annealing temperature T_a during thermal ramps at 3 °C s^{-1} in purified He for 10-nm-thick Ni layers deposited on a) undoped b) B-doped and c) P-doped c-Si(001) d) Corresponding *in situ* resistance (thick lines) and light scattering data (thin lines) . Resistance is normalized to the value at the beginning of the reaction..... 156

Figure 6.4: a) XRD intensity contour map ($\lambda = 0.1797$ nm) plotted as a function of annealing time during the 43min isothermal annealing at 260°C in purified He of a 10-nm-thick Ni layer deposited on B-doped c-Si(001) b) Bright-field TEM Cross-sectional micrograph of the sample annealed in a) with c) and d) convergent beam electron diffraction (CBED) patterns acquired from regions labeled in b)..... 157

Figure 6.5: a)-c) XRD intensity contour maps ($\lambda = 0.1797$ nm) plotted as a function of annealing temperature T_a during thermal ramps at 3 °C s^{-1} in purified He for 10-nm-thick Ni layers deposited on c-Si(001) implanted with F at doses ranging from $3 \cdot 10^{14}$ to $3 \cdot 10^{15}$ at cm^{-2} d) Corresponding *in situ* resistance including the data for undoped Si. Resistance is normalized to the value at the beginning of the reaction..... 159

Figure 6.6: Bright-filed TEM cross-sectional micrographs of a) 10 nm Ni with a20 nm TiN cap as deposited on F-implanted SOI ($3 \cdot 10^{15}$ cm^{-2}), and b) 10 nm Ni as deposited on undoped SOI, as well as c) 10 nm Ni with a 20 nm TiN cap on

F-implanted SOI ($3 \cdot 10^{15}$ cm^{-2}) after a thermal ramp at 3 °C s^{-1} in purified He quenched at 380°C. d) CBED pattern acquired from the region labeled in c). 161

Figure 6.7: a) *in situ* bending force plotted as a function of annealing temperature T_a during thermal ramps at 0.3 °C s^{-1} in purified He for 10-nm-thick Ni layers deposited on c-Si(001) implanted with F doses ranging from $3 \cdot 10^{14}$ to $3 \cdot 10^{15}$ at cm^{-2} b) and c) corresponding *in situ* XRD intensity contour maps ($\lambda = 0.1797$ nm) for the un-implanted and $3 \cdot 10^{15}$ cm^{-2} F-dose cases..... 162

Figure 6.8: SIMS depth profiles of ionic species F^+ and SiF^+ in samples with 10nm Ni on c-Si(001) implanted with $3 \cdot 10^{15}$ F cm^{-2} after deposition - ● -, after thermal ramps at 3 °C s^{-1} in purified He quenched at 330 °C (θ-Ni_2Si) - ● - and 600 °C (NiSi) - ● - 163

Figure 6.9: XRD intensity contour maps ($\lambda = 0.1797$ nm) plotted as a function of annealing temperature T_a during thermal ramps at 3 °C s^{-1} in purified He for 10-nm-thick Ni layers deposited on c-Si(001) implanted with Si at doses of $1 \cdot 10^{15}$ and $5 \cdot 10^{15}$ d) Corresponding *in situ* resistance data. Resistance is normalized to the value at the beginning of the reaction. 165

Figure 6.10: XRD intensity contour maps ($\lambda = 0.1797$ nm) plotted as a function of annealing temperature T_a during thermal ramps at 3 °C s^{-1} in purified He for 10-nm-thick Ni layers deposited on c-Si(001) implanted with N at doses of $1 \cdot 10^{15}$ and $5 \cdot 10^{15}$ d) Corresponding *in situ* resistance data. Resistance is normalized to the value at the beginning of the reaction. 165

Figure 6.11 : XRD intensity contour maps ($\lambda = 0.1797$ nm) plotted as a function of annealing temperature T_a during thermal ramps at 3 °C s^{-1} in purified He for 10-nm-thick Ni layers deposited on a) c-Si(001) and b) a-Si. c) Corresponding *in situ* resistance data. Resistance is normalized to the value at the beginning of the reaction. 167

Figure 7.1: (a) XRD intensity contour map ($\lambda = 0.1797$ nm) plotted as a function of annealing time during the isothermal annealing at 250 °C in purified He of a 10-nm-thick Ni layer deposited on c-Si(001). (b) Single spectrum taken along the dotted line in (a) together with typical fitting results. Circles (o) represent data points, the different fitted peaks are plotted in light grey, and the resulting sum of all fitted peaks in plotted in solid black. The hatched area represents the integrated intensity. 179

Figure 7.2: XRD intensity contour map ($\lambda = 0.1797$ nm) plotted as a function of annealing time during the isothermal annealing in purified He of 10-nm-thick Ni layer deposited on c-Si(001) at (a) 240, (b) 250, (c) 260, (d) 270 and (e) 280 °C. 182

Figure 7.3: (a) and (b) Integrated diffracted intensity I_i along with (c) and (d) position of the θ-Ni_2Si (110) and δ-Ni_2Si (013)/(211) XRD peaks as a function of time during the growth of the θ-Ni_2Si and the concurrent consumption of δ-Ni_2Si during isothermal annealing of 10-nm-thick Ni layer deposited on c-Si(001) at temperatures between 240 and 280°C in purified He. The dashed lines indicate critical points for the 260 °C anneal. The dashed circle in (b) indicates the strong decrease of the δ-Ni_2Si (013)/(211) peak. 183

Figure 7.4: (a) Raw summed intensity under the θ-Ni_2Si (110) (red) and δ-Ni_2Si (002) (black) XRD peaks in the early stages of the growth during the reaction of a 10nm Ni layer on c-Si(001) at 260°C in purified He. (b) XRD intensity contour map ($\lambda = 0.1797$ nm) plotted as a function of annealing time with the angular ranges over which the summations are performed: [54.75 56.25] (red) and [56.25 58]. 185

Figure 7.5: XRD intensity contour map ($\lambda = 0.1797$ nm) plotted as a function of annealing temperature T_a during thermal ramps in purified He of 10-nm-thick Ni layers deposited on c-Si(001) at (a) 0.3 °C/s, (b) 1 °C/s, (c) 3 °C/s, (d) 9 °C/s and (e) 27 °C/s from 100 °C to 450 °C. 187

Figure 7.6: (a) XRD intensity summed over a range of 2° about the θ-Ni_2Si (110) peak (56.2°) during ramp anneals of Figure 7.5. (b) Derivative of the XRD summed intensity (a) (growth rate). (c) and (d) Kissinger's analysis for the growth and consumption of θ-Ni_2Si using the critical temperature values obtained from (b) and summarized in Table 7-2. 188

Figure 7.7: (a) Avrami plots of the θ-Ni_2Si (110) intensity summed (not fitted) over a range of 2° (2θ) about 56.2° for isothermal anneals in purified He of 10nm Ni layers on undoped c-Si (001) at temperatures between 240 and 280 °C and (b) Arrhenius plot of the Avrami constant..... 190

Figure 7.8: XRD intensity contour map (λ = 0.1797 nm) plotted as a function of annealing time during the isothermal annealing in purified He of 10-nm-thick Ni layer deposited on c-Si(001)) implanted with 0, 3×10^{14}, 1×10^{15} and 3×10^{15} F at. cm^{-2}. (a)-(c) 250 °C and (d)-(g) 280 °C isothermal annealing. 192

Figure 7.9: Ratio of XRD peak intensities (raw data, not fitted) during the isothermal annealing at 280 °C in purified He of 10-nm-thick Ni layer deposited on c-Si(001)) implanted with 0, 3×10^{14}, 1×10^{15} and 3×10^{15} at. F cm^{-2} (c.f. Figure 7.8 (d)-(g)). ■ δ-Ni_2Si (013) after its angle shift / initial Ni(111), ● δ-Ni_2Si (002) after its angle shift / initial Ni(111), ● θ-Ni_2Si (110) at the maximum of its development / initial Ni(111) and ● θ-Ni_2Si (110) at time of its maximum development / δ-Ni_2Si (013) after its angle shift..... 193

Figure 7.10: Integrated intensity of the θ-Ni_2Si (110) peak as a function of time during the isothermal annealing in purified He of 10 nm Ni layers on undoped and F-implanted Si(001). (a) Annealing at constant temperature of 280°C with doses of 0, 3×10^{14}, 1×10^{15} and 3×10^{15} F atoms cm^{-2}, and (b) between 270°C and 300°C with a constant F dose of 3×10^{15} at. cm^{-2}. 194

Figure 7.11: (a) XRD intensity summed over a range of 2° about the θ-Ni_2Si (110) peak (56.2°) during ramp anneals at 0.3, 1, 3, 9, and 27 °C/s in purified He of 10nm Ni layers deposited on c-Si(001) implanted with 3×10^{15} F at. cm^{-2} (b) Derivative of the XRD summed intensity in (a) (growth rate). (c) Kissinger analysis of the growth regime associated to the consumption of the δ-Ni_2Si (2nd regime). (d) Kissinger's analysis of the growth regime in absence of δ-Ni_2Si (3rd regime). 195

Figure 7.12: Avrami plots of the θ-Ni_2Si (110) intensity summed (not fitted) over a range of 2° (2θ) about 56.2° for isothermal anneals in purified He of 10nm Ni layers on c-Si (001) implanted with (a) 3×10^{14} and (b) 1×10^{15} F at. Cm^{-2} at temperatures between 250 and 300 °C along with (c) the Arrhenius plot of the Avrami constants in (a) and (b). (d) Kissinger's analysis of the θ-Ni_2Si consumption during ramp anneals at 0.3, 1, 3, 9, and 27 °C/s in purified He of 10nm Ni layers deposited on c-Si(001) implanted with 3×10^{14}, 1×10^{15}, and 3×10^{15} F at. cm^{-2}. 197

Figure 7.13: Illustration of the Coffey-Clevenger-Barmak-Rudman-Thompson (CCBRT) model. 199

Figure 7.14: (a) Apparent activation energy for the site-saturated nucleation-controlled growth during the 1ststage of the reaction determined using the formalism of the CCBRT model, (b) $Log(I_i^2-I_{i0}^2)$ vs $Log(t-t_0)$ plot assuming diffusion-controlled thicknening during the 2nd growth stage using the formalism of the CCBRT model, (c) $(I_i^2-I_{i0}^2)$ vs $(t-t_0)$ assuming diffusion-controlled thicknening during the 2nd growth stage and d) apparent activation energy for the diffusion-controlled thicknening. 204

Figure 7.15: Transformed θ-Ni_2Si volume fraction as a function of time during the isothermal annealing of 10 nm Ni layers on c-Si (001) at different temperatures. Comparison of the CCBRT model with the experimental data.

Dashed curves represent simulations and colored data markers represent experimental data. 207

Figure 7.16: Arrhenius plot of the growth rates *dr/dt* (blue lines) and *dz/dt* (red lines). Growth rates *dr/dt* are evaluated for nucleation site density η values of 1×10^{14} cm^{-2} (top blue curve) and 2.5×10^{9} cm^{-2} (bottom blue curve). Growth rate *dz/dt* evaluated for a thickness of 15 nm. 209

Figure 7.17: non-planar growth microstructure of Nb_2Al 210

Figure 7.18: Modified CCBRT model with a second stage consisting of the non-planar diffusion-controlled penetration of θ-Ni_2Si into the grains of the overlying δ-Ni_2Si. 211

Figure 7.19: (a) Avrami analysis of the second stage of the θ-Ni_2Si growth according to the modified CCBRT model and (b) Arrhenius plot of the Avrami constant obtained in (a). 214

Figure 7.20: (a)Comparison of the modified CCBRT model with the experimental data on a logarithmic time scale for all the investigated temperatures (240 – 280 °C). (b) Comparison of the original and modified CCBRT models with the 260°C experimental data on a linear time scale. 216

Figure 7.21: a) Avrami analysis of the growth data simulated using the original CCBRT model. b) Diffusion-controlled growth analysis [$\mathrm{Log}(\chi_v^2-\chi_{v0}^2)$ vs $\mathrm{Log}(t-t_0)$] for the growth data simulated using the modified CCBRT model. 217

Figure 7.22: a) Simulation of Avrami-like growth with an exponent of 1.5. The different colors indicate different values of the transformed fraction at which the growth is interrupted. b) Avrami analysis of the data in a). 218

Figure 7.23: a) Avrami plot of the δ-Ni_2Si consumption using the integrated intensity under the (013)/(211) XRD peak. b) Arrhenius plot of the Avrami constant. 219

Figure 7.24: Unit cell of θ-Ni_2Si. The hatched and cross-hatched atoms build the motif which serves for the calculation of the structure factor. 222

Figure 7.25: a) Structure factor of the θ-Ni_2Si (110) reflection as a function of the occupancy of the Ni sites (crosshatched atomes in Figure 7.24) and composition (top x-axis). b) Position of the θ-Ni_2Si (110) XRD peak as a function of composition. 224

Figure 7.26: Simulations of growth using the CCBRT model incorporating a compositional variation. The diffusion constant K_{d0} and structure factor F_{hkl} vary as √time on the left and as time on the right. a),e) K_{d0} and F_{hkl} vs time, b),f) comparison of the simulations with the experimental data, c),d) Avrami Analysis and d),h) diffusion-controlled growth analysis. 226

Figure 7.27: Comparison on a linear time scale of the growth data at 280°C with a modified CCBRT model where the third growth stage consists of 1D diffusion-controlled growth. 228

Figure 7.28: Comparison of two modifications of the CCBRT model with the experimental data on samples with 3E15 F cm^2. Data plotted on logarithmic (left) and linear (right) time scales. (a)-(b) Varying diffusion coefficient and (c)-(d) Varying diffusion coefficient and composition. 229

Figure 7.29: Kinetics analyses of the experimental and simulated growth data. (a),(c) and (e) Avrami Analysis, (b),(d) and (f) Diffusion-controlled growth analysis. Growth data simulated using the modified CCBRT model with (c), (d) varying K_2, and (e), (f) varying K_2 and F_{hkl}. 230

LIST OF ACRONYMES AND ABBREVIATIONS
(Alphabetical)

a-Si	Amorphous Silicon
BNL	Brookhaven national laboratory
CCD	Charge coupling device
CMC	Congruently melting compound
CMOS	Complementary metal-oxide-semiconductor
c-Si	Monocrystalline silicon
EHF	Effective heat of formation
EPD	Equilibirum Phase Diagram
FEG	Field emission gun
GB	Grain Boundary
JEOL	Japanese electron optics limited
LS	Light scattering
MRC	Materials Research Corporation
MS	Mass spectrometer
NSLS	National Synchrotron Light Source
OCAR	Ordered Cu_3Au rule
OME	Oxide mediated epitaxy
PID	Proportional integral derivative
poly-Si	Polycrystalline silicon
PPB	Parts per billion
RBS	Rutherford backscattering spectroscopy
SIMS	Secondary ion mass spectroscopy
SOI	Silicon on insulator

TEM	Transmission electron microscopy
TOF	Time of flight
UHP	Ultra-high purity
XRD	X-ray diffraction

LIST OF SYMBOLS
(In order of appearance in the text)

Chapter 2

$J_{diff\text{-}I}$	Diffusion flux of species i
D_i	Diffusion coefficient of species i
C_i	Concentration of species i
m_i	Mobility of species I
μ_i	Chemical potential of species i
k	Boltzmann's constant (8.316 E-5 eVK^{-1})
T	Temperature
Δg_A	Molar Gibbs free energy change for species A
Δg_B	Molar Gibbs free energy change for species B
E_η	Total energy of a nucleus
$\Delta G_{A_mB_n}$	Gibbs free energy of formation of the compound A_mB_n
r	Radius of a nucleus
σ_{surf}	Surface energy of a nucleus
r^*	Critical radius of a nucleus
E_η^*	Energy of nucleus with a critical radius
g(T)	Nucleation rate
E_{diff}	Activation energy for the diffusive atomic rearrangement
a,b	Geometrical factors for nucleation with anisotropic surface energy
$\Delta H'$	Effective heat of formation of an arbitrary compound
ΔH^0	Heat of formation of an arbitrary compound
t	time
v_t	volume of a growing nucleus
Γ	Line growth velocity

τ	Birth time of nuclei or incubation time
V_β	Transformed volume
V	Total volume of the host matrix
V_e^β	Extended transformed volume
ξ	Transformed volume fraction
I^v	Nucleation rate
N_0^v	Initial number of nucleation sites
υ_I	Nucleation frequency
k_{Avrami}	Avrami growth constant in the usual formalism
n	Avrami growth exponent
$C_{\alpha\beta}^{eq.}$	Equilibrium concentration on the $A_\alpha B$-side of the $A_\alpha B/A_\beta B$ interface
$C_{\beta\alpha}$	Actual concentration on the $A_\beta B$-side of the $A_\alpha B/A_\beta B$ interface
D_β	Diffusion coefficient of species A in in the $A_\beta B$ compound
$x_{\alpha\beta}$	Position of the $A_\alpha B/A_\beta B$ interface
C_β^A	Concentration of species A in the compound $A_\beta B$
$C_{\beta\gamma}$	Actual concentration on the $A_\beta B$-side of the $A_\beta B/A_\gamma B$ interface
$C_{\beta\gamma}^{eq.}$	Equilibrium concentration on the $A_\gamma B$-side of the $A_\beta B/A_\gamma B$ interface
$x_{\beta\gamma}$	Position of the $A_\beta B/A_\gamma B$ interface
J_β^A	Flux of species A in the compound $A_\beta B$
x_β	Thickness of the compound $A_\beta B$ layer
$\kappa_{\alpha\beta}$	Reaction rate constant at the $A_\alpha B/A_\beta B$ interface
$\kappa_{\beta\gamma}$	Reaction rate constant at the $A_\beta B/A_\gamma B$ interface
G_β	Geometric and stoechiometric factor for the growth of compound $A_\beta B$ from the reaction of $A_\alpha B$ and $A_\gamma B$

$\Delta C_{\beta}^{eq.}$	Concentration gradient accross the $A_{\beta}B$ layer in the absence of reaction barriers
κ_{eff}	Effective reaction rate constant for the growth of compound $A_{\beta}B$ in the case of one layer growth
$G_{\beta\gamma}$	Geometric and stoechiometric factor for the growth of compound $A_{\beta}B$ from the reaction of $A_{\beta}B$ and $A_{\gamma}B$
x_{β}^{*}	Changeover thickness defining the boundary between the linear growth and diffusion-controlled growth regimes for the compound layer $A_{\beta}B$
J_{γ}^{A}	Flux of species A in the compound $A_{\gamma}B$
x_{γ}	Thickness of the compound $A_{\gamma}B$ layer
G_{γ}	Geometric and stoechiometric factor for the growth of compound $A_{\beta}B$ from the reaction of $A_{\beta}B$ and $A_{\delta}B$
$G_{\gamma\beta}$	Geometric and stoechiometric factor for the growth of compound $A_{\gamma}B$ from the reaction of $A_{\beta}B$ and $A_{\gamma}B$
$\kappa_{\beta eff}$	Effective reaction rate constant for the growth of compound $A_{\beta}B$ in the case of two layers growth
J_{γ}^{A}	Flux of species A in the compound $A_{\gamma}B$
$\Delta C_{\gamma}^{eq.}$	Concentration gradient accross the $A_{\gamma}B$ layer in the absence of reaction barriers
$\kappa_{\gamma eff}$	Effective reaction rate constant for the growth of compound $A_{\gamma}B$ in the case of two layers growth
D_{γ}	Diffusion coefficient of species A in in the $A_{\gamma}B$ compound
$\kappa_{\beta\gamma}$	Reaction rate constant at the $A_{\beta}B/A_{\gamma}B$ interface
$x_{\gamma}^{crit.}$	Critical thickness of the $A_{\gamma}B$ compound layer
c	Avrami constant used in the formalism of Mittemeier

c_0	Avrami constant exponential prefactor
E	Activation energy of the Avrami constant
β_A	Exponential factor of the Avrami-like growth
ϕ	Heating rate
T_0	Initial temperature of the Kissinger's analysis
$T_{\xi'}$	Temperature corresponding to a given transformation stage ξ'
$\beta_{\xi'}$	Exponential factor of the Avrami-like growth at the transformation stage ξ'

Chapter 4

n	Diffraction order
λ	X-ray wavelenght
d_{hkl}	Inter-planar spacing of crystallographic planes of indices (h,k,l)
θ	Diffraction angle
b	Vector perpendicular to the diffracting planes
θ_{CCD}	Angle along the CCD detector
S	Position along the CCD detector
R	Radius of curvature of a hypothetical curved CCD detector
L	Distance between the center of the detector and the X-ray incident point on the sample's surface
$I_{hkl}(t)$	Diffracted intensity integrated under the peak associated to the planes of indices (h,k,l)
I_0	Incident X-ray intensity
$K(\theta,T)$	Diffraction constant
$\upsilon_{compound}$	Volume of the growing compound
V_{tot}	Total volume of interaction between the X-rays and the sample
ε_0	Permittivity of vacuum (8.854E-12 F/m)
e	Charge of the electron(1.610E-19 C)

m	Mass of the electron (9.109E-31 kg)
r	Diffractometer's arms radius
F_{hkl}	Structure factor of the diffraction from planes of indices (h,k,l)
p	Multiplicity of the (h,k,l) reflection
M	Temperature factor
μ_{abs}	Linear X-ray absorption coefficient
h	Planck's constant (6.626E-34 $m^2kg\ s^{-1}$)
Θ	Debye's temperature
ϕ_D	Tabulated function of Θ/T
T_{max}	Temperature of the maximum reaction rate for the Kissinger's analysis

Chapter 7

$I_I(\theta)$	Diffracted intensity at diffraction angle θ
K_{hkl}	Proportionality factor between the volume of the growing compound and the diffracted intensity
v_{growth}	Volume of the growing compound
$f(\theta)$	General function of θ
M	Gaussian – Lorentzian mixing factor
FWHM	Full width at half maximum
I_i	Integrated diffracted intensity
n	Avrami exponent
k	Avrami constant
E_{act}	Activation energy

CCBRT model

χ_A	Transformed surface fraction
η	Nucleation site density
r	Nuclei radius
z	Thickness of the slab during diffusion-controlled growth regime
z_0	Thickness of the growth zone in the nucleation-controlled regime
K_{i0}	Expoential pre-factor for the growth in the nucleation-controlled regime
Q_i	Activation energy for the nucleation-controlled growth
k_B	Boltzmann's constant
K_{d0}	Diffusion-controlled growth constant
Q_d	Activation energy for the diffusion
χ_v	Transformed volume fraction
z_{max}	Maximum thickness reached during the diffusion-controlled growth regime
t_0	Time of nuclei coalescence in the nucleation-controlled growth regime. Defines the transition with the diffusion-controlled growth regime
χ_{v0}	Transformed volume fraction at the transition between the nucleation- and diffusion- controlled growth regimes
K'_{d0}	Effective diffusion-controlled growth constant taking into account the proportionnality constant for the diffracted intensity
I^2_{i0}	Squared integrated diffracted intensity at the transition between the nucleation- and diffusion- controlled growth regimes
t_{offset}	Offest parameter taking into account the stages of the reaction prior to the θ-Ni_2Si formation
k_d	Diffusion-controlled nuclei radius growth constant
Q_d	Activation energy for the diffusion

Modified CCBRT model

z_1	Thickness of the growth zone in the nucleation-controlled growth regime
z_2	Maximum thickness during the non-planar diffusion-controlled growth model
χ_{v2}	Volume fraction transformed during the non-planar diffusion-controlled growth regime
N_0	Initial number of growth initiating sites or "entry points"
A	Area of the growth front
χ_{tot}	Total transformed volume fraction
$I_I(t)\|_{t>to}$	Integrated diffracted intensity in the non-planar diffusion-controlled growth regime
$I_I(t_0)$	Integrated diffracted intensity at the transition between the nucleation- and the non-planar diffusion-controlled growth regime
$I_{I\text{-}max}$	Maximum integrated diffracted itensity reached during the θ-Ni_2Si growth growth

Non-constant composition CCBRT model

F_{hkl}	Structure factor for the diffraction
f_{Ni}	X-ray scattering factor of Ni
f_{Si}	X-ray scattering factor of Si
$\chi_{\theta\text{-Ni}}$	Internal site occupancy fraction
F_{110}	Structure factor of the θ-Ni_2Si (110) reflexion

Chapter 1 : INTRODUCTION

1.1 Technological importance of silicides

In their currently most widespread application, transition metal silicides are used as low-resistance Ohmic-contact materials in the microelectronics industry.[1] They constitute essential components of modern complementary-metal-oxide-semiconductor (CMOS) transistors, the switching devices that serve as basic building blocks for integrated logic circuits and computer processors. The structure is detailed in Figure 1.1, the cross-sectional micrograph of four neighboring transistors, where we can see the silicon substrate, the channels, the highly doped Si sources and/or drains, the poly-crystalline Si gates and the very thin gate oxides.[†] Silicides are found everywhere a contact is made to a transistor.

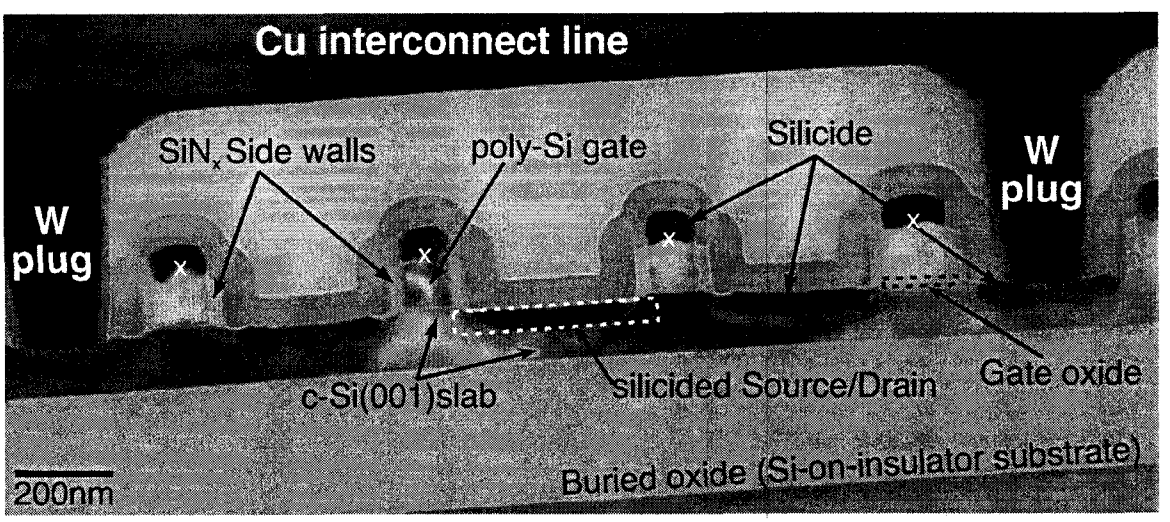

Figure 1.1: Cross-sectional transmission electron micrograph of four contemporary CMOS transistors. Structures marked with a white "X" extend over long distances perpendicular to the plane of the page.

[†] Nowadays, it is more accurate to talk about gate dielectric since SiO_2 will soon be replaced by other so-called High-K materials such as HfO_2.

In CMOS technology, silicides are synthesized through solid-state reactions as illustrated in Figure 1.2. Thin films of metal typically thinner than 100 nm are deposited onto silicon and the structure is subsequently heated. Following chemical potential gradients, metal and/or Si atoms diffuse, intermix, and react to form metal-silicon compounds.

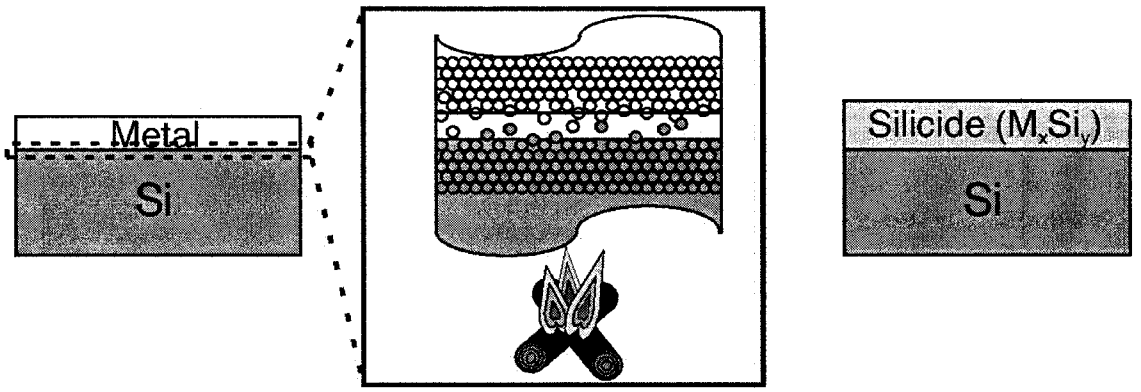

Figure 1.2: Illustration of the silicide synthesis by thin-film solid-state reaction. Cross-sectional view.

In the typical fabrication of a CMOS processor, the metal layer is deposited onto the Si wafer after building all transistor structures. As illustrated in Figure 1.3, the metal covers the Si and dielectric regions of an entire circuit and will only react upon heating where it is in contact with Si. The thickness of the resulting silicide layer is determined mostly by the amount of deposited metal, but also by the process temperature, which usually lies below 900°C, and the annealing time. Any unreacted metal left on the various dielectric structures is removed through selective wet etching processes. Without the use of lithography, the low resistance contact regions become automatically aligned with every exposed Si areas of the wafer. This process is key to the production of advanced devices.

Several different compounds can form when a metal reacts with silicon upon heating. For instance, up to three phases can be expected during reactions between Co and Si below 1125°C, as indicated by the equilibrium phase diagram (EPD) shown in

Figure 1.4. If the reaction occurs between two semi-infinite slabs of reactants, and the anneal temperatures are sufficiently high and time sufficiently long, all the stable compounds appear and co-exist at the interface in a stacking order following the composition gradient as shown in Figure 1.5 (a). For thin films however (Figure 1.5 (b)), due to the limited reactant supply and the kinetic nature of the growth process, the different compounds typically form sequentially in time (e.g. Co_2Si-CoSi-$CoSi_2$), each new one consuming the previous as it grows. While several compound layers can co-exist, rarely more than two have been observed simultaneously.

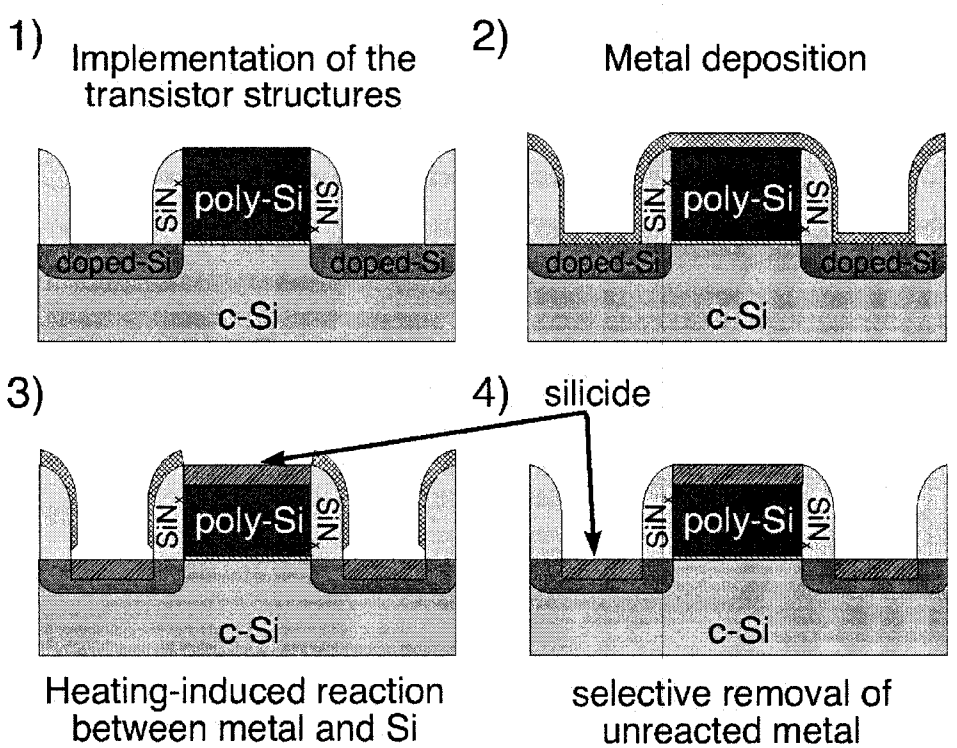

Figure 1.3: Self-aligned silicide solid-state synthesis in a typical CMOS integrated circuit fabrication process.

Typically, in metal-silicon systems of choice for microelectronics, one compound is targeted for its low resistivity (e.g. $CoSi_2$). The presence of high-resistivity compounds that may form before or after the technologically relevant one, lead to increases in RC time constants and overall decrease in circuit frequency and performance. Moreover,

roughness at the reaction fronts, stress caused by volumetric changes, and the presence of impurities can come into play to degrade the quality of the silicides layers, especially when the formation occurs in very small regions such as the source, drain, and gate of device structures. A good understanding of the various phenomena at play during the solid-state synthesis is therefore instrumental to achieving optimized silicided contacts and transistors.

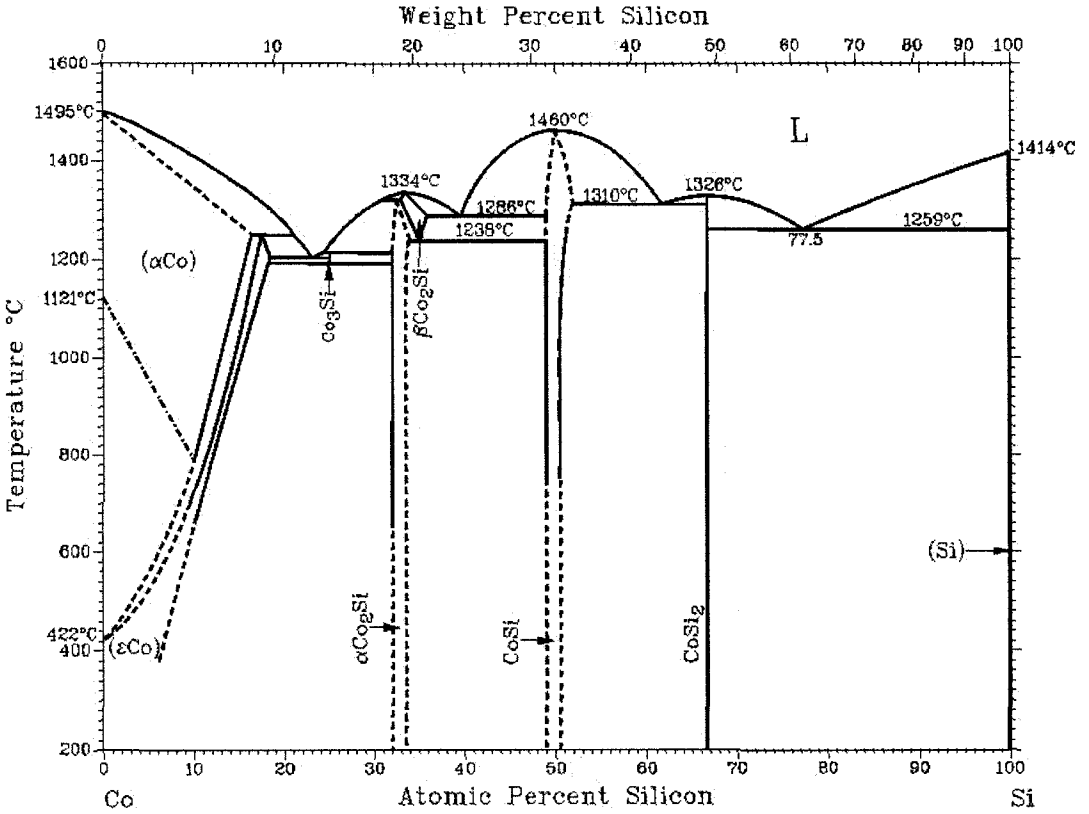

Figure 1.4: Co-Si equilibrium phase diagram.

1.2 Scaling issues with silicide processes

The microelectronics industry is well known for its continued efforts to reduce the size of integrated devices as a mean to increase processor performances. The aggressive down scaling that took place in the last three decades has been accompanied by a number

of challenges on the materials front, one of which being serious fundamental issues with the silicidation processes. Problems inherent to the formation of the low-resistivity compound required changes of contact materials, eventually leading to the use of nickel monosilicide (NiSi) in today's generations of processors. In what follows, we present two examples of problems encountered with the Ti-Si and Co-Si contact metallurgies, which have lead to the introduction of NiSi in current technologies.

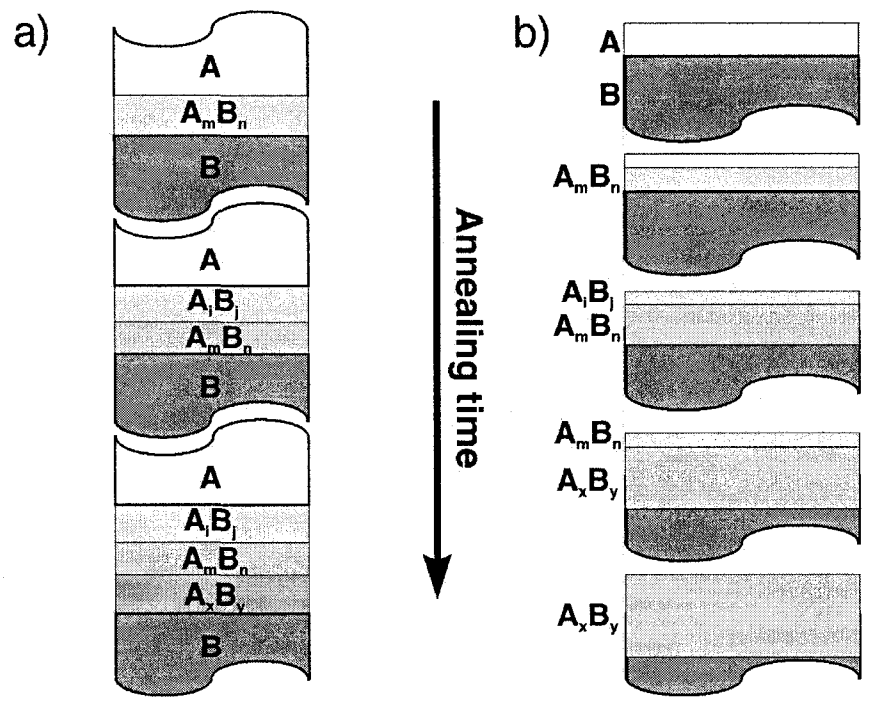

Figure 1.5: a) Reaction of two semi-infinite solid slabs. b) Reaction between a thin film and a thick substrate. The compositions of the compounds are arbitrary however the figure suggests that i/j>m/n>x/y The chronological order of appearance of the compounds is also arbitrary.

In the 1990's, the C-54 crystalline structure of $TiSi_2$ was the preferred choice of the industry. Its solid-state synthesis involves, among others, a transformation from the high resistivity (60-70 μOhm-cm) C-49 to the low resistivity (10-12 μOhm-cm) C-54 polymorphs of the compound.[2] As will be discussed later in this thesis, the small difference in Gibbs free energy associated to polymorphic transformations results in large nucleation barriers and in consequently low densities of stable nuclei. As the production

of transistors reached smaller dimensions, this lack of C-54 nuclei lead to entire circuits regions remaining in the high-resistivity C-49 phase. The situation, illustrated in Figure 1.6, forced the migration towards a cobalt-based silicide process where the nucleation site density was known not to be a problem. $CoSi_2$, the low resistivity compound of the Co-Si system, has therefore been the material of choice from the 0.25μm technological node on.[†,2,3] It is found for instance in the processors of Sony's Playstation II ® and Playstation III® famous video game platforms.

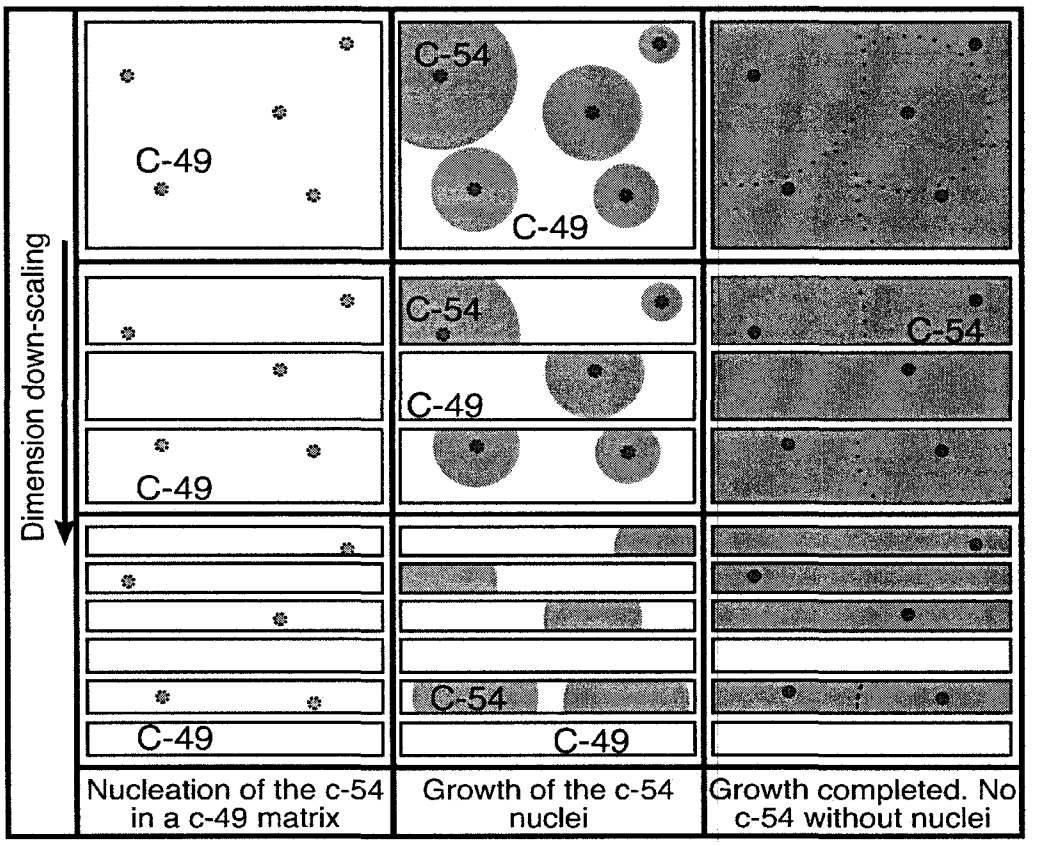

Figure 1.6: Schematic illustration of the effect of low stable nuclei density on the silicide synthesis in small dimension features. As the silicided structures get smaller, conversion to C54 $TiSi_2$ is prevented in nucleus-free regions. The reaction process is viewed from the top.

[†] Processor generations are identified by the numerical value of the half pitch of the densest array of poly-silicon lines. The transistor gates are often trimmed to half of that.

As the technology kept evolving, $CoSi_2$ also became gradually inadequate. Down scaling the transistor size requires a decrease of the silicide thickness. However, the magnitude of the interface roughness resulting from the nucleation-controlled growth of $CoSi_2$ remains approximately constant.[4] It therefore assumes an increasing relative importance as smaller devices are produced (up to 30% of a 25 nm thick silicide).[5] This translates to undesirably high resistances of the contacts in addition to increasing the leakage current. Also, in the phase sequence leading to the formation of $CoSi_2$, one finds a stage where Si atoms diffuse massively from their original location in the substrate, introducing vacancies in the silicon as described in Figure 1.7a).[6,7] As the compressive stress accompanying the formation of $CoSi_2$ increases with the decreasing size of the polysilicon lines, vacancies tend to migrate from the Si towards the silicide/Si interface, where they coalesce into voids to alleviate part of the stress. The relative size of these voids became critical in sub-0.090μm processor generations, where the silicide would be cut open on some of the fine poly-Si gate lines, causing an important increase in their resistance. Adding to these problems the difficulty of forming a low resistivity Co silicide phase on the SiGe-based CMOS technology, the industry was forced to migrate towards a Ni-based silicide process.

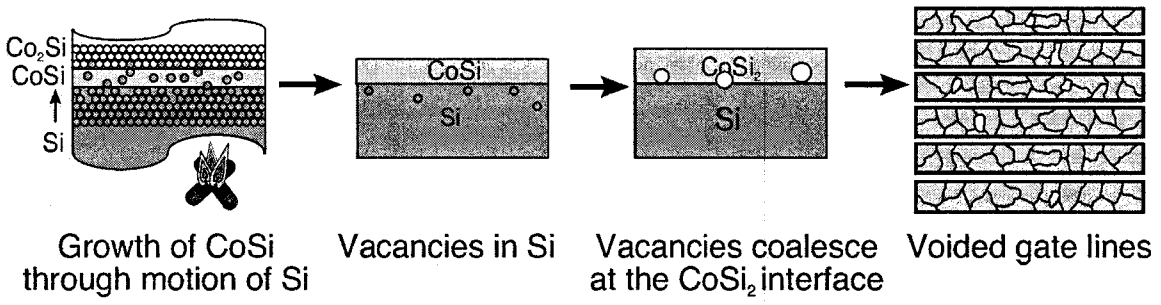

Figure 1.7: Schematic illustration of the formation process of CoSi. Si diffuses through the growing layer and reacts with Co_2Si to form CoSi. Vacancies left in the Si coalescence into voids at the silicide/Si interface.

In spite of a considerably more complex equilibrium phase diagram (see Figure 1.8), the reaction sequence typically reported in the literature for Ni-Si thin film reactions

is similar to that with Co and Si: Only the three compounds, Ni_2Si, NiSi, and $NiSi_2$ are found to form successively. However, as they were beginning to work on the integration of NiSi, scientists of the IBM T.J.Watson research centre observed a more complex reaction scheme whereby an additional compound forms after Ni_2Si and before NiSi. [8,9]

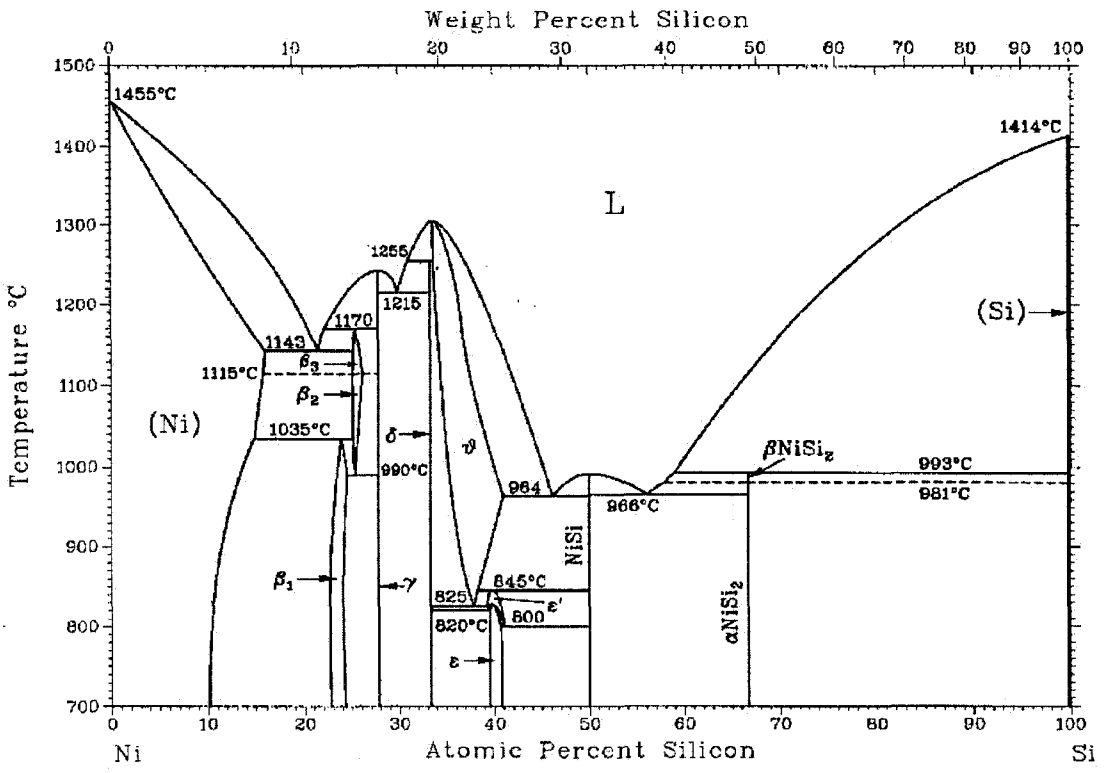

Figure 1.8: Nickel-Silicon equilibrium phase diagram.

From a technological point of view, a detailed understanding of the reactions leading to the formation of the low-resistivity compound is a key issue to a successful integration. However, the roughness, the growth-controlling mechanism(s), and the dominant diffusing species prevailing during the formation of the additional compound are currently unknown. Also unknown are the effects of processing parameters and substrate variations on these properties. Beyond this technological aspect, it was believed so far that the Ni-Si reaction system was fairly well understood. As will be shown in

chapter 2, it has been used as a reference to test the applicability of several general solid-state reactions models. From a materials science point of view, the apparently increased complexity of the reaction has fundamental consequences that will be reviewed in this thesis.

1.3 Objectives of the thesis

The objective of the thesis is to develop a fundamental understanding of the thermally induced solid-state reactions that lead to the formation of the NiSi. In addition to leading to a better understanding of solid-state reactions in thin films, it should permit a better planning of the integration of NiSi in current and future generations of processors.

Our work was planned so as to fulfill the three following specific objectives: *i)* Identify the growing compound and characterize its microstructure *ii)* Investigate the influence of processing parameters such as the initial Ni thickness and the presence of impurities on the formation of the compound *iii)* Study its growth kinetics to explore the possible growth-limiting mechanisms and those through which impurities affect the reaction.

A challenge of the proposed experimental work resides in the limited silicide thickness that is relevant to current CMOS processor generations (about 20 nm). The reaction volumes of interest are therefore extremely small and difficult to measure. The use of powerful techniques such as state-of-the-art transmission electron microscopy and intense probing beams are necessary for this research. In particular, we will exploit the capabilities of a unique *in situ* X-ray diffraction set-up that uses a high-intensity synchrotron X-ray beam. This source allows for monitoring the formation of crystalline compounds in real time during heating experiments even in systems with extremely small reaction volumes.

1.4 Structure of the document

This document is structured in 8 chapters. Chapter 2 gives a brief overview of the basic concepts and theory of solid-state reactions. The formalism and the language that will be used throughout the thesis are presented along with highly cited models of compound growth and kinetics analysis. Chapter 3 presents a critical and exhaustive review of the literature pertaining to the reactions between nickel films (both thin and thick) and silicon substrates. The chapter is separated in three sections respectively focusing on the compound formation sequence, the growth kinetics of the different Ni silicides, and the effect of impurities on the reactions. Chapter 4 describes the experimental methodology and focuses on the details of the *in situ* XRD technique, as well as the method for preparing transmission electron microscopy specimens. Brief descriptions of the Rutherford backscattering spectroscopy (RBS) and the secondary ions mass spectroscopy (SIMS) techniques are also given.

The main body of the thesis consists of chapters 5 to 7. In chapter 5, we present the results of an in-depth study of the reaction sequence by *in situ* XRD in combination with *ex situ* transmission electron microscopy and RBS. In this chapter, we identify the additional compound as the hexagonal θ-Ni_2Si and we report on the microstructure of the reacted layer stacks. The force driving the formation of the compound and possible reaction pathways are discussed. In chapter 6, we investigate the influence on the reaction sequence of Ni alloying with Pt and Co and implantation of arsenic, phosphorus, boron as well as fluorine prior to Ni deposition. SIMS is used to assess the redistribution of fluorine during the reaction. In chapter 7, we present a study of the growth kinetics of the θ-Ni_2Si compound and its sensitivity to fluorine implantation. Using a phenomenological model for which we suggest three modifications, we discuss the possible growth-limiting mechanisms and suggest an explanation for the effect of fluorine. A general discussion followed by the conclusions and future perspectives are presented in chapter 8.

Chapter 2 : Thin-film solid-state reactions in the Ni-Si system

This thesis focuses on the investigation of compound formation resulting from the reaction of a thin metal layer on a Si substrate. In this chapter we present theoretical and experimental background information pertaining to solid-state reactions in general. The topics of diffusion, nucleation, selection of the first compound, compound formation sequence as well as some important growth and kinetics analysis models will be covered.

2.1 Background: Formation of new compounds from the reaction of two adjacent solid phases

Four important phenomena occur when a system composed of two elemental materials in intimate contact is heated: *i)* interdiffusion and mixing at the interface, *ii)* formation of new chemical bonds, *iii)* nucleation of a new compound and *iv)* further growth and expansion of this compound at the expense of the available material. Depending on a number of parameters such as the nature of the growing compound, the microstructure at the growth front and the annealing temperature, one or more of these phenomena will be limiting the reaction process.

2.1.1 Diffusion in the solid-state

Bringing two initially separated elemental materials in contact disturbs their equilibrium state. According to Fick's first law, this will result in an atomic diffusion flux in a direction such as to counter the newly established concentration gradients. This flux is expressed through the well know equation:

Equation 2-1 $$J_{diff-i} = -D_i \vec{\nabla} C_i$$

where D_i is the diffusion coefficient and C_i the concentration of the atomic species i. The minus sign indicates that atom fluxes follow negative concentration gradients. Figure 2.1 represents the situation schematically at two different stages: a) immediately after the A and B slabs with arbitrary dimensions are brought in contact and b) after some arbitrary time of inter-diffusion. At this point no assumption is made about the microstructure of the interdiffusion region, which is allowed to sustain concentration gradients of any magnitude and where both A and B atoms are assumed to have comparable diffusivities.

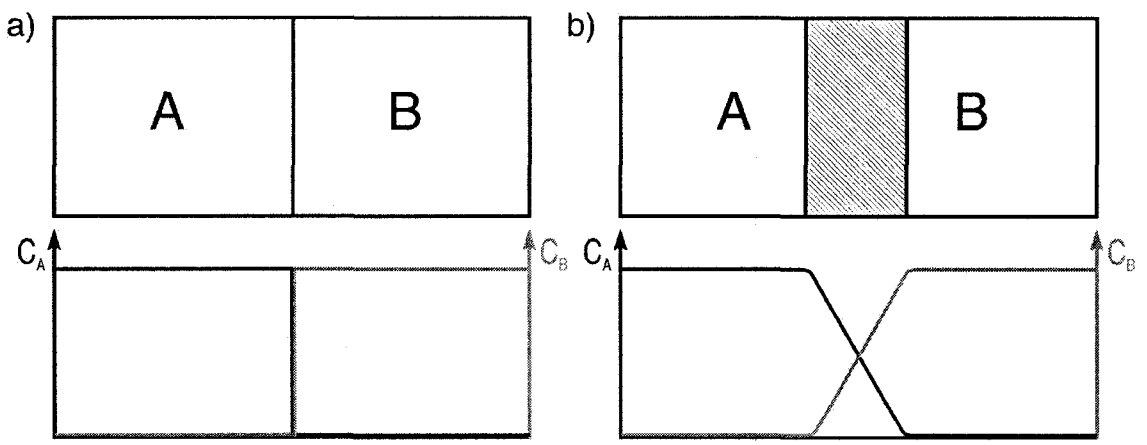

Figure 2.1: Diffusion at the interface between two elemental materials. The concentration gradients are arbitrarily drawn as linear although it may not be the case.

Equation 2-1 is only valid for ideal gases or liquid solutions. Unfortunately solid-state reactions rarely lead to the formation of ideal mixtures and in many cases, concentrations cannot be used to predict the magnitude or even the direction of atomic diffusion fluxes. A great example of this is found in silicon-containing steel alloys as demonstrated by Darken:[10] If a piece of Fe-Si-C is put in contact with a piece of Fe-C with a higher carbon content, C atoms will effectively diffuse from Fe-Si-C to Fe-C

against the concentration gradient. This so-called uphill diffusion highlights the real driving force behind diffusion, which is the gradient in chemical potential. In the case of the Fe-Si-C, adding Si raises the chemical potential of carbon compared to that in Fe-C even though its concentration is lower. It is thus more appropriate to express diffusion fluxes in terms of the gradient of chemical potential as follows:

Equation 2-2 $$J_{diff-i} = -c_i m_i \vec{\nabla}\mu_i$$

where c_i, m_i and μ_i are respectively the concentration, mobility, and chemical potential of atomic species i. Since mobility is somehow difficult to measure and because materials scientists prefer to use diffusion coefficients, equation 2-2 can be rewritten using the Nernst-Einstein relationship:

Equation 2-3 $$D_i = kTm_i$$

where D_A is the diffusion coefficient, k is Boltzmann's constant and T is temperature. Equation 2-2 thus becomes:

Equation 2-4 $$J_{diff-i} = -c_i D_i \frac{\vec{\nabla}\mu_i}{kT}$$

Equation 2-1 can be seen as a special case of Equation 2-4 since $\nabla\mu_i = kT\nabla c_i / c_i$ in ideal solutions.

In equations 2-1 to 2-4, it is assumed that the diffusion coefficient D_i is independent of the composition and constant if experiments are conducted in the isothermal regime. While this is generally not accurate, it is a reasonable approximation when diffusion occurs through crystalline compounds with narrow homogeneity ranges

via mechanisms involving vacancies. If diffusion is to occur through non-stoichiometric compounds, where vacancy concentrations may vary appreciably, or in compounds where the lattice is so large that the moving atoms will diffuse as interstitials, the compositional-dependence of D_i may have to be considered explicitly. The topic of composition-dependant diffusion coefficient will be addressed in chapter 7.

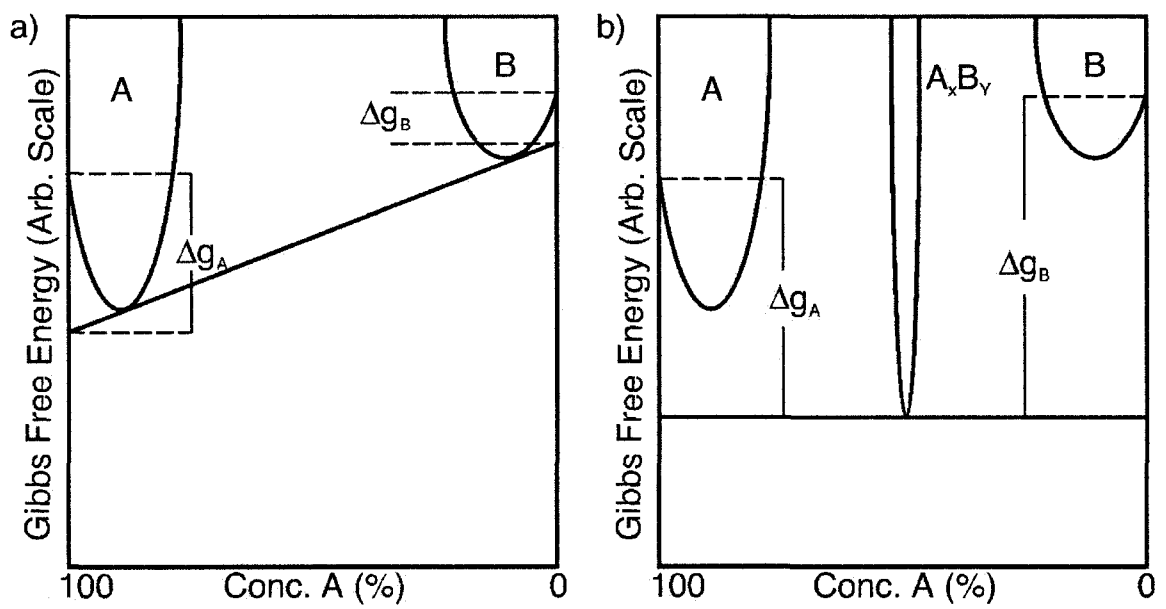

Figure 2.2: Schematic molar Gibbs free-energy diagrams of a A-B binary system showing the origin of the gradients in the chemical potentials.

Figure 2.2 represents the mixing between elements A and B at the interface in terms of molar Gibbs free energy. The parabola-shaped solid lines represent the molar free energy curves of the A and B pure phases and of an arbitrary A_xB_y compound. The tie-line in Figure 2.2 (a) represents the energy of the interdiffusion region if A and B were thoroughly mixed as an ideal solution. In Figure 2.2 (b), we show the case where a stable compound A_xB_y separates the A and B slabs. In both cases the figure highlights the decrease in molar free energy Δg_i, which corresponds here to the chemical potential, experienced by the atoms of each element upon mixing. The driving force leading to atomic motion in most solid-state reactions consists of these chemical potential gradients. Figure 2.2 (b) emphasizes that the presence of a compound at the A-B interface can have

a great influence of the magnitude of these gradients and that as long as some A and B remain on each side of the intermixed region, there will be a driving force for further inter-diffusion.

After some interdiffusion has occurred, the microstructure of the resulting intermixed region is generally unknown, especially in thin films reactions where it can be extremely thin and difficult to characterize. Figure 2.3 represents this region in terms of molar Gibbs free energy with three possible stable compounds, energetically favored with respect to the case of ideal mixing or any other higher energy state (e.g. amorphous intermixed region). Note that only the tie line associated to the ideal mixing is represented. The total molar Gibbs free energy changes $\Delta G_{A_iB_j}$ for compound formation, referenced to the ideal mixing state, are given by the vertical lines ***ab***, ***cd*** and ***ef***. According to the figure, any of the A_iB_j compounds may a priori be allowed to form provided the intermixed region has reached the appropriate composition.

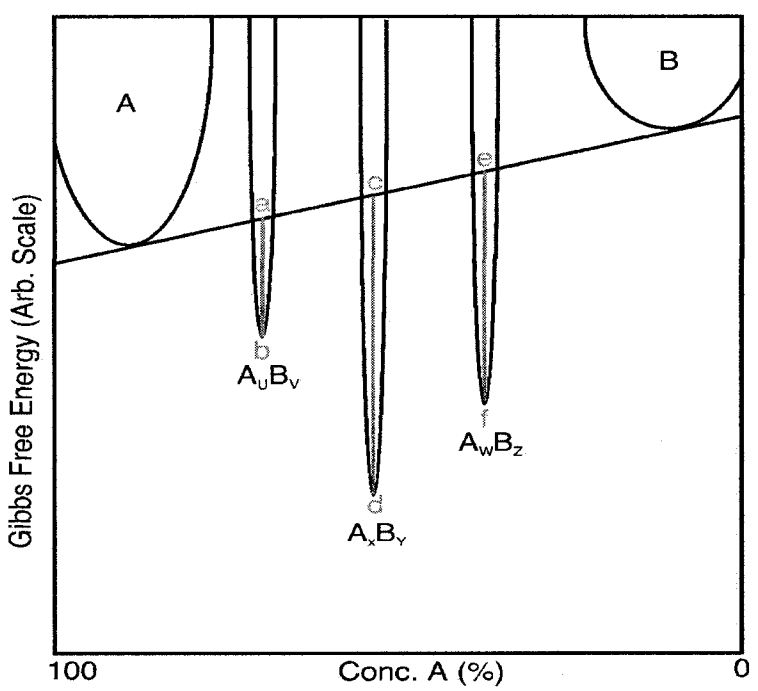

Figure 2.3: Schematic molar free-energy diagram illustrating the driving force for compound formation the intermixed region.

2.1.2 Nucleation of a new crystalline compound in the intermixed region

In order for a new compound to form in the intermixed region, it needs to nucleate. This means that nuclei of finite dimensions, where atoms are organized with the appropriate composition and crystal structure, need to precipitate from the host matrix. While the free energy changes associated to the formation of new volumes of stable compounds are usually negative, the energy associated with the creation of new interfaces is positive. Successful nucleation requires that the balance between these two opposing effects be negative (i.e. that the system evolves towards a lower energy state).

Nucleation during solid-state reactions can be understood qualitatively in terms of the classical theory of nucleation, initially developed to model the condensation of liquid droplets from a vapor phase. According to this theory, assuming spherical and isotropic nuclei, the energy E_η of a nucleus is given by:

Equation 2-5

$$E_\eta = \Delta G_{A_m B_n} \cdot \frac{4}{3}\pi r^3 + \sigma_{surf}\pi r^2$$

where $\Delta G_{A_m B_n}$ is the Gibbs free energy of formation (negative), σ_{surf} is the energy of the interface between the nuclei and the host matrix (positive) and r is the radius. Figure 2.4 shows the evolution of the two terms of Equation 2-5 and how their competition is responsible for the existence of a critical radius r^*, obtained by setting the equation's derivative to zero:

Equation 2-6

$$r^* = \frac{-\sigma_{surf}}{2\Delta G_{A_m B_n}}$$

Nuclei with a critical radius have a critical energy E_η^* given by:

Equation 2-7

$$E_\eta^* = \frac{\pi}{12}\frac{(\sigma_{surf})^3}{(\Delta G_{A_m B_n})^2}$$

In Figure 2.4, we observe that nuclei with a radius smaller than r^* are unstable since any increase in volume will cause an increase in energy. While sub-critical nuclei may exist in a certain equilibrium distribution, only those with a radius above r^* will remain and tend to grow. The rate of nucleation γ will then be proportional to the concentration of critical nuclei, which depends on E_η^*, but also on the rate at which they can assemble. The assembly process requires diffusive atomic rearrangement, although atoms only move over short distances.

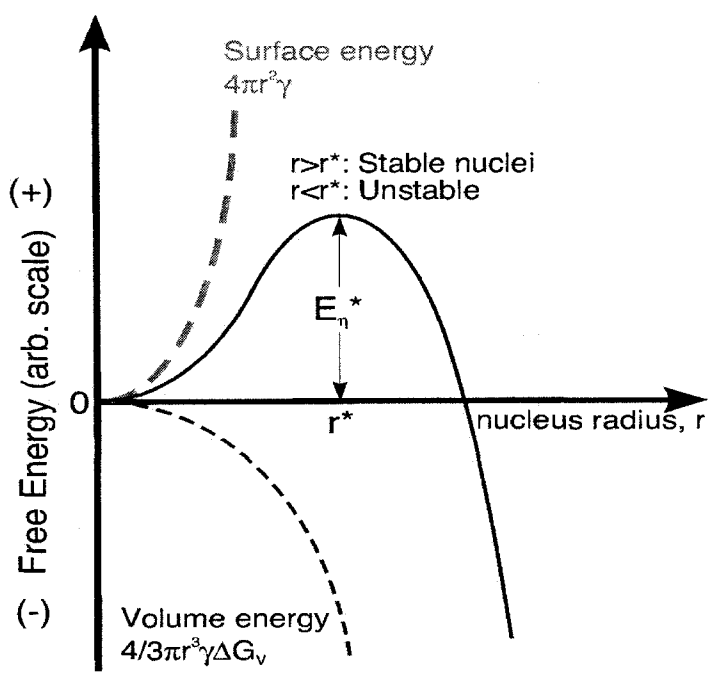

Figure 2.4: Schematic diagram of the nucleation barrier arising from the existence of an interface energy.

The effective rate of nucleation will therefore have a form like:

Equation 2-8

$$\gamma(T) = Ce^{-\left(\frac{E_\eta^*}{kT}\right)} \times e^{-\left(\frac{E_{diff}}{kT}\right)} = Ce^{-\left(\frac{E_{nucleation}}{kT}\right)}$$

where C is an arbitrary constant, E_{diff} is the activation energy for the diffusive atomic rearrangement and $E_{nucleation}$ is the overall effective activation energy for nucleation.

Transformations associated with small free energies of formation are generally expected to proceed with low nucleation rates because E_η^* is large (c.f. Equation 2-7). d'Heurle has suggested that ΔG values below 400 J/cm^3 usually result in sufficiently low values of $\gamma(T)$ to prevent nucleation in solid-state reactions.[11] However, large values of ΔG do not guaranty large nucleation rates because slow diffusion or complex crystal structures, requiring important atomic re-organization to assemble the critical nuclei, may be associated to large E_{diff}, values hence low values of $\gamma(T)$.

The approximation of the spherical nuclei can apply to solid-state reactions as long as the critical radius is small. However, for compounds with low free energy of formation, large critical nuclei may become faceted because of their crystal structure or elongated because of sharp composition gradients. Equation 2-5 and Equation 2-6 must then be rewritten to account for the anisotropic σ_{surf}:

Equation 2-9

$$E_\eta = \Delta G_{A_m B_n} \cdot ar^3 + b\sigma_{surf} r^2$$

Equation 2-10

$$r^* = \frac{-2b\sigma_{surf}}{3a\Delta G_{A_m B_n}}$$

where a and b are geometrical factors. d'Heurle suggested that σ_{surf} should lie between values approaching zero and 2×10^{-4} J/cm^2, respectively for epitaxial and completely random interfaces.[11]

2.1.3 Selection of the first phase and phase formation sequence

In the hypothesis that local equilibrium is achieved, no more than two compounds are expected to be in direct contact during the reactions between two elemental materials. In order to predict the selection of the first and second compounds that will form at the interface, two schools of thought have evolved over the last 30 years, opposing thermodynamic and kinetic considerations. While these two schools propose different approaches, they both assume however that the different compounds nucleate at essentially planar interfaces between the reacting layers (or slabs) and will necessarily expand as continuous, although possibly rough, layers after nucleation.

In the thermodynamic school, Walser & Bené suggested that the first compound to form is the congruently melting compound closer in composition to the lowest-temperature eutectic.[12] They argue that most common thin film deposition techniques (evaporation and sputtering) leave an intermixed layer at the interface between the as-deposited film and the substrate, which they suggest to be a metallic glass with a composition close to that of the lowest-temperature eutectic. Upon heating and crystallization of this amorphous mixture, congruently melting compounds would be favored because they require less short-range order changes, thus offering a lower barrier to nucleation. Their predictions were compared against the observed first compound in 14 silicide systems with a reasonable degree of success.[12]

Also in the thermodynamic school, Pretorius proposed the use of an effective heat of formation (EHF) to determine the first compound to form.[13,14] The EHF, noted $\Delta H'$

and defined by Equation 2-11, is the heat of formation ΔH^0 of a compound (present in the phase diagram), weighted by the ratio of a variable concentration (that of the interface) and the stoechiometric composition of the compound. Figure 2.5 shows the EHF and equilibrium phase diagrams for the Ni-Si system.

Equation 2-11 $$\Delta H' = \Delta H_0 \cdot \frac{\text{Local concentration of the main diffusing element}}{\text{Concentration of main diffusing element in the compound}}$$

Based on the assumption that the composition of the interface between the deposited material and the substrate is that of the minimum of the liquidus in the phase diagram, compounds are compared on the basis of their EFH calculated using this value for the effective interfacial concentration. The compound with the largest absolute (most negative) EHF is expected to grow first. In other terms, the compound that would form the lowest-energy ideal mixture with one of the system's end members (lowest lying tie line) would be favored.

Figure 2.5 illustrates how, based solely on the magnitude of the EHF at the composition of the liquidus minimum, Ni_3Si_2 and NiSi should be favored as candidates for the first compound to form. However, since they are respectively not a congruently melting compound and not the one with the highest congruent melting point, neither of both may form. Ni_2Si will therefore prevail as the first compound.

Pretorius extended the model to the prediction of the subsequent compounds by arguing that as the reaction unfolds, the concentration of the moving interface transfers from one local minimum of the liquidus curve to the next. The formation of the subsequent compounds can then be predicted by successively calculating the EHF for the next interfacial composition and taking the compound with the highest value, provided it is congruently melting. Non-congruently melting compounds are expected to be skipped on the basis that they are more difficult to nucleate.

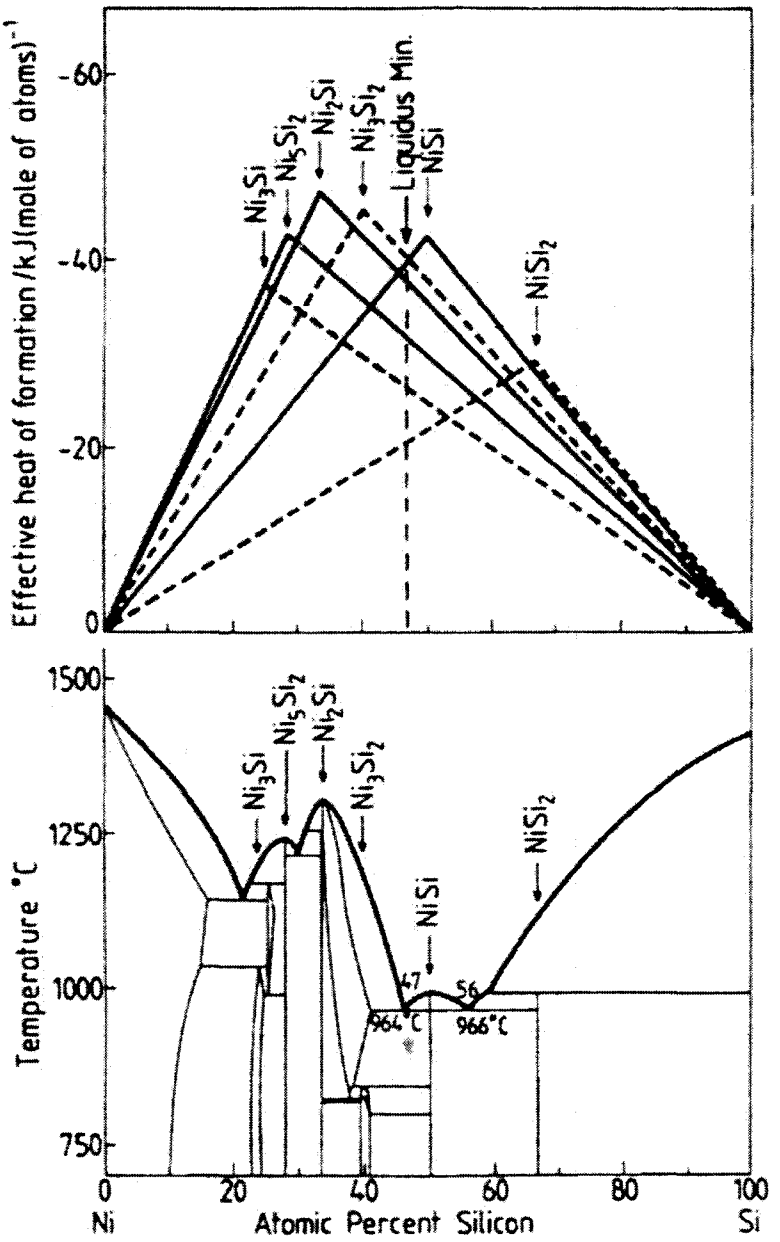

Figure 2.5: EHF diagram and phase diagram for the Ni-Si system. (Taken from Ref. [13]).

Pretorius and Walser & Beney do not claim their models to be applicable to other systems than silicides. Still, their validity is even questionable for silicides. First of all,

one does not necessarily find congruently melting compounds (CMC) in the immediate vicinity of eutectics in all binary systems. More generally, one does not necessarily find CMCs in all binary system; Zr/Si and Cr/Ge are some examples. Even though a certain link may exist between the high temperature and congruence of the melting of a compound and the ease of nucleation, basing predictions of compound formation solely on thermodynamics argument seems rather restrictive.

In the kinetics school, d'Heurle, Gas and Philibert[15,16,17] as well as Canali [18] and Tu[19] have suggested that low nucleation barriers are not sufficient to determine which compound forms first. In fact, d'Heurle *et al.* stress the important difference between the compound that actually nucleates first from the intermixed region and the one that effectively develops and can be measured. While the former may be selected on the basis of a complex combination of thermodynamic and kinetic factors (including the ability of one of the two pure elemental phases to first become supersaturated in the other element [20]), nothing precludes the simultaneous nucleation of more than one compound in the intermixed region. It is therefore suggested that compounds in which diffusion is easier will develop faster than the others, most likely at the expense of the latter, and will prevail in the first stages of the reaction.

d'Heurle *et al.* [15-17] proposed a general rule to qualitatively rank and compare compounds in terms of their expected diffusion properties. The model is known as the "ordered Cu_3Au rule" which states the following: In materials of the type A_mB_n, where the ratio m/n is greater than 2, the majority element A diffuses much faster than B. This statement itself does not readily confer predictive properties to the rule but four of its corollaries, summarized as follows, do:

1) Diffusion in compounds of the form A_mB_n with an m/n ratio greater than 2 must be similar to that in the bulk A phase provided no change in the electronic state of element A occur upon compound formation.

2) The first compound to develop should consequently be richest in the element that diffuses faster, provided no nucleation barrier precludes it.
3) In the absence of nucleation barriers, the subsequent compounds should form sequentially in order of decreasing content in main diffusing element (i.e. in order of decreasing m/n ratio).
4) Stress should be larger during the formation of compounds A_mB_n with high m/n ratios than in compounds with m/n close to 1 because their formation is faster.

The authors mention that the predictive value of their model is limited to cases where *i)* the atomic densities of the compounds are such that interstitial diffusion is negligible (i.e. diffusion takes place dominantly through vacancies on the A sublattice), *ii)* the different compounds competing for growth have significantly different diffusion properties and *iii)* no peculiar vacancy distribution exist so as to favor the minority element (as in some non-stoichiometric compounds). While thermodynamic considerations cannot be evacuated, the overall idea that the first compound to develop is selected on the basis of its diffusion properties seems applicable to a greater variety of systems then the above thermodynamic models, regardless of the structure of their equilibrium phase diagram.

2.2 Some important thin film growth kinetics models

Depending on which of the nucleation, the interface reaction or the diffusion is rate limiting, the volume of new phase that forms will vary with respect to time according to different predictable trends. In this section, we present four important models of compound growth and kinetics analysis, which are often referred to in the field of solid-state reactions.

2.2.1 The treatment of Johnson-Mehl-Avrami (JMA) for Nucleation-controlled growth

As mentioned earlier, nucleation can become rate limiting when compound growth is associated to small changes in free energy or when the new compounds have complex crystal structures. The formation is then characterized by an incubation time, and/or a threshold temperature, above which it exhibits a sudden and rapid increase in rate. The detailed study of nucleation-controlled growth processes can become very complex when the nature of the host matrix and compositional changes occurring during the nuclei growth are considered. The JMA treatment presented here is highly simplified and idealized although often used and referred to in the literature because of its general applicability. In the following demonstration, it is assumed that transformations occur without compositional changes and that growth velocities are independent of the crystalline directions (isotropic). Two assumptions that may quickly fail to apply to nucleation of crystalline compounds in crystalline matrices. However, under these assumptions, we can describe the growth process in general terms without the need to refer to any system-specific parameters such as crystalline directions, diffusion coefficients, stoichiometry factors, etc.

The JMA model is concerned with the evolution of the volume of transformed material after the nucleation has started. In Figure 2.6 the growth process is shown at two different stages; a) Just after the hatching of a number of stable nuclei, and b) after the growing nuclei started impinging. This impingement changes the way the experimenter will perceive the rate at which the total transformed volume will vary.

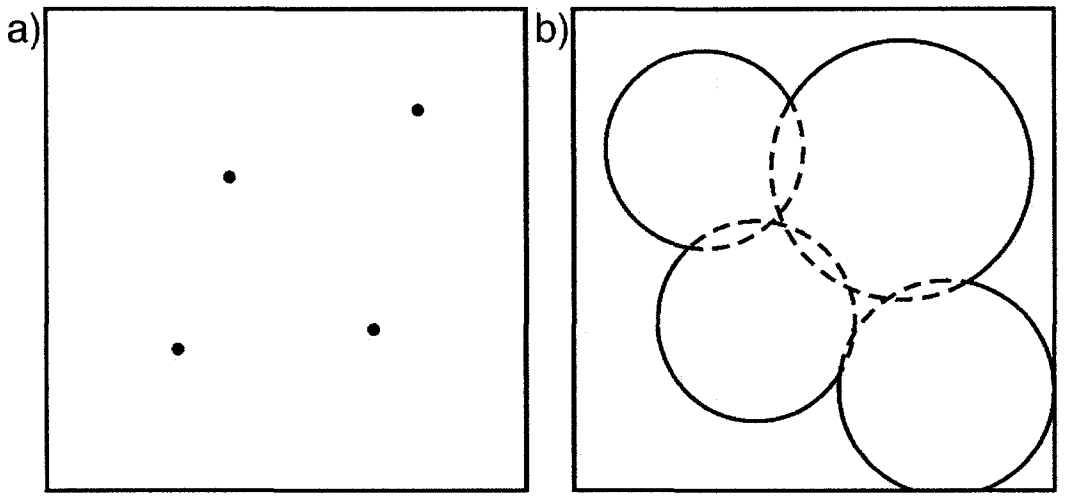

Figure 2.6: a) 2D view of nucleation in a matrix of uniform composition, b) Impingement of nuclei.

Before grain impingement can start, it is found experimentally[21] that in most of the reactions where there is no compositional change in the host matrix and the final phase, each dimension of the transformed volume scales linearly with time. The volume of each nucleus will therefore increase with the third power of time -t^3- (and so will the total transformed volume) as follows:

Equation 2-12

$$v_t = \left(\frac{4\pi}{3}\right)\Upsilon^3(t-\tau)^3$$

where Υ is the line growth velocity (isotropic) and τ is a nuclei "birth" time (incubation time). As soon as growing nuclei start impinging, previously transformed regions (bounded by dashed lines in Figure 2.6) cannot transform again so that Equation 2-12 ceases to describe correctly the evolution of the total volume. The problem is mainly geometrical and was treated by Avrami around 1940. [22,23,24] By introducing the concept of *extended* transformed volume fraction†, he was able to eliminate the contribution of the

† Johnson and Mehl intuitively used such a device, but Avrami provided the formal mathematical justification in 1940. Komolgorov should however be credited with the first mention of such a concept but has long been ignored having published in Russian.

phantom and already transformed regions in a very elegant and mathematically simple way.

Figure 2.7 presents the extended volume fraction schematically. This virtual quantity is in fact the total volume that would be obtained by summing the individual volumes of all the nuclei as if they had not impinged. Assuming a uniform nucleation probability throughout the whole host matrix of volume V, a fraction V_β/V of dV_e^β will lie in a previously transformed region. Conversely, a fraction $(1- V_\beta/V)$ of dV_e^β will lie in an untransformed region and will effectively contribute to increasing the transformed volume. Consequently we obtain:

Equation 2-13

$$dV^\beta = (1 - \frac{V_\beta}{V})dV_e^\beta$$

Or, once integrated,

Equation 2-14

$$\ln(1 - \frac{V_\beta}{V}) = \frac{V_e^\beta}{V}$$

where (V_β/V) is the effective transformed volume fraction usually noted ξ. Considering a nucleation rate I^v given by:

Equation 2-15

$$I^v = N_0^v \upsilon_1 e^{-\upsilon_1 t}$$

where N_0^v is some initial number of possible nucleation sites and υ_1 the frequency at which these favorable sites hatch into stable nuclei. One can obtain an expression for the transformed volume fraction by integrating and assuming two limits of nucleation rate:

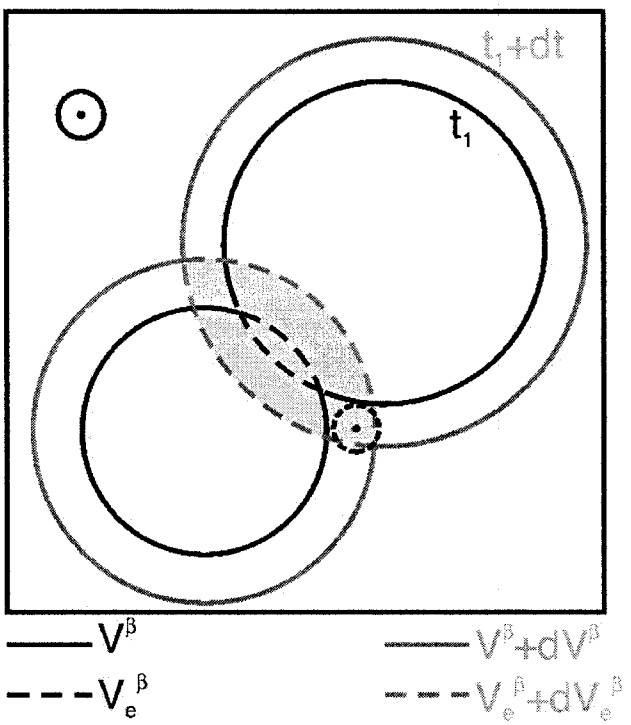

Figure 2.7: Treatment of the impingement between growing nuclei. The extended transformed volume fraction includes the shaded area while the effective volume fraction excludes it.

Equation 2-16 $$\xi = 1 - e^{-(\frac{4\pi}{3} I^{v} \Upsilon^{3} t^{4})}$$

when the nucleation rate is constant and nucleation sites are constantly replenished during the growth and :

Equation 2-17 $$\xi = 1 - e^{-(\frac{4\pi}{3} N_0 \Upsilon^{3} t^{3})}$$

when the nucleation rate vanishes rapidly so that nucleation sites, which number remains almost constant, are quickly exhausted as they transform into growing nuclei.

Carrying out the same analysis for growth in a thin sheet of material yields time exponents of 3 and 2 for the two limiting cases since nuclei become cylindrical with a

volume scaling with the second power of time t^2. Finally, one would obtain exponents of 2 and 1 when growth occurs in only one dimension.

In summary, nucleation-controlled growth processes can be described by the general expression:

Equation 2-18 $$\xi = 1 - e^{-k_{Avrami} t^n}$$

where n, the so-called Avrami exponent, carries information about the growth geometry and k_{avrami} is the Avrami growth constant. Measuring the transformed volume fraction ξ as a function of time during an isothermal annealing experiment and plotting Log{Ln[1/(1-ξ)]} vs Log(t) will yield a straight line of slope n and y-intercept log(k_{Avrami}). Repeating the same experiment at different temperatures, one can obtain the activation energy of the growth constant k_{Avrami}, which is the sum of the activation energy for nucleation and n[†] (or n-1)[‡] times the activation energy of the line growth velocity Υ.

The beauty of this analysis is that it remains valid even for reactions where the growth velocity is anisotropic, but constant in time (i.e. no compositional changes). In such anisotropic cases, even though the prefactors in equations 2-12 and 2-16 are modified by geometrical factors, the time exponents remain the same.

[†] for the site-saturated case
[‡] for the constant nucleation case

2.2.2 The linear-parabolic growth model of Gösele and Tu

Whenever nucleation is not a limiting step, interface reaction and diffusion across the growing phase will control the reaction rate. Gösele and Tu proposed a model that unifies both phenomena under a unique analytical treatment and introduced a parameter whose magnitude defines the regime (interface-reaction or diffusion-controlled) that will prevail. [25]

Figure 2.8 shows the model system on which Gösele and Tu's treatment is based. The motion of each interface is related to local concentration gradients through the following equations:

Equation 2-19

$$(C_{\alpha\beta}^{eq.} - C_{\beta\alpha})\frac{\partial x_{\alpha\beta}}{\partial t} = D_{\beta}\left(\frac{\partial C_{\beta}^{A}}{\partial t}\right)\Bigg|_{\beta\alpha}$$

Equation 2-20

$$(C_{\beta\gamma} - C_{\gamma\beta}^{eq.})\frac{\partial x_{\beta\gamma}}{\partial t} = -D_{\beta}\left(\frac{\partial C_{\beta}^{A}}{\partial t}\right)\Bigg|_{\beta\gamma}$$

where $C_{\alpha\beta}^{eq}$ is the equilibrium concentration of A in the $A_{\alpha}B$ compound, $C_{\beta\alpha}$ is the concentration of A in the $A_{\beta}B$ compound close to the $A_{\alpha}B/A_{\beta}B$ interface resulting from the existence of a reaction barrier. $C_{\beta\gamma}$ is the corresponding concentration of A at the opposite interface and $C_{\gamma\beta}^{eq}$ is the equilibrium concentration of A in the $A_{\gamma}B$ compound. $x_{\alpha\beta}$ is the position of the $A_{\alpha}B$/ $A_{\beta}B$ interface while $x_{\beta\gamma}$ is that of the opposite interface. D_{β} is the diffusion coefficient of A atoms in the $A_{\beta}B$ compound and C_{β}^{A} is the variable concentration of A atoms inside the $A_{\beta}B$.

Figure 2.8 illustrates how the reaction barriers hinder the passage of atoms across the interfaces, resulting in a depletion of A atoms on the right side of the $A_{\alpha}B/A_{\beta}B$

interface and in accumulation on the left side of the $A_\beta B$/ $A_\gamma B$ interface with respect to the barrier-less case.

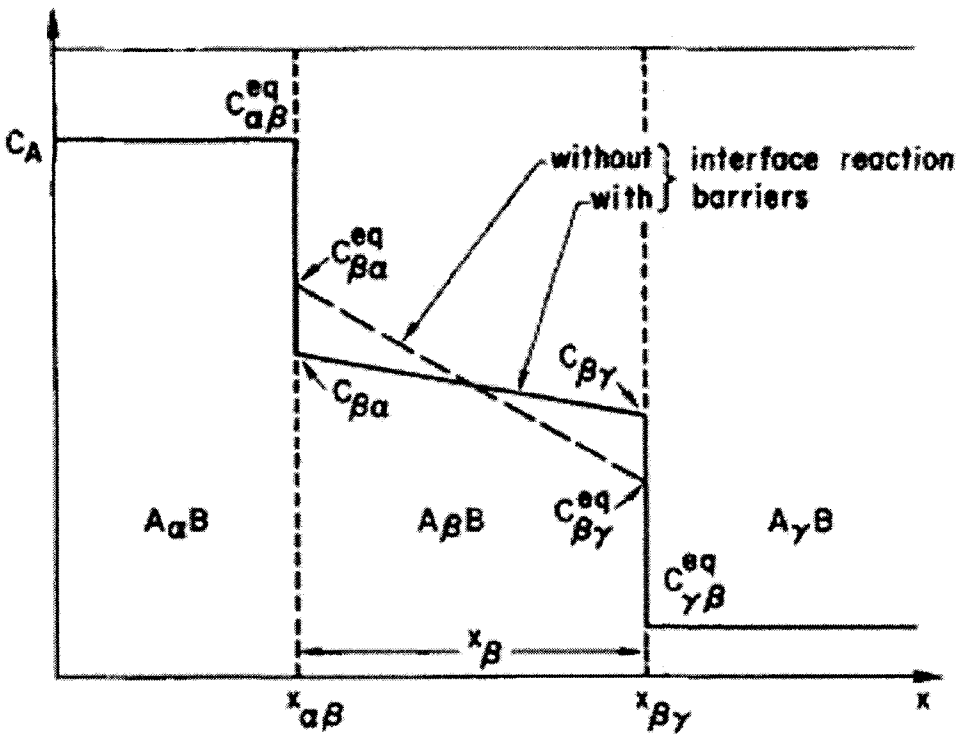

Figure 2.8: Concentration gradients across a layer growing at the interface between two solid phases. (From reference 25.)

Equation 2-19 does not bear a minus sign because the interface goes backwards for a negative A-concentration gradient.

The right hand part of both equations has the structure of Fick's first law and thus corresponds to atomic diffusion fluxes. Under steady state these fluxes are assumed equal, therefore:

Equation 2-21 $$J_\beta^A = -D_\beta \left(\frac{\partial C_\beta^A}{\partial x} \right)_{\beta\alpha} = -D_\beta \left(\frac{\partial C_\beta^A}{\partial x} \right)_{\beta\gamma} = -D_\beta \frac{(C_{\beta\alpha} - C_{\beta\gamma})}{x_\beta}$$

As can be seen from the rightmost part of this equation, concentration gradients are assumed to be linear.

Upon reaching the interfaces, atoms must cross them. This process occurs at a finite pace, established by the interface reaction, which can be expressed as follows:

Equation 2-22 $$J_\beta^A = \kappa_{\beta\alpha}(C_{\beta\alpha}^{eq.} - C_{\beta\alpha})$$

Equation 2-23 $$J_\beta^A = \kappa_{\beta\gamma}(C_{\beta\gamma} - C_{\beta\gamma}^{eq.})$$

where the κ_i terms represent interfacial reaction constants. Combining Equation 2-19 through Equation 2-23, we can write the evolution of the thickness of the interlayer as a function of time:

Equation 2-24 $$\frac{\partial x_\beta}{\partial t} = \frac{G_\beta \Delta C_\beta^{eq} k_{eff}}{1 - \left(\frac{x_\beta k_{eff}}{D_\beta} \right)}$$

where G_β is a factor taking into account the molar volume of the β compound and the stoechiometries α, β and γ, $\Delta C_\beta^{eq}=(C_{\beta\alpha}^{eq} - C_{\beta\gamma}^{eq})$ and $1/k_{eff}=[1/k_{\beta\alpha}+1/k_{\beta\gamma}]$. Equation 2-24 can be reduced to the following expressions when considering two limit cases:

i) $x_\beta << \frac{D_\beta}{k_{eff}}$

Equation 2-25 $$\frac{\partial x_\beta}{\partial t} \approx G_\beta \Delta C_\beta^{eq} k_{eff}$$

ii) $x_\beta >> \frac{D_\beta}{k_{eff}}$

Equation 2-26

$$\frac{\partial x_\beta}{\partial t} = \frac{-D_\beta G_\beta \Delta C_\beta^{eq}}{x_\beta} \Rightarrow x_\beta^2 \propto (-D_\beta G_\beta \Delta C_\beta^{eq})t$$

In summary for small β thicknesses, the growth is controlled by the reaction at the interfaces so that the thickness scales linearly with time and at larger values, we obtain the diffusion-limited growth regime and its characteristic signature whereby the square of the thickness scales linearly with time.

Although often cited and referred to, this model involves many parameters that cannot be measured, namely the interfacial concentrations and reaction-rate constants. Moreover, it relates atomic fluxes to concentrations rather than chemical potential gradients, which was shown earlier to be incorrect. However, it bears a valuable qualitative understanding purpose.

2.2.3 Simultaneous growth of several compound layers

The simultaneous growth of several layers has been addressed by at least three sets of authors, namely Gösele & Tu,[25] d'Heurle & Zhang,[26] and Dybkov [27,28]. We present here the treatment of Gösele and Tu, an extension of the single compound layer case presented above.

Figure 2.9 illustrates the situation where two compound layers grow between two initial phases. Similarly to the single-layer case, the rate of thickening of layers β and γ can be expressed as:

Equation 2-27

$$\frac{\partial x_\beta}{\partial t} = G_\beta J_\beta^A - G_{\beta\gamma} J_\gamma^A$$

Equation 2-28

$$\frac{\partial x_\gamma}{\partial t} = G_\gamma J_\gamma^A - G_{\gamma\beta} J_\beta^A$$

where G_β, G_γ, $G_{\beta\gamma}$ and $G_{\gamma\beta}$ are geometrical factors taking into account the molar volume and stoechiometries of phases β and γ. Diffusion fluxes and interface reaction fluxes are respectively expressed as:

Equation 2-29

$$J_\beta^A = \frac{\Delta C_\beta^{eq} k_\beta^{eff}}{(1 + x_\beta \frac{k_\beta^{eff}}{D_\beta})}$$

Equation 2-30

$$J_\gamma^A = \frac{\Delta C_\gamma^{eq} k_\gamma^{eff}}{(1 + x_\gamma \frac{k_\gamma^{eff}}{D_\gamma})}$$

Equation 2-31

$$J_\beta^A = k_{\beta\gamma}(C_{\beta\gamma} - C_{\beta\gamma}^{eq})$$

Equation 2-32

$$J_\gamma^A = k_{\gamma\beta}(C_{\gamma\beta}^{eq} - C_{\gamma\beta})$$

where the k^{eff}_i quantities have analogous meanings than in the one-compound-layer case, and $k_{\beta\gamma}$ and $k_{\gamma\beta}$ represent the reaction barriers against the growth of the $A_\beta B$ at the expense of the $A_\gamma B$ and conversely.

The condition for the growth of the $A_\beta B$ phase is given by:

Equation 2-33

$$\frac{J_\beta^A}{J_\gamma^A} > \frac{G_{\beta\gamma}}{G_\beta} = \frac{(1+\gamma)(\alpha-\beta)}{(1+\beta)(\alpha-\gamma)}$$

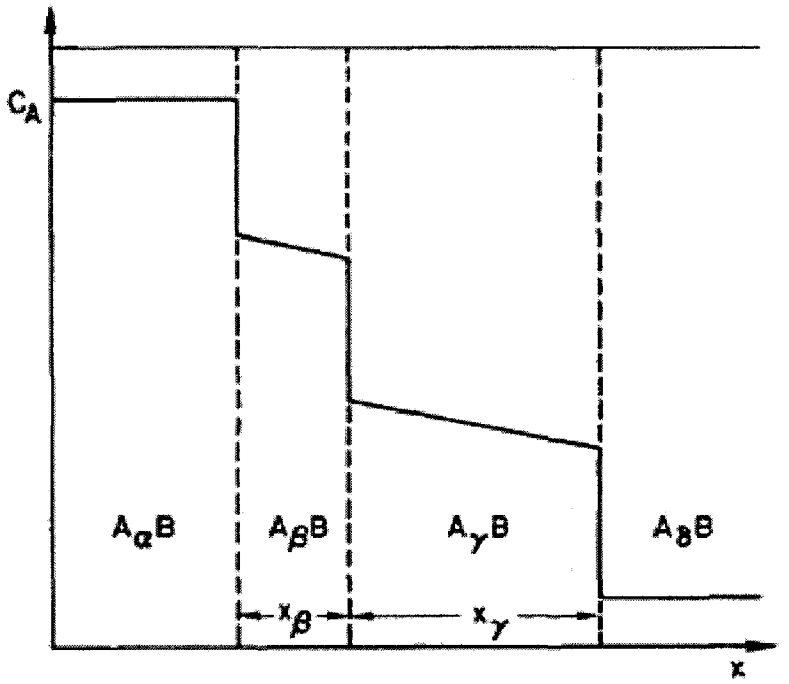

Figure 2.9: Concentration gradients across two layers growing at the interface between two solid phases. (From reference 25)

Conversely, the condition for the growth of the $A_\gamma B$ phase is:

Equation 2-34

$$\frac{J_\beta^A}{J_\gamma^A} < \frac{G_\gamma}{G_{\gamma\beta}} = \frac{(1+\gamma)(\beta-\delta)}{(1+\beta)(\gamma-\delta)}$$

Equation 2-33 and Equation 2-34 indicate that if $(G_{\beta\gamma}/G_\beta) < (J^A{}_\beta/J^A{}_\gamma) < (G_\gamma/G_{\gamma\beta})$, both $A_\beta B$ and $A_\gamma B$ phases will grow. For $(J^A{}_\beta/J^A{}_\gamma)$ ratios outside this range, one of the two intermediate phases will shrink, depending on the magnitude of the quantities x_β, x_γ, D_β, D_γ, $k^{eff}{}_\beta$ and $k^{eff}{}_\gamma$. Assuming that the diffusion coefficients D_i and the effective reaction constants $k^{eff}{}_i$ do not vary during the growth, the thicknesses x_i is the primary factor determining whether there shall be growth or shrinkage of one of the intermediate phases. Ref 25 reviews the different combinations whereby the limiting mechanism for the growth of both compounds is either diffusion or interface reaction. In all cases where diffusion is the limiting mechanism in the growth of at least one layer, a critical ratio of

thicknesses and/or a critical thickness, e.g. x_γ^{crit}, is found below which the other layer, e.g. $A_\beta B$ will shrink. Figure 2.10 summarizes the results for the different cases. It is assumed that the layers where diffusion is growth-controlling are thicker than x_i, the minimum thickness, defined in section 2.2.2, required for switching from reaction-controlled to diffusion-controlled growth.

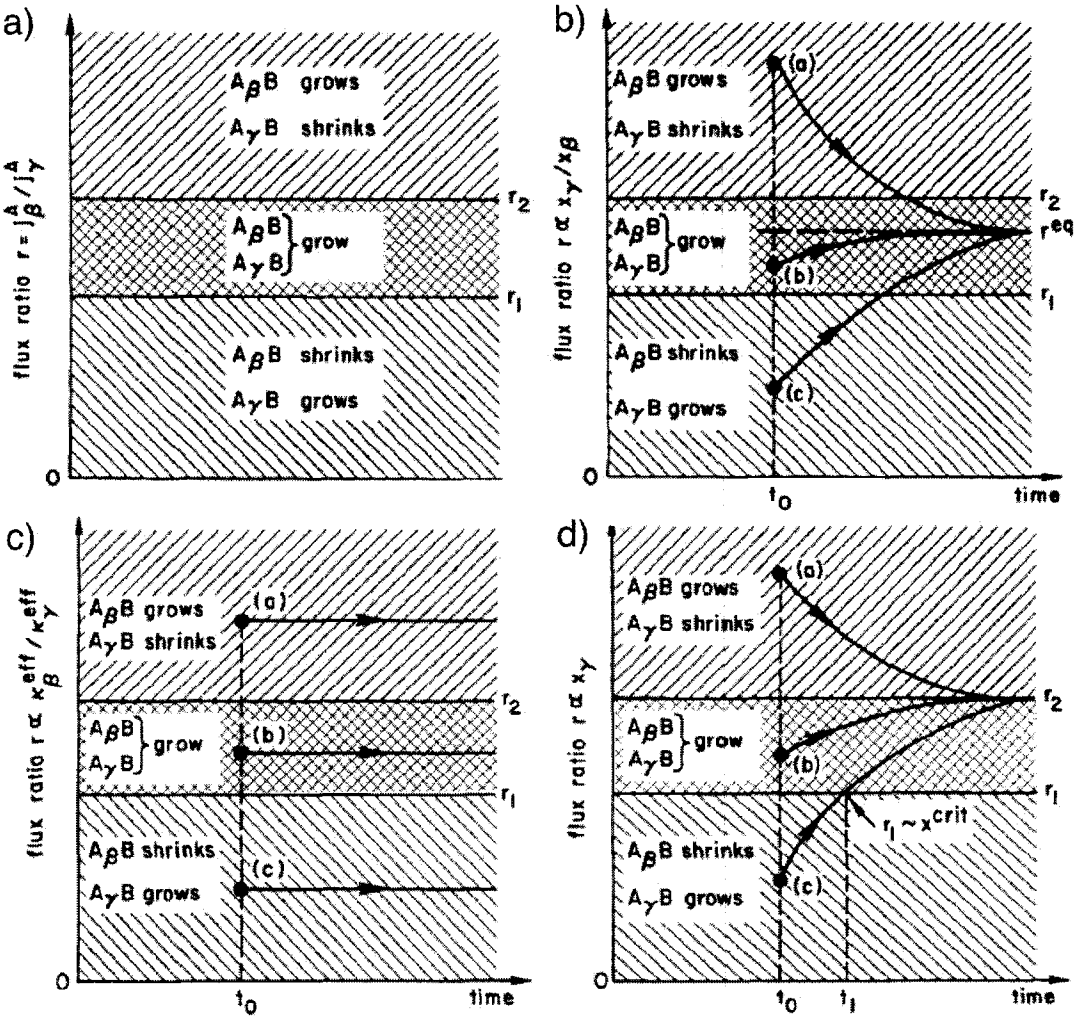

Figure 2.10: Growth regime diagrams for a) the general case and the cases where b) diffusion is limiting in both phases, c) interface reaction is limiting in both phases and d) diffusion and interface reaction are respectively limiting in $A_\gamma B$ and $A_\beta B$. From reference 25.

2.2.4 Kissinger's analysis

Kissinger's analysis is not a growth model as such. On the contrary it consists of a procedure to analyze the results of reactions in the ramp-type annealing regime to obtain the activation energy (apparent) of a growth process without the recourse to a specific model[29]. The analysis correlates the activation energy to the shift in the maximum reaction rate temperature occurring upon increasing the heating ramp rate. Colgan and d'Heurle have shown that it could be used to determine the activation energy of the diffusion-controlled growth of Ni_2Si and NiSi,[30] and Mittemeier has shown that it could be applied to nucleation-controlled growth processes.[31,32] We detail here the demonstration of Mittemeier as its result will be used extensively in chapter 7.

The starting point of Mittemeier's formalism is the following Avrami-like equation for isothermal annealing:

Equation 2-35

$$\xi = 1 - e^{-(ct)^n}$$

where $c = c_0 e^{(-E/kT)}$. In the ramp-type annealing regime, the term ct is replaced by its integral with respect to time :

Equation 2-36

$$\beta_A = \int_0^t c\,dt'$$

For an experiment with constant ramp-rate ϕ=dT/dt, Mittemeier approximates β by :

Equation 2-37

$$\beta_A = \frac{c_0}{\phi}\int_{T_0}^{T} e^{-\frac{E}{kT'}}dT' \approx \frac{kT^2}{E\phi}ce^{-\left(\frac{e}{kT}\right)}\left(1-\frac{2kT}{E}\right)$$

where T_0 is assumed much smaller than T so that all terms in T_0 were neglected. If one is able to measure the temperature $T_{\xi'}$ at which a given transformation stage ξ' is reached

for a number of experiments at different ramp rates ϕ, the activation energy can be deduced by plotting $\mathrm{Ln}(T_{\xi'}^2/\phi)$ vs $1/kT_{\xi'}$:

Equation 2-38

$$\ln\left(\frac{T_{\xi'}^2}{\phi}\right) = \frac{E}{kT_{\xi'}} + \left[\ln\left(\frac{E}{kc_0}\right) + \ln\left(\beta_{\xi'}\right)\right]$$

where $\beta_{\xi'}$ is the value of β at ξ'. Such plots should yield straight lines of slope E and y-intercept equal to the term between brackets. The exact stage ξ' and the Avrami exponent need not be defined exactly as long as one can locate the same stage for each ramp-rate experiment. Also, unless a specific model is used, i.e. specific Avrami exponent and a specific growth stage, c_0 cannot be determined.

Mittemeier has shown that the maximum reaction rate occurs at approximately the same value of β regardless of the reaction rate during ramp-type annealing experiments. One can therefore use the temperature of this event as a rather easily measurable marker for the Kissinger's analysis.

Comparing Equation 2-35 with Equation 2-18, we find that $c = k_{Avrami}^{(1/n)}$. The activation energy obtained with the Kissinger's analysis of a nucleation-controlled growth is thus $(1/n)$ times that obtained from the Avrami analysis presented earlier.

Chapter 3 : Formation of Ni silicides by solid-state reaction between Ni and Si: literature review

In this section, we make a critical overview of the publications that are most often cited or that we believe are key to understanding heating-induced solid-state reactions between Ni films and Si substrates. In the first section, we cover the formation of the first compound and the reaction sequence as observed over a wide range of experimental conditions. We review the reactions in the thin-film and bulk diffusion couple regimes as well as the influence of the substrate's crystallinity on the reactions. The second section focuses on the growth kinetics of nickel silicides and on the dominant diffusing species. Finally, in the third section we review the effect of impurities on the reactions, whether introduced *in situ* during the thin film deposition or implanted in the substrate.

In most of the covered literature, reaction systems are produced by depositing Ni thin films through thermal evaporation or magnetron sputtering of materials with at least 99.9% purity on bulk Si substrates. The traditional approach for studying solid-state reactions and their kinetics (in thin films or not) consists in heating the samples, quenching them at different times and measuring changes in some compound-dependant physical property. The measured properties must be extensive, i.e that they scale with the volume of product phase. Thickness[1], resistivity and intensity of X-ray diffraction peaks are often appropriate in addition to being accessible in a rather timely and non-destructive fashion. Reactions are generally studied using isothermal anneals of variable durations because the data is easier to analyze especially for kinetics. Therefore the formation temperatures cited in this section correspond almost exclusively to isothermal annealing regimes.

---

[1] Thickness can be measured non-destructively by X-ray reflectivity, RBS and also indirectly through resistance mesurements.

3.1 Formation of the first compound and compound sequence

The Ni-Si equilibrium phase diagram is presented again in Figure 3.1.[33] We see that Ni can take up to 10% Si in solution, while the Ni solubility limit in Si is too low to appear clearly on the diagram. In addition to Ni and Si, we find eight compounds lying below the lowest eutectic point (964°C), six of which are stable below 600°C, most likely down to room temperature. These eight compounds are the ones normally expected to form during solid-state reactions occurring below 900°C, Table 3-1 summarizes their composition and crystal structure.

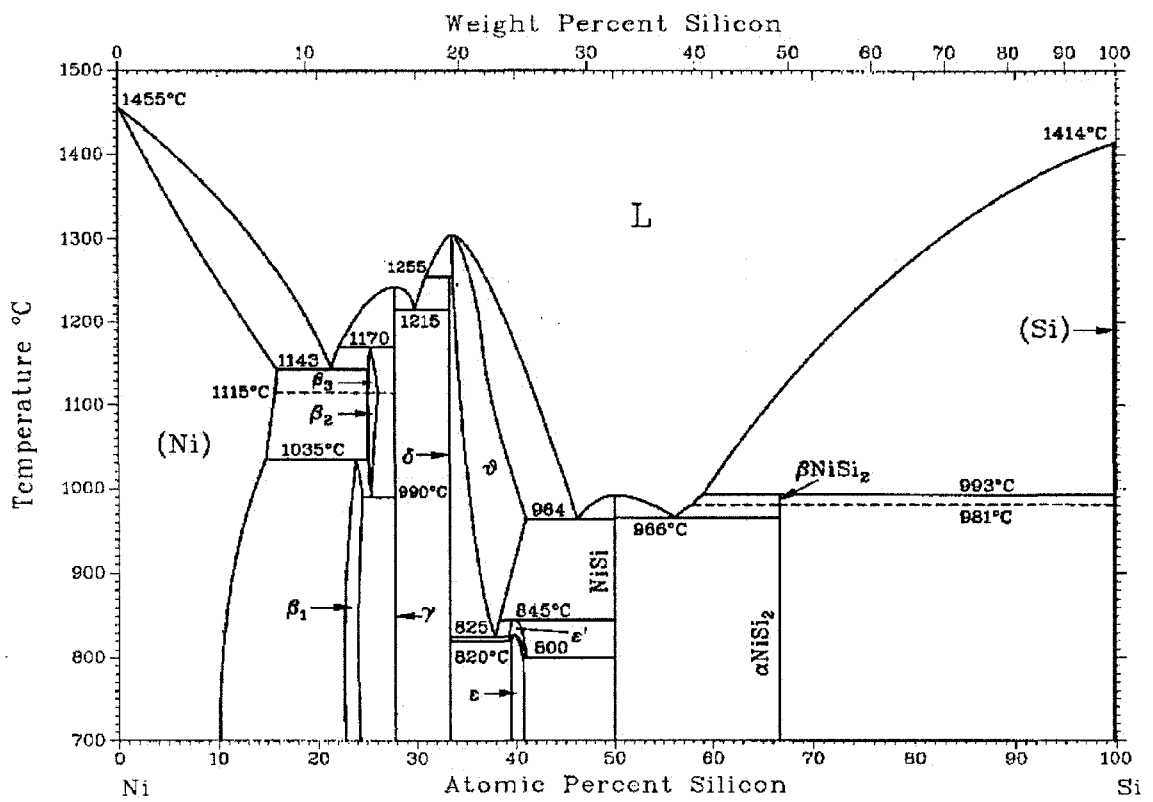

Figure 3.1: The Ni-Si phase diagram

Table 3-1: Composition and crystal structures of selected Ni-Si compounds

Compound Name	Composition (%Si)	Crystal structure	Prototype	Lattice param. (Å)
Ni	0-15	FCC *Fm3m*		a=3.81
β_1-Ni_3Si	22-25	FCC *Fm3m*		a=3.85[34]
γ-Ni_5Si_2 ($Ni_{31}Si_{12}$)	28.5	Hexagonal	--	a=6.661 c=12.227[35]
δ-Ni_2Si	33	Orthorhombic *Pnma*	$PbCl_2$	a=4.99, b=3.72, c=7.06[36]
$\nu(\theta)$-Ni_2Si	33-42	Hexagonal	Ni_2In	a=3.81, c=4.89[37]**
ε-Ni_3Si_2	39-41	Orthorhombic *Cmc1*	--	a=5.23, b=3.26, c=5.66[38]
NiSi	50	Orthorhombic *Pnma*	MnP	a=,b=,c=[39]
α-$NiSi_2$	66	FCC Fm3m	CaF_2	a=5.41[15]
Si	100	FCC Fm3m	--	a=5.43

* the ε' compound is not well characterized and has no published crystal structure
** Lattice parameters correspond to a composition of 41% at. Si.

Reactions between thin Ni films and thick Si substrates

There is a general agreement in the literature about the reactions between thin Ni films and thick Si substrates. δ-Ni_2Si is the first compound to grow, followed in sequence by NiSi and $NiSi_2$ [2,12,13,14,15,40,41,42,43,44,45] such that five of the eight compounds listed in Table 3-1 do not form. The growth of δ-Ni_2Si layers is generally observed above 200°C[1]

[1] Defining a formation temperature usually implies a nucleation-controlled growth. As will be shown later, Ni_2Si grows with a diffusion-controlled kinetics. For compounds which growth is not limited by nucleation, "formation temperatures" usually define arbitrary markers above which significant amounts of the compound form within technologically relevant times.

and as will be seen later in this section, this compound is characterized by a very large critical thickness (c.f.section 2.2.3). The formation of NiSi occurs only after the δ-Ni_2Si growth has completely consumed the initial Ni layer, unless the δ-Ni_2Si has exceeded its critical thickness. According to the model of Gösele and Tu, as long as the metal layer is present, the Ni atom flux arriving at the silicide/Si interface is so large that it causes a systematic conversion of any NiSi grain eventually present at the silicide/Si interface to δ-Ni_2Si, thus preventing the growth of the monosilicide. Hodaj and Gusak however proposed another explanation whereby the Ni atom flux maintains an important concentration gradient at the δ-Ni_2Si/Si interface that hinders the nucleation of NiSi.[46] The exact temperature for the NiSi formation therefore depends on the initial Ni thickness but generally lies above 300°C. $NiSi_2$ is the terminal compound of all reactions with excess Si, being the only one to be in equilibrium with Si (c.f. Figure 3.1). A minimum of 700°C is necessary to observe its formation, unless its nucleation is promoted by various means to be described later.

As seen in Table 3-1, $NiSi_2$ and Si have similar crystal structures. The disilicide consequently grows epitaxially with Si, regardless of the substrate's orientation and of the initial Ni thickness.[5,47,48,49] Epitaxy was also observed by Foll *et al.* for NiSi at low temperature (300°C) in reactions between Ni films with Si(111) substrates.[50] NiSi assumed a hexagonal crystal structure there is no hexagonal compound with a 50:50 Ni:Si composition the Ni-Si equilibrium phase diagram. The θ-Ni_2Si phase is hexagonal but its homogeneity range is bounded between 33 and 42% at. Si. It was later established by d'Heurle *et al.*, who reported similar observations, that the commonly observed orthorhombic MnP prototype crystal structure of NiSi is in fact a deformed hexagonal NiAs prototype structure, which is obtained by stretching the basal plane of the latter.[51] They argued that the hexagonal form would be favored by the possibility of epitaxy with the Si(111) planes, which stabilize its structure, but only for very thin films. The compound was only observed over a narrow range of temperature. References 50 and 51

are the only ones we found whereby the formation of another compound than δ-Ni_2Si, NiSi and $NiSi_2$ is reported for thin Ni films on thick Si substrates.

Reactions of thin Ni films with amorphous Si substrates

In reactions between Ni thin films and amorphous Si substrates, the formation of the first compound proceeds in three steps: *i)* the growth of an amorphous (α[1]) Ni silicide layer at the Ni/Si interface, *ii)* the nucleation and lateral growth of the crystalline δ-Ni_2Si in the amorphous silicide, and *iii)* the one-dimensional thickening of the crystalline δ-Ni_2Si layer after coalescence of the grown nuclei.[52,53,54] The poly-crystalline δ-Ni_2Si nucleates at the interface between the Ni and the α-silicide only once the latter reaches a critical thickness (that has not been determined exactly).[52] The α-silicide has a composition lying between 50 and 60% at. Ni,[52,55] which Ma *et al.* correlated with the composition of the lowest eutectic point of the phase diagram,[55] and it is characterized by a rather fast growth compared to the crystalline Ni_2Si.[55,,56] Depending on the initial Si and Ni deposited thicknesses, the α- and poly-crystalline silicides grow simultaneously or in sequence.[52,55] Thin Ni layers[53] or low annealing temperature and thermal budget[56] delay the nucleation of the crystalline phase. This is consistent with the claims of Clevenger *et al.* who stressed that the formation of an amorphous silicide, which is thermodynamically favored[2] at low temperature, is the sign that nucleation barriers prevent the growth of the crystalline phase [52]

Once all the available Ni is exhausted, NiSi starts growing at the δ-Ni_2Si/α-Silicide interface.[53,57,58] Olowolafe *et al.* reported the simultaneous formation of δ-Ni_2Si and NiSi before the Ni is completely exhausted[59] but Lien *et al.* claim that this result

---

[1] This is a general notation for amorphous compounds. Not to be confused with an eventual α phase on an equibrium phase diagram

[2] If the growth occurs on amorphous Si.

may be explained by the presence of oxygen impurities[58]. None of the references 57,58, and 59 report the existence of the amorphous silicide layer, which may have been missed since all the reported anneals were performed well above 200°C. Finally, Lien *et al.* observed the growth of $NiSi_2$ much earlier on amorphous silicon (between 350 and 425°C) then in the crystalline case, after the formation of NiSi with a diffusion-controlled growth kinetics.[57,58]

Reactions of thin Si films with thick Ni substrates

Reactions schemes involving excess Ni are similar to those with excess-Si in that only three compound are observed: Ni_2Si, $Ni_{31}Si_{12}$ and Ni_3Si.[60,61] δ-Ni_2Si is the first compound to form and the ensuing phase sequence proceeds in order of increasing Ni content.[62] $Ni_{31}Si_{12}$ (often referred to as Ni_5Si_2) forms at the Ni/ δ-Ni_2Si interface at temperatures around 350°C only once all the available Si has been consumed by the δ-Ni_2Si growth (similarly to the growth of NiSi). Ni_3Si forms only above 450°C at the $Ni_{31}Si_{12}$/Ni interface.

Reactions in bulk and lateral diffusion couples

Although they are not representative of thin-film reactions, bulk and lateral diffusion couples are very useful to highlight the kinetic phenomena controlling the growth of the various compounds. Figure 3.2 presents both kinds of structures. Bulk diffusion couples consist of binary assemblies of large "bulk" pieces of materials A and B, brought into intimate contact and annealed at high temperatures (typically 800°C) for long times (typically 10-24hrs). The pieces are sufficiently large so that none of the species A and B is ever exhausted. In lateral diffusion couples, a thin film of material A is deposited through a mask limiting its lateral extent onto another thin-film of material B. Because of the mask, the B layer is only partially covered. Although the films are rather thin compared to bulk couples, about 100nm in thickness, species diffuse laterally

over lengths comparable to the bulk case. The advantage of thin-film lateral couples is that they are easily prepared in vacuum deposition systems, which allows for reliably clean interfaces and highly reproducible results.

In both types of arrangement, all the compounds allowed by the phase diagram are observed, including Ni_3Si_2, after long, high-temperature treatments.[63,64,65,66,67] The two end phases (Ni_3Si and $NiSi_2$) are very difficult to nucleate: Tu *et al.* did not observe Ni_3Si and it took 5 days of annealing at 750°C before to observe $NiSi_2$ in bulk couples.[63] Zheng *et al.* did not observe $NiSi_2$,[64] but Ni_3Si was present although not as a continuous layer. Gülpen *et al.*[66] also observed a late and discontinuous formation of Ni_3Si which they attributed to the presence of Kirkendall voids[68,69] congregating at the Ni/$Ni_{31}Si_{12}$ interface, and compromising the Ni supply for the Ni_3Si growth.

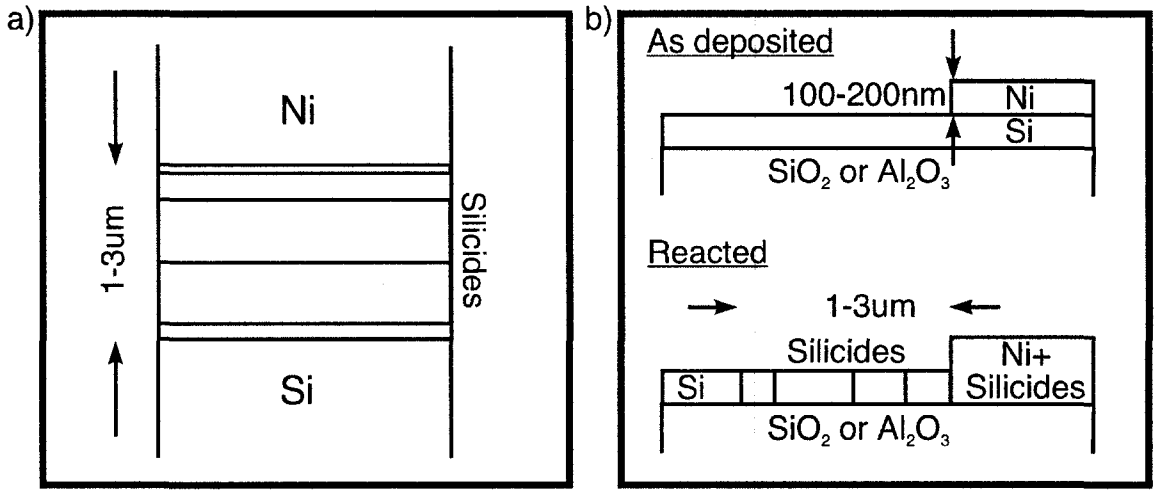

Figure 3.2: a) bulk and b) Lateral diffusion couples.

Just as in the thin-film case, the reaction invariably begins by the formation of δ-Ni_2Si, which must reach thicknesses (or lateral extents in the case of lateral couples) of about 1.5μm (at 500°C) before any other compound may be observed.[70]. At the other interface, the local availability (and/or chemical potential) of Ni atoms being also

controlled by the magnitude of the diffusion flux across the δ-Ni_2Si, Ni-richer phases may not form until the former reaches the critical thickness. Zheng *et al.*[64] reported a critical thickness around 25μm at 600°C, but we believe that a lack of spatial or time resolution resulted in the compounds $Ni_{31}Si_{12}$ and NiSi not being detected in earlier stages. Moreover, Gösele and Tu evaluated the critical thickness of δ-Ni_2Si to around 2-3μm at 350°C based on thin-film diffusion data.[25]

From the work of Zheng *et al.* it appears that Ni_3Si_2 forms before NiSi at the δ-Ni_2Si /Si interface, while Chen *et al.*[70] suggest the opposite. The results of the latter are more consistent with the prevailing formation mechanism observed by Gas *et al.* for the Ni_3Si_2 compound[71].

The sequence in which compounds appear can be summarized as δ-Ni_2Si, followed by NiSi and $Ni_{31}Si_{12}$, then Ni_3Si_2 and finally $NiSi_2$ and Ni_3Si (compounds noted in italic are on the Ni side of the δ-Ni_2Si layer). No compound other than δ-Ni_2Si is therefore observed before NiSi at the silicide/Si interface. Once all the compounds have formed, they co-exist with different thicknesses representative of their kinetic parameters (diffusion coefficient, interfacial reaction constants etc, c.f. sections 2.2.2 and 2.2.3). In all the cases reviewed, δ-Ni_2Si and Ni_3Si_2 show the most important development, followed by $Ni_{31}Si_{12}$ and then NiSi. Ni_3Si and $NiSi_2$ are usually minority. The important development of the Ni_3Si_2 phase is the greatest difference between the thin-film and diffusion-couple growth regimes, since the compound is totally absent of the former scheme, whether Ni or Si is in excess. Finally, the larger critical thickness of δ-Ni_2Si (1.5-3μm) explains why no compound other than δ-Ni_2Si can grow as long as Ni is still available during thin-film reactions with excess Si.

Figure 3.3 summarizes the sequence of Ni-silicide formation in the growth regimes with excess Si and excess Ni. It highlights the absence of Ni_3Si_2 from thin-film

reactions while this phase is clearly observed with a considerable development in diffusion couples (bulk and or lateral). In all the reviewed publications, except for the cases of Ni_3Si and Ni_3Si_2 in diffusion couples, compounds always form continuous layers when they co-exist.

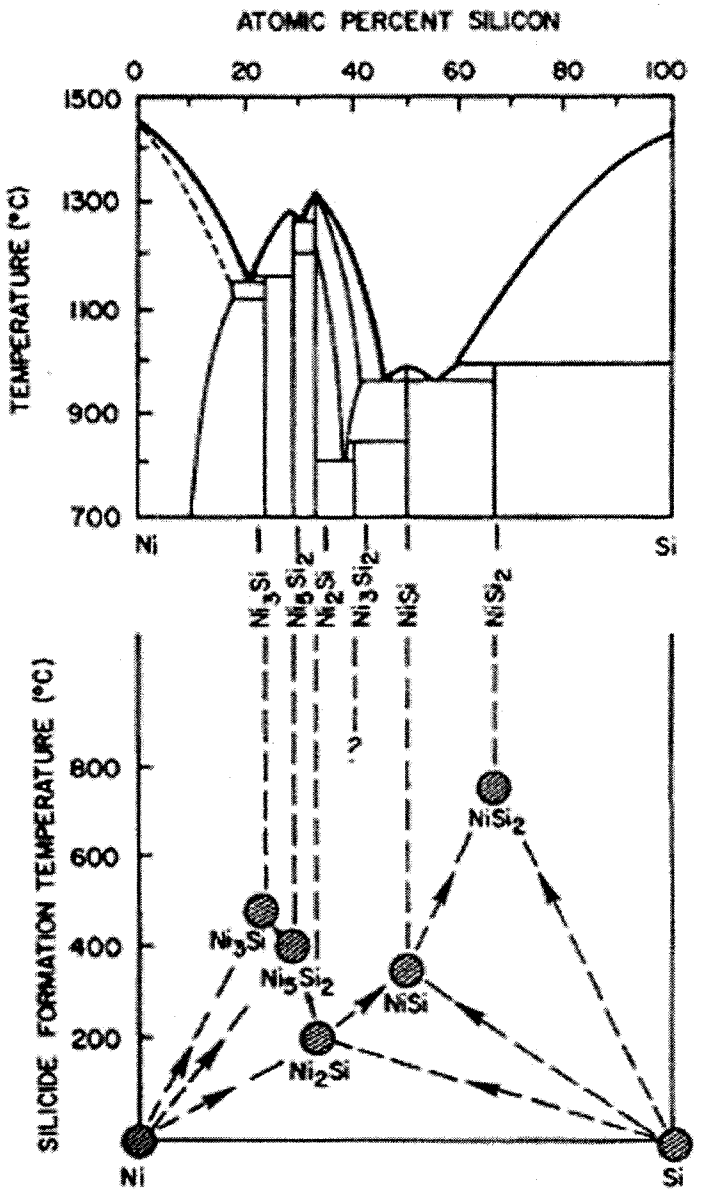

Figure 3.3: Summary of the formation of Ni silicides, actual figure 5 of Tu *et al.* (Reference 63).

3.2 Mobile species and growth kinetics

Ni is the main moving species during the formation of compounds Ni_3Si, $Ni_{31}Si_{12}$, δ-Ni_2Si, and NiSi in thin films,[66,72,73,74,75,76,77] while no information could be found for Ni_3Si_2. Given the complex atomic plane stacking characteristic of this compound's structure, it is very difficult to predict which of Ni or Si will be most mobile. Gas *et al.* and Cicariello *et al.* have demonstrated that diffusion of Ni in grain-boundaries was the most effective mass transport mechanism in the growth of δ-Ni_2Si, which forms at low temperature.[72,78] Given the temperature at which Ni_3Si_2 is reported to nucleate (~450°C), we speculate that Ni transport in grain boundaries should still be the most efficient mechanism. However, nothing a priori precludes Si from being substantially mobile in that compound or in its grain boundaries.

d'Heurle *et al.*[6,79,] suggested that Ni is also the main diffusing species during the formation of $NiSi_2$, and Gülpen *et al.*[66] claimed that Ni and Si have comparable diffusivities at higher temperature. The work of d'Heurle *et al.* was concerned with thin films while that of Gülpen *et al.* focused on bulk diffusion couples. The latter stressed that the dominant mass transport mechanism switches from grain-boundary to lattice diffusion between the thin-film and bulk reaction regimes. Since the formation of $NiSi_2$ usually occurs at high temperatures (above 750°C), lattice diffusion of Si can become significant and comparable to the diffusion of Ni in the long and interrupted grain boundaries of bulk systems. Note however that $NiSi_2$ and $CoSi_2$ are known to be special cases where the ordered Cu_3Au rule (OCAR) exposed in section 2.1.3, does not readily apply.[80] Applying blindly the OCAR, leads to the conclusion that Si is the most mobile species in $NiSi_2$. However, there is no continuous Si sublattice where vacancies can diffuse easily in the CaF_2 structure of the dilsilicide, while the Ni sub-network is continuous. Ni is therefore the main diffusing species. Finally, Chen *et al.* observed the presence of voids at the Si/NiSi interface in diffusion couples at temperatures above 600°C, which they attribute to the possibly high mobility of Si at high temperatures.[70]

We have shown that the first compound to form in every Ni-Si reactions is δ-Ni_2Si and it grows according to a Ni-diffusion-controlled kinetics. The growth is characterized by an apparent activation energy of 1.4 and 1.7eV when the reactions take place on Si(001) and (111) substrates respectively.[2,44,51,59,64,81,82,83] The parabolic growth rate constant[1] lies between $2.5 \cdot 10^{-14}$ and $1.65 \cdot 10^{-11}$ cm^2/s between 275°C and 450°C.[72,83,84] At 300°C, 100nm of δ-Ni_2Si take approximately one hour to grow on Si(001)[85] and it is almost 4 times longer on Si(111) as reactions are slower on the latter type of substrate.[48,51,59,81] This is consistent with the dominant grain-boundary diffusion scheme mentioned above and the results of Olowolafe who showed that the average size of δ-Ni_2Si grains is smaller on Si(001) than on Si(111)[59]. NiSi also grows with a Ni-diffusion-controlled kinetics showing apparent activation energies ranging between 1.5-1.87 eV.[2,51,81,85,86] At 350°C, 100nm of NiSi take about one hour to grow on Si(001). [85] $NiSi_2$ growth is controlled by nucleation,[6,51,79] but we did not find a quantitative assessment of its kinetics.

d'Heurle *et al.* have shown qualitatively that the kinetics of Ni_3Si_2 growth in thin films is controlled by the nucleation at the interface between δ-Ni_2Si and NiSi.[71] Very recently Kittl *et al.* quantitatively analyzed the process, in conditions similar to those used by d'Heurle *et al.*, and obtained an Avrami exponent of 2.1,[87] suggesting a site-saturated lateral two-dimensional growth of the nuclei. This result is consistent with the lateral growth reported by d'Heurle.

It appears clear from the results of Zheng *et al.*,[64,65] Chen *et al.*,[67,70] and Majni *et al.* [60] that the formation of Ni_3Si is hindered and in most cases completely prevented by nucleation barriers both in thin films and in diffusion couples. It follows logically that its growth kinetics should be controlled by the nucleation of the crystalline phase, but to our knowledge, no quantitative analysis has been published to date at least for thin films and

---

[1] Defined as the slope of $(\text{thickness})^2$ vs time plots, which yield straight lines when growth is 1-dimensional and diffusion-limited (c.f. section 2.2.2).

lateral diffusion couples. It should be noted however that Ni and Ni_3Si are completely homostructural, it might therefore be very difficult to distinguish a very Ni-rich Ni_3Si from Ni. The growth of the $Ni_{31}Si_{12}$ compound is controlled by the diffusion of Ni atoms as inferred from the results of Majni *et al.*[60] for thin films and as suggested by Gülpen *et al.* for diffusion couples at high temperature.[66] The latter reports a parabolic growth rate constant of about $1.4 \cdot 10^{-13}$ cm^2/s at 600°C.[88]To our knowledge, no quantitative kinetics data is available for thin-film formation of the compound at lower temperatures. We conclude that the absence of $Ni_{31}Si_{12}$ from the phase sequence in excess-Si reaction schemes is not due to nucleation barriers, but rather to a kinetic competition that δ-Ni_2Si wins.

On amorphous Si the growth of the α-silicide phase is diffusion-controlled with a growth constant evaluated to lie between $2.9 \cdot 10^{-14}$ and $4 \cdot 10^{-13}$ cm^2/s at 250°C, which is 5-7 times faster than the growth of the crystalline Ni_2Si.[55,56] The nucleation of the crystalline δ-Ni_2Si compound occurs around 200°C and its subsequent planar growth is controlled by the diffusion of Ni with an activation energy between 1.4 and 1.5eV, similarly to the formation on crystalline Si.[57,58,59,89] The same holds for the formation of NiSi which is characterized by an activation energy around 1.55eV.[58,59] While the growth of $NiSi_2$ is reported to be nucleation-controlled on crystalline Si, Lien *et al.* observed its advanced diffusion-controlled growth at low temperature, with an activation energy of 1.65eV on amorphous Si.[57,58]

We close this section with the following remark: Regardless of the crystalline structure of the substrate, the formation of δ-Ni_2Si and NiSi proceeds with similar activation energies of about 1.6eV. It has been demonstrated, especially in the case of δ-Ni_2Si, that Ni diffusion in the grain boundaries is the most effective mass transport mechanism and that it controls the growth of at least these two compounds. The activation energies around 1.6eV for transformation processes in the Ni-Si system between 200 and 400°C is most likely a signature of Ni diffusion in grain boundaries.

3.3 Influence of impurities

Impurities can be introduced in several ways in silicidation reactions. Depending on their nature, position and proportion in the reaction system, they will affect the properties of the compounds, the formation sequence, the growth kinetics or the energetics in different ways.[90] Typical methods of introducing impurities are *i)* deposition of thin layers between or on top of the reacting materials, *ii)* co-deposition together with the reacting materials films and *iii)* ion implantation. The first two methods are generally employed to introduce metallic or semi-conducting impurities into the metal films (e.g. Au, Pt, Co, Ti, Ge) up to quantities that can result in the formation of ternary alloys (e.g. Ni-X-Si). The third one allows for introducing a wider spectrum of species (in addition to those mentioned above) such as C, As, P and B as well as gases (e.g. O_2, N_2 and F).

3.3.1 Impurities deposited as interlayers: Ti, Ge, and SiO_2

There has been a considerable amount of work on the impact of interlayered impurities on Ni/Si reactions, however most of the studies have focused on the thermal stability of the technologically important NiSi compound. The early stages of the silicidation reaction, which this thesis is mostly concerned with, have not attracted much attention in earlier studies. It is observed that interposing layers of a vast variety of elements such as Mo, Pd, Pt, Ti, W or Zr has the effect of improving the stability of the NiSi compound by delaying the nucleation of $NiSi_2$.[91,92,93,94,95,96,97] Co, and Ir on the contrary reduce the formation temperature of the disilicide.[98] Of course, inserting foreign elements in direct contact with the Si can result in the formation of foreign silicides, especially in the early stages of the reaction. This can give rise to complex competitions between the different silicides, especially when the impurity layers are relatively thick.

Such cases fall outside the scope of this thesis. We present below the case of two interlayered impurities, Ti and Ge, for which publications dealing with very thin interlayers and providing information about Ni-Rich compounds were found.

Reactions between thin Ni films and Si substrates with thin interposing Ti layers

When a thin (3nm) Ti interlayer is used, no reaction is observed before reaching about 400°C during 5°C/min ramp-type heating experiments. The formation of δ-Ni_2Si is delayed and the compound is found to co-exist with NiSi even when Ni is still available.[99] The formation of $NiSi_2$ is delayed until about 800°C and it coexists with minute amounts of C49- and C54-$TiSi_2$. Experiments using longer isothermal annealing (30min) and similar Ti thicknesses (3nm) suggested the formation of epitaxial layers at temperatures as low as 350°C.[100] The authors claim that the epitaxial phase is $NiSi_2$, although they base their identification solely on the absence of diffraction peaks in XRD experiments where the substrate was tilted to avoid the Si substrate's peaks. Aside from the annealing regime, the main difference between the two studies above lies in the thickness of the initial Ni layer, which was 30nm for Chiu *et al.* [99] and 9nm for Nakatsuka *et al.*[100]. The results above thus suggest that Ti interlayers mostly act as physical barriers to diffusion, which limit the Ni atom flux towards the Si substrate. The formation of δ-Ni_2Si or $NiSi_2$ as the first compound is then dictated by the magnitude of the Ni atom flux, which depends on the availability of unreacted Ni, the thickness of the different layers, and mostly the strength of the diffusion barrier.

Reaction of thin Ni films and Si substrates with thin interposing Ge layers

When a thin Ge interlayer is interposed between the Ni film and the Si substrate, no Ni germanide formation is reported, and no results about the effect on the δ-Ni_2Si formation can be found for dilute Ge cases. The formation temperature of the NiSi is not

measurably affected by the presence of the thin interlayer,[1] [101] but some Ge segregates at the NiSi/Si interface and at the NiSi surface.[102] The nucleation of the $NiSi_2$ compound is however delayed by more than 150°C and Ge is expelled from $NiSi_2$ grains, accumulating in the Si substrate.[102,103]

This last result, and many others to be presented in this section, can be explained by extending the principles of the Humes-Rothery rule to intermetallics systems. It states that metals should exhibit extensive solid solubility if their respective elemental solid phases share the same crystal structure with lattice parameters differing by less than 15%. NiGe and NiSi share the same orthorhombic MnP prototype structure with lattice parameters differing by less than 5%. As was proposed for δ-Ni_2Si and Co_2Si,[104] their mixing enthalpy should be close to zero, but the mixing should increase the entropy slightly. This increase in entropy stabilizes the Ni(Si,Ge) by reducing the free energy change associated with the transformation from the mono- to the disilicide. As explained in section 2.1.2, a smaller ΔG increases the nucleation barrier, which results in a higher nucleation temperature. This phenomenon is often referred to as the mixing-entropy effect.[105] In the case of Ge, the barrier is further raised by the absence of a NiGe $_2$ counterpart to $NiSi_2$. Ge must therefore be expelled from $NiSi_2$ nuclei before they achieve the appropriate crystal structure and be stable.

The little effect of thin Ge interlayers on the formation temperature of NiSi comes from the fact that δ-Ni_2Si and Ni_2Ge also share the same crystal structure. The solubilities of Ge in δ-Ni_2Si and NiSi, although certainly different, must be comparable so that significant Ge additions are required before any delay can be observed in the formation of NiSi[101]. Since the lattice parameter differences are smaller between Ni_2Ge and δ-Ni_2Si

---

[1] Studies involving silicidation on $Si_{0.8}Ge_{0.2}$ revealed an increase of about 50°C in the formation temperature of NiSi.

(≤3%) than between NiGe and NiSi, the delay could be explained by a slightly higher solubility of Ge in δ-Ni_2Si than in NiSi.

Reaction of thin Ni films and Si substrates with thin interposing SiO_2 layers

When Si (001) substrates are left with a thin chemical oxide (such as a Shiraki oxide[106]) before thin-film Ni deposition, $NiSi_2$ is found to form as the first phase at rather low temperatures (300°C).[107] As the temperature is increased, the disilicide layer becomes discontinuous and $NiSi_2$ pyramids protrude in the Si substrate. Then, if Ni is still available, NiSi grows epitaxially[1] on top of the mixed Si/$NiSi_2$ layer. Both compounds coexist until 800°C, where full conversion of NiSi to $NiSi_2$ is achieved. The advanced formation of the $NiSi_2$ occurs because the oxide slows down the Ni flux arriving in the Si. On one hand, this reduction in flux hinders the formation of Ni-Rich compounds by forcing a lower local concentration in Ni. On the other hand, the free energy change upon the formation of $NiSi_2$ from Ni and Si is much larger than the one from NiSi and Si. The presence of the oxide therefore reduces the barrier to the nucleation of the disilicide. This phenomenon is known as oxide mediated epitaxy (OME) and has been observed for $CoSi_2$ as well.[108,109]

3.3.2 Co-deposited impurities : Pt and Co

One of the most discussed metallic impurities for Ni silicides is Pt because it recently solved many problems related to the integration of NiSi as a contact material in the CMOS technology.[110,111] Co-depositing Ni and Pt (5% at.) has no effect on the early compound sequence: δ-Ni_2Si is the first compound to form, and NiSi only forms once the Ni(5%Pt) layer is completely consumed.[112] No platinum silicide is observed, but Pt segregates at the metal/Ni_2Si interface and remains there until it reaches some critical (yet

[1] [001] NiSi // [001] Si and (020) NiSi // (040) Si

undefined) concentration and starts redistributing.[112,113] This concentration is most likely achieved once a critical amount of Ni left the alloy layer. Once the latter is completely consumed, a slight Pt accumulation remains at the silicide surface throughout the rest of the reaction. Very little Pt is found in δ-Ni_2Si, while it is rather uniformly distributed in NiSi. When the formation of monosilicide has consumed all the δ-Ni_2Si, i.e. after 30s between 450°C and 550°C depending on the initial alloy thickness, some Pt accumulation is found at the NiSi/Si interface.

These redistribution characteristics of Pt can be explained in terms of its solubility in the different compounds. Pt, has a low solubility limit in Si[114] and will tend to remain out of it (it will rather form a silicide). δ-Ni_2Si and Pt_2Si don't have similar crystal structures while PtSi and NiSi are homostructural with little differences in their lattice parameters.[115,116] The solubility of Pt is therefore expected to be smaller in δ-Ni_2Si than in the Ni-Pt alloy and in the NiSi.[117,118]

It should be mentioned that Cojocaru-Mirédin *et al.*[118] observed a slightly different behavior than Corni *et al.*[112,113] First, they found that δ-Ni_2Si and NiSi grow simultaneously even when Ni(5%Pt) alloy is still available. Second, they observed a Pt accumulation at the δ-Ni_2Si /NiSi interface that was not reported by Corni *et al.* The extent of these NiSi and Pt-accumulation regions, which were measured by atomic probe tomography by Cojocaru-Mirédin *et al.*, is such that it might have been missed by the RBS measurements of Corni *et al.* In fact, the presence of a NiSi layer between the Si and the δ-Ni_2Si, growing necessarily at the expense of the latter, could contribute to explain the kinetics results of the Corni *et al.*: They find that Pt does not impede the growth kinetics of δ-Ni_2Si at the beginning, but they observe an unexpected decrease of the growth rate when the layer exceeds about 45nm. We speculate that accumulation of Pt at the metal/δ-Ni_2Si interface could act as a barrier for the Ni atoms, lowering the Ni atom

flux at the δ-Ni_2Si /Si interface. This would promote the growth of NiSi, impeding on the δ-Ni_2Si growth.

As mentioned earlier, the greatest interest from a technological point of view, lies in the effect of Pt on the last stages of the compound sequence. Similarly to Ge case, Pt and Si do not form a disilicide while NiSi and PtSi are homostructural. The presence of Pt in NiSi therefore delays the nucleation of the $NiSi_2$. [110,116,117,118] This considerably increases the thermal stability of the NiSi by eliminating one of its degradation mechanisms, namely the formation of the disilicide. Additionally, Pt reduces the impact of a second thermally induced degradation mechanism of NiSi, which is agglomeration.[119]

Finstad investigated the early stages of the reaction in samples consisting of Pt/Ni bilayers on Si substrates and observed a compound sequence that was similar to the one observed by Corni *et al.*[120]

Mangelinck *et al.* found that the use of Ni(5%Pt) alloys resulted in a stabilization of the epitaxial relationship between NiSi and Si(111) substrates which was observed earlier with pure Ni.[51,50,117] The same group later reported the lateral co-existence of the orthorhombic MnP and hexagonal NiAs forms of NiSi, both of them epitaxial with their Si(111) substrates.[117,121] They suggested that Pt dissolution in NiSi changes the c/b ratio of the MnP structure bringing it closer to a value of $\sqrt{3}$, whereby atomic positions become completely equivalent to those of the hexagonal NiAs structure.

Reactions between Ni(Co) alloy thin films and Si substrates

Co-depositing Ni and Co (5% at.) has no effect on the overall compound sequence. Ni_2Si is the first phase to form and transforms to NiSi only once all the metal is consumed.[104] The growth of δ-Ni_2Si is slightly slower compared to the pure Ni case, but

the main diffusing species is still the metal (Ni or Co).[122] Co_2Si and δ-Ni_2Si are remarkably similar as the parameters of their identical crystal structure differ by less than 2%. They are consequently thoroughly mixed as a single ternary compound. The monosilicides however have differing crystal structures and tend not to be as miscible (CoSi is cubic with the FeSi prototype structure). Even with dilute Co alloying, phase separation occurs and XRD indicates the presence of trace amounts of CoSi in samples annealed into the monosilicide phase.[104] It has not been confirmed whether it forms as a continuous layer or not in the case of the dilute alloy, but if it does, NiSi should be the layer in contact with the Si as observed for richer alloys.

In contrast with reactions schemes produced by Pt alloys, the disilicide forms much earlier with Co. It is observed after annealing at temperatures of 525°C, which is more than 200°C below the pure Ni case and some 75°C below the nucleation temperature of $CoSi_2$. [110,104,117,122] This result illustrates eloquently the role of the mixing entropy in stabilizing the mixture of the compounds with respect to their pure states by increasing its entropy. $CoSi_2$ and $NiSi_2$ are both cubic with the CaF_2 structure and their respective lattice parameters are respectively 5.37Å and 5.41Å.

The location where the $NiSi_2$ nucleates in Ni-Co silicide layers stack is quite interesting. As mentioned above, $NiSi_2$ forms at the NiSi/Si interface in samples with pure Ni, and the same scheme holds for the pure Co case.[15] In samples with Ni(5%Co), the disilicide nucleates at the free surface of the monosilicide.[104,122] It is suggested that both easier stress relaxation and the presence of a cobalt rich region near the surface would facilitate the nucleation. In fact, d'Heurle *et al.* have shown that the exact location where the disilicide nucleates depends on the Co content in the alloy, highlighting the competition between volume and surface energies in determining the nucleation barrier.[104]

Because of the enhanced ability of δ-Ni_2Si and Co_2Si to mix as a continuous phase, one obtains almost identical results then those mentioned above when Co/Ni or Ni/Co bilayers react with Si substrates[122]. The only difference is the formation of Co_2Si as the first compound in samples where the Co layer is in contact with the Si.

3.3.3 Implanted impurities

In this section we present the effect of three categories of implanted impurities : *i)* gaseous species O_2, N_2 and C, *ii)* usual Si doping impurities such as As, B and P which are electrically activated (i.e. incorporated to the Si crystal network by high temperature activation anneals, and *iii)* Other gaseous impurities such as BF_3 and F used in the CMOS technology.

Effect of oxygen implantation

The effect of O_2 is very interesting as it changes dramatically depending on where it is implanted.[123,124] When located in the Ni layer (~3%at.), O_2 accumulates at the Ni/ δ-Ni_2Si interface eventually hindering the diffusion of Ni. NiSi then appears at the δ-Ni_2Si /Si interface before the Ni is consumed, but its growth kinetics is three times slower than in the un-implanted case. From XPS measurements, O_2 is found to bind to Si forming SiO_2 at the Ni/δ-Ni_2Si interface where it remains segregated throughout the whole silicidation process.[123,124,125] No O_2 is incorporated to either of the NiSi or δ-Ni_2Si (to within detection limits). This behavior is similar to the one observed when pure Ni layers react with Si substrates in a O_2-contaminated vacuum.[18]

The O_2 content of the annealing ambient has an impact on the results obtained with implantations as the formation of the SiO_2 barrier is delayed when anneals are performed in a very high vacuum.[124] The authors claim that the O_2 contamination present

in a conventional vacuum furnace could participate to the barrier formation by diffusing through Ni grain boundaries as they effectively observe a O_2 uptake in some of their samples. However it was shown that impurities implanted in metal layers could be lost to the ambient when anneals are performed in high vacuum.[126] The delay observed in barrier formation in the case of the high vacuum annealing could therefore be caused in part by a loss of O_2 to the ambient. When less O_2 is implanted, e.g. 1%, interfacial oxide is still found, but the silicide formation is not hindered and the growth rate is similar to the unimplanted case.

When O_2 is implanted in the Si (~2% at.), no SiO_2 barrier is observed.[123,124] δ-Ni_2Si is the first compound to form, and NiSi only forms once the Ni layer is consumed. While no oxygen penetrated the silicides in the case of implantation in the Ni, it is now redistributed extensively. The implantation profile is conserved, with corrections only due to changes in density when going from Si to the silicides, as if the oxygen atoms were pinned to the Si atoms. Initially equal to that in the unimplanted case, the growth rate of δ-Ni_2Si decreases after some time, presumably when the growth front hits the peak of the O_2 implantation profile in the Si. The presence of O_2 seems to interfere slightly with the diffusion of Ni atoms or perhaps with the interface reaction.

If O_2 is implanted in δ-Ni_2Si (~1% at.) after it was grown, the growth rate of NiSi is slower[123]. The observed decrease is not clearly related to the presence of O_2 and may be due in part to implantation damage in the δ-Ni_2Si layer as it does not scale with the implanted dose. The O_2 initially present in the δ-Ni_2Si is redistributed in the NiSi without interfacial accumulation similarly to the case of implantation in the Si.

The differences in behavior with implantation locus are a consequence of the combined effect of the asymmetries in the affinity of O_2 for Si and Ni and in the mobility of Ni[123,124]. O_2 binds strongly to Si and weakly to Ni, which is the mobile species. As Ni atoms move, O_2 remains rather immobile and sticks to Si if it is available. A barrier forms

in the case of implantation in the Ni because all the O_2 initially spread throughout the whole volume of the Ni layer segregates into a layer of SiO_2. It was evaluated that the latter must be at least 25Å to block Ni diffusion, which is the typical thickness of the native oxide found on Si surfaces. It is therefore surprising that no promotion of $NiSi_2$ nucleation, similar to the results of Teodorescu *et al.*[107] is ever reported for O_2 implantations.

Effect of nitrogen implantation

Nitrogen behaves in a similar way to O_2, but is much more mobile in Ni[123,127] because it does not form stable compounds with Ni (whereas a stable NiO exist). When N_2 is implanted in the metal layer, it moves so fast, that it builds up an interfacial barrier preventing any reaction even for lower implantation doses than with O_2 (between 0.4 and 0.8% at. in Ni). For low doses, δ-Ni_2Si is found to form first, but for intermediate doses NiSi is the only compound observed. The threshold dose for the complete suppression of the reaction was shown to depend on the areal density of Si at the interface, being larger on Si(111) than on Si(001) substrates. These results indicate that the reaction is blocked by the formation of a Si-N compound at the interface.[127]

When N_2 is implanted in the Si, no complete suppression is observed even at doses over the threshold value for implantations in the Ni layer. The growth rate of δ-Ni_2Si is however increasingly slowed down with increasing N_2 dose.[124,127]

Effect of Carbon implantations

Scott found that, at least for similar doses than O_2 and N_2, C implanted in Ni does not form a total barrier to reaction. However, it is found to slow down the growth rate of δ-Ni_2Si by up to a factor of two.[123] It should be mentioned that all the implantations

(O_2,N_2 and C), used by Scott *et al.*[123,124,127] were performed after the deposition of the Ni layer.

3.3.4 Effect of common implanted CMOS doping impurities : arsenic, boron and phosphorous

The particular feature of doping impurities is that they are usually introduced in relatively small concentrations, i.e below the solubility limits of silicon, which are 0.34%, 1.7% and 3.4% respectively for B, P and As at 1000°C.[128] Redistribution can induce changes in local concentrations but it is usually observed to remain within the solubility limits of silicides as well. It is not clear a priori whether we should expect the effects of dopants on solid-state reactions to be small or not. As, B and P can form binary compounds with Ni[129,130], and their free energies of formation are quite close to those of Ni silicides. For instance, the respective heats of formation for NiSi, NiB, NiP and NiAs are –92, -102, -133 and –93 kJ/mol[130], which suggest that the impurities could compete with Si for Ni-bond formation.[1] Nonetheless, one may expect the effects to be more kinetic than thermodynamic, since none of the Ni_xD_y phases (where D is the dopant atom) have a crystal structure that is miscible in the corresponding Ni_xSi_y counterpart, except for NiAs and NiP_2. These compounds have structures that could respectively be compatible with the two forms of NiSi (hexagonal and orthorhombic) and with $NiSi_2$.

Effect of arsenic doping

Similarly to the case of O_2, arsenic redistribution differs whether it is implanted in the layer of the moving species (Ni) or the stationary species (Si). In the case of implantation in Ni, As (~0.7 at. % As) is found to segregate and accumulate at the Ni/δ-

[1] We assume here that dopants atoms are substitutional on the Si sublattices of the silicides just like they are in Si[130].

Ni_2Si interface and in the case of Si, (~3 at. % As), it distributes quite extensively with a high degree of profile conservation in the growing silicide.[131] When implanted directly in δ-Ni_2Si (~0.5% at.), the arsenic profile is not altered by annealing at 275°C, revealing an almost inexistent diffusion of As in the compound. While it may ensue from the low temperature at which the silicide grows, a similar behavior is observed for $CoSi_2$ at temperatures above 600°C.[132] These two silicides are surely different and so can be the mechanisms explaining the low diffusion. However the comparison illustrates well that the temperature is not necessarily the only factor at play.

Using the very sensitive technique of neutron activation, Ohdomari *et al.* found a certain degree of As redistribution in the Si during the formations of δ-Ni_2Si and NiSi, through a so-called snowplow effect. About 10% of the As atoms initially present (i.e. ~3% at. Si) are pushed deeper into the Si by the advancing growth front.[133] Of these snowplowed As atoms, at most 6.5%, is estimated to be still electrically active in the Si.

No significant differences were found in the growth rates of δ-Ni_2Si and NiSi, with respect to the undoped case when the As is implanted in the substrate (poly- or mono-crystalline), even for doses between 3 and 5% at., which are higher than the solubility limit of As in Si.[133,134,135,136] As a comparison, arsenic was shown to decrease the diffusion-controlled growth rate of PtSi, without changing however the activation energy.[137] Rinderknecht *et al.*[138] reported a delay in the formation of $NiSi_2$, which could be related to the low solubility of As in the compound, requiring its expulsion, thus raising the nucleation barrier.

Effect of phosphorus doping

No information was found in the literature about redistribution properties of phosphorus in growing Ni silicides. However, it is reported to diffuse quite readily in $CoSi_2$ where it was implanted after the silicide growth.[132] NiSi formation was found to

be completed earlier in samples where the Si was implanted with ~2.5% at. P, despite the high concentration.[138] This is consistent with the report of Takai and Tu who observed an accelerated growth rate of δ-Ni_2Si on LPCVD grown poly-Si containing ~1.6% at. P.[75] They showed that the diffusivity of Si in δ-Ni_2Si was increased by a factor of 4, while that of Ni remained practically unaffected. In both cases the P concentration exceeded the solubility limit of the Si yet to different extents. Rindeknecht *et al.* observed a delay in the nucleation of $NiSi_2$.[138]

Effect of boron doping

When 0.04 at.% to 0.2 at. % boron are implanted in the Si, it piles-up at the Ni/silicide interface upon formation. Redistributions in the silicides are found to occur, to levels between 0.0002 to 0.001 at.%, depending on the compound.[139] The diffusion-controlled growth kinetics of the silicides is slowed down[135,136] and once the Ni is completely consumed, the piled-up B ends up at the surface.[139] It is proposed that the diffusion of B in grain boundaries of the silicide explains the accumulation towards the surface. This is consistent with the fact that boron was found to diffuse rapidly in $CoSi_2$.[132] Rinderknecht *et al.* observed a delay in the nucleation of $NiSi_2$[138] both on poly- and c-Si.

One study reported the formation of $NiSi_2$ as the first and only compound at temperatures as low as 250°C in B-implanted samples with doses of about 0.5% at. in Si[140]. The δ-Ni_2Si compound is completely skipped while NiSi forms at temperatures above 330°C. Although a significantly long activation annealing was performed and the interfacial oxide was removed prior to Ni deposition, the influence of a pre-amorphization implant and the presence of a remaining interfacial oxide cannot be ruled out given the experimental protocol employed. Even if the presence of various dopants was found to have an influence on the formation of $NiSi_2$ in other studies from the same group,[141,142] we believe that the main mechanism responsible for the results they report in

reference 140 is not the presence of B atoms, based on the following facts : *i)* Experiments with boron implantations without pre-amorphization did not result in the same reaction scheme, with namely the formation of δ-Ni_2Si as the first compound,[142] *ii)* B implantations are commonly used in the CMOS industry, while such a premature formation of $NiSi_2$ is never reported *iii)* the literature review presented above has shown that only a strong barrier to the diffusion of Ni atoms can result in the formation of $NiSi_2$ at low temperature, and *iv)* the reaction scheme and the plan-view TEM morphology of $NiSi_2$ reported in references 140 and 142 are almost identical to that observed by Teodorescu *et al.* in their oxide mediated epitaxy experiments[107].

3.3.5 Effect of BF_2^+ and fluorine

It is a common practice in the microelectronics industry to use BF_2^+ molecular ions as vectors to implant boron. First of all, the use of heavy ions allows for better implant depth control in shallow junctions, secondly fluorine slows down the diffusion of boron in Si, which helps preserving the implantation profiles during heat treatments.[143] However, it inevitably results in the presence of fluorine atoms in the Si. On one hand it has been reported to improve the thermal stability of NiSi,[144,145] but on the other hand it has also been proposed to have a dramatic impact on the Ni silicidation reactions[140, 141,142].

Effect of BF_2^+ implantation

Keeping in mind the caveats exposed above concerning references 140,141, and 142, we mention the results of Chen *et al.* for BF_2^+ and F^+ implantations. As for boron implantations, they report again the formation of epitaxial $NiSi_2$ at temperatures as low as 250°C [140,141,146]. In most of the cases, the epitaxial layer co-exists with δ-Ni_2Si or NiSi to various extents depending on the exact experimental conditions. In an attempt to isolate

the sole effect of implantation-induced amorphization, they ran control experiments with Si^+ implantations instead of BF_2^+.[146] They observed different schemes whether the implantation damages were annealed or not prior to Ni deposition.

In samples without post-implant annealing (BF_2^+ or Si^+ ions), the observed compound sequence is the same than in un-implanted samples, except that $NiSi_2$ forms at 400°C instead of 700°C and it is polycrystalline (not epitaxial). Complete transformation to $NiSi_2$ is achieved above 500°C. This reaction scheme resembles closely that observed for amorphous Si.[56,57,58]

In samples with post-implant annealing (BF_2^+ ions only), δ-Ni_2Si is the first compound to form, but it starts to co-exist with $NiSi_2$ above 250°C. NiSi then forms above 300°C at the δ-Ni_2Si/$NiSi_2$ interface, which results in the consumption of the δ-Ni_2Si and some of the $NiSi_2$. The disilicide remains present in all subsequent stages, becoming the only compound present at temperatures above 800°C.

Fluorine bubbles were found to accumulate at the grain boundaries of $NiSi_2$ in BF_2^+-implanted samples.[146] Unfortunately, no experiments involving Si^+ implantations followed by an activation annealing were performed in order to isolate the possible contribution of the annealing conditions to the final results.

Effect of fluorine implantation

Fluorine implantation without activation anneals results in the formation of δ-Ni_2Si as the first compound, followed by a stage where NiSi and epitaxial $NiSi_2$ co-exist at 230°C.[142] Adding the activation annealing results in the formation all three compounds at the same time at temperatures between 220 and 260°C.

For the same reasons than mentioned for B implantations above, we believe that the behaviors observed by *Chen et al.* are not caused by the sole chemical nature of the implanted impurities. Although their As and especially P implantations did not result in the formation of epitaxial $NiSi_2$ at low temperature, they did hinder the formation of δ-Ni_2Si in a similar way to oxygen implanted in the Ni layer as presented earlier. The authors themselves mention that oxygen contamination (e.g. knocked-in during through-oxide implantations) may contribute to a certain extent to the observed behaviors.[141] Also, if the experiments using Si^+ implantations may help discriminating the influence of the implantation-induced amorphization,[140,146] they don't allow for isolating the influence of the dopant atoms on *i)* the recrystallization of Si and *ii*) the oxide growth that takes place during the high temperature activation anneal in O_2 and its subsequent etchability during the dilute HF dips. We conclude that the effects of F+ and BF_2^+ are not clear and well understood.

3.4 Conclusion of the literature review

First and foremost, it emerges from all the reviewed papers that the magnitude of the Ni atoms flux arriving at the silicide/Si interface is the main phenomenon that dictates the selection of the growing compounds. This is especially true for $NiSi_2$. Except for cases where impurities are at play, δ-Ni_2Si is always the first crystalline compound to form. Nucleation barriers delay the formations of $Ni_{31}Si_{12}$ and $NiSi_2$ and they almost completely prevent the formations of Ni_3Si_2 and Ni_3Si. The thin film growth schemes exhibit a layer-by-layer morphology in the vast majority of the cases reviewed, which appears to originate in *i)* the ease of nucleation of the compounds that form and *ii)* the rapid diffusion of the reactants (namely Ni) both in the growing compounds and at the reaction interfaces.

A limited number of publications report the formation of an hexagonal metastable form of NiSi on Si(111) substrates. The compound co-exists laterally with δ-Ni_2Si or NiSi, but no such compound, nor any other than δ-Ni_2Si, NiSi and $NiSi_2$, is reported to form on thick Si(001) substrates in any of the conditions studied.

The main mobile species for the formation of all the Ni silicide phases are the Ni atoms. The growth of δ-Ni_2Si and NiSi are diffusion-controlled in almost all the experimental conditions reviewed (even those involving impurities) while those of Ni_3Si, $Ni_{31}Si_{12}$, Ni_3Si_2 and $NiSi_2$ are controlled by nucleation when no impurities are at play.

The effect of alloying impurities can be classified in two categories: *i)* The added elements form silicides that are soluble in either one of the existing Ni silicides, in which they redistribute more or less uniformly and influence the compound formation through the mixing entropy effect. *ii)* The added elements do not form silicides or form silicides that are not soluble in the existing Ni silicides. They will segregate at interfaces, surfaces or grain boundaries and will influence the compound formation by altering mainly the kinetics and, in a less measurable fashion, interface energies. For some impurities, both effects may be at play at the same time.

The effect of implanted impurities can be subdivided into three categories using their location in the samples and their mobilities.[90] The mobility is determined both by the diffusivities and the solubility of the impurities in the host layer and in the growing silicide layers:

a) Immobile impurity located in the main diffusing species layer (in our case Ni),
b) Immobile impurity, located in the stationary species layer (in our case Si)
c) Mobile impurity without restrictions on its location.

Cases *a)* and *c)* can result in accumulation of dopant atoms at the surface and in loss to the ambient through evaporation. Cases *b)* and *c)* can results in accumulation at the silicide/Si interface. Depending on their ability to form bonds with Si or Ni, the impurities will slow down the reactions, but no compound stabilization phenomena comparable to the mixing entropy effect have been observed.

While impurities in general are found to have a strong effect on the formation of $NiSi_2$, none were found to enhance the formation of Ni_3Si, $Ni_{31}Si_{12}$ or Ni_3Si_2.

Chapter 4 : Experimental Techniques

Regardless of the physical properties monitored to study solid-state reactions, the quench-and-measure process mentioned in the introduction of Chapter 3 is generally lengthy, work-intensive and has a time resolution limited by the patience of the experimenter. In this thesis, we have taken advantage of a unique non-destructive and fast characterization technique that combines the real-time measurements of three physical properties: diffracted x-ray intensity, electrical resistance, and diffuse light scattering, acquired *in situ* during controlled heating experiments.

Following the description of sample preparation and metal deposition most of the chapter is devoted to the presentation of the *in situ* XRD technique. We then review the details of the transmission electron microscopy (TEM) specimen preparation. TEM was used extensively in the work presented in chapter 5 to confirm the compound identification deduced from the *in situ* XRD and investigate the microstructure of the reacted samples. Finally, brief descriptions of Rutherford backscattering spectrometry and secondary ion mass spectroscopy (SIMS), used respectively to support the compound identification in chapter 5 and assess the fluorine distribution profiles in chapter 8, are provided.

4.1 Sample preparation

All samples investigated in this thesis consist of Ni thin films with thicknesses between 2 and 500 nm, deposited either on SOI or bulk c-Si substrates with (001) crystallographic planes parallel to their surface. Both types of substrates were used interchangeably depending on their availability as they yield results that are not distinguishable with the characterization techniques used in this work as far as solid-state reactions are concerned. The more expensive SOI substrates are particularly well suited

for *in situ* resistance measurements because they allow for isolating the contribution of the silicide layers. The Si slabs being rather thin (120nm), their resistance remains large compared to that of the silicides, even at high temperatures, so that their contribution to the total resistance remains small.

All substrates were dipped in dilute (10%) HF solutions for 55s prior to Ni thin film deposition to strip the native oxide and passivate the surface. The excess HF was subsequently blown dry with pure N_2, without rinsing, before loading the substrates in the vacuum chamber of the deposition system.

Depositions were carried out in a MRC-643 magnetron sputtering system under 10 mTorr of high-purity Ar with the following procedure: After inserting the samples, the load-lock is evacuated successively by mechanical, turbo-molecular and cryogenic pumps down to 1×10^{-8} Torr. A sliding carriage scans the sample holder in front of a rectangle-shaped Ni target (99.999% pure), which is sputtered under constant plasma excitation conditions. The deposition rate being constant, the total Ni thickness is controlled by the carriage speed as it passes in front of the target. Samples with thicknesses up to 100nm Ni were deposited in one pass, while thicker samples required multiple passes separated by 10-minute pauses for cool-down. Such schemes were found to be necessary to avoid undesired reactions caused by excessive heating during deposition.

4.2 In situ real time X-ray diffraction

4.2.1 Principles and concepts

General X-ray diffraction

Diffraction of x-rays by crystalline materials follows the very well known Bragg's law:

Equation 4-1 $$n\lambda = 2d_{hkl}\sin\theta$$

which links the diffraction angle θ to the inter-planar spacing d_{hkl} through the x-rays wavelength λ and a constant n, which is usually set to unity. By definition, Equation 4-1 implies that the angle θ is such that the bisector b is normal to the hkl planes, as illustrated in Figure 4.1.

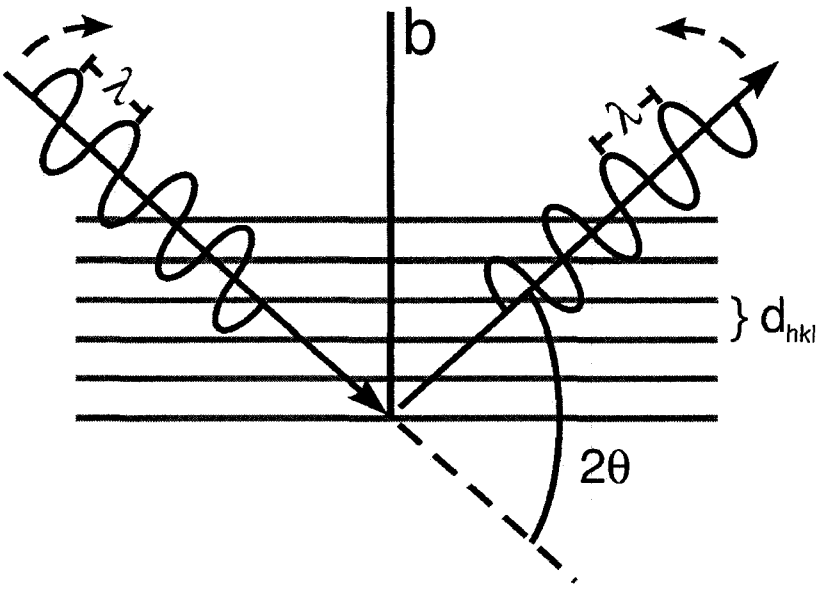

Figure 4.1: Diffraction at an angle 2θ from crystallographic planes spaced by a distance d.

The silicide compounds formed during solid-state reactions are most of the time polycrystalline. Such materials are comprised of multitudes of grains, each of which is an individual crystal that can diffract x-rays. In powders, grains are oriented randomly such that when an x-ray beam hits a sample at fixed incidence angle, several diffracted beams can arise, each $2\theta_i$ angle corresponding to a different value of crystallographic plane spacing d_{hkl}, (Figure 4.2). Given an appropriate detection apparatus, all of these diffracted beams can be measured simultaneously. While the same logic applies to thin films, grains may assume preferential orientations to minimize their interface energy with the

substrate, such that fewer crystal planes may be oriented so as to produce diffracted beams from the interaction with a fixed x-ray beam. Our *in situ* XRD measurement system is designed for measuring simultaneously several diffracted beams that may arise from the interaction of a fixed X-ray beam with poly-crystalline thin films, and to do it in a dynamical way that allows for performing real-time experiments.

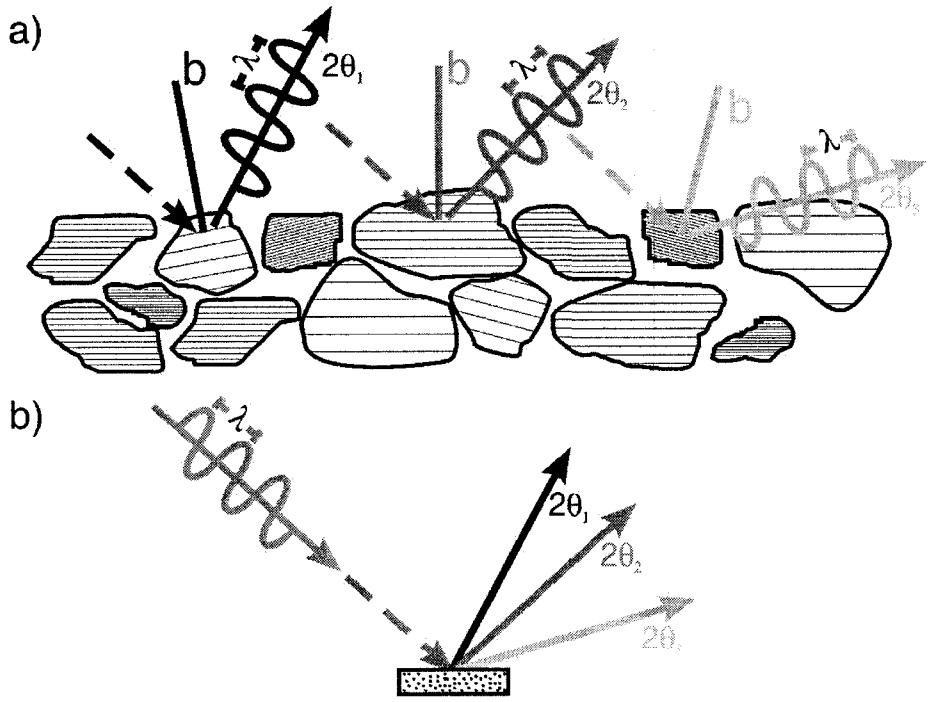

Figure 4.2: a) Each grain of a polycrystalline sample is an individual crystal. Diffraction occurs whenever a hkl plane familiy satisfies the Bragg's law, i.e. that the bisector b is perpendicular to the planes. a) Diffraction from a polycrystalline sample yields several diffracted beams with fixed angle incident beam.

4.2.2 Experimental setup

The *in situ* XRD measurement system is divided in three parts which will be presented in the following order: *i)* the diffractometer and the detector, *ii)* the x-ray source and *iii)* the controlled-environment annealing chamber.

The detector and the diffractometer

The x-ray detector consists of a 25mm-long line-shaped solid-state CCD strip of 1024 pixels. Located at 10 cm of the chamber's rotation axis (which coincides with the surface of the sample), it allows for covering a 2θ span of 14°. The response of the CCD detector to the x-rays is linear, which allows for direct conversion of the measured electrical signal to intensity. The camera can be operated in a constant acquisition mode, with exposure times down to 0.1sec per frame, which allows for easy and accurate real-time acquisition.

The annealing chamber, which holds the samples, is installed on a Huber four-circle diffractometer. Our configuration uses a fixed x-ray source such that the incidence angle is varied by tilting the chamber. Because of the vacuum pipes attached to the chamber and the electrical connections made to the detector, the accessible ranges of incidence (θ) and diffraction angles (2θ) are limited to 0-30° and 0-60° respectively. All angles are usually kept fixed during annealing experiments, but θ and 2θ can be scanned in a continuous and synchronous mode to acquire pre- or post-annealing θ-2θ like spectra over the accessible range.

The X-ray source

Time-resolved experiments, especially when they are conducted on very thin films at high annealing ramp rates (up to 50C/s), require large incident x-ray intensities. Our system is consequently installed at the end of the beam line of a synchrotron accelerator, a very high intensity X-ray source presented schematically in Figure 4.3. It consists of a long and closed polygonal vacuum tunnel, or more correctly storage ring, in which electrons are accelerated and maintained at relativistic speeds. Along their path, electrons pass through different types of magnets (undulators, wigglers and benders) which alter their actual trajectory, sometimes causing them to oscillate, or simply

redirecting them from one polygon straight to the other. In all cases, the large acceleration that ensues from steering the relativistic electrons results in the emission of radiation, which mostly lies in the x-ray part of the electromagnetic spectrum. This radiation is collected and transferred to the laboratory through extractions ports and beam-patterning "optics". Depending on the type of magnet, the emitted radiation will have different properties of intensity, polarization, coherence, spectral and power distributions.

All our experiments were performed at beam line X-20C of the National Synchrotron Light Source (NSLS) in Brookhaven National Laboratory (Long Island, New York). The beam line exploits the radiation of a bending magnet and we selected a wavelength of 1.797A, which corresponds to a photon energy of 6.9keV, in order to operate at the maximum brilliance allowed by the source/monochromator couple.

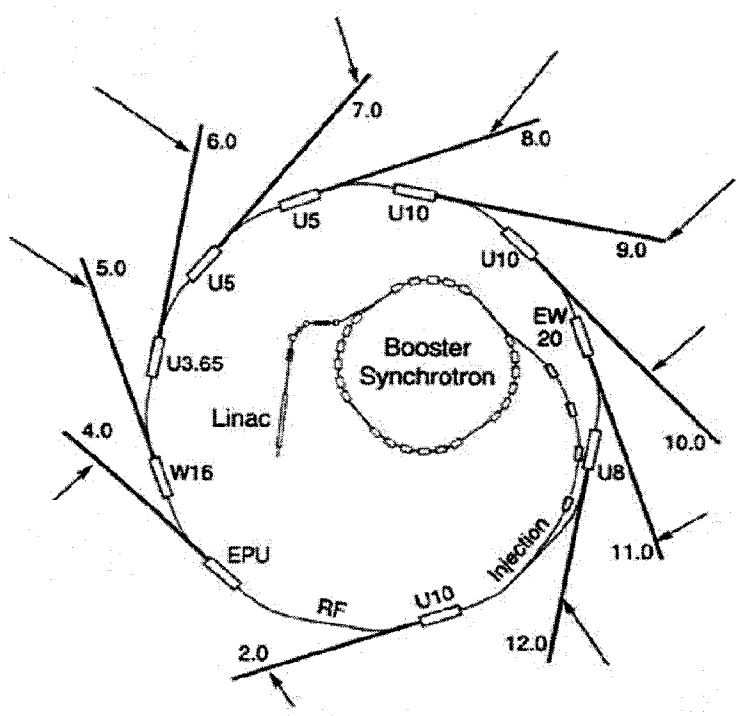

Figure 4.3: Schematic bird's eye view of a synchrotron. Arrows indicate the position of end stations.

A concave grazing-incidence metallic mirror focuses the x-rays before they enter a scanning double-crystal, fixed exit-angle multilayer monochromator. Each "crystal" (the term is abusive) consists in fact of stacks of alternating 23nm thick W and Si layers. This monochromator achieves a relative spectral width $\Delta\lambda/\lambda$ of 1.5% while yielding almost 2 orders of magnitude more intensity then Si or Ge double-crystal monochromators (which have typical spectral widths between 0.01 and 0.5%). After focalization and monochromatization, the beam's shape is patterned by horizontal and vertical slits, which yields a final flux at the sample of about 1×10^{13} photons/s for a beam size of 1mm x 1mm. The CCD detector being easily destroyed by excessively strong diffracted beams, one can limit if necessary the incident flux by inserting up to 400μm of copper shims in increments of 25μm, upstream from the slits. At our operation wavelength, the absorption length of x-rays in copper is 14.38μm so that each shim attenuates the beam by a factor of 0.176. Two sets of proportional ionization gauges, respectively located downstream of the copper shims unit and of the last set of slits, monitor changes in the incident X-ray intensity at all times. Under our current operation conditions, the X-ray fluence at the sample is typically 5 to 6 orders of magnitude larger than with conventional static anode sources.

The controlled-environment annealing chamber

Figure 4.4 presents a schematic side view of the chamber. It consists of a 6-inch (diameter) cylindrical stainless-steel vacuum chamber mounted on the Huber diffractometer using the back flange. The heating element, the resistance leads and the optical fibers from the light scattering apparatus are mounted on a sample-holding stage fixed to the removable front flange (not drawn). The chamber is equipped with a 1-inch wide beryllium window that fits its cylindrical shape, covering an angle span of 180°, to allow for x-rays to enter and exit the chamber while keeping a controlled atmosphere. This control is achieved through a combination of pumping and back-filling with ultra-pure He. The vacuum is provided by mechanical and turbo-molecular pumps, which

typically reach pressures below 1×10^{-6} Torr. The vacuum pipes and gas tubing connect to the chamber by the back flange. A heated titanium bed installed upstream from the chamber reduces the oxygen content of commercial compressed ultra high-purity grade (UHP) He below the parts per billion (PPB) level through a gettering reaction. All our experiments are conducted under a steady He flow of about 1 liter per minute at 1atm.

The sample holder's stage is made of copper. It is supported by two horizontal water-cooled braces, which ensure accurate dynamic temperature control and fast quenching. During the experiments, the samples, about $1cm^2$ in size, lay flat on a molybdenum block, which sits on the heating element and houses the thermocouple. Samples are held in place by the four spring-loaded tantalum leads used for the resistance measurement. Mo and Ta are used because of their thermal stability and Ta is preferred for the spring-loaded leads because of its better flexibility and formability. The heating element is electrically insulated from the Mo block and thermally insulated from the cooled Cu block by a quartz spacer. The current is brought from the feed-through connector of the front flange through hand-made Ta strips and the temperature is controlled to within 3°C by a standard PID loop. Annealing recipes can be performed both in isothermal regimes or ramped-type with rates ranging from 0.1 to 50°C/s. The target temperatures of isothermal anneals are usually reached at rates of 27°C/min. Temperature calibration is critical and will be described in a following section.

The light scattering technique uses the interference resulting from the interaction of coherent light with surfaces and interfaces to measure their in-plane roughness.[147] In our system, a set of three optical fibers are used to feed the light from a He-Ne laser into the chamber at an angle of 65° and extract the signals reflected along two non-specular angles of –20° and +52° off the sample's normal. The angles correspond to correlation lengths of the roughness of respectively 0.5 and about 5μm.

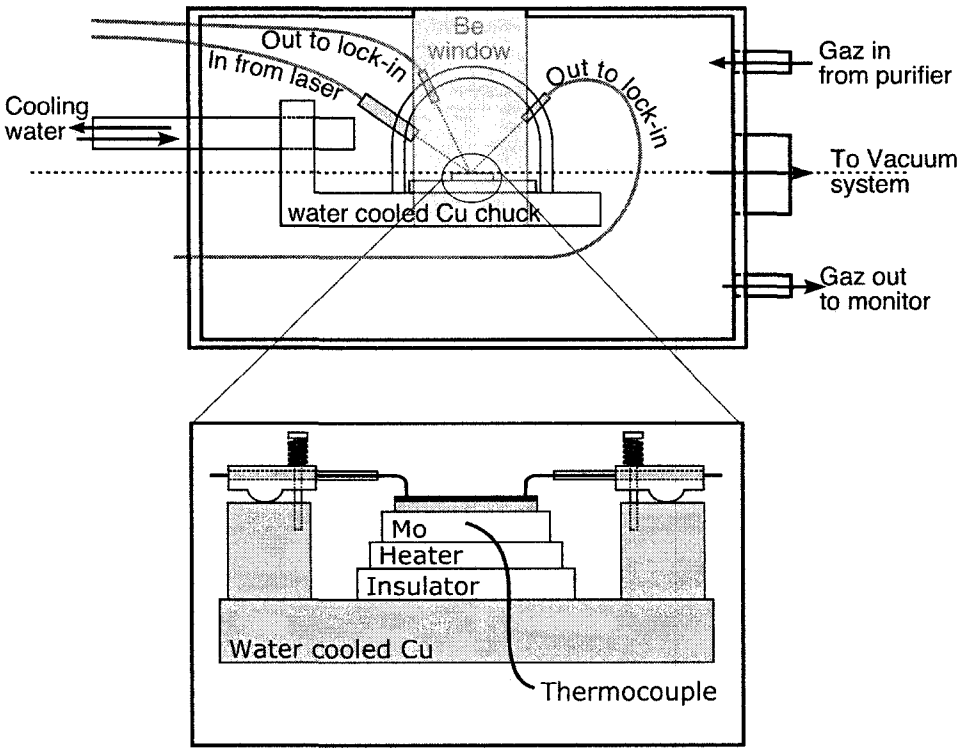

Figure 4.4: Schematic diagram of the *in situ* annealing chamber.

Typical in situ XRD data

Figure 4.5 (a) and (b) show the typical result of the 3°C/s ramp annealing of a 100 nm Ni layer on crystalline Si (001) as monitored by in situ XRD, resistance and light scattering. The upper plot is a 14° (2θ) wide diffraction spectrum where the diffracted intensity is represented as grey scale (light and dark corresponding respectively to high and low intensities) and by level curves. It is plotted against 2θ angle (ordinate) and temperature in °C (abscissa). In the lower plot, the normalized resistance (in black) and light scattering signals for correlation lengths of 5μm and 0.5μm are also plotted against the same temperature scale. A detailed peak indexation is superimposed on Figure 4.5 for indicative purposes. Note that the resistance curve follows the different peak transitions

and highlights clearly the formation of the low-resistivity NiSi compound around 400°C. The sharp peak in the light scattering signal around 375°C indicates that important modifications took place in the layer stack's roughness with a length scale of 0.5μm.

Combining these results highlights the efficiency of simultaneous measurements performed *in situ* to study the formation of solid compounds. At most 20 minutes are required to install the sample, load the chamber, pump, purge, perform a 3°C/s ramp-type annealing from 100°c to 950°C, treat and plot the data presented in Figure 4.5. We can therefore obtain very quickly a comprehensive survey of the reactions occurring in a sample over a large range of temperatures and easily study the impact of different parameters such as doping, alloying, metal thickness and substrate crystallinity on the solid-state reactions.

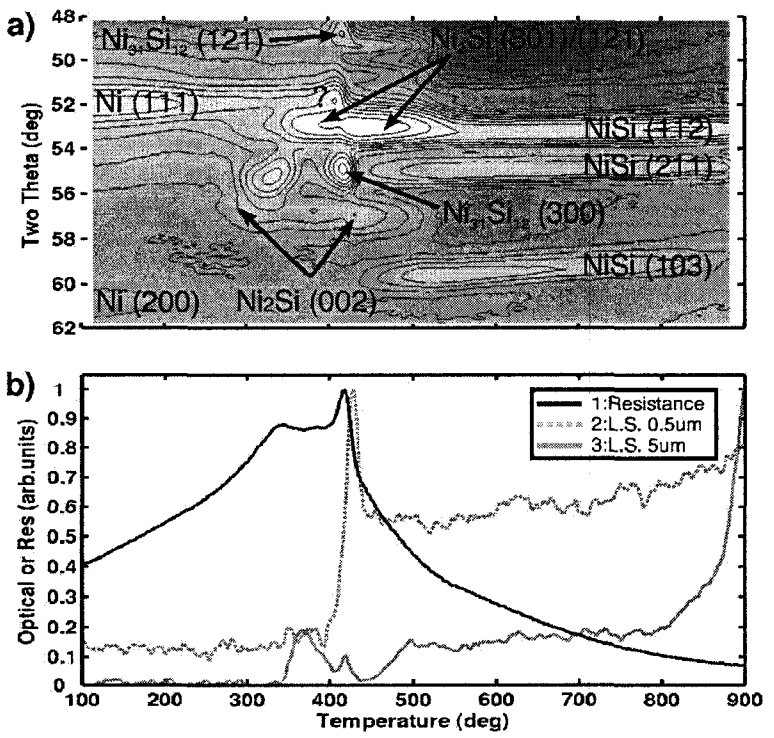

Figure 4.5: a) Typical *in situ* x-ray diffraction result obtained during the annealing of a 100nm Ni layer on a Si (001) substrate along with b) the corresponding resistance and light scattering traces for two different length scales.

4.2.3 Calibrations and assumptions

Temperature scale calibration

The temperature scale calibration mainly corrects for the positioning-dependant temperature difference (or lag) between the sample's surface and the thermocouple. The procedure uses the eutectic melting points of three alloy systems: Au-Si, Al-Si and Ag-Si. With respective eutectic temperatures of 363°C, 577°C and 835°C, this combination of choices allows for reliably covering most of the 100-1000°C range. Eutectic points being thermodynamic invariants, we use the shift in the measured melting temperatures to correct to zero lag. Because the magnitude of this lag changes with the heating rate, a complete calibration requires annealing samples of all three eutectic systems for each of the ramp rates to be used during an experimental session.

The samples we use for calibration consist of 200nm thick M-Si polycrystalline bi-layer stacks (where M is Au, Al or Ag) deposited onto oxidized Si wafers. We rely on the inevitable interdiffusion resulting from raising the temperature to produce intermixed regions at the M-Si interfaces. Since all three binary couples are simple eutectic systems, the first liquids should form at the eutectic temperatures regardless of the compositions of the intermixed regions. From then, dissolution of the atoms from the solid into the liquid phases occurs very rapidly, resulting in a fast consumption of both the initial elemental layers. When monitoring the evolution of the diffraction peaks of any of the initial metals (Au, Al or Ag), a sudden and rapid decrease in intensity will take place upon melting of the intermixed region. We determine the position of the eutectic melting temperature as the point at which the derivative of the diffracted intensity of the metals (111) XRD peaks is minimal.

Flat detector effect

The output of the detector control software consists of data where x-ray intensity is given in photons counts as a function of the position (pixel number) along the CCD strip. We convert these intensity-vs-position data into intensity-vs-angle. If the detector were curved, the relationship between position and angle would be simple and independent of the position along the CCD strip as given by:

$$\theta = S/R$$

where θ is the angle, S the position along the CCD strip and R the radius of curvature of the detector as defined on Figure 4.6.

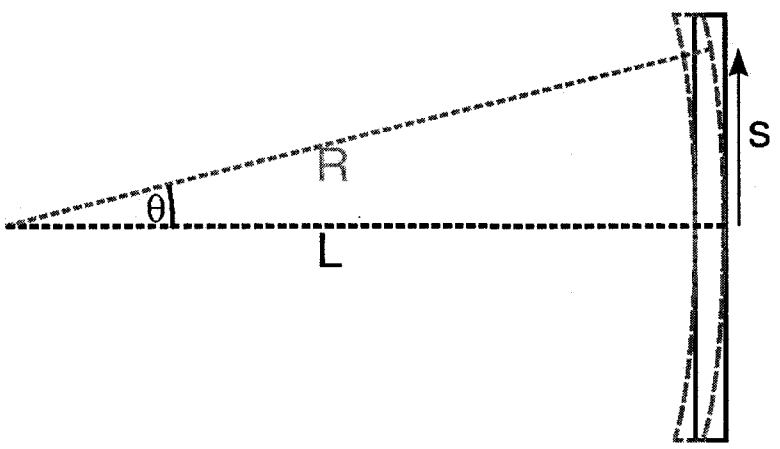

Figure 4.6: Diagram of the flat versus curved detector. The data from the detector's controller provides a measure of intensity versus S.

For our flat detector, θ/S is a function of S as given by :

$$\theta = \mathrm{Atan}(S/L)$$

where L is the distance between the center pixel of the detector and the position chamber's rotation axis, which also happens to be the rotation acix of the diffractometer. As mentioned earlier, L is about 100mm while S is between –12.5mm and +12.5mm (the total CCD strip's length is 25mm, 1 inch). The S/L ratio varies between –0.125 and +0.125, a range over which atan(S/L) is almost identical to (S/L) to within 0.5% (maximum deviation at each end of the strip). For our experimental geometry, the relationship between θ and S can hence be considered independent of the position along the CCD strip, such that the XRD peak shapes are not significantly distorted by the flat nature of the detector. This is especially true for peaks positioned within 3° from the center, where the difference between atan(S/L) and (S/L) is below 0.1%.

Every time the detector is replaced or moved along L (c.f.Figure 4.6), the exact pixel/angle ratio is re-calibrated by recording the pixel positions where the direct beam, incident at θ=0, hits the detector when its center is positioned at respectively –7° and + 7° 2θ. This number is then used to convert positions on the CCD to angular values. The angular resolution of the experimental setup is directly related to the distance between pixels. In our typical geometry, the pixel-to-pixel distance correspond to 0.013°, however we usually bin the pixels eight-by-eight to speed up the data treatment such that this value is closer to 0.1°.

4.2.4 Measurement of growth kinetics by X-ray diffraction

Provided the solid-state reactions are not photo-sensitive, the study the compound layer's growth kinetics can be achieved by monitoring $I_{(hkl)}(t)$, the integrated intensity of its x-ray diffraction peaks during annealing experiments. The integrated intensity under a diffraction peak is directly proportional to the ratio of the compound's volume to the total interaction volume, i.e the volume effectively probed by the x-rays:

Equation 4-2

$$I_{(hkl)}(t) = I_0 K(\theta,T) \times \frac{v_{compound}(t)}{V_{tot}}$$

where I_0 is the incident intensity and V_{tot} the interaction volume. The $K(\theta,T)$ term depends on several factors including the distribution of the grain orientations. Its exact analytical expression is therefore difficult to establish for thin films where texture effects often result in particular non-random orientation distributions, which are generally not well known. An expression is however very well known for the case of powder samples and it can be used to illustrate the various assumptions we make in our analysis [148]:

Equation 4-3

$$I_{(hkl)} = I_0 \underbrace{\left[\left(\frac{\mu_0}{4\pi}\right)^2 \left(\frac{e^4}{m^2 r^2}\right)\right.}_{\text{Scattering efficiency}} \underbrace{\left.\left(\frac{1+\cos^2 2\theta}{2}\right)\right]}_{\text{Polarization term}} |F|^2 \, p \underbrace{\left(\frac{1}{\sin^2\theta\cos\theta}\right)}_{\text{Lorentz factor}} \frac{e^{-2M}}{2\mu_{abs}}$$

where I_0 is the incident x-ray intensity, θ is the diffraction angle, μ_0 is the permittivity of vacuum, e and m are respectively the electron's charge and mass, r is the diffractometer's arms radius (here the detector position L), F is the structure factor, p is the (hkl) reflection's multiplicity, M is a temperature-dependant factor that will be detailed later and μ_{abs} is the linear x-ray absorption coefficient (m^{-1}). The polarization factor is expressed for the case of unpolarized radiation. It would be unity for a linear polarization where the electric field vector perpendicular is to the plane of incidence. The Lorentz factor is a measure of the probability that the *hkl* planes being probed are oriented so as to satisfy the diffraction condition. This grain-orientation-dependant term is expressed here for the case of the random distribution characteristic of powders.

In the framework of our experiments, we make the assumption that the interaction volume, the scattering efficiency, the polarization term, and the multiplicity p are

constant. We also assume that the Lorentz factor is constant, which implies that the texture of the compound layers do not vary as they grow. The structure factor F may vary in time if the growing compound changes composition while keeping the same crystal structure (as could occur for instances in non-stoichiometric compounds). This latter effect will be dealt with in greater details in Chapter 7. In what follows we will show that the variations of the M and μ_{abs} factors, hence that of the $K(\theta,T)$ term, can be neglected during both isothermal and ramp-type annealing experiments.

In Table 4-1 we present the attenuation lengths of x-rays in six particularly relevant Ni silicide phases. Using the value for pure Ni (the most absorbing material in the case of Ni silicides), we calculate an intensity loss of less than 1% (0.75%) after passing through a 30nm thick layer at an angle of 30°. All our kinetics measurements will be performed in samples where the total silicide thickness will not exceed 22nm[1]. Consequently, absorption can be neglected when analyzing the data, which is particularly convenient when multiple compounds form simultaneously in various possible geometries (stacked layers or layers with lateral non uniformities).

Table 4-1: X-ray attenuation lengths in some Ni silicides

Phase	Attenuation length (μm)
Ni	15.49
Ni_2Si-θ	17.66
N_2Si-δ	16.53
Ni_3Si_2	19.04
NiSi	20.99
Si	45.25

[1] 10nm of Ni will consume 18nm of Si to form 22nm of NiSi. We are interested in the growth of compounds forming before NiSi, which are therefore thinner.

The exact analytical expression of the temperature factor M expressed in Equation 4-3 is crystal-structure dependant. Nickel silicides have either an orthorhombic or hexagonal structure for which the expression of M is not known. For cubic materials it has the form:

$$M = \frac{6h^2T}{mk\Theta^2}\left[\phi(\frac{\Theta}{T}) + \frac{\Theta}{4T}\right]\left(\frac{(\sin\theta)}{\lambda}\right)^2$$

where h is Plank's constant, m is the compound's average atomic molar mass, k is Boltzmann's constant, T is the temperature, Θ is the Debye temperature, θ is the diffraction angle and λ the x-rays wavelength. The Debye temperature is not known for the different silicides, but those of Ni and Si are respectively 400K and 625K. Between 230°C and 330°C, the range over which all our isothermal experiments are conducted, these Debye temperatures translate to variations of e^{-2M} of at most 1.8%. This is typically within the uncertainty generated by the peak fitting procedure and will therefore be neglected. Moreover, since the factor will be essentially constant for each isothermal experiment, it will not affect the shape of the time evolution of the peak's intensity.

The study of growth kinetics in the ramp-type annealing regime is generally conducted using a procedure called Kissinger's analysis, which was described in Chapter 2. This method allows for determining the growth's apparent activation energy by tracking the variation of the temperature (T_{max}) of maximum growth rate $d\xi/dT$ as the heating rate is increased. This is typically achieved by tracking the position where $(\delta I_{hkl}/\delta T)$ is maximal on the temperature scale. Figure 4.7 presents the evolution of the e^{-2M} factor as a function of temperature over the 100°C-900°C range for Ni and Si. The variation is monotonic and almost linear, so that $\delta M/\delta T$ should be small and surely slow varying. While no analytical expressions for M or $\delta M/\delta T$ are available for the silicide materials we study here, their variation is also expected to be monotonic and slow varying. Consequently, the variation of $\delta M/\delta T$ for the different silicides will be neglected

especially over the narrow temperature ranges where we measure the sharp variation of intensities caused by the phase changes.

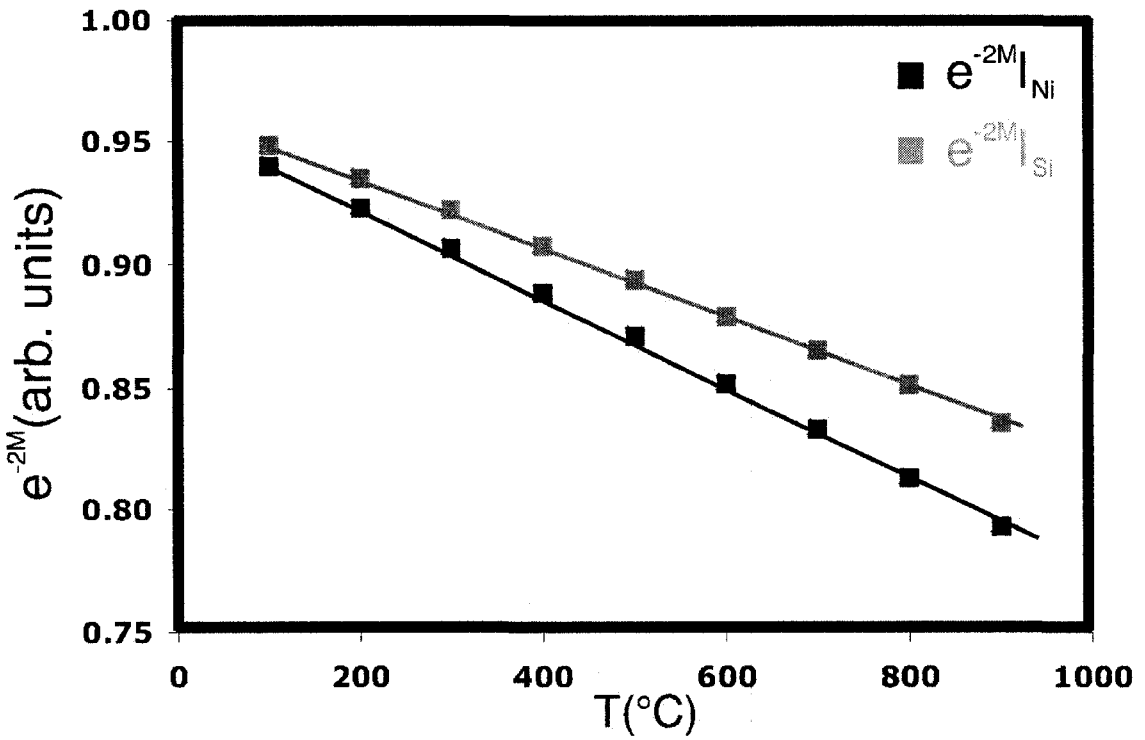

Figure 4.7: Evolution of the temperature correction factor as a function of temperature for Ni and Si. (Calculations made with the analytical form associated to cubic materials).

4.3 Transmission electron microscopy

All our microscopic observations were made on a JEOL JM2100F transmission electron microscope, at an acceleration voltage of 200kV. It is equipped with a highly coherent field emission electron gun (FEG), state-of-the art electron optics and a high-precision motorized stage. Combined, these features allow for obtaining high-resolution imaging conditions and greatly facilitate the controlled tilting required to achieve convergent beam electron diffraction on nanometer-size compound grains.

In the typical preparation process of electron-transparent specimens suitable for TEM investigations, samples will encounter heating steps. If uncontrolled, the heating can alter the nature and the microstructure of the compounds present in samples after carefully planned quenches in selected stages of the reactions. In what follows, we describe the details of the TEM specimen preparation with particular attention given to the precautions implemented to limit the heating.

TEM investigations were mainly done in a cross-sectional mode. Figure 4.8 summarizes the different steps of a) dicing and gluing with epoxy, b) boring, c) tubing d) slicing, e) polishing, f) dimple grinding and g) ion milling. Note that in step a) two pieces from the same sample are glued together face to face. This maximizes the chances of obtaining a region that will be observable under optimal conditions in the sample of interest.

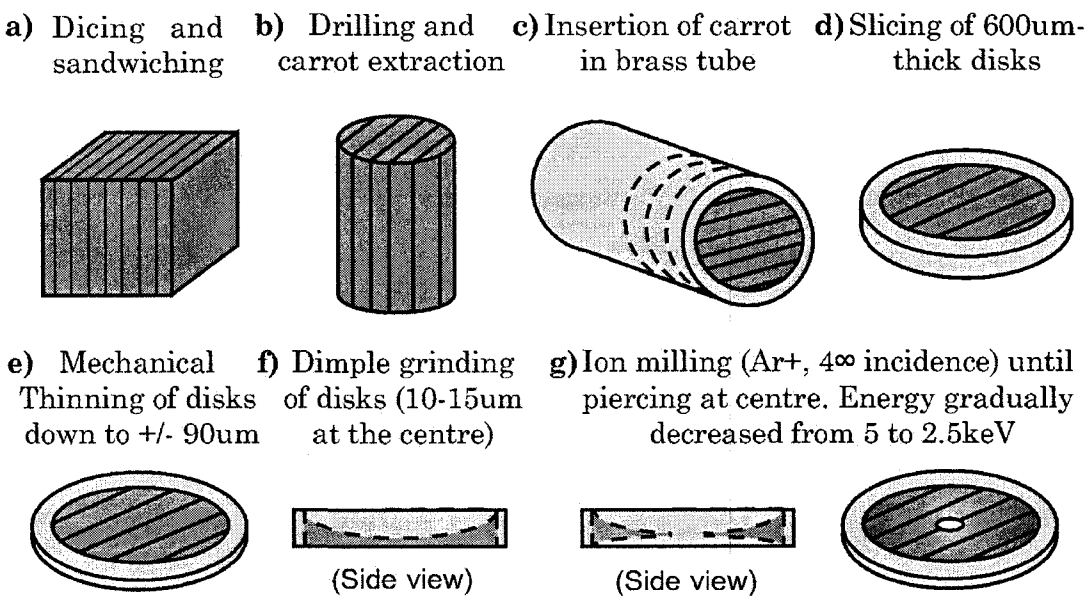

Figure 4.8: Process flow of TEM specimen preparation.

Samples were glued with vacuum-safe conducting epoxy. Boring was done with a Gatan-601 ultrasonic hollow-bit drill and slicing of the intubed cylinder was done with a

rotating dicing saw. Polishing was done with a Gatan-623 disk grinder on a digitally controlled rotating mat. Dimple grinding was done with a Gatan-656 grinding tool. Finally the ion milling was carried out in a Gatan-692 precision ion polishing system (PIPS) using Ar ions.

Specimens will encounter heat in steps b) and g). For step b) the imparted thermal budget is easily limited by using a digitally–controlled heating plate and setting a maximum temperature of 120°C for curing the epoxy.

Heating during ion milling has drawn some attention since the technique was introduced[149,150,151]. Estimates of the temperature rise range from 75°C to as much as 500°C[151] depending on the specimen and sample holder. In our case, the sliced, polished and dimpled specimens typically lay flat directly onto hollow Cu chucks and are held in place by thermo-softening heat-conducting wax.

In an attempt to establish an upper boundary for the temperature reached during the ion milling process, test runs were conducted using indium and tin (Sn95.8%Ag3.5%-Cu0.7%) pellets with respective melting points of 160°C and 217°C. The pellets were welded onto plan view TEM Cu grids, which were placed onto the Cu chuck both with and without wax. Prior to insertion in the ion-milling chamber, cut marks were carved with a razor blade on the surface of the solidified welded blobs to help the observation of the melting in the darkness of the chamber. It was found that without wax, both types of pellets melt within 3 seconds after starting the 5keV Ar+ beam incident at 4° off the horizontal. However, when wax is used, the In pellets do not melt, even after prolonged operation, indicating that the temperature does not exceed 160°C. Our data obtained with the *in situ* XRD system show that Ni-Si reactions are extremely sluggish and, to all intents and purposes, negligible below 180°C. TEM observation of as-deposited samples do reveal the presence of thin interfacial layers (about 2nm thick in samples with 10nm Ni and about 17nm thick in samples with 100nm Ni) but they are believed to form during

the deposition process, where we have virtually no control on the thermal budget and the ion bombardment.

4.4 Complementary techniques

4.4.1 Rutherford backscattering spectroscopy (RBS)

RBS is a technique that allows for determining chemical composition profiles as a function of depth in thin film stacks in a non-destructive way. High energy (1-10Mev) ions (generally He+), are accelerated towards the sample to analyze (commonly referred to as the target) where they undergo scattering reactions. This scattering can be either elastic or inelastic, but RBS is concerned only with the former.

As its name states it, RBS is restricted to ions that are scattered at angles above 90° of their initial course. Although elastically scattered, the ions usually don't keep their initial incident kinetic energy. The total energy is conserved, but it is now redistributed between the probe ions and the target atoms. This redistribution is typically dependant on the scattering angle and, more interestingly, on the ratio between the masses of the probe and target ions. When an ion beam hit a target containing atoms of different kinds, the scattering, as measured at fixed angle, will result in a spectral distribution of the outgoing ions. Analysis of such spectra leads to the determination of the target's chemical composition.

Figure 4.9 presents a schematic diagram of the working principle of RBS. The technique is typically sensitive to elements with atomic number Z above 5 (Boron). The detection limit depends on Z and ranges between 0.001% for heavy atoms to 10% for lighter atoms. The same applies to the depth resolution which is between 5 and 20nm (depending on the collection angle) over measurement areas up to 2mm x 2mm.

Ions can penetrate up to a certain depth in the targets before they are scattered. Conversely they can travel over great distances after they are scattered. If the scattering interactions themselves are elastic, ions lose energy as a consequence of their journey in the target. Various loss phenomena can cause this, but the most important one is the interaction with the electron clouds of the target atoms. Elastic scattering alone would cause the appearance of peaks in the backscattered energy spectra, but energy loss phenomena smear these peaks towards low energy. This phenomenon is at the origin of the depth sensitivity of the technique; the deeper in the target the scattering occurs, the lower the measured energy of the backscattered ions. Consequently the actual backscattering spectrum of a single thin film containing different atoms will appear as a succession of plateaus as depicted in Figure 4.9. In a stack of thin films with different compositions, the plateaus may become uneven, larger and some of them may overlap. Spectra may become even more complex in the presence of roughness, lateral non-homogeneity or concentration gradients, which will result in greater analysis difficulties.

Many different target configurations can lead to similar (or even identical) spectra. The analysis process requires simulating spectra from hypothetical sample configurations through software means. The two most popular software packages are currently GenPlot RUMP© and SIMNRA©. The first one is the oldest and most used but still has a command-line interface. The second one has a more user-friendly graphical interface but was released only 3 years ago and is consequently less spread-out and common. The two packages differ mostly in their treatment of interfacial roughness but SIMNRA is less convenient to simulate concentration gradients. All the simulations results presented in chapter 4 were obtained with RUMP but were verified using SIMNRA to ensure consistency.

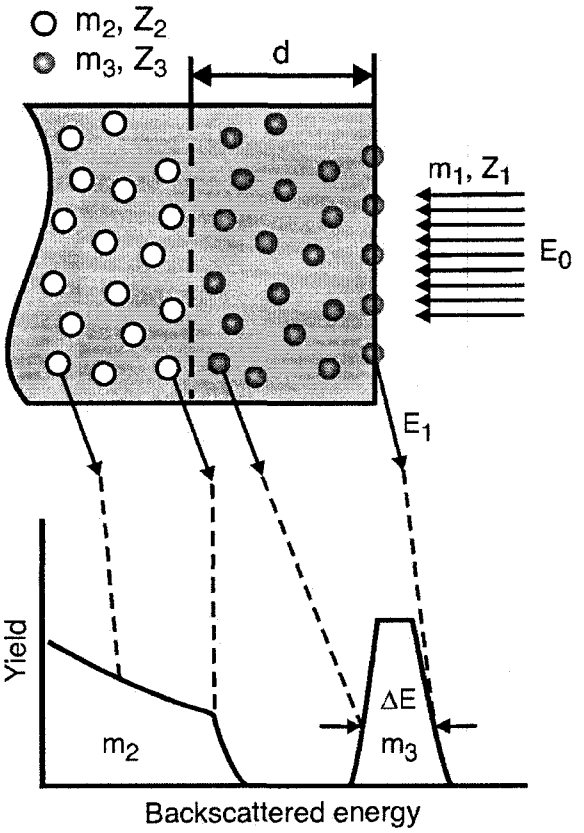

Figure 4.9: Schematic diagram of the energy spectrum of ions (m_1, Z1, E_0) scattered from a sample composed of a substrate (m_2, Z_2) and a surface film (m_3,Z_3) of thickness d.

The RBS results presented in this thesis were acquired with a He^{2+} beam of 2.3MeV, incident at 7° off the sample's normal and backscattered ions were collected at an angle of 78° off the normal (115° from the incidence direction). These conditions allow for maximizing the depth resolution by probing the layer stack at grazing angle.

4.4.2 Time-of-flight Secondary Ion Mass Spectroscopy (TOF-SIMS)

SIMS is a destructive technique that also involves accelerated ions to determine depth composition profiles but with much finer depth resolution and compositional sensitivity than RBS. Heavy ions (typically Ga) are accelerated at energies between 0.5

and 15 keV towards the target where they will sputter particles upon hitting the surface. Depending on the chemical bonding in the target, atoms, molecules or atom clusters get sputtered in an ionic form. Following their ejection from the target, these so-called secondary ions enter a mass spectrometer where they are separated according to their mass before they hit a current detector. Figure 4.10 presents the technique schematically.

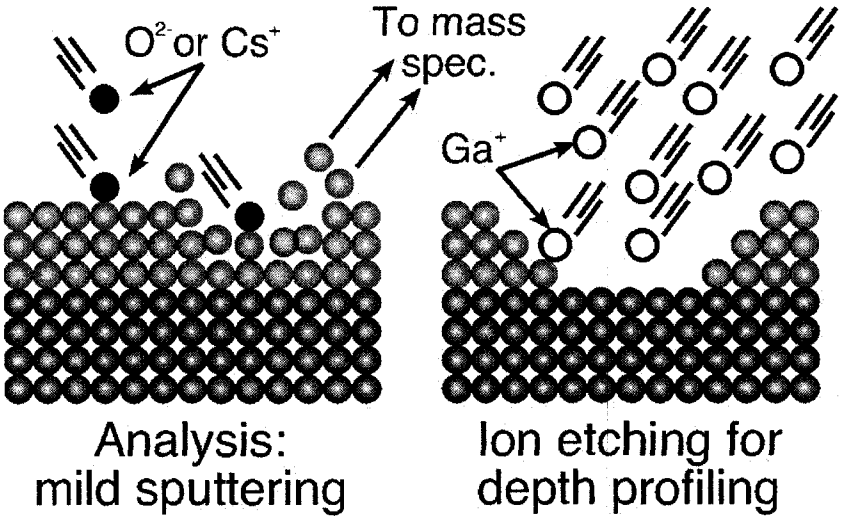

Figure 4.10: Schematics of the SIMS technique.

Depending on the structure of the mass spectrometer column, secondary ions species are analyzed simultaneously or one by one. As primary ions keep hitting and etching the surface, deeper regions of the samples become exposed and measured. By continuously measuring the current corresponding to each secondary ion mass, a distribution profile as a function of depth is established.

SIMS can be used to perform quantitative analysis, but it requires calibration with standard samples. Each chemical species is sputtered with a different efficiency, which biases the measured intensities. The depth scale also needs to be calibrated, which is typically achieved by measuring the final depth of the crater in the measured standard sample by means of some profilometry tool or calibrated electron beam imagery. Typical depth resolution is in the order of the nm or slightly lower.

Three types of mass spectrometer (MS) columns can be used; *i)* Sector field MS, which separate species by their charge/mass ratio through a combination of electric and magnetic fields, *ii)* Quadrupole mass analyzer which selects the masses by using resonant electric fields and *iii)* Time-of-flight MS which accelerates all incoming species to the same kinetic energy and then measures their speed by the time required to travel across a path of known length - knowing the speed and energy, the Q/m ratio is known. In order for TOF measurements to be feasible, the primary beam must be pulsed so that secondary ions arrival rates at the entry of the drift path can be controlled. Charge detection at the end of the mass analyzer is generally achieved with faraday cups coupled to charge multipliers. The various types of MS enable detection limits from the percent down to the tens of PPB levels.

The results presented in chapter 6 were acquired on a IONTOF GmbH SIMS IV TOF-SIMS using a bunch-mode operated 15keV Ga+ primary analysis beam and Cs^- ions for the profiling beam.

Chapter 5 : Non-sequential formation and lateral co-existence of compounds during solid-state reactions in the Ni-Si system

5.1 Introduction

Metal/silicon couples are model systems for solid-state reactions.[4] Many theoretical models aiming to predict the phase formation and sequence during thin film reactions [12,13,16,25] have been devised for or tested with metal silicides, especially Ni-Si and Co-Si because of their importance for the microelectronics industry. It is generally assumed and believed that the reaction of a thin layer on a much thicker substrate proceeds through a sequential, layer-by-layer, succession of compounds.[40] It is expected that the first compound to form is the one with the highest diffusivity for the main diffusing element[16] (e.g. δ-Ni_2Si and Ni in the Ni-Si system). The subsequent compounds then appear in a decreasing order of the content in that element.

During the reaction of Ni and Co thin films with Si substrates, a M_2Si layer forms first (M being the metal atom), followed by a MSi layer.[49,51,61,104,122,152] In both cases MSi_2 is the last compound to form at the silicide/Si interface through a nucleation-controlled growth, which occurs at high temperature (600-800 °C), only after MSi became the only silicide layer present. In both cases, M_2Si is therefore the sole metal-rich compound to form.[41,42,43,44,51]

While a three-compound sequence is consistent with the Co-Si equilibrium phase diagram (EPD), the observation of a single Ni-rich compound is rather surprising since four metal-rich compounds that are stable at room temperature are found in the Ni-Si EPD, in addition to four more compounds stable at higher temperatures. Nonetheless, in the last 30 years, Ni-Si thin film reactions have been studied over a rather large range of

initial metal thicknesses (between 20 and 500 nm), yet no differences have been reported about the reaction scheme.[5,51,61,49] Reports showing deviations from the three-compound sequence focused on systems in which either impurities were present or the supply in one or both of Ni and Si was infinite. For example, the formation of $NiSi_2$ before NiSi[107] has been reported when its epitaxial growth is mediated by a thin oxide layer at the Ni-Si interface.[108] Also, Ni_3Si, $Ni_{31}Si_{12}$ and Ni_3Si_2 were observed in thick lateral diffusion couples annealed for long times at high temperature.[63,70] They were also observed in the late stages of experiments with excess Ni, [62] where the composition reached at the end of the reactions force their formation. Their presence was however not reported in conventional thin-film reactions with excess Si, even by experiments using high brilliance synchrotron x-ray sources.[153]

The absence of some compounds from a given reaction sequence is usually explained by the existence of activation barriers that prevent their nucleation at the interface. These compounds are said to be thermodynamically unfavored. It is therefore generally assumed that Ni_3Si, $Ni_{31}Si_{12}$ and Ni_3Si_2 do not form because of nucleation barriers, but aside from Ni_3Si_2 for which it was suggested,[71] no clear evidence has been published in that regard to our knowledge.

Given the results we present in this chapter, we quickly review the different possible kinetic origins of the sequential layer-by-layer growth scheme commonly observed in thin film reactions. All these kinetic explanations [46] rely on the same basic assumption that nucleation at the interface is laterally uniform:

i) **Competition between the compounds based on their diffusivities and growth rates.** The compounds that usually grow first are the ones where the mobile atoms move faster.[16] Other growing compounds would be consumed faster at one interface than they could grow at the other even if nucleation was possible. [25,28] Consequently if they do form, their layers are so thin that they

are not detected, at least until the fast growing compounds reach a critical thickness or until the atom source for their growth is exhausted. When one of these two conditions is fulfilled, the diffusional atoms flux decreases and the growth of the fast compounds slow down. The slow compounds can then grow at a slower yet finite rate.

ii) **Existence of interfacial reaction barriers that slow down the growth rate of compounds.** [25] If diffusion through a given compound layer to bring atoms to the reaction interface is not a limiting factor, the reduced ability of the different reacting atoms to bond together may hinder the growth. Compounds that are characterized by high interface reaction barriers thus become slow growing phases, which result in a competitive behavior analogous to that described in *i)*.

iii) **Existence of strong interfacial concentration gradients that can suppress nucleation attempts**[46] and forbid the growth of compounds at an interface. This usually leads to the existence of an amorphous interfacial region where nucleation will only become possible once the concentration gradient falls below a critical value, i.e. when the region reaches a minimum thickness.

Contrasting with the traditionally reported Ni-Si reaction sequence, real-time *in situ* XRD measurements during thermal anneals have recently revealed that several nickel-rich phases form before NiSi in samples with thin blanket Ni films deposited on single-crystal Si(001) substrates. [8,154,155] Results from our group also suggest that the observed reaction scheme depends on the initial Ni film thickness. [9,156,157]

In this chapter we revisit the Ni-Si thin film reactions using a combination of several techniques such as *in situ* real-time XRD and wafer curvature measurement as well as *ex situ* transmission electron microscopy (TEM) and Rutherford backscattering

spectrometry (RBS). We have studied the compound formation sequence as well as the growth microstructure in samples with initial Ni film thickness between 2 and 500 nm. In addition to the formation of three additional Ni-rich compounds before NiSi, we report about the non-sequential growth and lateral co-existence of several compounds (within the same layer) in many instances, at reaction stages that depend on the initial Ni thickness and as a consequence of laterally non-uniform nucleation of compounds competing for growth.

5.2 Experimental Procedure

All the investigated Ni films were deposited at room temperature in a magnetron sputtering system with a base pressure of $2x10^{-7}$ Torr. Deposition from a 99.999% pure Ni target was carried out in a MRC-643 system under 10 mTorr of high-purity Ar. The depositions of 2 to 100-nm-thick samples were done in a single pass whereas the 500-nm-thick Ni samples were made using a 10-pass interrupted deposition scheme, allowing for 10 min cool-down between passes without breaking the vacuum. This procedure was used to prevent unwanted heating-induced reactions as a result of long exposure times to the plasma.

Three types of substrates were used: 700-μm-thick p-doped Si(001) wafers; 250-μm-thick p-doped Si(001) wafers; and Silicon-on-insulator (SOI) wafers with a 100-nm-thick Si layer on 120-nm SiO_2. All substrates yield identical results as far as Ni-Si reactions are concerned, but the thicker substrates are more easily handled during *in situ* XRD experiments while the thinner substrates were used for *in situ* stress measurements. Prior to the Ni deposition, the substrates were etched for 55 s in dilute (10%) HF, then blown dry with high-purity N_2. Since all samples were uncapped, they were kept in dry boxes under nitrogen before measurements and anneals.

The microstructure and microchemistry of both as-deposited and annealed samples were determined using a combination of x-ray diffraction (XRD), cross-sectional transmission electron microscopy (XTEM), and Rutherford backscattering spectrometry (RBS). Ni-Si reactions were monitored *in situ* during ramp anneals in a purified He atmosphere using time-resolved XRD, diffuse light scattering, and resistance measurements. The concurrent measurements were performed at the X20C beamline of the National Synchrotron Light Source (NSLS) at Brookhaven National Laboratory. As-deposited samples were mounted in an annealing chamber aligned along the beamline and equipped with an x-ray-transparent Be window.

To minimize the contamination by oxygen, the chamber was evacuated twice to 5×10^{-6} Torr (7×10^{-4} Pa), back-filling each time with purified He following the sample insertion. As-deposited samples were annealed using linear temperature ramps from 100 to 950 °C at rates ranging from 0.3 to 3 °C s^{-1} as well as isothermal anneals in which the dwell temperature was reached with a 30 °C s^{-1} ramp starting at 100 °C. Substrate temperature was measured with a thermocouple calibrated to better than ±3 °C using the Si-Au, Si-Al, and Si-Ag eutectic melting points. A W-Si multilayer monochromator provided an energy resolution of 1.5% at 6.9 keV ($\lambda = 0.1797$ nm) with a typical intensity at the sample of 3×10^{13} photons s^{-1}. The incident X-rays illuminated a sample area of 1×2 mm^2 typically sampling millions of grains. Each diffraction curve was collected with an acquisition time ranging from 0.5 to 2 s using a position-sensitive detector covering a 2θ range of 14°. Unless otherwise specified, the X-ray beam was incident at an angle of 27.5° from the plane of the sample and the detector was centered at $2\theta = 55°$. *In situ* light-scattering measurements[147] were carried out using a He-Ne laser light with a wavelength of 633 nm. An incidence angle of 65° with respect to the surface normal was used and scattered light was measured at angles of -20 and 52° (with two separate detectors), which provided information on changes in surface roughness for in-plane correlation lengths of 0.5 and 5 μm, respectively.

Changes in sample resistance during annealing were measured in situ using non-colinear four point probe geometry. The indexation of the XRD peaks of the crystalline phases Ni, $Ni_{31}Si_{12}$, δ-Ni_2Si, θ-Ni_2Si, Ni_3Si_2, NiSi, and Si was done using JCPDS datasheets No. 04-0850,71-0638, 72-2092, 73-2093, 17-0881, 38.0844, 43-0989 and 05-0565 respectively.

High-resolution X-ray pole figure measurements were carried out at the NSLS X20A beamline. A Si monochromator was used to select the energy of the photon beam ($\lambda = 0.154$ nm). This wavelength was chosen to simplify comparison with laboratory-based measurements carried out using Cu Kα radiation. The sample was mounted on a four-circle diffractometer (Schultz geometry). A scintillation counter was used to detect the diffracted intensity. By fixing the sample and detector at given θ-2θ angles sets, one fixes the d-spacing of the crystallographic planes in the films for which diffraction will be detected. The pole figure is then obtained by rotating the sample around the axis normal to its surface (ϕ scan) and around the axis formed by the intersection of the sample surface and diffraction plane (χ scan). The pole figures were acquired in steps of 0.5° in χ and ϕ ($0 \leq \chi \leq 85°$ and $0 \leq \phi \leq 90°$). Reference χ and ϕ values were determined using peaks from the Si substrate.

XTEM images were recorded on a JEOL-2100F microscope at an acceleration voltage of 200 kV. Unless specified otherwise, bright-field images were recorded with the [110] zone axis of the Si substrate parallel to the electron beam, so that thicknesses can be directly measured on the micrographs. Cross-sectional samples were prepared by standard mechanical boring, slicing, and polishing down to 10 μm. Further thinning down to electron transparency was performed in a Gatan Precision Ion Polishing System (PIPS) using Ar^+ at an energy of 5 keV and at an incidence angle of 4°. Two final rounds of 5 minutes at 3 keV and 2.5keV were used to clear as much ion damage as possible. Samples were always glued to the PIPS Cu sample holder to insure adequate heat

dissipation. In experiments using indium pellets, no evidence of melting was observed, so it is assumed that the samples temperature remained below 160 °C during the ion milling process.

High-resolution RBS was used to investigate the detailed layer structure of the reacted samples and to complement the phase identification obtained by XRD. The probe beam consisted of 2.3 MeV $^{4}He^{+}$ ions incident at an angle of 7° relative to the sample normal with the detector set at a 100° scattering angle to optimize the depth resolution. Backscattered spectra were analyzed using the RUMP simulation code.[158] The fits for samples showing significant interfacial roughness were verified with the SIMNRA software package using SRIM 2006 stopping powers. Layer thicknesses determined by XTEM were used to minimize the number of free parameters in the RBS fits (see below for details).

In situ stress measurements were performed during ramp anneals at 0.3 °C s^{-1} from 20 to 600 °C on 100 nm Ni films deposited on 100-mm in diameter, 250-μm-thick complete wafers using a Flexus furnace. The stress, or the bending force, can be calculated from the measured radius of curvature using Stoney's equation.[159] The 100-nm-thick Ni film had an initial tensile stress of about 740 MPa, assuming a Young's modulus of 125 GPa and a Poisson's ratio of 0.28 for Si (values for the <100> direction of Si).

5.3 Results

5.3.1 Compound sequence and microstructure in 10-nm-thick Ni/Si(001) samples

Synchrotron XRD was used to follow Ni/Si(001) interfacial reaction kinetics during annealing with 3 °C s^{-1} linear ramps. Figure 5.1 (a-c) show three contour plots of the logarithm[1] of the scattered synchrotron x-ray intensity as a function of diffraction angle 2θ and temperature T_a during the reaction of a 10-nm-thick Ni film with a Si(001) substrate. Since the angular range of the position-sensitive detector for the synchrotron measurements is limited to 14°, the three plots represent three consecutive measurements on nominally identical samples and covering different 2θ windows. The diffuse light scattering and resistance data plotted in Figure 5.1(d) are useful in revealing microstructural changes in the film (e.g. agglomeration) that might not be visible in the X-ray diffraction signal.

The Ni(111) peak is observed at 2θ = 52.1° at T_a = 100 °C (the beginning of the experiment), which is 0.3° lower than its expected position. This small shift is attributed to the lack of precise sample height adjustment in the annealing chamber, which results in a systematic displacement of XRD peak positions as compared to those obtained in a powder diffractometer.

---

[1] In fact, the graphs present the third order log of the intensity I defined as Log(Log(Log(I))). This allows for plotting intensities spread over several orders of magnitude on a simple grayscale. Each XRD graph carries its own relative intensity scale so that the rather intense background increasing from 43° to 48° (2θ) around 150 °C in Figure 5.1 (b) corresponds to the tail of the Ni (111) peak in Figure 5.1((c). This means that the XRD peaks in Figure 5.1 (a) and (b) are generally less intense than those in Figure 5.1 (c), although the greyscale contrast does not obviously suggests this.

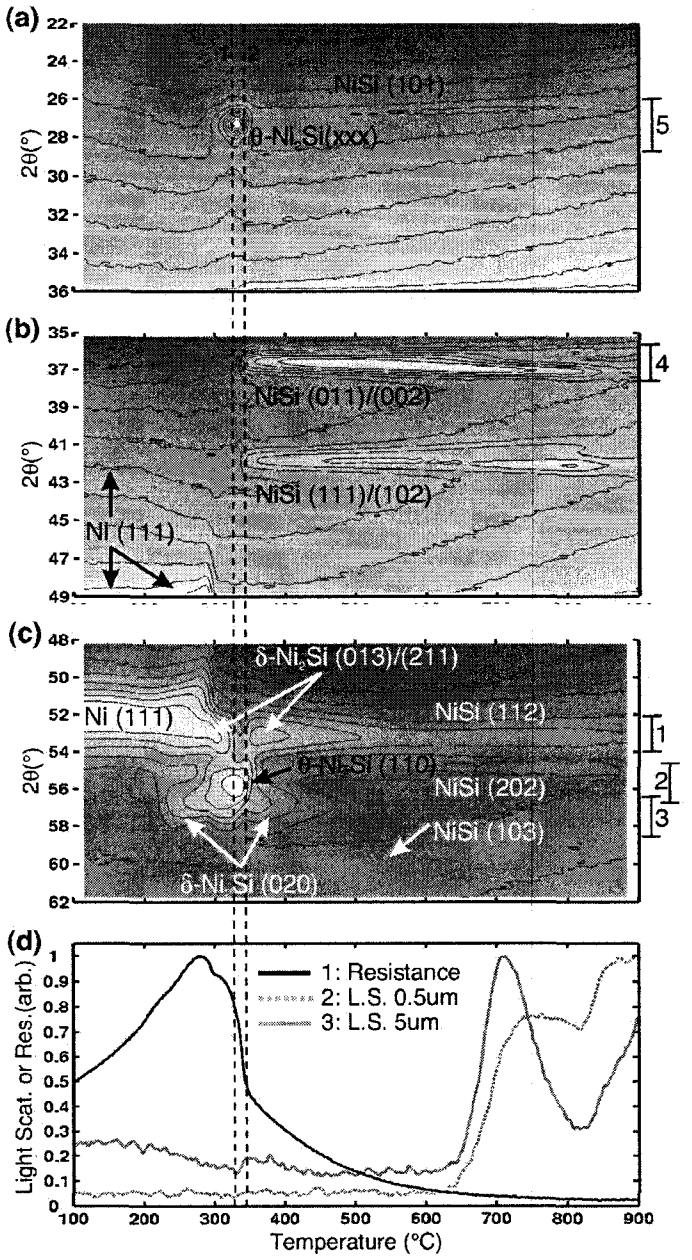

Figure 5.1: XRD intensity contour maps ($\lambda = 0.1797$ nm) plotted as a function of annealing temperature T_a during a thermal ramp at 3 °C s^{-1} in purified He for a 10-nm-thick Ni layer deposited on c-Si(001) for three different 14° wide 2θ windows centered at (a) 27°, (b) 42°, and (c) 55°. (d) Resistance and light-scattering signals measured in situ during the same annealing experiments. LS 0.5 μm and LS 5 μm correspond to the light scattering intensity signals measured at angles selected to probe surface roughness variations for in-plane correlation lengths of 0.5 and 5 μm, respectively.

Several phase transformations are detected by XRD during annealing. The XRD peak positions for the first silicide compound that appears near 225 °C correspond to δ-Ni_2Si. We also clearly observe the formation of NiSi at around 340 °C as evidenced by the (002)/(011) and (102)/(111) degenerate reflections in Figure 5.1 (b) and a corresponding low resistance signal in Figure 5.1 (d). These results are in agreement with the typically reported compound sequence. Nevertheless, our results also indicate the formation of an additional compound for T_a around 315 °C (peaks at 2θ = 27 and 56°) which seems to consume δ-Ni_2Si as indicated by the decrease of its (013)/(211) and (020) peak intensities. These two peak positions could possibly be attributed to two of the six stable compounds in the Ni-Si phase diagram. Both Ni_3Si_2 and NiSi show peaks that could match these positions. Our earlier identification of Ni_3Si_2[156,157] relied on a peak that is not present on the JCPDS datasheet which was calculated as a low intensity reflection by Pilstrom.[160] In the current work, we demonstrate that these peaks do not correspond to either compounds but rather arise from the metastable hexagonal θ-Ni_2Si.

The integrated intensities of the peaks labelled on the right-side of Figure 5.1 are presented in Figure 5.2 as a function of annealing temperature. These five intensity traces show well not only the formation of the expected δ-Ni_2Si and NiSi but also the fast intensity increase of the extra compound forming at 315 °C. Figure 5.2 also reveals that the intensity of the two δ-Ni_2Si peaks (curves 1 and 3) increases between 330 and 360 ° while the NiSi (011)/(002) peak (curve 4) emerges. Curves 1 and 3 then decrease monotonically as NiSi grows further. These results suggest that the consumption of the additional compound leads to the formation of some new δ-Ni_2Si which is then consumed by the formation of NiSi. The compound sequence therefore deviates from a monotonic evolution of the composition. As the temperature increases further, we note in Figure 5.1 (b) that the degenerate (011)/(002) and (111)/(102) reflections of NiSi become distinct above 700 °C as a consequence of the thermal expansion coefficient being very anisotropic in NiSi (negative coefficient along the b axis).(161)

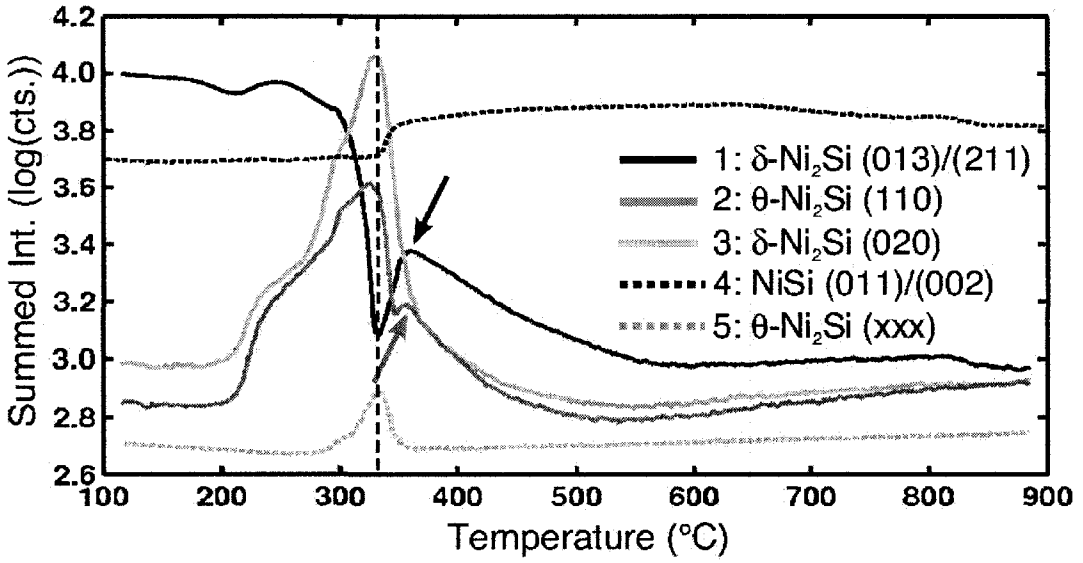

Figure 5.2: XRD intensities, integrated over angular ranges indicated in Fig. 1, as a function of annealing temperature during a thermal ramp at 3 °C s^{-1} in purified He for a 10-nm-thick Ni layer deposited on c-Si(001). Curve 1 is for δ-Ni_2Si (013)/(211), curve 3 for δ-Ni_2Si(020), curves 2 and 5 for θ-Ni_2Si, curve 4 for NiSi(011)/(002).

The resistance trace in Figure 5.1(d) follows closely the different peak transitions visible in the XRD data. The resistance increases steadily from 100 to 200 °C as expected from the increase in phonon scattering in the Ni. The formation of δ-Ni_2Si is marked by a kink in the resistance curve, which then progresses with a different slope owing to the different thermal coefficient of resistance (TCR) of this compound. The resistance reaches a maximum around 280 °C as Ni becomes completely consumed. We also note that the resistance has already decreased significantly when the XRD peaks for the second silicide compound reach their maximum intensity. Above 350 °C, the resistance drops continuously being dominated by the semiconducting behavior of the thick Si substrate. Aside from the step observed in the 5 μm trace around 340°C, light scattering signals are almost featureless until about 650 °C where their dramatic increase is a signature of the NiSi agglomeration.

Figure 5.3 shows two XRD pole figures which were measured in order to identify the compounds present in a sample ramp-annealed up to 345 °C and then rapidly quenched. The two d-spacing values were selected to determine if the extra peaks observed in the phase sequence could be the result of Ni_3Si_2. The d spacing of 1.91 Å corresponds to the peak measured at 56.1° in Figure 5.1 while the d spacing of 2.03 Å corresponds to a position of 52.5° where both the Ni (111) (which is consumed at the selected quench temperature) and the intense Ni_3Si_2 (600) reflections would be measured. The four intense peaks in Figure 5.3 (a) arise from the Si(220) substrate reflections that we inevitably probe in these diffraction conditions. We observe a thick fiber-texture ring centered at χ = 59° and spreading between χ=55° and χ=63° that neither of NiSi or Ni_3Si_2 can explain. The faint but sharp arc of circles correspond to the axiotaxial growth of NiSi in contact with the Si substrate.[119,162,,163] Besides the Si(220) peaks – weakened as we move further from the exact Bragg condition for these peaks – Figure 5.3(b) is virtually featureless. The lack of diffraction intensity at this Bragg condition clearly eliminates the possibility that the extra compound be the Ni_3Si_2 since the (600) planes would strongly scatter as a ring at χ=62° in this figure.

Among the 11 possible compounds of the Ni-Si equilibrium phase diagram, the best match to the ring at χ=59° is achieved with the {110} fiber texture of the hexagonal θ-Ni_2Si. Since the presence of this metastable compound is not expected at room temperature, we have carried out further pole figure measurements,[164] which confirm this identification. The details concerning this compound and how it matches the rest of our results will be discussed later in the chapter. In the following, we refer to this compound as θ-Ni_2Si.

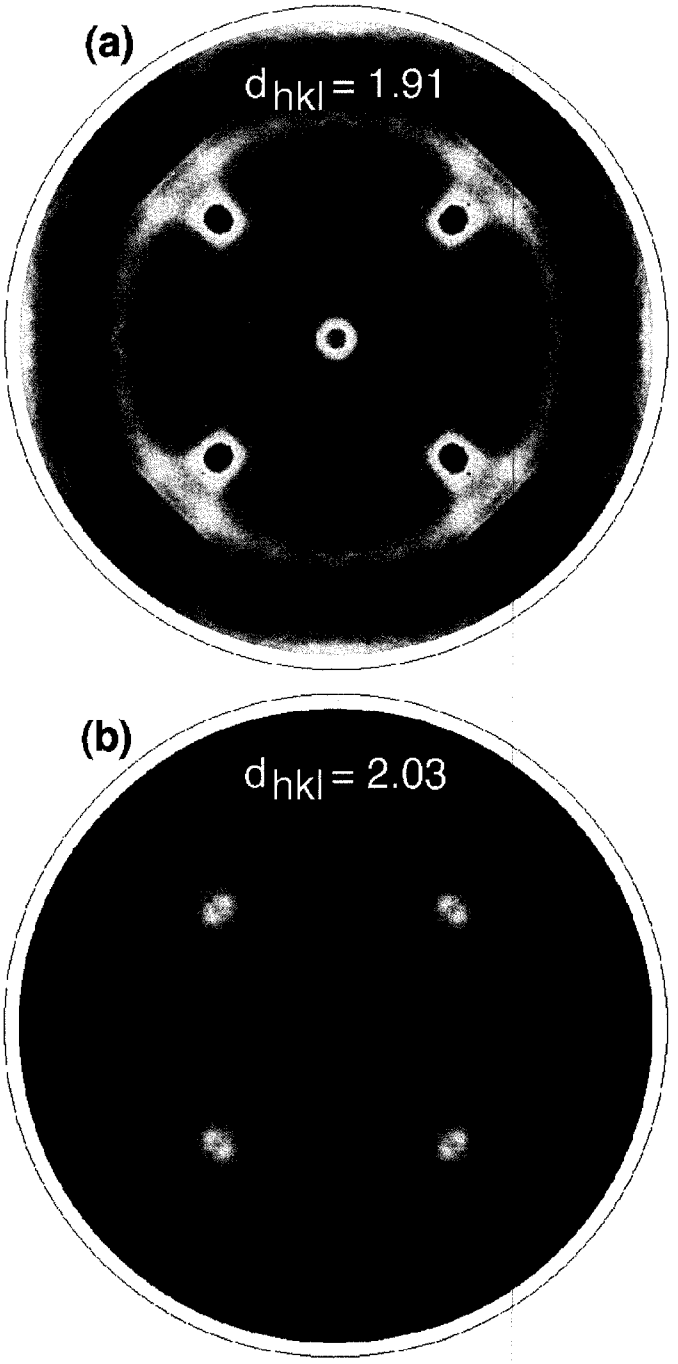

Figure 5.3: Pole figures from a 10-nm-thick Ni layer deposited on c-Si(001) annealed at 3 °C s^{-1} in purified He up to 325 °C (dashed line 2 in Fig. 1) and then quenched. (a) is for d = 0.191 nm and (b) is for d = 0.203 nm.

The use of low temperature isothermal anneals is an effective method for slowing down a reaction thus improving the effective time resolution of the *in situ* XRD measurements. Figure 5.4 presents the results of an isothermal anneal at T_a = 260 °C for a 10-nm-thick Ni film on c-Si(001). The XRD data in Figure 5.4 (a) indicate that the reaction is very similar to that observed in ramp-type anneals. The integrated intensities plotted in Figure 5.4 (b) show, however, that the θ-Ni_2Si(110) to δ-Ni_2Si (013)/(211) ratio is smaller than for the ramp-type annealing case when the θ-Ni_2Si(110) peak is maximum. This suggests that the compound forms in smaller quantity during low temperature isothermal anneals, thus consuming less δ-Ni_2Si.

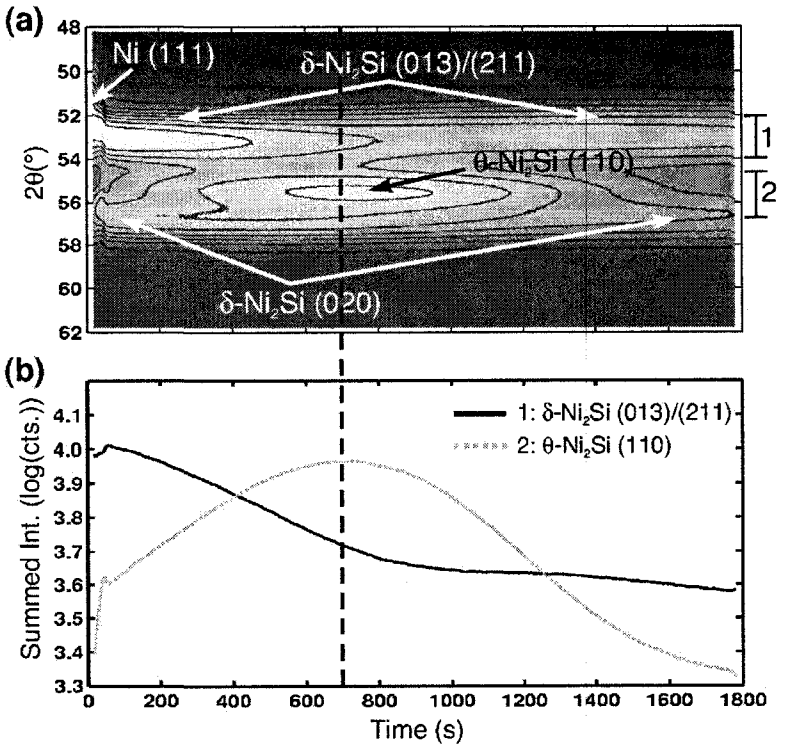

Figure 5.4: (a) XRD intensity contour map (λ = 0.1797 nm) plotted as a function of annealing time t_a during an isothermal anneal at T_a = 260 °C for a 10-nm-thick Ni layer deposited on undoped SOI (001). (b) XRD intensities, integrated over the angular ranges indicated in (a), vs t_a for δ-Ni_2Si(013)/(211), θ-Ni_2Si, and δ-Ni_2Si(020).

The bright-field XTEM image from a sample annealed at T_a = 260 °C and rapidly quenched after t_a = 700 s (vertical dashed line in Figure 5.4) is presented in Figure 5.5. The image reveals the presence of a relatively continuous interfacial layer together with a second layer on the top part of the reacted film in several areas. The striking contrast uniformity of the bottom layer suggests that it is amorphous, single-crystal or highly oriented. We also observe a significant interface roughness although Ni-Si solid-state reactions have been known to produce smooth interfaces with c-Si.[5] Higher-magnification images from different areas of that sample, together with their associated convergent-beam electron diffraction (CBED) patterns, are presented in Figure 5.6. All grains could be matched to one of the three compounds detected by *in situ* XRD. A careful examination reveals that θ-Ni_2Si and δ-Ni_2Si coexist in the top layer while NiSi is located at the interface with the substrate.[1]

[1] Acquiring images under different diffraction conditions also indicate that the bottom interfacial layer is polycrystalline. Although TEM imaging bares little statistical meaning, all CBED patterns obtained from the bottom layer could only be indexed with NiSi zone axes, suggesting that this phase predominantly occupies the interlayer. This is in agreement with the presence of the axiotaxy rings in the statistically meaningful pole figure of Figure 5.3.

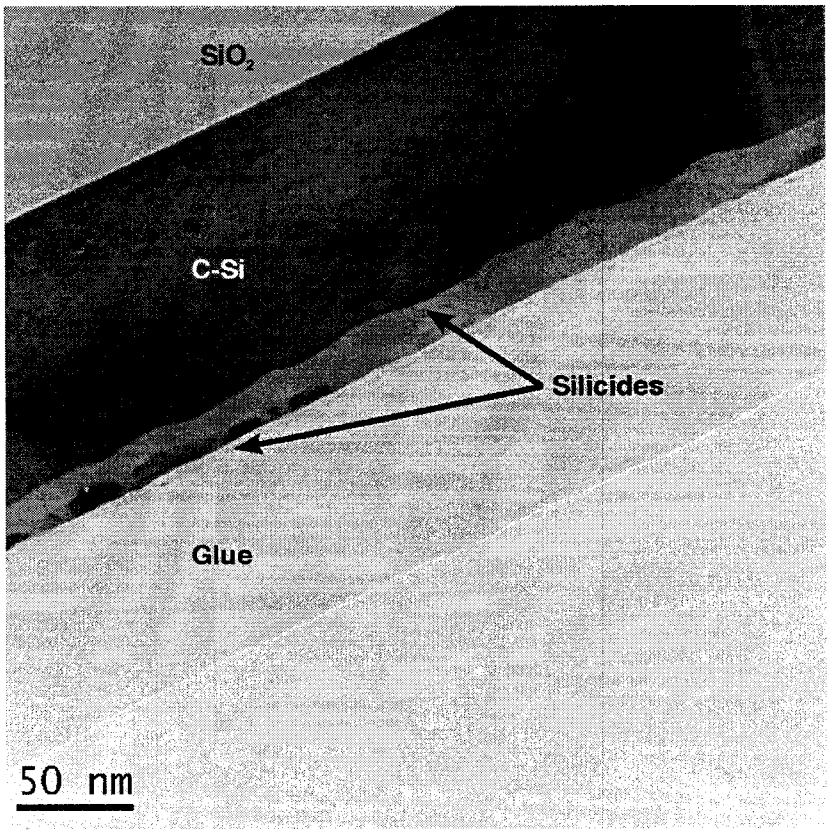

Figure 5.5: Bright-field XTEM micrograph from a 10-nm-thick Ni layer on SOI (001) substrate isothermally annealed at T_a = 260 °C for t_a = 700 s (see dashed line in Figure 5.4). The image was recorded with the electron beam parallel to the [011] direction of the top Si slab of the SOI substrate.

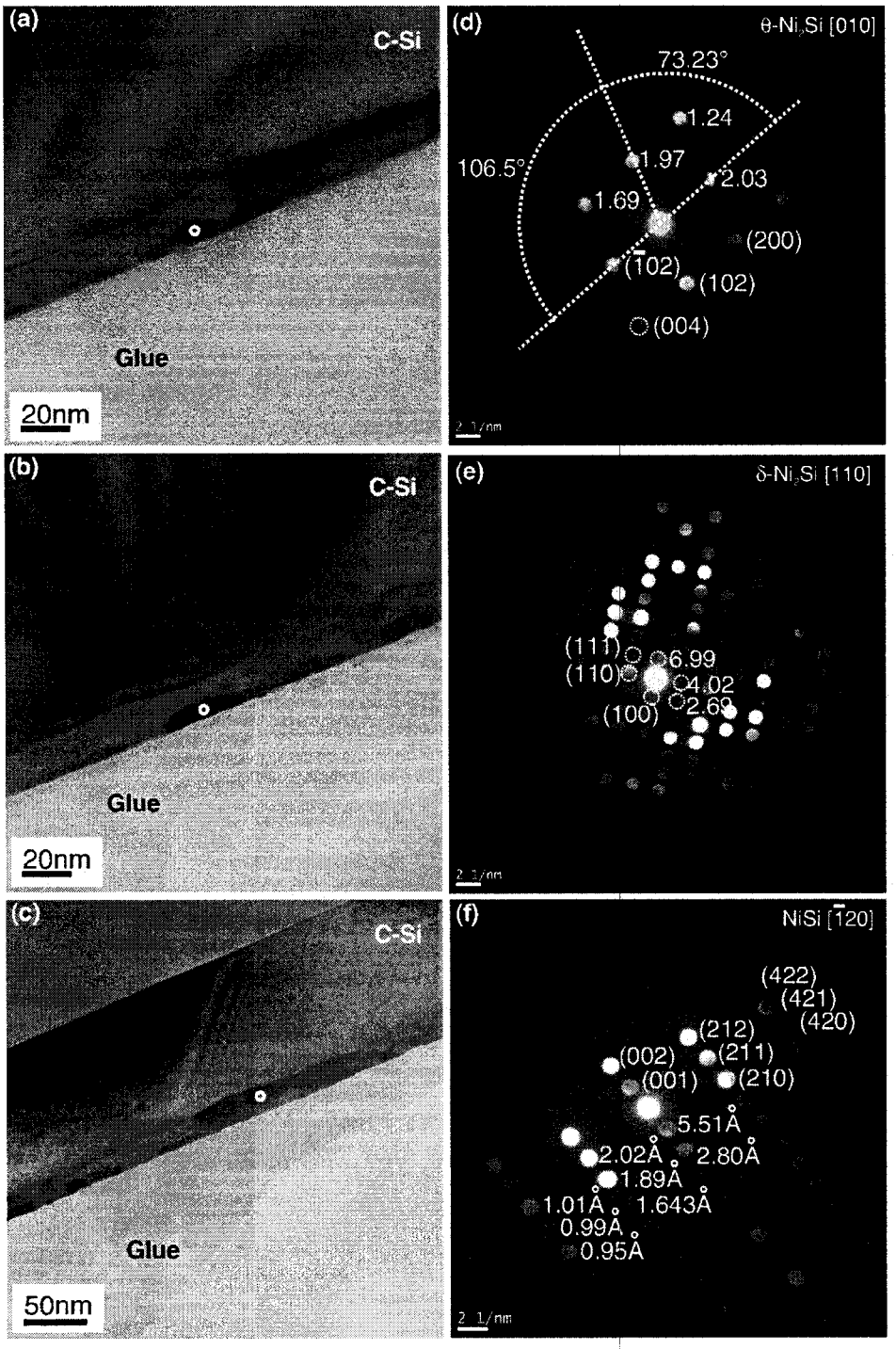

Figure 5.6: Higher-magnification bright-field XTEM micrographs (a)-(c) together with convergent beam electron diffraction (CBED) patterns acquired in the location indicated by white circles (d)-(f) taken in different areas of the sample shown in Figure 5.5. Micrographs were recorded with the electron beam parallel to the zone axes for the CBED patterns.

The compound sequence we deduce from the results presented above for the reaction of 10nm Ni layers with Si(001) substrates is summarized schematically in figure Figure 5.7, where it is compared with the traditionally reported sequence. This figure represents clearly the occurrence of an additional reaction step before the complete conversion of the Ni layer to NiSi as well as the deviation from a monotonic evolution of the compounds composition.

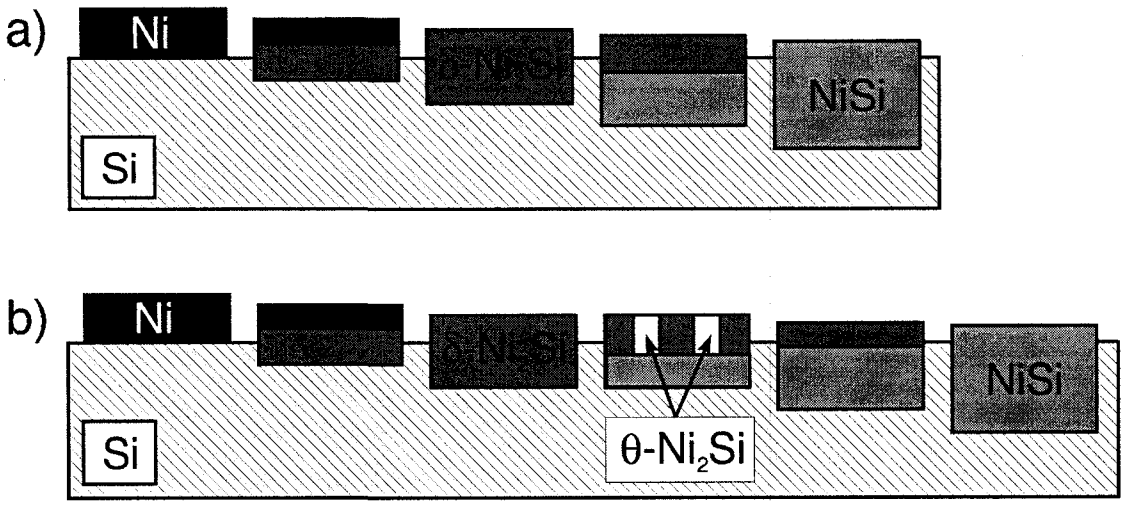

Figure 5.7: a) Schematic representation of the traditionally reported reaction sequence compared with b) the sequence we observed during the reactions between 10nm Ni layers and Si (001) substrates during both ramp-type and isothermal anneals.

5.3.2 Compound sequence and microstructure in 100-nm-thick Ni/Si(001) samples

An investigation of the solid state reaction between 100-nm-thick Ni layers with c-Si(001) yields interesting results. Figure 5.8 and Figure 5.9 reveal that the early stages of the reaction are similar to those observed with 10-nm-thick Ni films: δ-Ni_2Si forms first, followed by the θ-Ni_2Si. The θ-Ni_2Si(110) peak reaches its maximum intensity value at $T_a = 330$ °C during this ramp anneal at 3 °C s^{-1}. Still, instead of an obvious

consumption of δ-Ni_2Si by the formation of the θ-Ni_2Si, we rather observe a pause in the growth of δ-Ni_2Si.[1] We also notice two additional weak peaks around 28.7° and 31.3° in Figure 5.8 (a), which coincide with the presence of the θ-Ni_2Si compound. The peak at 31.3° can be indexed to the (100) planes of θ-Ni_2Si, while the peak at 28.7 does not match with any plane of that compound. However, both positions agree well with Ni_3Si_2 (030) and (102) respectively. As soon as the intensity of the θ-Ni_2Si peaks starts to decrease (and so those of Ni_3Si_2), we observe a new increase in the δ-Ni_2Si (013)/(211) peak intensity along with a brief appearance of NiSi (Figure 5.8 (b) around 36 and 42 °2θ).

After NiSi disappears, δ-Ni_2Si keeps growing and becomes the only compound present for a short duration. A new peak, believed to arise from a structural reorganization of the Ni overlayer, emerges at 2θ = 52° for T_a = 410 °C. After a further 10 °C increase, the rapid decrease of the 52° peak coincides with the formation of yet an additional silicide compound, this time marked by four distinct diffraction peaks all indexed to $Ni_{31}Si_{12}$. This stage of the reaction is accompanied by a sharp increase in resistance, which is consistent with the consumption of Ni and the formation of the high-resistivity $Ni_{31}Si_{12}$ compound.

[1] The apparent increase of the δ-Ni_2Si(020) intensity until T_a = 330 °C is believed to be caused by the shoulder of the rising θ-Ni_2Si(110) peak.

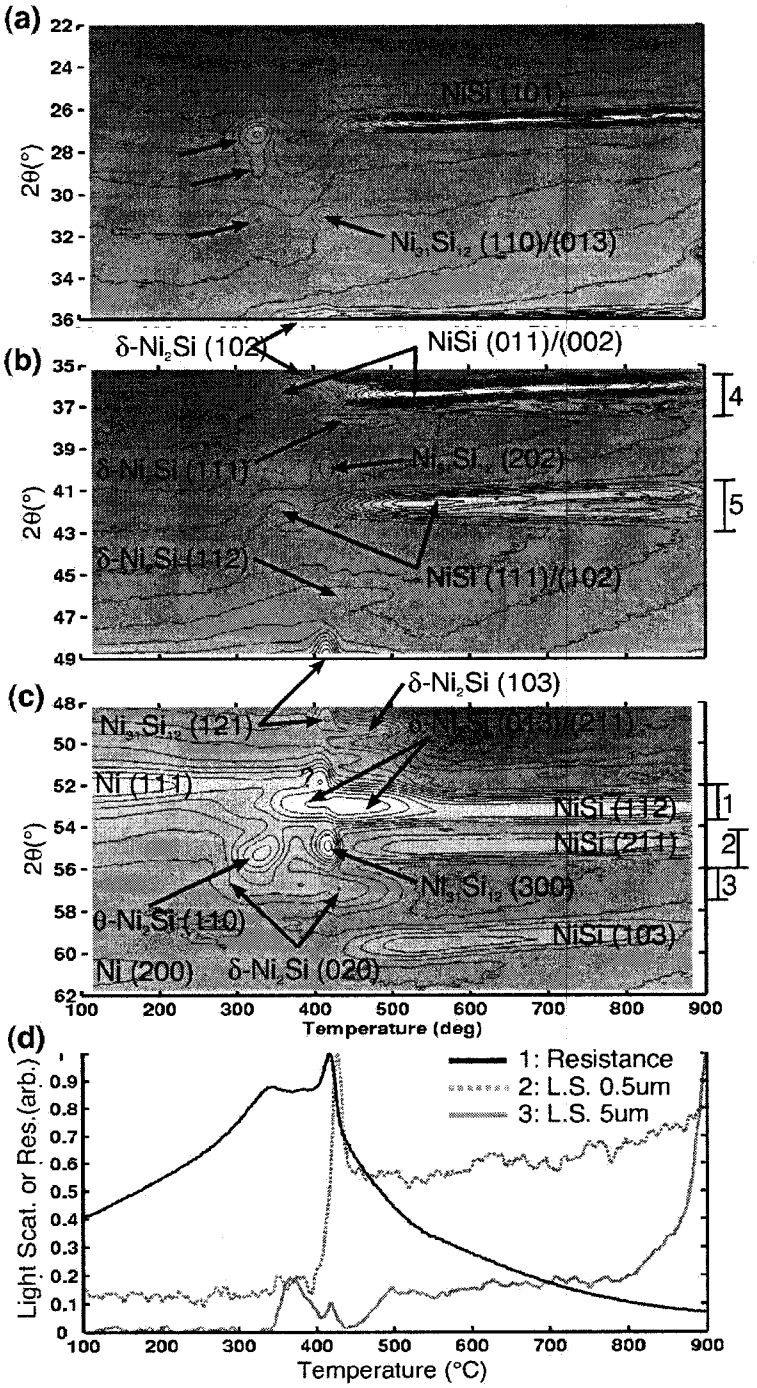

Figure 5.8: XRD intensity contour maps ($\lambda = 0.1797$ nm) plotted as a function of annealing temperature T_a during a thermal ramp at 3 °C s^{-1} in purified He for a 100-nm-thick Ni layer deposited on c-Si(001) for three different 14° wide 2θ windows centered at (a) 29°, (b) 42°, and (c) 55°. (d) Resistance and light-scattering signals measured in situ during the same annealing experiments.

As shown in Figure 5.9, the formation of the θ-Ni_2Si consumes δ-Ni_2Si while its consumption leads to both formation of δ-Ni_2Si and NiSi. Finally, the second set of δ-Ni_2Si peaks decrease as the NiSi grows. This last compound stays uniform until 800 °C, where it starts to agglomerate. This value is approximately 150 °C higher than for 10-nm-thick films. At this temperature, a decrease in the NiSi peak intensities can also be related to formation of $NiSi_2$.

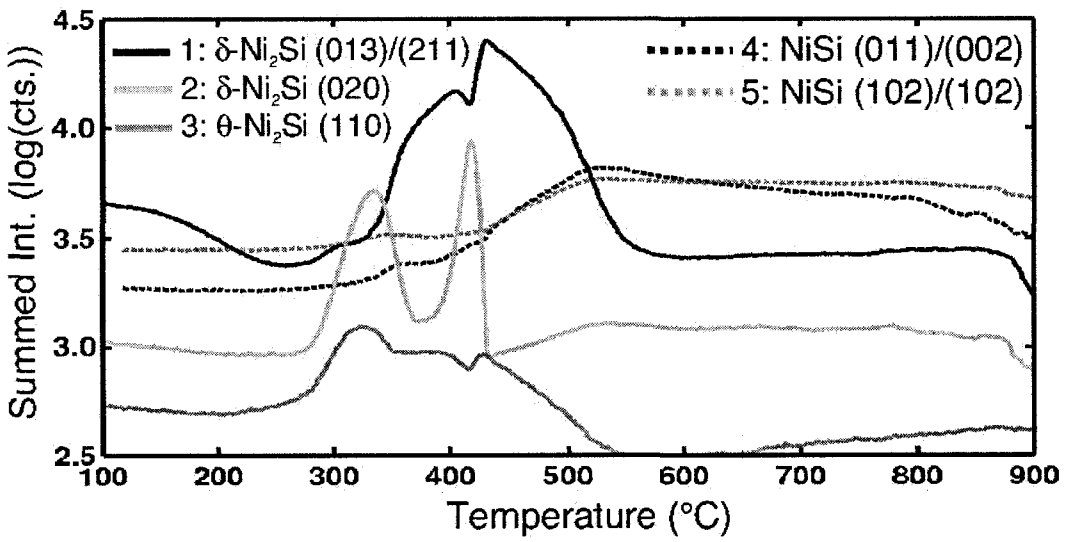

Figure 5.9: XRD intensities, integrated over angular ranges indicated in Fig. 7, as a function of annealing temperature during a thermal ramp at 3 °C s^{-1} in purified He for a 10-nm-thick Ni layer deposited on c-Si(001). Curve 1 is for δ-Ni_2Si (301)/(121), curve 2 for δ-Ni_2Si (002), curve 3 for θ-Ni_2Si, curve 4 for NiSi (011)/(002), and curve 5 for NiSi (111)/(102).

In order to investigate the role of stress on film formation and microstructure, we have carried out *in situ* stress measurements during a 0.3 °C s^{-1} ramp anneal from 20 to 650 °C (Figure 5.10(a)). The sample used for this measurement consisted of a 100 nm-thick Ni film on a complete 100-mm (diameter), 250-μm-thick Si(001) wafer. Both heating and cooling curves appear in Figure 5.10 (a). For comparison, we have carried out the same ramp anneal on an identical film in the *in situ* XRD setup (Figure 5.10 (b),

this time on the typical 750-μm-thick c-Si(001) substrate. Vertical dashed lines (a) to (g) correspond to six quenches at 295, 310, 335, 355, 373, 400, and 600 °C used for *ex situ* RBS and TEM investigations described below.

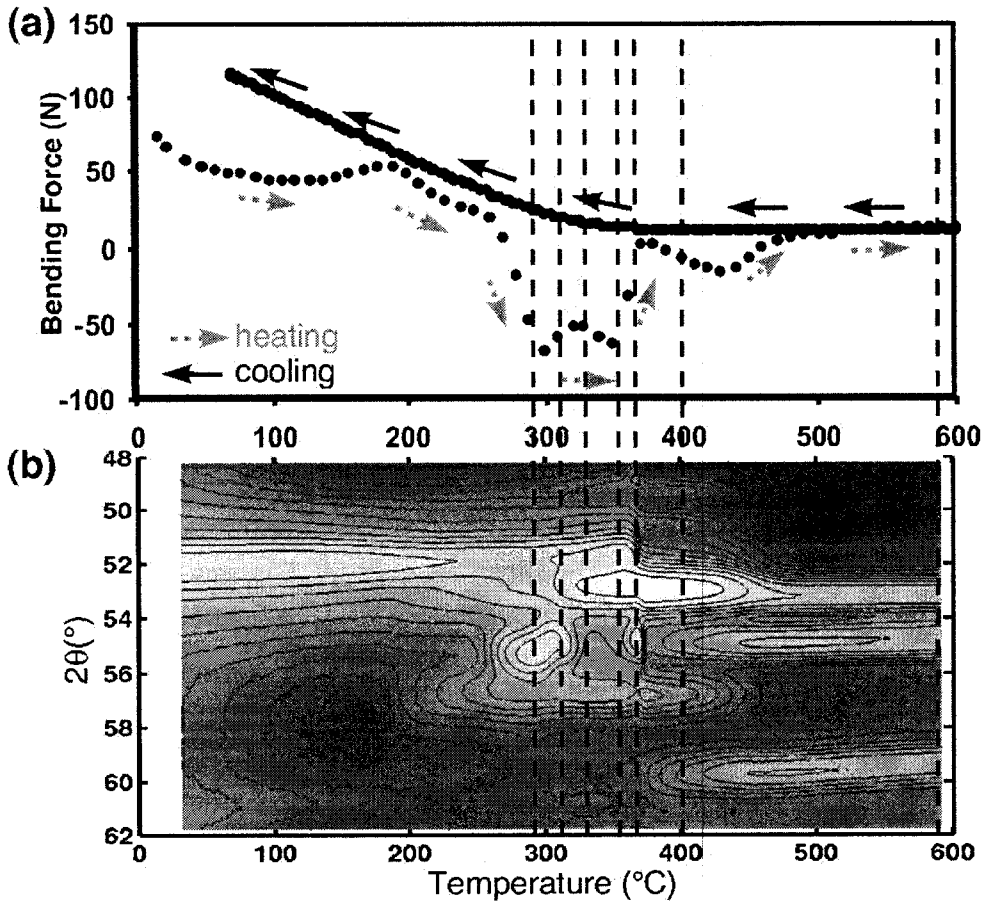

Figure 5.10: (a) Bending force and (b) XRD intensity with the detector centered at 2θ = 55°C as a function of temperature acquired *in situ* during a 0.3 °C s^{-1} ramp anneal for a 100-nm-thick Ni layer on c-Si(001). Dashed lines indicate quench temperatures for the XTEM investigations presented in Figure 5.11.

A comparison of Figure 5.10 (b) and Figure 5.8 (c) reveals that the phase formation sequence is the same but that the slower ramp rate causes the transitions to occur at slightly lower temperatures. Features visible in the *in situ* bending force curve upon heating coincide with compound formation events indicated by XRD. The first

significant inflexion point at 200 °C corresponds to the growth of δ-Ni_2Si. At 260 °C, the θ-Ni_2Si starts forming and the film becomes under considerable compressive stress until the θ-Ni_2Si (110) peak shifts towards lower angles near 300 °C. Between 300 and 340 °C the stress follows the same trend as between 200 and 260°C, two ranges where the XRD data indicate the presence of only Ni and δ-Ni_2Si. At 340°C, the significant relaxation coincides with an increase of the Ni (111) peak, which is followed by a return towards compressive values as δ-Ni_2Si is consumed by the NiSi growth between 375 and 410 °C. Finally, the stress gradually approaches zero as the temperature exceeds 450 °C and diffusional relaxation mechanisms become important.

These results show that for 100nm Ni films, the formation of the θ-Ni_2Si phase coincides with a strong stress build-up, which is then partially relieved upon its consumption. Indeed, the inflection point in the bending force curve at $T_a = 300$ °C coincides with a slight angular shift in the θ-Ni_2Si (110) peak in Figure 5.8 (c). While this shift could be caused by stress relaxation, compositional changes cannot be ruled out since the θ-Ni_2Si can exist over a significant composition range. In temperature ranges where δ-Ni_2Si is the main phase present (200-250, 320-350, and 370-420°C) the slopes in the bending force curve are similar, which suggest a single origin to these changes, namely the growth of δ-Ni_2Si from the reaction of Ni with Si. Finally, the sharp decrease in compressive stress around 370°C is consistent with the complete consumption of the top Ni layer. We thus index the peak near $2\theta = 52°$ at 410 °C in Figure 5.8 and 365°C in Figure 5.10 to the Ni (111) planes.

XTEM images from the samples corresponding to the quenches indicated in Figure 5.10 are presented in Figure 5.11. Film and layer thicknesses obtained from these images are summarized in Table 5-1. Each numerical value corresponds to averages of 5 to 7 measurements done in different regions of the XTEM specimens. For very rough layers, the interface was considered as being in the mid point of the rough region.

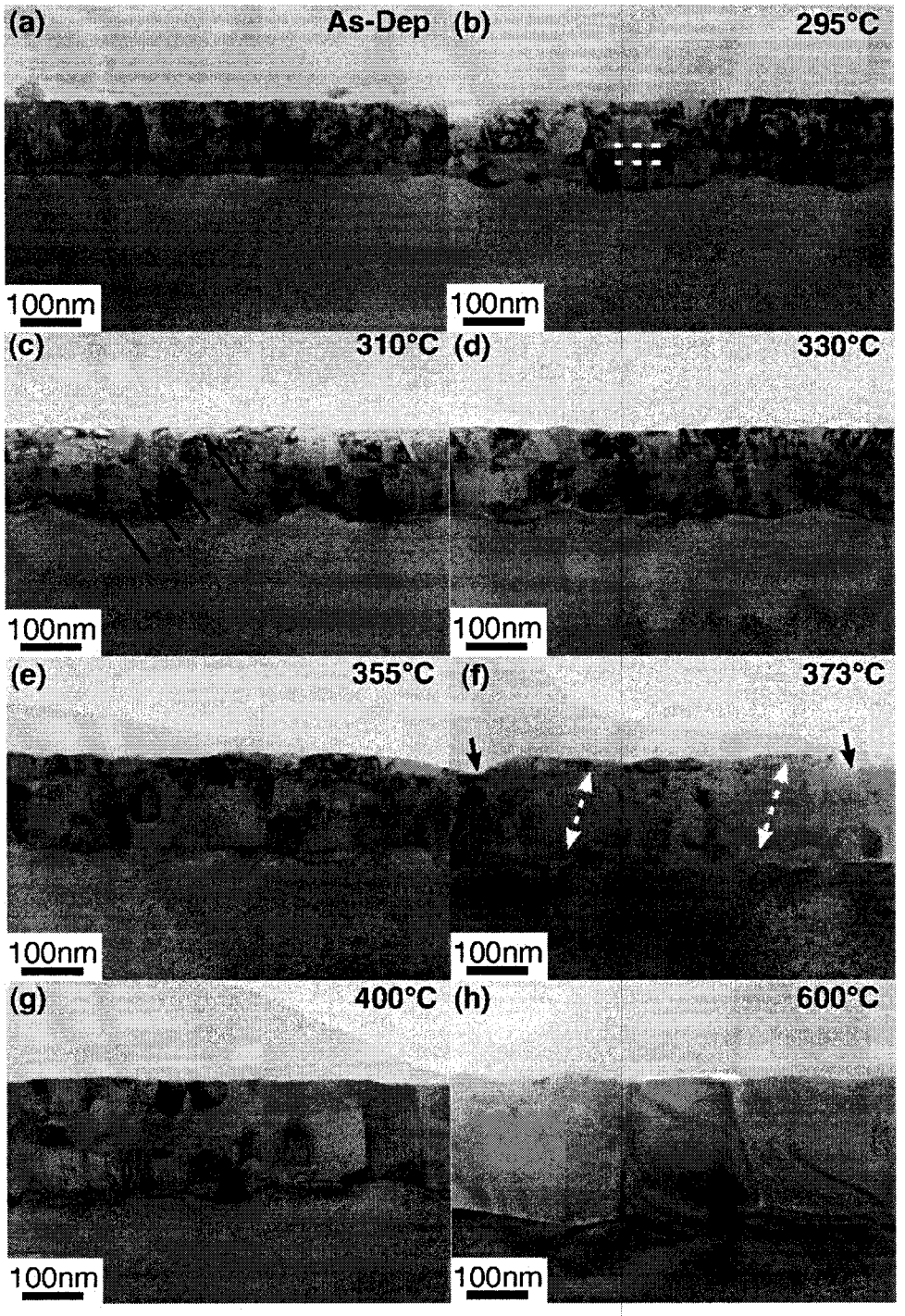

Figure 5.11: Bright field XTEM micrographs from 100-nm-thick Ni layers on c-Si(001): (a) as deposited and quenched at T_a values of (b) 295, (c) 310, (d) 330, (e) 355, (f) 373, (g) 400, and (h) 600 °C – as indicated by dashed lines in Figure 5.10– following a 0.3 °C s^{-1} ramp anneal. All images were recorded with the electron beam parallel to the [011] direction of the Si substrate.

Figure 5.11 (a), which corresponds to the as-deposited Ni film, reveals the presence of a 17-nm-thick layer at the interface with the substrate, presumably due to heating or ion-induced mixing during sputter deposition. As described below, RBS indicates that this layer has a composition close to 50:50 Ni:Si although XRD peaks associated to crystalline NiSi could not be detected at the beginning of the reaction.

The XTEM image for the sample annealed at 295 °C, in which Ni_2Si has formed, highlights the presence of three distinct layers as well as considerable roughness at the interface with the Si(001) substrate. A slight increase in annealing temperature, to 310 °C, results in the appearance of a fourth layer (Figure 5.11 (c)), concurrent with a significant decrease in the top Ni layer's thickness. A detailed analysis of this sample is presented in Figure 5.12, where we present a bright-field image taken in a region of the XTEM thin foil that was thinned to the extent that only the interfacial layers remained. Three CBED patterns, corresponding to the grains identified in (a), are also presented. The three additional lines in Figure 5.12 (a) point to the thin interfacial layer. These results convincingly show that at least three compounds coexist laterally in the second layer from the silicide/Si interface, similarly to the case for the 10-nm-thick Ni sample: θ-Ni_2Si, Ni_3Si_2 and NiSi.

Table 5-1: Silicide layer thicknesses (nm) determined by TEM (Figure 5.11) and RBS.

		As Dep.	295 °C	310 °C	330 °C	355 °C	373 °C	400 °C	600 °C
TEM	**Top**	101	79	65	53	35	24		
	Middle 1		19	26	71	126	72	115	
	Middle 2			45 [a]			82		
	Interface	18	39	<15 [a]	24			74	249
	Total	119	137	151	148	161	178	189	249
	Interface Rough.	NA	25	29	30	34	27	40	50
RBS	**Top**	102 Ni	79 Ni	64 Ni	53 Ni	35 Ni	10 Ni		
	Middle 1		19 Ni_2Si	26 Ni_2Si	71 Ni_2Si		80 Ni_2Si**	120 Ni_2Si	
	Middle 2		10 Ni_3Si_2	36 Ni_3Si_2			40 Ni_2Si†		
	Interface	17 NiSi	28 Ni_3Si_2*	22 Ni_3Si_2*	23.5 NiSi	115 Ni_2Si	30 Ni_2Si	66 NiSi	249 NiSi
	Total	119	136	148	147.5	150	160	186	249
Required initial Ni Thickness at 100% density		109	111	111	111	111	110	110	109

a:While four layers are clearly visible in the XTEM image, it is difficult to determine the individual thicknesses of the bottom two layers considering magnitude of interface roughness. The combined thickness of these two layers is 59 nm.

*:Interface roughness was simulated using the "fuzz" function of Rump. When roughness was too important, it was implemented as a linear diffusion profile of Si in the interfacial silicide. Sometimes for better fit, a given layer may be split into two sublayers so that roughness is applied only on the one that is closest to the interface

** and †: Ni_2Si alone cannot account for the height of the Ni peak in the 373°C quench. A layer of composition $Ni_{0.68}Si_{0.319}$ plus a linear gradient of Ni coming in form the top is needed to fit the slope of the peak close to the leading edge. This requirement is consistent with a matrix of Ni_2Si containing $Ni_{31}Si_{12}$ inclusions.

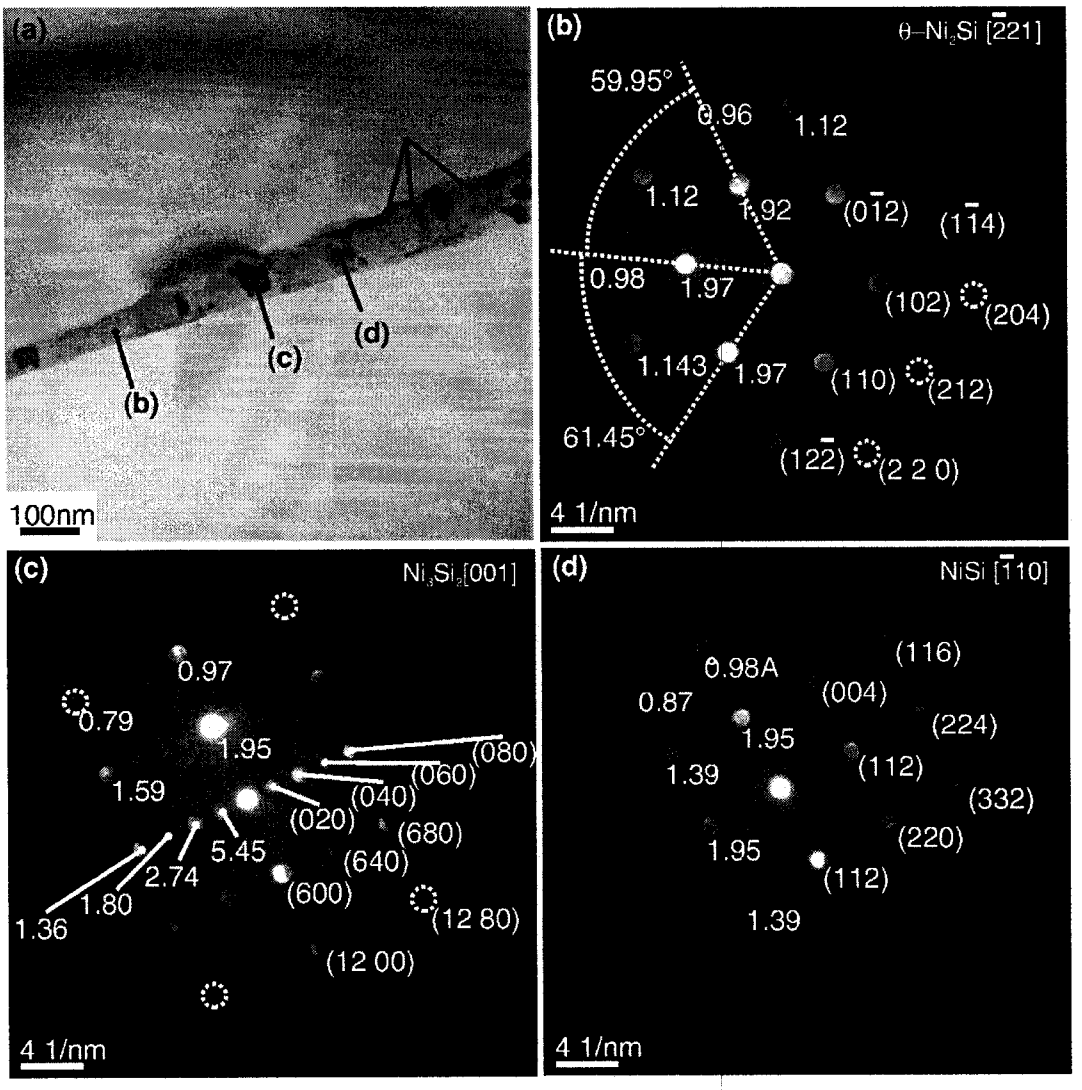

Figure 5.12: (a) Bright-field XTEM micrograph together with (b)-(d) CBED patterns taken at locations indicated in (a) from a 100-nm-thick Ni layer annealed at 0.3 °C s^{-1} up to 310 °C. The XTEM image and the corresponding CBED patterns were acquired in a region of the TEM specimen that was thinned such as the top part of the layer stack visible in Figure 5.11 (c) was removed.

Following the consumption of θ-Ni_2Si at 330 °C (Figure 5.11(d)), the sample's microstructure returns to three layers (with the middle layer becoming the thickest) while the overall thickness remains essentially constant (see Figure 5.11). The 355 °C sample (Figure 5.11 (e)) is composed of Ni (top) and δ-Ni_2Si (bottom).

At 373 °C, when the Ni (111) peak is almost completely extinct in Figure 5.10 (b), the XTEM image reveals the presence of a discontinuous Ni layer on top of a layer comprising many small grains together with a few large ones. Whereas the XRD data presented above suggest the coexistence of Ni, δ-Ni_2Si and $Ni_{31}Si_{12}$ at this stage of the reaction, XTEM and CBED investigations in Figure 5.13 clearly demonstrate that the large grains are $Ni_{31}Si_{12}$. Indeed, the bright-field image in Figure 5.13 (a) was taken with the electron beam parallel to the [010] zone axis of the $Ni_{31}Si_{12}$ grain (see CBED pattern in Figure 5.13 (b)). From the magnitude and direction of the tilt with respect to the substrate's [110] zone axis, we could determine that $Ni_{31}Si_{12}$ {100} planes are essentially parallel to the sample surface. The XRD peak at $2\theta = 56°$ is thus indexed as $Ni_{31}Si_{12}$ (300).

A further increase to $T_a = 400$ °C results in a sample comprising two well distinct layers. We assign the top layer to δ-Ni_2Si and the interfacial one to NiSi based on Figure 5.8 (b-c) and Figure 5.10 (b). Finally, at $T_a = 600$ °C, once NiSi is the only phase present according to XRD, the morphology consists of a single layer of large grains. Despite the fact that NiSi is reported to have a diffusion-controlled growth, the interface with the substrate remains rough, presumably as an inheritance from the earlier stages of the reaction.

RBS spectra from all the samples shown in Figure 5.11 are presented in Figure 5.14. For the sake of clarity, the eight spectra are shown in two sets; the expected levels for Ni, δ-Ni_2Si, and NiSi are indicated by horizontal dashed lines. All spectra were analyzed using the RUMP simulation software package[180]. Simulated spectra are indicated as solid lines in Figure 5.14 and the layer thicknesses and compositions extracted from these fits are indicated in Table 5-1.[1]

[1] The calibration of the TEM instrument was such that in order for RBS thicknesses to follow as closely as possible those measured by TEM, the Ni and silicides densities had to be set at 95% of their bulk value.

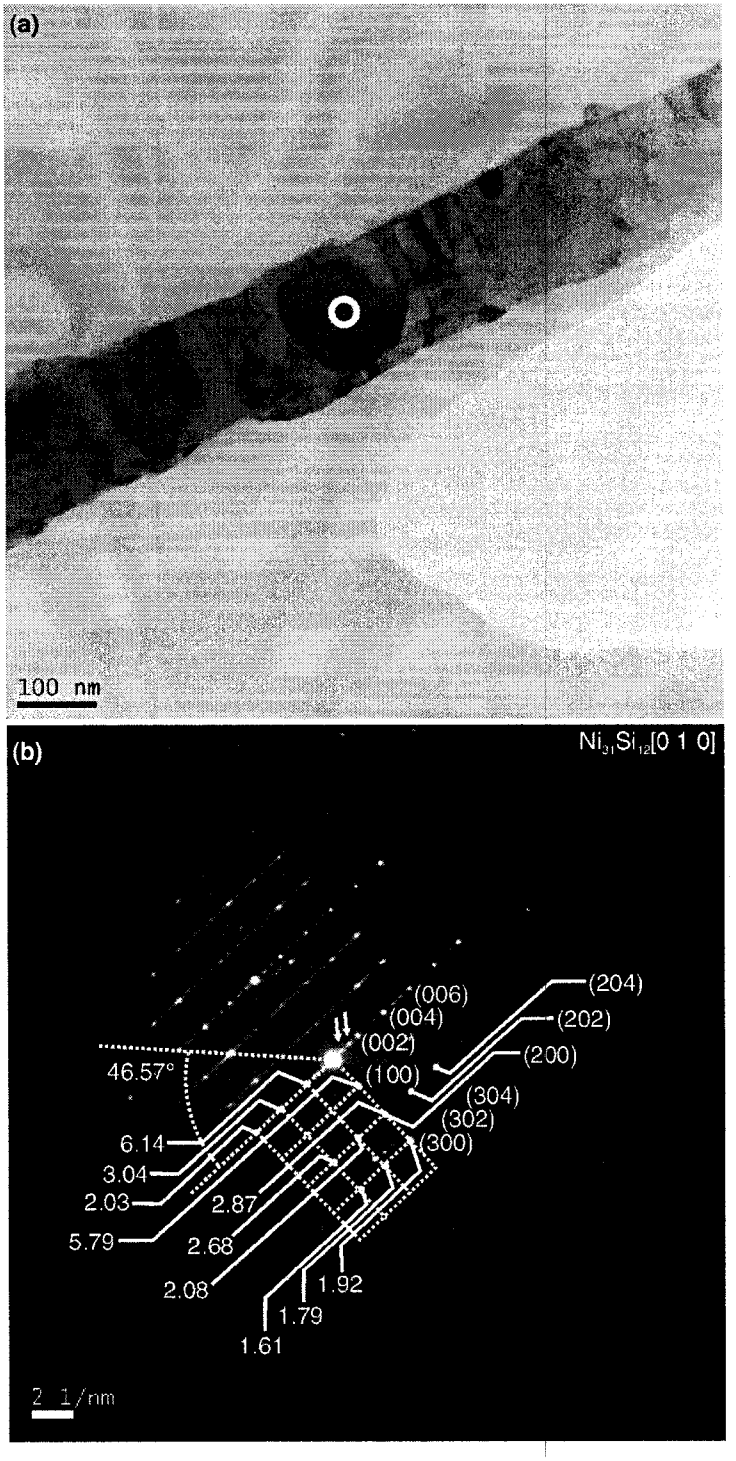

Figure 5.13: (a) Bright-field XTEM micrograph together with (b) a corresponding CBED pattern taken at the location indicated in (a) from a 100-nm-thick Ni layer annealed at 0.3 °C s^{-1} up to 373 °C.

As indicated above, the best fit for the as-deposited sample uses a NiSi layer at the interface with the Si.[1] For the samples quenched at 295 and 310 °C, we simulated a stack of Ni, δ-Ni_2Si, and a bottom layer having a composition and density close to those of Ni_3Si_2. We found that splitting this bottom layer into two enabled us to improve the overall quality of the RBS fit. As a matter of fact, to simulate the important interface roughness, we introduced a composition gradient such that the Si/Ni_3Si_2 ratio ranges from 0 to 50% from the bottom to the top of the interfacial layer.[2] The requirement for such a graded layer at the interface is also consistent with the co-existence of NiSi, Ni_3Si_2 and θ-Ni_2Si as revealed by XTEM/CBED analyses. For the sample quenched at 330 °C, RBS fits confirm that the total thickness is the same than at 295 °C, but that the middle δ-Ni_2Si layer almost tripled in thickness. The clear increase in the measured intensity in channels 320 to 330 between 295 and 310 °C in Figure 5.14 (dashed circle) is a strong indication that the Ni content increases in the layer at the silicide/Si interface, going from somewhere between Ni_2Si and NiSi back to Ni_2Si.

At 355 °C, the Ni signal is flat over a large range of channels at a level corresponding to Ni_2Si. In contrast, the Ni signal for the sample quenched at 373 °C lies slightly above the δ-Ni_2Si level while the leading edge has flattened. This is consistent with the co-existence of $Ni_{31}Si_{12}$ and δ-Ni_2Si throughout the whole silicide thickness as suggested by XTEM. Similarly, the signal decrease between channels 310 and 325 for the sample at 400 °C confirms that the interfacial layer has a composition closer to NiSi. Finally, at 600 °C, the RBS spectrum confirms the existence of a single phased NiSi film as previously suggested by the XRD and XTEM analyses presented above. The increase in signal for this spectrum around channel 300 arises from the overlap of the signals from Ni and Si as this last element is now present throughout the whole film up to the surface.

---

[1] Considering the thicknesses of the Ni and interfacial layers, we conclude that the actual deposited Ni thickness was 110 nm assuming Ni_2Si/Ni and NiSi/Ni theoretical thickness ratios of 1.5 and 2.2, respectively.

[2] Even in SIMNRA, which is more rigorous in its handling of the interface roughness, a concentration gradient had to be included in order to obtain good fits. This software being much less flexible than RUMP for the simulation of concentration gradients, we favored the manual implementation described above.

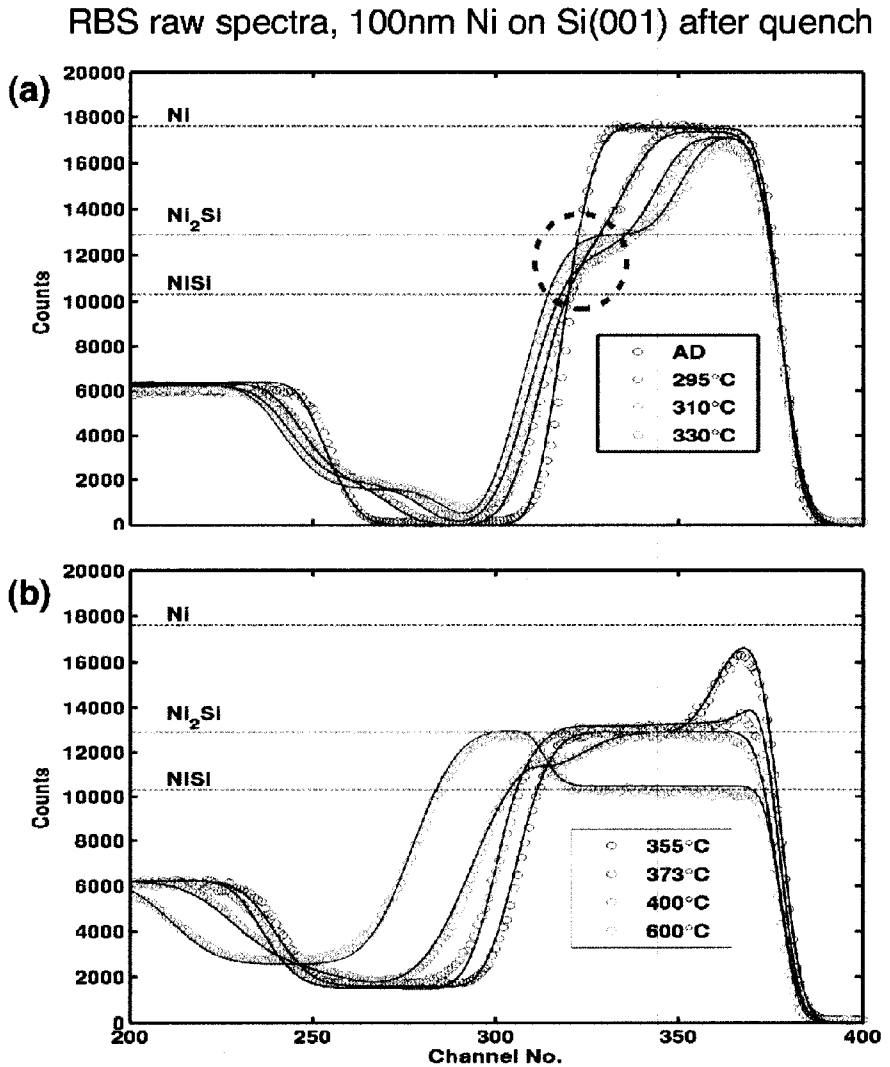

Figure 5.14: Glancing angle RBS spectra from as deposited 100-nm-thick Ni layers on c-Si(001) and subjected to a 0.3 °C s^{-1} ramp anneal: (a) as-deposited and annealed at T_a = 295, 310, and 330 °C, (b) annealed at T_a = 355, 373, 400, and 600 °C. Solid lines correspond to RUMP simulations summarized in Table 5-1

The compound sequence we deduce from the results presented above for the reaction of 100nm Ni layers with Si(001) substrates is summarized schematically in Figure 5.15 where it is compared with the traditionally reported sequence. This figure represents clearly the occurrence of two additional reaction steps before the complete conversion of the Ni layer to NiSi.

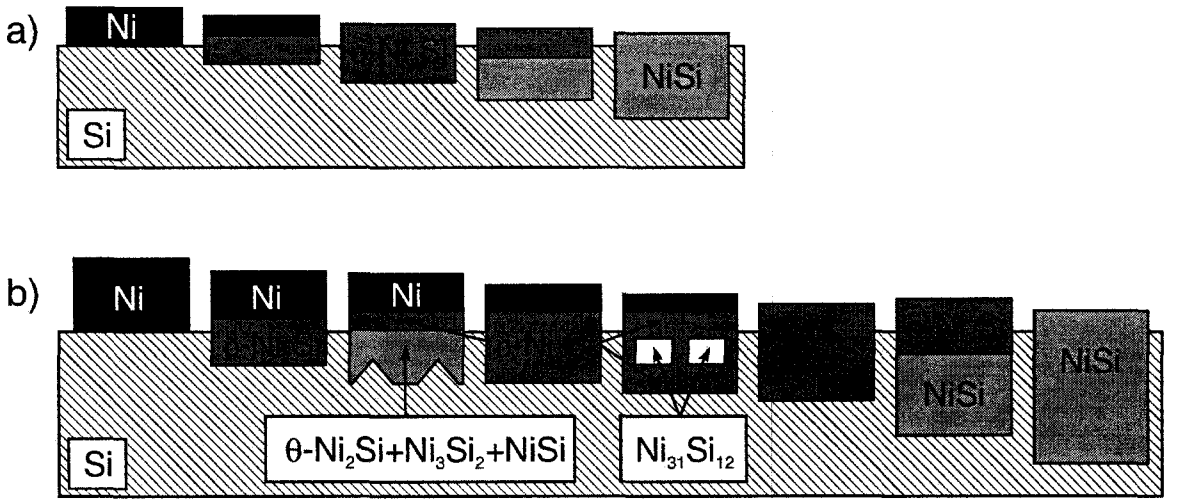

Figure 5.15: a) Schematic representation of the traditionally reported reaction sequence compared with b) the sequence we observed during the reactions between 100nm Ni layers and Si (001) substrates during ramp-type anneals.

C. Influence of initial Ni thickness on the phase sequence

The results presented above indicate that, while the overall behavior is the same, changing the initial Ni film thickness lead to several interesting differences. In order to investigate this effect further, we have carried out *in situ* XRD analysis during ramp anneals at 3 °C s^{-1} for samples with thicknesses of 4, 6, 10, 15, 30, 50, 100 and 500 nm. The corresponding *in situ* XRD scans are presented in Figure 5.16 where all graphs were generated using the same intensity scale to facilitate comparison,.

First and foremost, Figure 5.16 reveals that the first two metal-rich phases (δ-Ni_2Si and the θ-Ni_2Si) always form at the same temperature while other transformations, such as the growth of NiSi, are thickness-dependent (the two vertical dashed lines serve to mark the position of these two transitions). Furthermore, the temperature for the disappearance of θ-Ni_2Si also seems to be insensitive to film

thickness.[1] We have plotted in Figure 5.17 the ratio of the maximum XRD intensities of the θ-Ni_2Si(110) and Ni(111) peaks as well as the temperatures for the appearance and disappearance of the θ-Ni_2Si (110) peak[2] as a function of the initial Ni film thickness. These data confirm that the θ-Ni_2Si formation temperature is independent of Ni film thickness whereas its consumption temperature increases very weakly. This is in sharp contrast with the 150 °C increase observed in the same samples for the NiSi formation temperature. The data in Figure 5.17 also highlights that the θ-$Ni_2Si(110)_{max}/Ni(111)_{max}$ intensity ratio decreases between 4 and 10 nm Ni, then remain relatively stable until 100-nm Ni, and decreases further for even larger initial Ni thicknesses.

Figure 5.16 also demonstrates that we observe an increasing number of metal-rich compounds in samples with an initially thicker Ni layer. In the 4-nm sample (Figure 5.16 (a)), the δ-Ni_2Si peaks do not reappear upon the consumption of the θ-Ni_2Si compound. Initial Ni thicknesses of more than 50 and 100 nm are required for the appearance of $Ni_{31}Si_{12}$ and Ni_3Si_2, respectively. We also note that the $Ni_{31}Si_{12}$ (300) remains visible over a much larger temperature range in the 500 nm sample compared to the 100 nm Ni sample. This, again, highlights the importance of a significant Ni supply for the existence of this compound. RBS results (not shown) suggest that $Ni_{31}Si_{12}$ develops as a full layer on top of δ-Ni_2Si in that 500-nm Ni sample.

---

[1] We have also investigated the solid state reaction for a 2-nm-thick film. The XRD map, however, did not reveal any peak. Nevertheless, the resistance trace still provided evidence of several reactions and transformations. The resistance reached a maximum at 300 °C and then decreased steadily until 400 °C. It then reached a plateau above 500 °C. The maximum near 300 °C would be consistent with the formation of δ-Ni_2Si, but no clear indication of θ-Ni_2Si formation is observed (i.e. the presence of an inflexion point or secondary increase/decrease in resistance). The fact that we do not observe XRD peaks could suggest the formation of epitaxial phases that escape detection in the geometry used for the measurement.

[2] Defined as the position of the local maximum of the derivative of the summed intensity under the peak with respect to temperature.

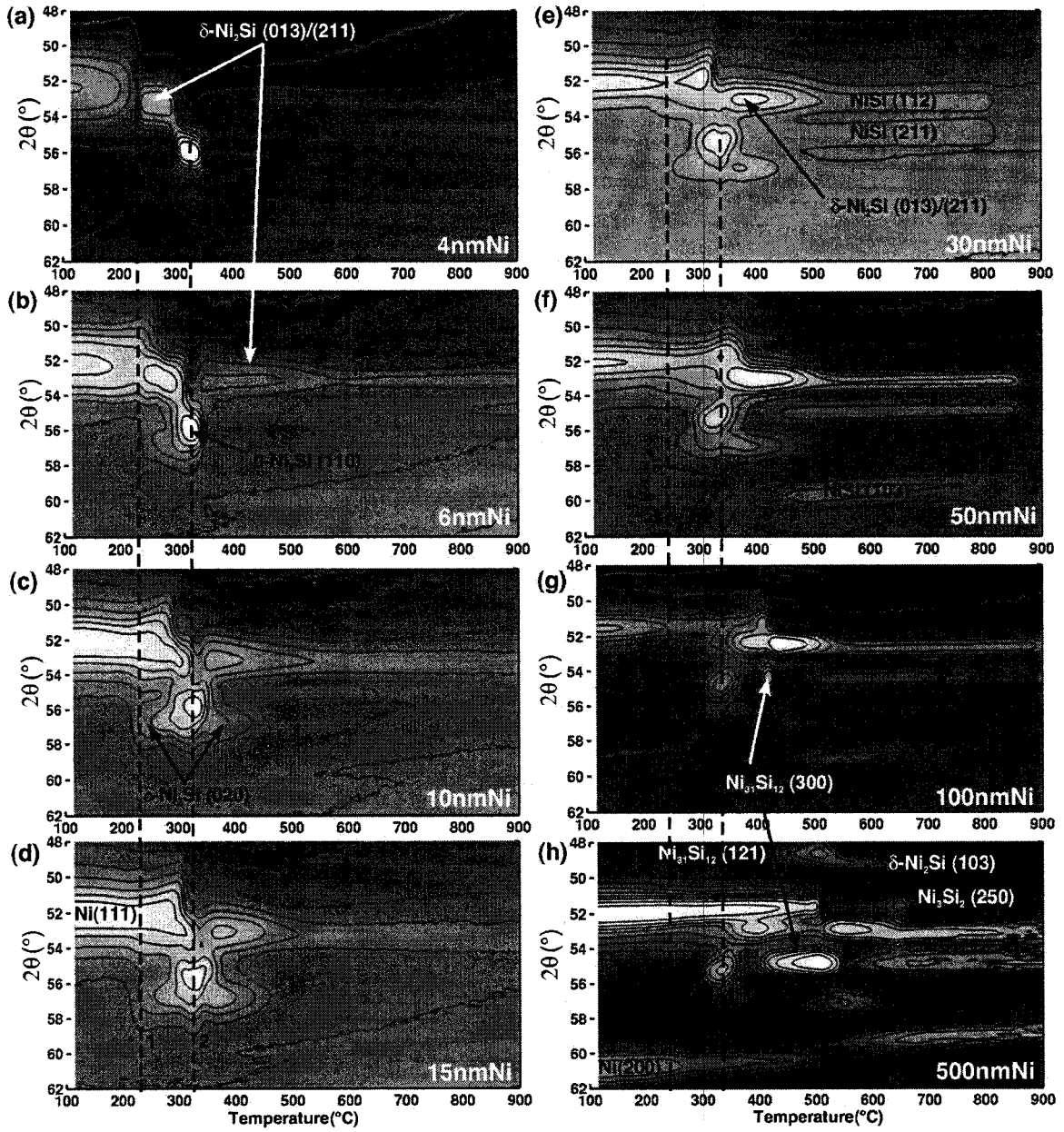

Figure 5.16: XRD intensity contour maps ($\lambda = 0.1797$ nm) plotted as a function of annealing temperature T_a during thermal ramps at 3 °C s^{-1} in purified He for (a) 4, (b) 6, (c) 10, (d) 15, (e) 30, (f) 50, (g) 100, and (h) 500 nm-thick Ni films on c-Si(001). The detector is centered at $2\theta = 55°$.

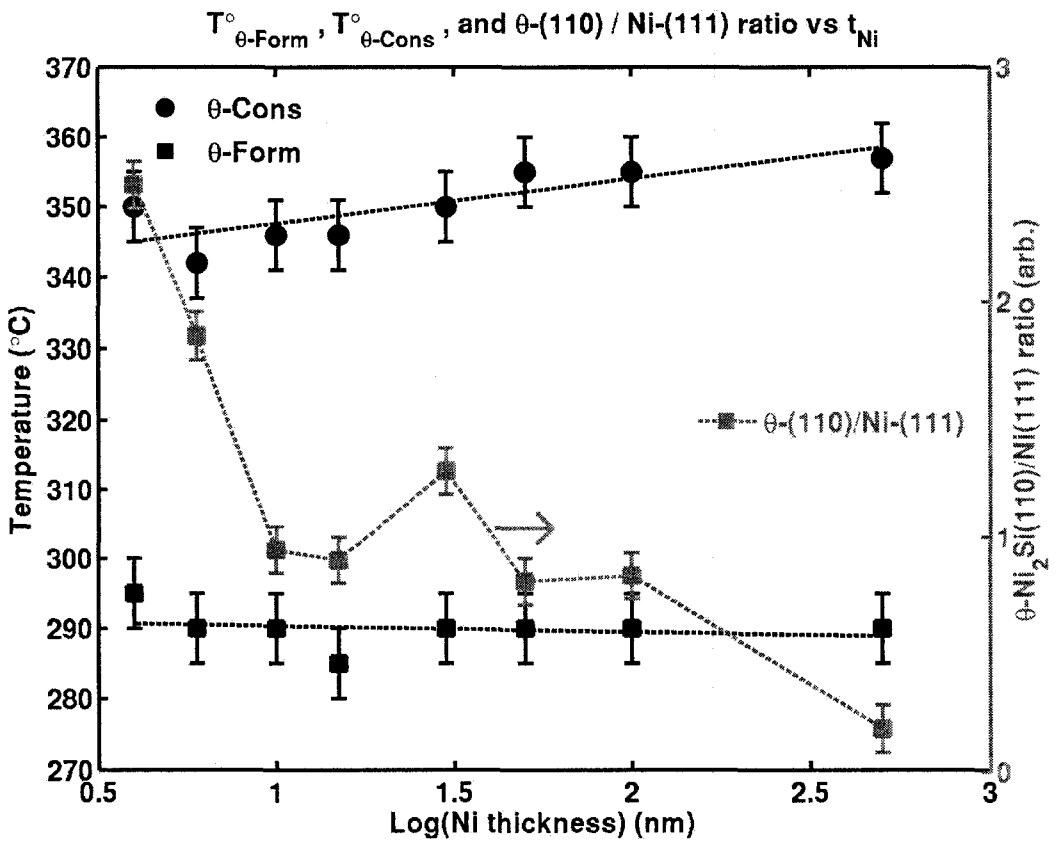

Figure 5.17: Ratio of the integrated θ-Ni_2Si(110) and Ni(111) peak intensities ($I_{\theta\text{-}Ni2Si}/I_{Ni}$) (■) together with the θ-Ni_2Si formation (■) and dissolution (●) temperature as a function of initial Ni film thickness. These temperatures were taken as the local minimum and maximum of the derivative of the integrated intensity under the θ-Ni_2Si (110) peak with respect to temperature. The error bar represent uncertainties of 5 °C on temperatures and 5% on intensities

As a general result, we find that δ-Ni_2Si is the dominant metal-rich compound in all but the thinnest sample presented in Figure 5.16. The formation of other metal-rich compounds systematically occurs at the expense of that dominant compound. Moreover, their consumption seems to lead to a restitution of some of the previously consumed δ-Ni_2Si as evidenced by the systematic increase of the δ-Ni_2Si (013)/(211) peak following the decomposition of θ-Ni_2Si and $Ni_{31}Si_{12}$.

The formation of NiSi has been reported to proceed at the expense of δ-Ni_2Si only once Ni becomes exhausted,[2,15,165,166] however, our results show that an additional Ni-rich phase is involved. Indeed, the beginning of the formation of NiSi always coincides with the consumption of another Ni-rich compound (θ-Ni_2Si in films with less than 50 nm Ni; $Ni_{31}Si_{12}$ in samples with 100 nm Ni or more). The consumption of the Ni-rich compounds leads to the growth of both δ-Ni_2Si and NiSi; followed by the expected growth of NiSi at the expense of δ-Ni_2Si. For the 4 nm Ni sample, our XRD results suggest that NiSi forms solely from the consumption of θ-Ni_2Si. While observing additional Ni-rich compounds was rather surprising considering the commonly accepted compound formation sequence for the thin-film Ni-Si reactions, the fact that compounds with a higher Ni content follow compounds with a lower one is a rather striking result.[1]

While δ-Ni_2Si and θ-Ni_2Si always form at the same temperature, Figure 5.16 indicates that their respective (013)/(211) and (110) XRD peak positions begin to shift at temperatures that depend in the initial Ni film thickness. Indeed, the δ-Ni_2Si peak clearly shifts to larger angles whenever Ni is consumed. The θ-Ni_2Si peak, in contrast, is subject to two opposite and consecutive shifts in the 15 and 30-nm Ni samples, while we observe a single shift towards higher angles in thinner samples and towards smaller angles in thicker films. These results reflect the fact that the time (or temperature) required for the complete consumption of Ni is initially shorter, but eventually exceeds that for the formation of θ-Ni_2Si as the initial Ni film thickness is augmented. This phenomenon will be discussed in more details below.

---

[1] It should be noted that the low-temperature portion of the reaction sequence observed in the 500 nm Ni sample (Fig. 14(h)) differs from that reported earlier. [156] In early experiments conducted with thick films deposited in a single pass, we observed two low intensity peaks in the as deposited film, which were attributed to the δ-Ni_2Si or $Ni_{31}Si_{12}$ phases. This phase was then immediately followed by intense δ-Ni_2Si peaks without evidence of θ-Ni_2Si. We attribute the difference to the fact that the single-pass deposition is likely to cause the sample temperature to exceed 200 °C for more than 10 minutes, which is sufficient to trigger significant silicide formation at the interface.

Although we did not attempt to investigate film textures and their impact on the reaction in this chapter, Figure 5.16 nevertheless shows that the NiSi layer texture does not depend significantly on the initial Ni film thickness. While the absolute intensities of the NiSi (112), (211) and (103) peaks increase with the Ni thickness, their relative intensities remain roughly the same except for the thinnest sample where the NiSi (112) peak appears to overcome the other two.

5.4 Discussion

5.4.1 Lateral co-existence of compounds and nucleation in grain boundaries

One of the fundamental results of this chapter is that in multiple instances, many compounds coexist laterally in a single layer. In thin film reactions, where the compounds are expected to form in sequence, a maximum of two could be expected within a single layer, mostly in cases where a significant barrier to nucleation is present. In nucleation-limited transformations, such as for instance the $TiSi_2$ C-49 to C54 transformation, nucleation and rapid lateral growth within the layer plane can lead to lateral coexistence of compounds in the same layer. The lateral growth is however expected to be rapid after the barrier to nucleation is overcome so that the co-existence should be transient. In cases where nucleation is not rate limiting, then one expects the growth fronts to be planar so that compounds coexist in a layered geometry. In the TEM cross sections studied here, the samples were annealed and quenched at stages corresponding to the maximum development of some featured compounds, as determined by *in situ* XRD. These samples should therefore not correspond to reaction stages representative of a "transition" between nucleation events and the eventual impingements of growing grains into continuous layers. Except in the case of $Ni_{31}Si_{12}$ in samples with 500 nm Ni, we do not find complete layers of θ-Ni_2Si, Ni_3Si_2 or $Ni_{31}Si_{12}$.

While such a lateral coexistence has not been frequently observed in thin films, we believe that there are no fundamental reasons that preclude the nucleation of multiple compounds at a single interface. d'Heurle suggested that compounds that may grow at an interface, especially the first of a sequence, are mostly selected by kinetics of growth and by the competition between compounds for the same reactants. At the interface between a polycrystalline material and a single-crystal Si substrate, one can presume that the conditions for nucleation and growth will vary locally depending on the microstructure and the local availability of reacting species. Indeed, as grain boundary angles can vary, diffusion and interfacial energies can vary as well so that several compounds can certainly be allowed to nucleate in different areas of a given interface. Over the total reaction time however, one compound may dominate and transform the whole inhomogeneous film into one single-phase layer. In this work, the availability of an x-ray beam ten thousand times more intense than that provided by a state-of-the-art rotating anode system allowed us to detect several compounds, sometimes in very small volumes, before they lose the competition for growth to the benefit of δ-Ni_2Si.

Because our layers are in multiple instances not laterally uniform in composition, we believe that the additional compounds we observe have nucleated at the junction of δ-Ni_2Si of grain boundaries and either interface. If the importance of grain boundaries in diffusion is part of the common knowledge, their importance in nucleation is far less well understood. Coffey and Barmak developed a model to understand the evolution of the chemical potentials in grain boundaries at the very beginning of interdiffusion (i.e. before thorough intermixing took place). They demonstrated that the competition between *i)* diffusion along the grain-boundaries and *ii)* transport between these and the bulk of the grains could significantly tailor the values of the chemical potentials at the interface between two materials.[167] They explained how the ensuing reduction of the effective change in Gibbs free energy could result in a more difficult nucleation of the compounds at the interface. They then used their model to explain why the formations of $NiAl_3$ and $NbAl_3$, which are the first compounds to form in their respective systems, are actually

nucleation-controlled. Their work focused on the grain boundaries at the interface of two infinitely pure phases, but their model clearly shows that the conditions of diffusion fluxes, stress and microstructure can have a direct influence on compound nucleation. Our results lead us to believe that an appropriate combination of such non-equilibrium conditions can exist in the Ni-Si thin film system so as to enhance the nucleation of new compounds at the grain boundaries of a previously existing compound (e.g. δ-Ni_2Si) instead of hindering it. This phenomenon would thus be the prelude to the lateral coexistence of compounds we report.

5.4.2 Non-sequential formation of compounds

A) Formation of θ-Ni_2Si

In the current work, we show that, for all film thicknesses, the first compound to form is the expected δ-Ni_2Si, which is clearly followed by the formation of θ-Ni_2Si before the low resistivity NiSi can grow. Beside the consistent XRD peak positions, the indexation of this metastable phase is supported by the XRD pole figure analysis and CBED analyses in TEM samples. In previous communications, the XRD peaks at 56° and 27° (e.g. Figure 5.1 (a) or Figure 5.8 (a)) that we now assign to θ-Ni_2Si were indexed to Ni_3Si_2 (350) and (310).[8,9,157] The data presented here in samples quenched when these peaks are maximum clearly show that this early indexation was incorrect (lack of Ni_3Si_2 (600) signature) and that θ-Ni_2Si is present.

According to the Ni-Si phase diagram, θ-Ni_2Si is a non-stoechiometric compound with a large homogeneity range (up to 8% depending on the temperature).[33] The compound is hexagonal with the prototype Ni_2In and lattice parameters a = 0.3805 nm, c = 0.489 nm, at a composition of 60:40 Ni:Si. Figure 5.18 shows a schematic of its unit cell. The Ni atoms, which constitute the hexagonal backbone, are in black while Si and

additional Ni are pictured in light and dark grey, respectively. As depicted here, the structure has the composition of Ni_2Si. Ni-deficiency of the compound occurs via the progressive depletion of the inner Ni atoms. Once fully depleted, the structure is identical to that of NiAs, the prototype structure of NiSi, which is a more symmetric version of the orthorhombic MnP form of NiSi, [51] although the lattice parameters are different.

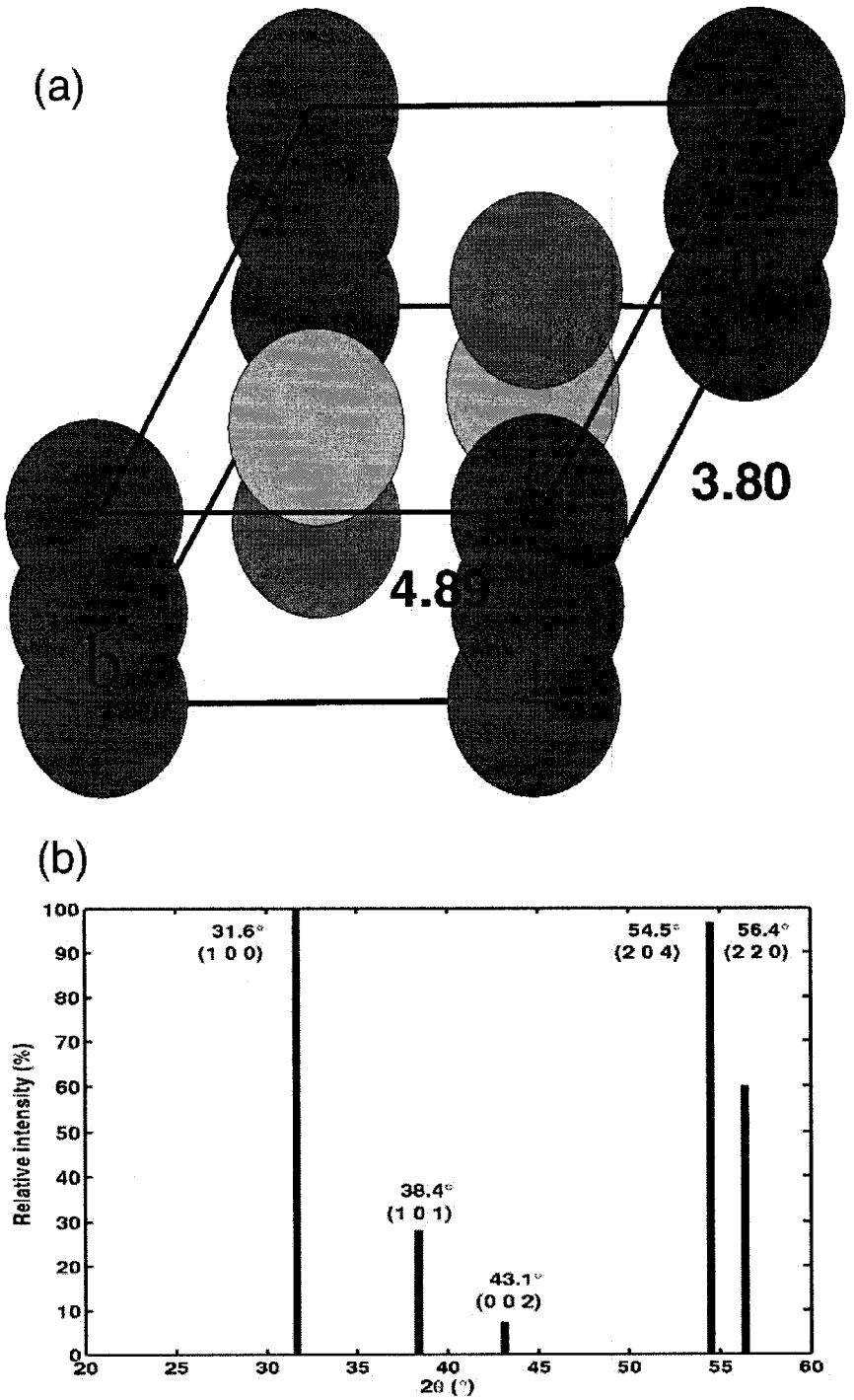

Figure 5.18: a) Unit cell of the hexagonal θ-Ni_2Si crystal structure and (b) corresponding calculated diffraction curve for λ = 0.1797 nm.

θ-Ni_2Si has its most intense XRD peaks at 54.27° and 56.44°, respectively indexed as (102) and (110) with d spacings of 0.197 nm and 0.190 nm. The first peak reported by the JCPDS datasheet # 70-2093 is the (101) at 31.6° (d_{101} = 0.330 nm), which indicates that θ-Ni_2Si cannot *a priori* give rise to the XRD peak at 27° (d_{hkl} = 0.385 nm) observed in all our experiments. If the (001) planes were allowed to diffract, they would do so at an angle of 21.2°. As the 2θ positions can be modified by thermal expansion and growth stress, we can assume that d_{hkl}= 0.385 nm is close enough to 0.380 nm, which is twice the value of d_{110}= 0.190 nm. The peak around 27° could thus be a superlattice reflection caused by the ordering of vacancies in a Ni-deficient θ-Ni_2Si, giving rise to a periodicity twice as large as the (110) interplanar distance. Vacancy ordering has been observed in systems such as $Ni_{1-x}Al$,[168] $Ni_{3-x}Te_2$,[169] $Cu_{3-x}Te_2$,[170] and ZrS_2.[171] In the latter two cases, superlattice reflections were observed in TEM diffraction patterns only, but we did not observe such reflections in our CBED experiments.

In Figure 5.19 we show two representations of a θ-Ni_2Si supercell along with the corresponding XRD curves as simulated with the CaRIne software package. The supercell has twice the dimensions of the unit cell in all directions and is thus built from 8 basic hexagonal cells. In each supercell, Ni atoms were removed from certain sites marked by white balls: The arrangement in Figure 5.19 (a) corresponds to a stoechiometry of Ni_3Si_2, versus Ni_7Si_4 for Figure 5.19 (b). Both cases present a periodicity that is twice that of the {110} planes, thus leading to the appearance of a weak diffraction peak at 2θ = 27° (assuming no changes in the lattice parameters). These are only two of many possible arrangements; the current work does not provide sufficient information to extract exact composition or vacancy position in the crystallites. Yet the simulations show that vacancy ordering can explain the peak at 27 °.

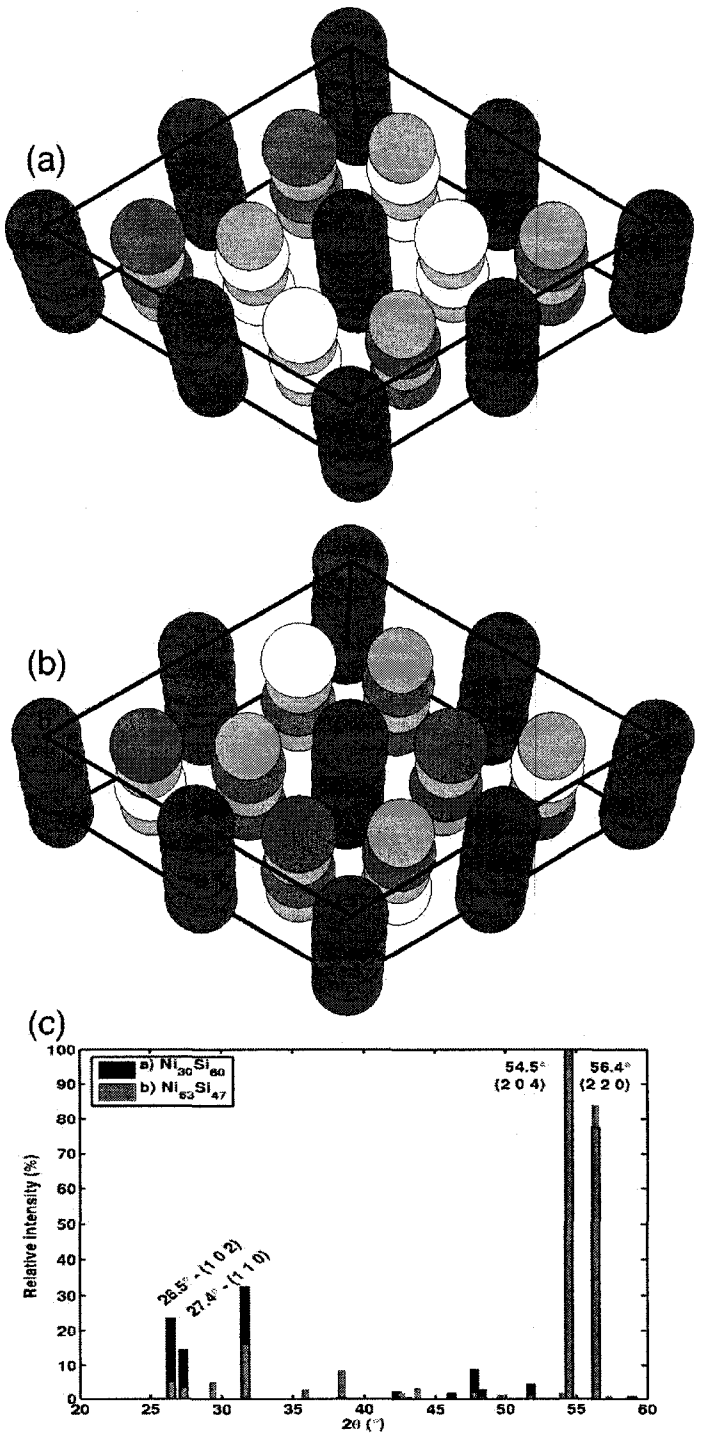

Figure 5.19: θ-Ni_2Si supercells consisting of 2x2x2 unit cells with vacancies arbitrarily ordered on the inner Ni sublattice to obtain compositions of (a) Ni_3Si_2 and (b) Ni_7Si_4. (c) corresponding calculated diffraction curves for $\lambda = 0.1797$ nm.

Three important points characterize the formation of θ-Ni_2Si:

1- Its formation temperature is independent of the initial Ni thickness.

2- The absolute quantity that forms increases with the initial Ni thickness.

3- The temperature range over which it exists increases only slightly with the initial Ni thickness.

The first point suggests the existence of constant nucleation conditions. The compound thus nucleate after a given thickness of δ-Ni_2Si has formed. Favorable conditions may be a combination of the temperature reached together with an appropriate value of the Ni atom flux in the grain boundaries or an appropriate structural arrangement therein.

Observing as we did the θ-Ni_2Si formation in solid state reactions occurring below 825°C is surprising because it is not normally stable in that temperature range according to the Ni-Si equilibrium phase diagram. A possible explanation of its formation lies in the existence of strong compositional gradients at the δ-Ni_2Si/Si interface. Such gradients have been shown to hinder the nucleation of stoichiometric compounds, especially that of NiSi.[172,173] In fact, Hodaj and Gusak have proposed that the requirement for the Ni to be exhausted before NiSi can form is explained by the existence of a strong Ni concentration gradient at the δ-Ni_2Si/Si interface.[46,173] Since θ-Ni_2Si is non-stoichiometric and stable over a rather large composition range it could possibly have an increased ability to nucleate in a composition gradient silicide/Si interface, which would favor its formation in the absence of NiSi.

Another very important parameter in the nucleation of a compound is the interfacial energy between the growing nuclei and the matrix in which it nucleates. It has been shown that low-energy interfaces can significantly reduce the overall energy of a system and stabilize compounds that are either not present in standard sequences or even absent from the equilibrium phase diagram. For instance, in the Co-Si and Fe-Si system,

cubic CoSi and tetragonal $FeSi_2$ were found to grow epitaxially on Si substrates up to thicknesses of 10 nm.[174,175] While θ-Ni_2Si does not seem to grow epitaxially, we have found that its texture is directly inherited from that of the δ-Ni_2Si. The crystal structures of these two compounds are very similar in density and also in the position of their constituting atoms. In Figure 5.20, we compare the atomic arrangement in the (020) planes of δ-Ni_2Si to that of the (110) planes of θ-Ni_2Si. Our diffraction data show that these families of planes are parallel to the surface of the sample. The lattice sizes given show how δ-Ni_2Si (020) and θ-Ni_2Si (110) surfaces can align with little stretching. More importantly, if we focus on a rectangle defined by four Si atoms, we clearly see that the atomic positions of both Si and Ni are almost identical so that very little rearrangement is required to growth one compound out of another. This should allow for a low energy of any interface between both compounds, which, combined with an enhanced ability to nucleate in a concentration gradient, could contribute to stabilize the otherwise unstable θ-Ni_2Si at temperatures below 825 °C.

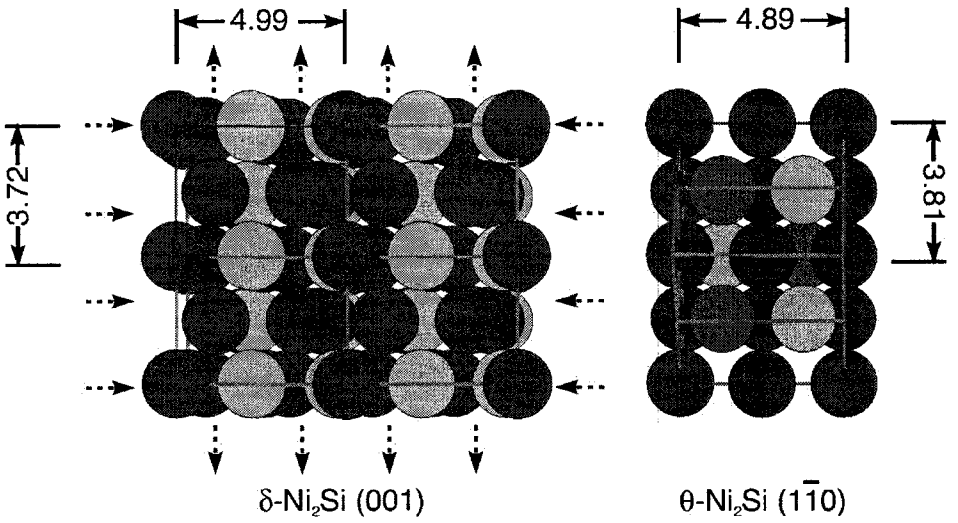

Figure 5.20: Projection of the (θ)-Ni_2Si unit cell perpendicular to [001] direction (left) compared to the θ-Ni_2Si projection perpendicular to [110] direction (right) demonstrating the close match between the d-spacings for the δ-Ni_2Si (020) and θ-Ni_2Si (110) planes. The two darker shades of grey identify Ni atoms and the lighter shade of grey identifies Si atoms.

Before we discuss the second and third particularities of the θ-Ni_2Si, we adress the phenomenon through which it is consumed. Indeed, while the formation of a metastable θ-Ni_2Si in Ni-Si reactions is already surprising, the mechanisms for its consumption are *a priori* even more unexpected. Our data show that the consumption systematically coincides with the simultaneous formation of NiSi and δ-Ni_2Si, a phenomenon that may be summarized by the reaction below:

$$\theta\text{-}Ni_2Si \rightarrow \delta\text{-}Ni_2Si + NiSi$$

To be possible, such a scheme requires that the composition of θ-Ni_2Si lies somewhere between those of δ-Ni_2Si and NiSi, which is consistent with the presence of multiple vacancies in the compound.

We suggested in earlier communications that θ-Ni_2Si (then identified as Ni_3Si_2) could dissociate because of the accumulation of strain energy. Our argumentation was based on the stress measurements results in samples with 100 nm Ni (Figure 5.10), where the dissociation of the compound coincides with a negative peak in the stress curve. The volume of θ-Ni_2Si surely varies with composition and assuming that Ni diffuses into the hexagonal structure enough to allow for a significant composition change, it is reasonable to see the volume increase. The θ-Ni_2Si formation should thus lead to compressive stress build-up, possibly rendering the system unstable and forcing dissociation. Still, it is unclear how the dissociation of an unstable layer would occur and difficult to imagine that it would result in a well defined layer.

The following scenario is more plausible: We believe that the consumption of θ-Ni_2Si is in fact triggered by the nucleation of NiSi at the interface. Indeed, based on the Ni-Si equilibrium phase diagram and assuming a large nucleation barrier to the formation of Ni_3Si_2 as suggested by Gas *et al.*,[71] a system with a composition between those of δ-

Ni_2Si and NiSi should evolve towards a state where both these compounds co-exist. As long as NiSi, and Ni_3Si_2, are not able to nucleate, θ-Ni_2Si may form and be metastable, but as soon as one of the former can nucleate, the metastable compound should become unstable. After it nucleated, NiSi can grow very rapidly into θ-Ni_2Si without long range diffusion of either Ni or Si simply by absorbing the many vacancies that fill its structure. With a θ-Ni_2Si composition not too far from to that of NiSi the growth velocity would relate directly to the diffusion of vacancies within the θ-Ni_2Si. Concurrently, the remaining θ-Ni_2Si would gradually increases in composition (with very little Ni diffusion) because of the vacancies gradually leaving the material. Eventually, when the composition of θ-Ni_2Si reaches the 2:1 ratio, δ-Ni_2Si simply reforms through a polymorphic transformation being the most stable phase at that composition.

In this scheme, the formation of NiSi should occur before the return of δ-Ni_2Si. From Figure 5.1, while it is clear that the θ-Ni_2Si XRD intensity decrease corresponds to an increase of NiSi, it is rather difficult to judge if δ-Ni_2Si returns only after some NiSi has formed. This apparent concurrence could however be the result of lateral non-uniformity. Following multiple nucleation events, the transformation front is not expected to be very uniform so that the reaction will not occur uniformly, both in space and in time. Our measurements would then become an average reaction rate over the size of the x-ray beam on the sample. It is then possible that the reaction be much sharper than what is actually measured. Nevertheless, the formation of NiSi from vacancy diffusion within θ-Ni_2Si followed by a polymorphic transformation of θ-Ni_2Si to δ-Ni_2Si once the right concentration is reached appears the most likely reaction path for this unusual behavior.

Such a scenario would explain the second characteristic of the θ-Ni_2Si's formation mentioned above. As the formation temperature/time of the compound is independant of the Ni starting thickness, it most likely occurs at a time where the δ-Ni_2Si has a given constant thickness. However, as the Ni gets thicker, it stays available longer, which could

contribute to sustain a strong concentration gradient at the silicide/Si interface, hindering the nucleation of the NiSi for longer times. The lateral co-existence of θ-Ni_2Si and δ-Ni_2Si being a sign that the former has still room to develop further, a delayed nucleation of NiSi would allow for more θ-Ni_2Si growth. The explanation for the third point above then follows, as a larger formed quantity of θ-Ni_2Si together with a delayed NiSi nucleation will result in a slighlty delayed consumption (c.f. Figure 5.17).

B) Structural reorganization in Ni

The sudden increase in XRD intensity of the Ni (111) peak preceding its consumption in samples with more than 15 nm Ni may be explained by a structural reorganization. Throughout the reaction process, as the Ni layer is consumed, vacancies are continually generated at the Ni/silicide interface. Most of these vacancies will be eliminated at the film surface but many could coalesce into voids given the right conditions. When the Ni layer becomes very thin, it becomes unstable and will tend to agglomerate. This reorganization will certainly be helped by the presence of vacancies and lead to changes in texture which could be the source of the measured increase in Ni(111) intensity. This agglomeration is consistent with the discontinuous Ni layer morphology observed in Figure 5.11 (f) and is concurrent with the sharp reduction of compressive stress observed in Figure 5.10 (a) between 350 and 375°C, which coincides with the increase in Ni(111) XRD intensity around 52° (2θ) in Figure 5.10 (b). The increase in Ni(111) intensity could also be related to grain growth where the Ni (111) grains would consume grains of different orientations. It is also expected that, above 400 °C, Si atoms becomes mobile and more readily available at the interface. The Ni could therefore simply be absorbing Si since up to 10 at.% can dissolve in Ni. As the concentration increases, both the intensity and the position of the diffraction peak could change, as we observe it. The addition of Si to the Ni film also sets the stage for the formation of $Ni_{31}Si_{12}$ which follows.

C) Formation of $Ni_{31}Si_{12}$ and Ni_3Si_2

From our results, it is clear that $Ni_{31}Si_{12}$ growth occurs at the expense of both δ-Ni_2Si and Ni layer. The reaction thus proceeds close to the Ni/δ-Ni_2Si interface, i.e. away from the silicide/Si interface. Assuming that the Ni is not saturated in Si, the equation below shows the most probable reaction pathway:

$$2Ni_2Si + Ni = Ni_5Si_2 \quad \Delta G=-45.36kJ \text{ @ } 400°C$$

The Ni_5Si_2 nomenclature is used here instead of $Ni_{31}Si_{12}$ because *i)* it corresponds to that of the thermodynamic data reference[176] and *ii)* it yields a more intuitive chemical equation. With such a large free energy change one would expect a diffusion-controlled growth [†,4,11], but the morphology and rate at which the formation takes place in the 100 nm Ni sample suggests a fast nucleation-controlled kinetics. This is certainly supported by the fact that $Ni_{31}Si_{12}$ is not observed below 400 °C where only a nucleation barrier could prevent its formation (since the growth occurs very rapidly above that temperature).

Although $Ni_{31}Si_{12}$ grains effectively end up propagating so as to form a continuous layer if there is enough Ni (e.g. in the 500 nm Ni sample), our TEM results indicate that their nucleation does not take place uniformly in an intermixed interfacial region between δ-Ni_2Si and Ni. If Si atoms diffuse sufficiently, nucleation could occur at grain boundaries in the Ni film and then proceed laterally to consume all of it. However, if Ni still dominates the growth, it is possible that the flux of Ni towards the lower layers favors the nucleation of $Ni_{31}Si_{12}$ in the grain boundaries of δ-Ni_2Si. We explain the lateral coexistence of $Ni_{31}Si_{12}$ and δ-Ni_2Si in the 100nm Ni sample by the fact that the Ni is

---

† *a fortiori* since $Ni_5Si_2/Ni_{31}Si_{12}$ has been shown by Gulpen in his doctoral thesis[88] to have a higher coefficient for Ni diffusion than Ni_2Si .

supplied through these grain boundaries but is still insufficient at that point for a complete coalescence of all δ-Ni_2Si grains in the top layer.

Upon shortage of the Ni supply, $Ni_{31}Si_{12}$ becomes the Ni-richest compound and therefore the most likely source of Ni. It shall then transform "back" to δ-Ni_2Si. At this temperature, the reaction could occur through diffusion of either of Ni and Si or both. In either case, the reaction pathways are given below:

Ni diffusion	1a-	**$2Ni_5Si_2 = 4Ni_2Si + Ni$**	**ΔG = +6.158 kJ/mol. at @ 500°C**
Ni diffusion	1b -	**$2Ni + Si = Ni_2Si$**	**ΔG = -48.99 kJ/mol. at @ 500°C**
Si diffusion	2-	$2Ni_5Si_2 + Si = 5Ni_2Si$	ΔG = -36.67 kJ/mol.at @ 500°C

While the overall energy for the Ni_5Si_2 formation through Ni diffusion is negative, the decomposition of Ni_5Si_2 into Ni_2Si and Ni is not. This reaction step is therefore not likely to occur, which suggests that the consumption of Ni_5Si_2 is achieved through Si diffusion at grain boundaries.

We proposed earlier a mechanism for the formation of Ni_3Si_2 in later stages of the reaction in samples with 500 nm [9]. The compound appears at high temperature when the top δ-Ni_2Si layer nears complete consumption and thus reaches the limit for stability. One possible mechanism for thin unstable films is to agglomerate to reduce the surface to volume ratio. Here, as the layer becomes unstable, we could be in a situation where the nucleation of Ni_3Si_2 and the rapid growth from the interface allows for the films to thicken and regain stability. This scenario would be consistent with the results of Gas *et al.* who observed the nucleation-controlled growth of Ni_3Si_2 at the δ-Ni_2Si/NiSi interface at temperatures above 600 °C.[71]

5.5 Conclusion

In this chapter, we have revisited the Ni-Si thin film reaction through the combined use of *in situ* real tim XRD, wafer curvature measurement, *ex situ* TEM, and RBS. We have shown that the reactions between Ni films and Si(001) are considerably more complex than historically reported. Indeed, we have provided evidence for the formation of θ-Ni_2Si, $Ni_{31}Si_{12}$ and Ni_3Si_2, in addition to δ-Ni_2Si, in samples with initial thicknesses ranging from 4 to 500 nm. These compounds are found to co-exist laterally with δ-Ni_2Si and/or NiSi, in addition to form non-sequentially, as δ-Ni_2Si is consumed by their formation and restituted upon their consumption. Our extensive experimental work has allowed us to propose explanations for the peculiar behaviors we have observed and which are in apparent contradiction with the current understanding of solid-state reactions,

The metastable θ-Ni_2Si compound forms consistently at the same time/temperature, regardless of the initial Ni thickness. Our XRD data suggest that the hexagonal crystal structure of this non-stoichiometric compound can sustain vacancies distributed with a certain degree of ordering over the internal Ni sublattice. The nucleation of θ-Ni_2Si is possible for two reasons. The first is the presence of very low interfacial energies with δ-Ni_2Si since the two crystal structures are extremely similar. The second is the wide composition range of θ-Ni_2Si which allows nucleation in strong concentration gradients at the interface. As soon as NiSi nucleates at the θ-Ni_2Si/Si interface, the growth of NiSi can rapidly occur without long range diffusion of neither Ni or Si, simply through the absorption of vacancies present, within θ-Ni_2Si. This rapid vacancy absorption leads to a gradual increase in Ni concentration in the remaining θ-Ni_2Si. As the compounds approach the concentration of Ni_2Si, the crystal structure reverts to the more stable δ-Ni_2Si. This δ-Ni_2Si is first consumed and then reappears when NiSi forms.

$Ni_{31}Si_{12}$ is only observed in samples with at least 100 nm Ni for temperatures above 400 °C. As for θ-Ni_2Si, this compound formation occurs before NiSi and is concurrent with a decrease in the XRD intensity of the δ-Ni_2Si peaks. This compound appears to form in the grain boundaries of the δ-Ni_2Si consuming the remainder of the Ni layer. We suggest that the formation occurs through the diffusion of Ni and possibly Si at such temperatures. As expected $Ni_{31}Si_{12}$ is consumed by a growing δ-Ni_2Si as the temperature increases and the Ni supply decreases.

Ni_3Si_2 was observed at temperatures above 600 °C when δ-Ni_2Si and NiSi are still available simultaneously (only in samples with 500 nm Ni). The presence of this last compound could be the result of a nucleation enhanced by the high temperatures or of a transformation at the δ-Ni_2Si /NiSi interface as δ-Ni_2Si becomes too thin and unstable. A transformation to a thicker Ni_3Si_2 layer would then allow for regaining stability for a narrow temperature range.

Chapter 6 : Effects of Ni-alloying, implanted impurities, and substrate crystallinity

6.1 Introduction

The results presented in Chapter 5 clearly demonstrate that the solid-state reactions between Ni films and Si(001) are considerably more complex than previously believed. The hexagonal θ-Ni_2Si phase, normally expected at high temperature, was observed in films reacted between 240 and 350 °C whereas $Ni_{31}Si_{12}$ formed above 450 °C in samples in which the initial Ni thickness was 100 nm or more. We also provided evidence for the lateral co-existence of these two compounds with δ-Ni_2Si.

The present chapter focuses on the formation of the metastable θ-Ni_2Si. This compound forms rapidly during ramps anneals, apparently consuming all δ-Ni_2Si for initial Ni films thickness of up to 10 nm. Its disappearance is also rapid and is correlated with both the growth of NiSi and to a surprising return of orthorhombic δ-Ni_2Si. A better understanding of this behavior is certainly of fundamental value to thin film physics and contact metallurgy but is also of critical importance for the development of next generation transistors in the microelectronics industry.

In Chapter 5 (Figure 5.16), we have shown that the formation temperature of the θ-Ni_2Si compound is independent of the initial Ni thickness. As this compound is not the first one to appear, such a behavior is not consistent with diffusion limited layer-by-layer growth as commonly observed for the formation of NiSi in planar geometry. Indeed, the formation of NiSi is delayed by an increasing initial Ni thickness. This result suggests that θ-Ni_2Si forms close to the silicide/Si interface, where its nucleation must be favored with respect to that of NiSi.

Compound nucleation in very thin films was shown to strongly depend on substrate crystallinity and defects as well as on the introduction of impurities either through implantation in the substrate or alloying of the Ni film. [133,50,52,53,59,104,110,117,121,127,135,138,142,146] However, none of these studies have evidenced the formation of θ-Ni_2Si, aside from a few reports of the formation of a hexagonal NiSi[50,51,121], which we believe is not exactly the same phase than what we observe. Here, we report on the effect of impurities on the formation of θ-Ni_2Si. Impurities were introduced both through alloying of the Ni films with either Pt or Co, and through Si substrate implantation. Implanted species covered the standard dopants (As, B and P), impurities known to stabilize the NiSi films against agglomeration (F and N),[145,177,178,179] as well as Si to evaluate the effect of substrate defects. Finally, we have investigated the reaction of Ni films with amorphous Si (a-Si) substrates. Using *in situ* XRD and resistance measurements during annealing at constant temperature ramp rates, we have monitored the reaction in samples with 10 nm Ni or Ni-alloy on undoped and ion-implanted Si(001) as well as on amorphous Si. In a separate *in situ* study of the stress development during the reaction on F-implanted samples, a Flexus® furnace has been used.

6.2 Experimental procedure

6.2.1 Implantation

Undoped, n-doped and p-doped silicon-on-insulator (SOI) 8-inch wafers were prepared at a CMOS production facility (IBM, Hopewell Junction). Wafers were implanted with 5×10^{15} P cm^{-2} at 12 keV or 3.5×10^{15} B cm^{-2} at 8 keV with their normal tilted 7° away from the ion beam axis to prevent channeling. Following implantation, the wafers were heated above 1000 °C to activate the dopants and anneal the damages induced by implantation. The projected ranges calculated using TRIM[180] were

respectively 18 and 32 nm for the as-implanted samples, indicating that the implantation depth is such that enough implanted Si is present to fully convert the 10 nm Ni layers into NiSi in both cases. Assuming no loss of dopant during the activation anneal, B and P concentrations in Si are 2.2 and 5.6 at.% respectively, calculated using the as-implanted projected range. These value overestimate the actual concentration by neglecting the redistribution occurring upon the activation anneal.

F, Si, and N were implanted at 2 keV using a commercial implanter with SOI wafers tilted by 7°. F was implanted to doses of 3×10^{14}, 1×10^{15}, and 3×10^{15} at. cm^{-2}, while doses of 1×10^{15} and 5×10^{15} at. cm^{-2} were used for Si and N. No activation annealing followed the implantations; the subsequent Ni depositions therefore took place on partially amorphized Si(001) surfaces. The F, Si, and N projected ranges – calculated using TRIM – are 5, 3, and 6 nm, respectively. These depth values are smaller than what is required to fully convert 10 nm Ni layers into δ-Ni_2Si, even if taking into account that the straggle values are about half of the projected range. Still, while all the implanted Si is likely to be consumed before the formation of θ-Ni_2Si, some of it should still be present when δ-Ni_2Si starts to form. For the *in situ* stress investigation, a separate set of 4-inch 250 μm-thick bulk Si(001) wafers were implanted with fluorine using the same parameters as indicated above. Table 6-1 summarizes the doses and the concentrations corresponding to each implantation.

6.2.2 Metal and alloy deposition

Prior to Ni deposition, the wafers were etched for 55 s in dilute (10%) HF, blown dried with high-purity N_2 and immediately loaded in one of two sputter deposition systems. The targets were 99.999% pure Ni, Co, and Pt. Pure Ni layers were deposited in a MRC-643 sputter deposition tool under 10 mTorr of high-purity Ar after reaching a base pressure of 2×10^{-7} Torr. The Ni-alloy layers (5, 10, and 15 at.% Pt or Co) were

deposited in a custom-built ultra-high vacuum magnetron sputtering system under similar conditions. For the F-, N- and Si- implanted substrates, the deposition of pure Ni layers was followed by a 15 nm TiN capping layer. The cap was sputtered without breaking the vacuum from a 99.999% pure Ti target with a N_2 plasma. To avoid the effect of the cap layer on overall measured stress, the TiN deposition was omitted for samples used in the stress study. All samples were cleaved into ~1×1 cm^2 dices for the *in situ* X R D experiments.

/

Table 6-1: Implanted concentrations as a function of dose determined using the implantation range simulated with TRIM® and assuming a Si density of 4.99_10^{22} at. cm^{-3}

Implanted species	Depth (nm)	Dose (at. cm^{-2})	Concentration (at.%)
N	6	1_10^{15}	3.3
		5_10^{15}	16.7
Si	3.5	1_10^{15}	5.7
		5_10^{15}	28.5
F	5	3_10^{14}	1.2
		1_10^{15}	4.0
		3_10^{15}	12

6.2.3 *In situ* XRD during annealing

Ni-Si reactions were monitored *in situ* during ramp anneals in a purified He atmosphere using time-resolved XRD, diffuse light scattering, and resistance measurements. The three simultaneous measurements were performed at the X20C beamline of the National Synchrotron Light Source (NSLS) at Brookhaven National Laboratory. As-deposited samples were introduced in a vacuum chamber with rapid

thermal annealing capabilities. To minimize the contamination from oxygen, the chamber was evacuated twice to 5×10^{-6} Torr (7×10^{-4} Pa), back-filling each time with purified He. Anneals were performed under a steady flow of 1 L/min of purified He at 1 atm. Samples were annealed using linear temperature ramps from 100 to 950 °C at 0.3 to 3 °C s^{-1} as well as isothermal anneals in which the dwell temperature was reached with a 30 °C s^{-1} ramp starting at 100 °C. The substrate temperature was measured with a thermocouple calibrated to better than ±3 °C using the Si-Au, Si-Al, and Si-Ag eutectic melting points. A W-Si multilayer monochromator provided an energy resolution of 1.5% at 6.9 keV ($\lambda = 0.1797$ nm) with a typical intensity at the sample of 3×10^{13} photons s^{-1}. The incident x-rays illuminated a sample area of 1×2 mm^2 typically sampling millions of grains. Each diffraction curve was collected with an acquisition time ranging from 0.5 to 2 s per frame using a position-sensitive detector covering a 2θ range of 14°. Unless otherwise specified, the x-ray beam was incident at an angle of 27.5° from the plane of the sample and the detector was centered at $2\theta = 55°$.

In situ light-scattering measurements [147] were carried out using a He-Ne laser light (λ=633 nm) at an incidence angle of 65° with respect to the surface normal. Two separate detectors collected the scattered radiation at angles of -20 and 52°, providing information on changes in surface roughness for in-plane correlation lengths of 0.5 and 5 μm, respectively. Changes in sample resistance during annealing were measured in situ using standard non-colinear four-point probe in a square geometry. The indexation of the XRD peaks of the crystalline phases Ni, $Ni_{31}Si_{12}$, δ-Ni_2Si, θ-Ni_2Si, Ni_3Si_2, NiSi, and Si was done using JCPDS datasheets No. 04-0850,71-0638, 72-2092, 73-2093, 17-0881, 38.0844, 43-0989 and 05-0565 respectively.

6.2.4 *Ex situ* analyses

Cross-sectional transmission electron microscopy (XTEM) images were recorded on a JEOL-2100F microscope at an acceleration voltage of 200 kV. Unless specified otherwise, bright-field images were recorded with the [110] zone axis of the Si substrate parallel to the electron beam, so that thicknesses can be directly measured on the micrographs. Cross-sectional samples were prepared by standard mechanical boring, slicing, and polishing down to 10 μm. Further thinning down to electron transparency was performed in a Gatan Precision Ion Polishing System (PIPS) using Ar^+ at an energy of 5 keV and at an incidence angle of 4°. Two final rounds of 5 minutes at 3 keV and 2.5keV were used to clear as much ion damage as possible. Samples were always glued to the PIPS Cu sample holder using heat-conducting wax to insure adequate heat dissipation. In ion milling test experiments using indium pellets, no evidence of melting was observed, so it is assumed that the sample temperature remained below 160 °C during the ion milling process.

In situ stress measurements were performed during ramp anneals at 0.3 °C s^{-1} from 20 to 600 °C on 100 nm Ni films deposited on 100-mm in diameter, 250-μm-thick complete wafers using a Flexus furnace. The bending force were calculated from the measured radius of curvature using Stoney's equation.[159]

Qualitative fluorine depth distribution profiles in as-deposited and reacted layers were determined with an IONTOF GmbH SIMS^4 TOF-SIMS using a bunch-mode operated 15 keV Ga^+ (primary analysis) and a Cs^+ (depth profiling) ion beams. The profiles depth scales were calibrated by measuring the craters left by the etching process using a Veeco Dektak 3030ST stylus profilometry tool.

6.3 Results

6.3.1 A. Effect of alloying

The effect of Pt alloying on the Ni-Si reaction is shown in Figure 6.1, where *in situ* XRD and resistance data from samples with 0, 5, 10 and 15 at.% Pt are compared. The resistances traces in Figure 6.1 (e) have been normalized to the maximum value reached during the formation of the Ni-rich compounds. The data reveal that adding Pt to Ni delays both the consumption of the metal layer and the growth of δ-Ni_2Si. We note that the intensities of X-ray peaks corresponding to θ-Ni_2Si and δ-Ni_2Si decrease with increasing Pt content. Figure 6.1 also shows that Pt alloying drastically accelerates the formation of NiSi as indicated by (i) a slight decrease in nucleation temperature (marked by the sharp drop in resistance above 300 °C), and (ii) a significant reduction of the temperature for the complete disappearance of δ-Ni_2Si from 550 °C, for pure Ni, to less than 350 °C in samples with 15 at.% Pt, as seen in both XRD and resistance data. The reason why the resistance is minimal in the 350-500 °C temperature range for the pure Ni even though some δ-Ni_2Si is clearly present remains unclear. One possible explanation could be that the NiSi layer has a lower resistance in this case than in Pt-containing samples.

We also observe that the thermal degradation temperature, characterized by the sudden increase in resistance above 600 °C, is dramatically increased with the addition of Pt.This known effect has been explained by a combination of two factors. First the nucleation of the δ-$NiSi_2$ compound is delayed by the mixing entropy effect[105]; PtSi is homostructural and fully miscible with NiSi, while there is no $PtSi_2$ compound to match with $NiSi_2$. Secondly, Pt alloying was shown by Detavernier *et al.*[119] to influence the NiSi film texture so as to delay its agglomeration, another important thermal degradation mechanism.[5]

The effect of Co alloying on the Ni-Si reaction is shown in Figure 6.2. Similarly to the Pt case, the consumption of the metal layer is delayed by the addition of Co (by more 50 °C during 3 °C s^{-1} ramps for the 15 at.% Co sample). However, the delay in the growth of δ-Ni_2Si and θ-Ni_2Si, is not as marked as for Pt additions. The decrease/re-increase cycle in the intensity of the δ-Ni_2Si (013) and (020) peaks fades away in the 15 at.% Co sample, clearly linking this behavior to the presence of the θ-Ni_2Si compound, which does not seem to form in these conditions. The splitting of the XRD peak at $2\theta = 58°$ into two separate peaks above 350 °C suggests a rapid texture reorganization of the δ-$(Ni,Co)_2Si$ or the precipitation of Co_2Si.

Although CoSi and NiSi have dissimilar crystal structures, the formation of the monosilicide phase is not significantly delayed by Co alloying but the associated resistance drop is sharper. The phase separation of Co_2Si suggested above could therefore be the result of the rapid formation of the NiSi requiring Co atoms to be expelled.

The resistance data of Figure 6.2 (e) also highlight the stabilizing effect of Co on the disilicide phase as its formation temperature drops to 620, 550, and 480 °C with respectively 5, 10, and 15 at.% Co. D'Heurle *et al.*[104] reported that the nucleation of the disilicide occurred at the free surface of the monosilicide during reactions of Ni(5 at.% Co) with Si substrates. If such a phenomenon were occurring in our samples, strong $NiSi_2$ diffraction peaks would have been expected since the compound would not be epitaxial with the Si(001) substrate. The different behaviors may simply be related to the different annealing conditions used in both experiments: d'Heurle carried out longer (1h) isothermal anneals whereas we used relatively rapid ramp anneals in the present case. Another possible reason for the observed discrepancy is that we are using much thinner Ni film than in previous experiments. The stress relaxation arguments invoked by d'Heurle may not be applicable in our case.

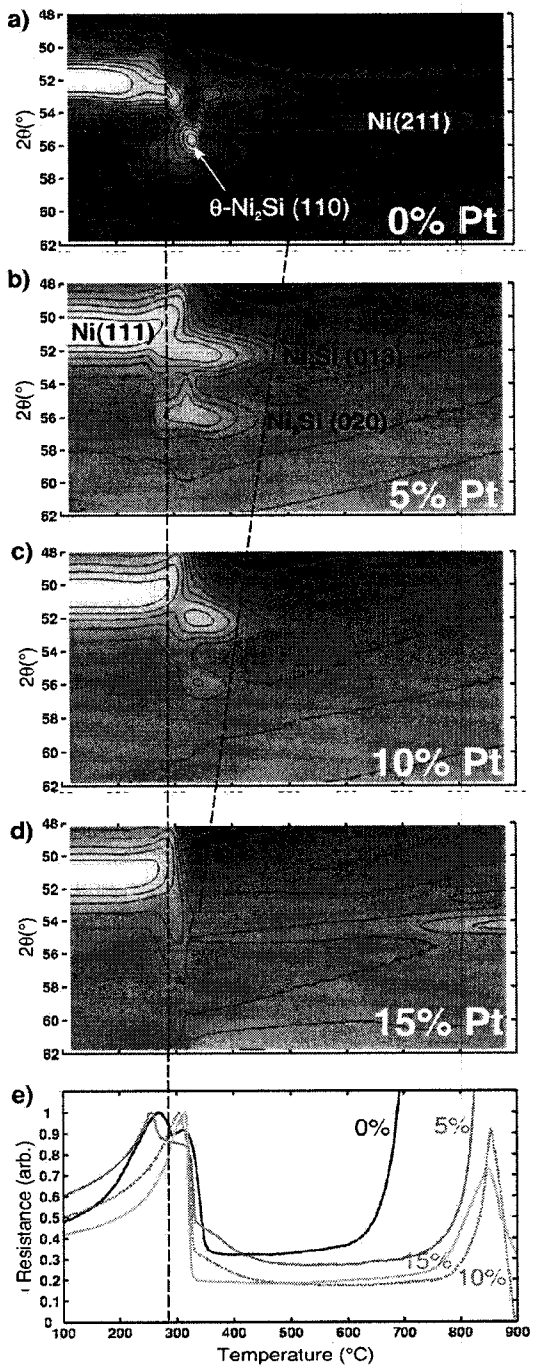

Figure 6.1: a)-d) XRD intensity contour maps ($\lambda = 0.1797$ nm) plotted as a function of annealing temperature T_a during thermal ramps at 3 °C s^{-1} in purified He for 10-nm-thick Ni(Pt)-Alloy layers deposited on c-Si(001) with Pt content ranging from 0 to 15 %. e) Corresponding *in situ* resistance data normalized to the maximum value reached during Ni-rich silicide formation.

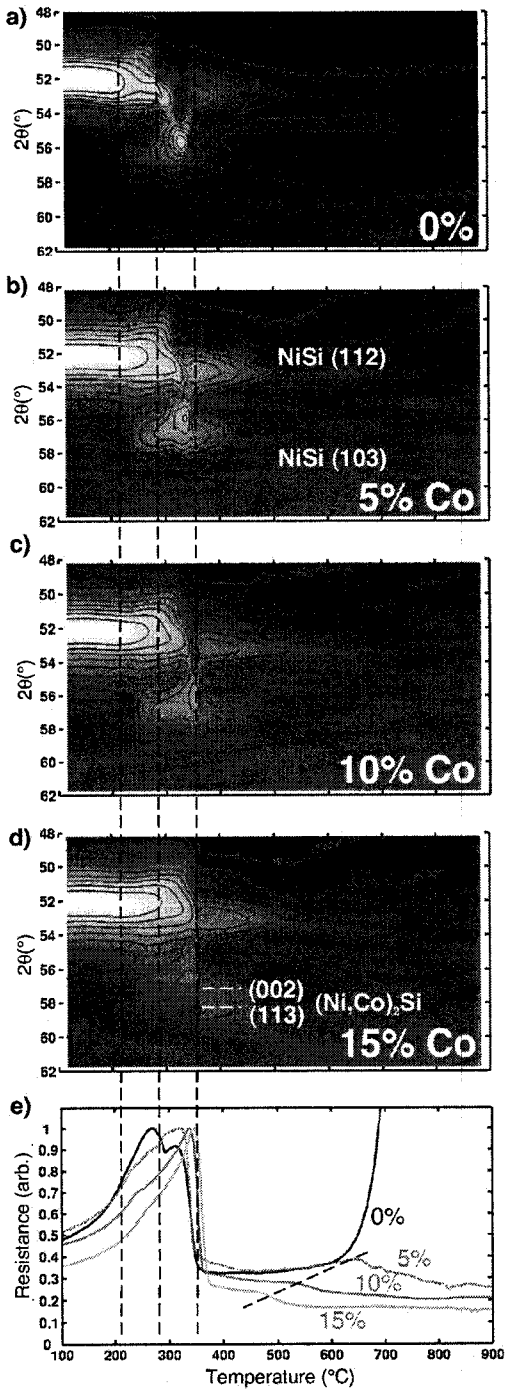

Figure 6.2: a)-d) XRD intensity contour maps ($\lambda = 0.1797$ nm) plotted as a function of annealing temperature T_a during thermal ramps at 3 °C s^{-1} in purified He for 10-nm-thick Ni(Co)-Alloy layers deposited on c-Si(001) with Co content ranging from 0 to 15%. e) Corresponding *in situ* resistance data normalized to the maximum value reached during Ni-rich silicide formation.

6.3.2 Effect of CMOS dopants

Silicides are used as zero-level contact materials in CMOS circuits: the Ni-Si solid-state reaction thus occurs in areas where the Si is usually doped with boron, phosphorus, or arsenic. The effects of B- and P- doping on the *in situ* XRD, resistance, and light scattering signals are presented in Figure 6.3. Resistance traces are normalized to their values at the beginning of the reaction as the resistivity of the initial metal layers should be the same for all samples. Figure 6.3 (a-c) indicate that the overall reaction scheme is not dramatically affected by B- and P- doping at these concentrations even though compound formation appears delayed. This delay affects all the compounds, θ-Ni_2Si and NiSi more than δ-Ni_2Si, and is larger with P than with B. As far as our study is concerned, a very interesting result is that the formation of θ-Ni_2Si, while delayed, is not suppressed by typical CMOS dopants for doses typically used in the microelectronics industry. The XRD data in Figure 6.3 (a-c) also indicate that the temperature for the disappearance of δ-Ni_2Si decreases from 550 ° for pure Ni to 450 °C in P-doped samples. This result confirms the observations of Rinderknecht *et al.*,[138] who noted that the completion of the NiSi formation occurred earlier with high-dose P implantation.[1]

The light scattering (LS) signal clearly demonstrates, in agreement with previous reports, that doping increases the temperature for the thermal degradation of NiS, which causes the scattered intensity to increase dramatically at high temperature.[138,181,144] The peak visible near 400 °C, especially for the doped samples, coincides with the sharp drop in resistance associated with both the disappearance of θ-Ni_2Si and the formation of NiSi. This peak is sharper and stronger in the P-doped LS sample, which correlates with the

[1] Care should be exercised in comparing our results with those of Rinderknecht *et al.* as they deposited the Ni layers at a substrate temperature of 150°C, while ours were deposited at room temperature. Also, it is not clear from the experimental details of their study whether the implanted substrates underwent an activation anneal or not.

higher temperature where the δ-Ni_2Si peaks return following the consumption of the θ-Ni_2Si compound.

In order to investigate the microstructure of the P-doped sample when the θ-Ni_2Si compound is present, we have carried out an isothermal anneal at 260 °C. The XRD contour plot in Figure 6.4 (a) shows the evolution of the XRD data until the sample was quenched immediately after the θ-Ni_2Si (110) peak reached its maximum intensity (43 min). Figure 6.4 (b) is a XTEM micrograph of that quenched sample while Figure 6.4 (c-d) are convergent beam electron diffraction (CBED) patterns acquired on the two grains identified in Figure 6.4 (b). Similarly what was observed in undoped samples in Chapter 5, the CBED pattern demonstrates that δ-Ni_2Si is present in the top layer while NiSi is in the bottom one. We have been unable, however, to observe θ-Ni_2Si grains in this sample even though post-anneal XRD scans confirm that this compound is still present after complete cool-down. Given the uniformity of the diffraction contrast in the interfacial layer and the very similar results in Chapter 5, we can only assume that θ-Ni_2Si must lie in the top layer of the sample.[1]

[1] The very similar microstructures observed for the B-doped sample (Figure 6.4) and for the undoped reference in Chapter 5 reveal that non-negligible heating occurs during TEM specimen preparation despite our best efforts to minimize those effects as explained earlier. Indeed, according to their respective in situ XRD data, the reaction was not stopped at the same stage in the two samples, the B-doped sample being quenched slightly later than the maximum of the θ-Ni_2Si. Yet, both samples yield the same microstructure. This links the presence of an apparently dominant NiSi interlayer to a later stage of the reaction than what is suggested by the XRD data. We therefore cannot rule out the possibility that θ-Ni2Si may form as a continuous layer at the δ-Ni_2Si/Si interface at a slightly earlier stage of the reaction. An uncontrolled over-reaction or heating during TEM sample preparation could have prevented us from accurately reaching this point.

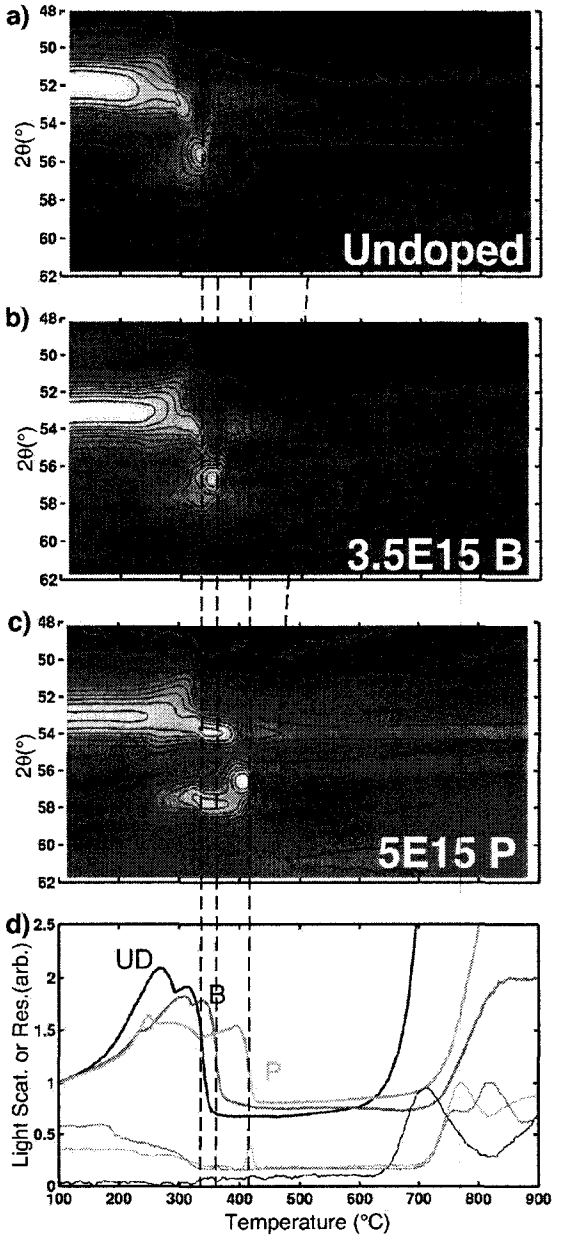

Figure 6.3: XRD intensity contour maps ($\lambda = 0.1797$ nm) plotted as a function of annealing temperature T_a during thermal ramps at 3 °C s^{-1} in purified He for 10-nm-thick Ni layers deposited on a) undoped b) B-doped and c) P-doped c-Si(001) d) Corresponding *in situ* resistance (thick lines) and light scattering data (thin lines) . Resistance is normalized to the value at the beginning of the reaction.

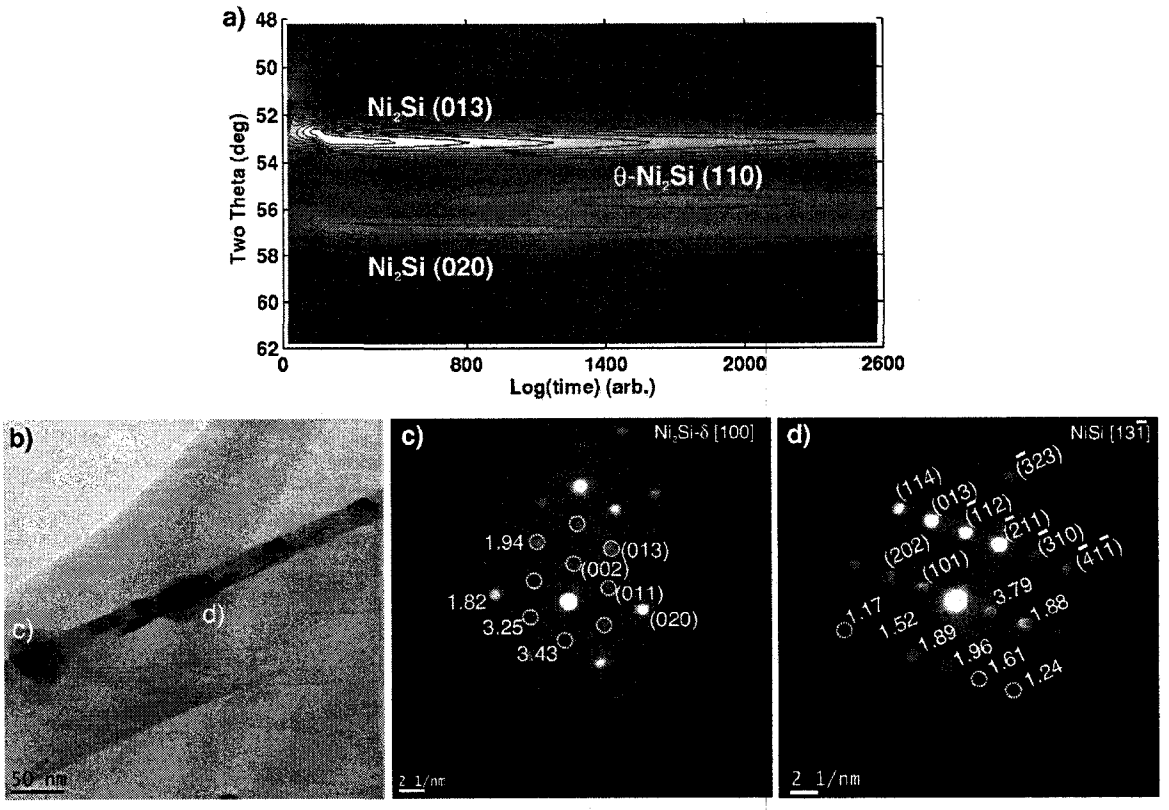

Figure 6.4: a) XRD intensity contour map (λ = 0.1797 nm) plotted as a function of annealing time during the 43min isothermal annealing at 260°C in purified He of a 10-nm-thick Ni layer deposited on B-doped c-Si(001) b) Bright-field TEM Cross-sectional micrograph of the sample annealed in a) with c) and d) convergent beam electron diffraction (CBED) patterns acquired from regions labeled in b).

6.3.3 Effect of F, Si and N implantation

Fluorine, originating from BF_2^+ molecular ions used as B implantation vectors, is often present in CMOS circuits. The effects of F-implantation at doses of 3×10^{14}, 1×10^{15}, and 3×10^{15} cm^{-2} on the *in situ* XRD, resistance, and light scattering signals are presented in Figure 6.5. Resistance traces are normalized to their values at the beginning of the reaction. Three major effects are easily observed with increasing F dose: *i)* θ-Ni_2Si is present over a wider temperature range and the monosilicide forms at higher temperature,

ii) the morphological stability of the monosilicide film is improved, and *iii)* the disilicide phase forms at higher temperature. Focusing on the low-temperature part of the reaction, we find that F stabilizes θ-Ni_2Si, as it delay its consumption by about 50 °C during a 3 °C s^{-1} ramp. The formation is also slightly delayed but to a much lesser extent. The growth of NiSi is pushed to higher temperature, linking again this event to the consumption of θ-Ni_2Si. We find no clear evidence that the formation of the δ-Ni_2Si is delayed, however, as in the B and P-doping cases, the return of that compound upon consumption of the θ-Ni_2Si is gradually suppressed by an increasing F dose. A slightly decreasing plateau between 350 and 400 °C in the 3×10^{15} cm^{-2} resistance trace suggests that θ-Ni_2Si has a resistivity that is between those of δ-Ni_2Si and NiSi, but also that further growth is occuring. Also, while the 3×10^{14} at. cm^{-2} F dose results in a significantly lower resistance in the temperature range below 400 °C compared to the undoped case, an increasing F dose raises the resistance trace towards the level obtained with undoped samples.

In order to investigate the microstructure prevailing in F-implanted samples, two specimens were prepared for XTEM investigation. Figure 6.6 compares the micrographs of samples with Ni layers as they were deposited on a substrate implanted with 3×10^{15} cm^{-2} F (Figure 6.6 (a)) and on undoped Si (Figure 6.6 (b)). Magnifications were calibrated using the inter-atomic spacing of pristine Si measured in high-resolution lattice-images. In the F-implanted sample, we observe two ~ 4.0 nm thick layers with a uniform contrast at the interface with the substrate. Comparing this microstructure with that of the undoped sample (Figure 6.6 (b)) indicates that the darker of the two layers is present at the interface of all Ni films regardless of the substrate, most likely as a consequence of intermixing at the interface during the metal deposition. The brightest layer is believed to consist of amorphized Si produced by the implantation process. As expected, the measured depth of this layer is slightly larger than the implantation range calculated using TRIM.

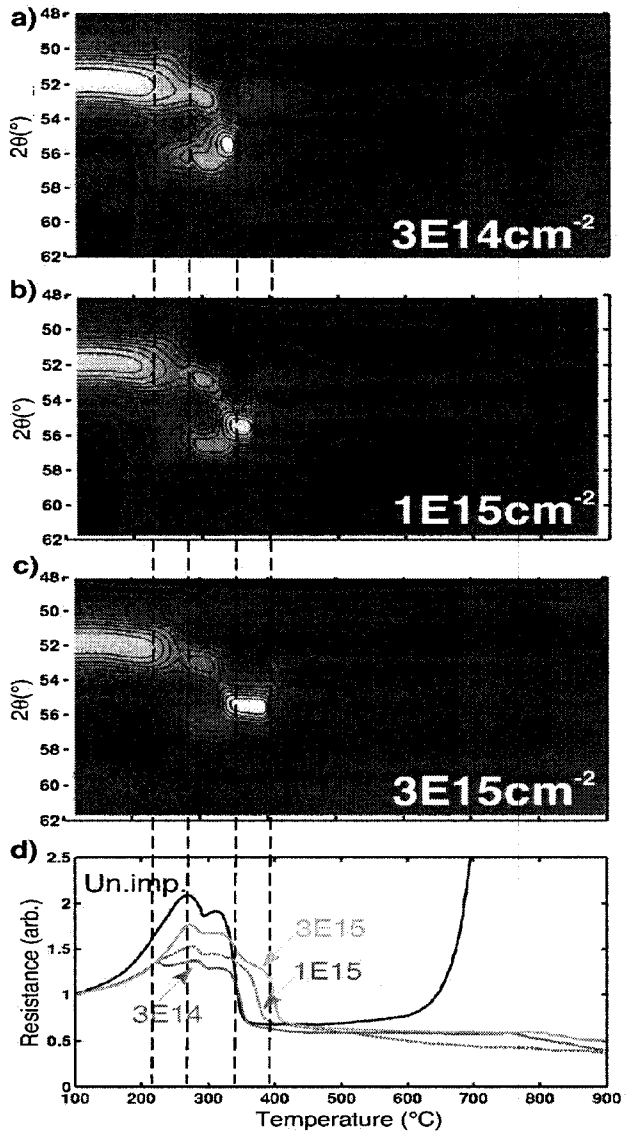

Figure 6.5: a)-c) XRD intensity contour maps ($\lambda = 0.1797$ nm) plotted as a function of annealing temperature T_a during thermal ramps at 3 °C s^{-1} in purified He for 10-nm-thick Ni layers deposited on c-Si(001) implanted with F at doses ranging from $3 \cdot 10^{14}$ to $3 \cdot 10^{15}$ at cm^{-2} d) Corresponding *in situ* resistance including the data for undoped Si. Resistance is normalized to the value at the beginning of the reaction.

The micrograph of Figure 6.6 (c) was acquired on a F-doped sample annealed at 3 °C s^{-1} and quenched at 380 °C, a condition that corresponds to the maximum intensity of the θ-

$Ni_2Si(110)$ peak in Figure 6.5 (c).[1] A CBED pattern obtained from the region identified by the white circle in Figure 6.5 (c), and indexed as θ-Ni_2Si, is displayed in Figure 6.6 (d). Since no δ-Ni_2Si is expected based on the *in situ* XRD data, we conclude that the thick top layer is comprised of a majority of θ-Ni_2Si grains.

Figure 6.6 (c) also highlights the presence of a thin interfacial layer that is not detected in our XRD geometry and that could not be sampled by CBED given its very small thickness. Pole figure experiments (not shown) have revealed the presence of diffraction features corresponding to a highly textured layer (close to an epitaxial layer) in a similar sample. The nature of the diffraction contrast in Figure 6.6 (c) suggests a thin interfacial layer with small grains at the quench temperature. The observed small grains could either represent the structure of this textured interlayer or simply the morphology of early NiSi formation.

Based on *in situ* curvature measurements, we have proposed in Chapter 5 that stress could be a driving force for the consumption of θ-Ni_2Si. Similar experiments were conducted on F-implanted samples coated with 10 nm Ni layers. The resulting bending force curves acquired during 0.3 °C s^{-1} ramps, as well as the corresponding XRD contour plots, are presented in Figure 6.7 for undoped as well as F-implanted samples. Each stress trace is the average of three measurements; it was set at zero force above 450 °C where relaxation mechanisms are known to be effective (See chapter 5).

[1] This micrograph was taken in an area of the specimen where the TiN capping layer has been etched off during the preparation process.

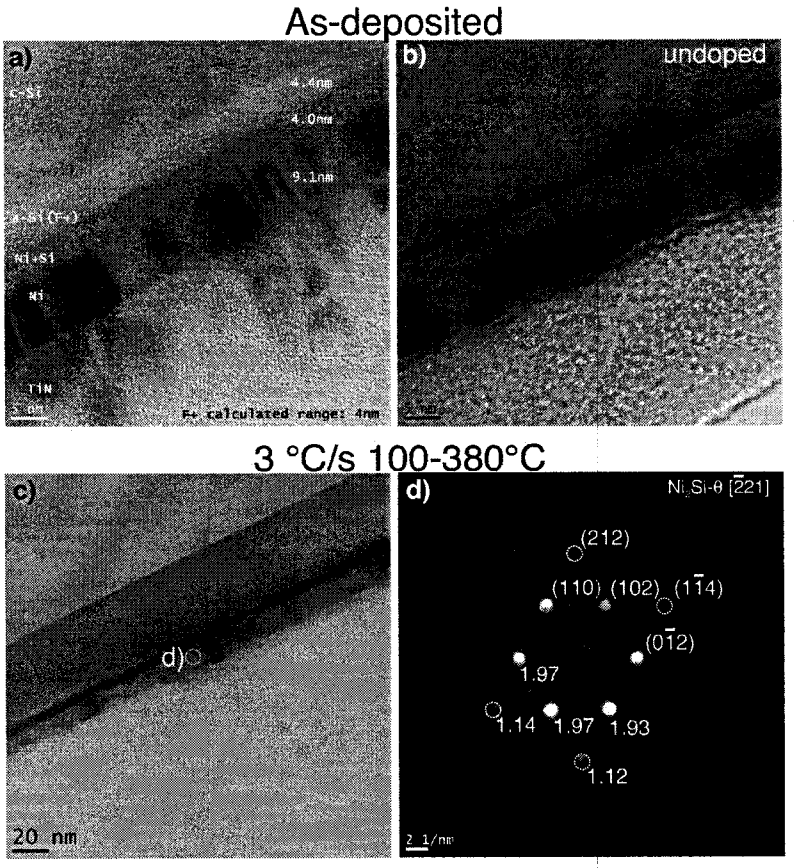

Figure 6.6: Bright-field TEM cross-sectional micrographs of a) 10 nm Ni with a20 nm TiN cap as deposited on F-implanted SOI ($3 \cdot 10^{15}$ cm^{-2}), and b) 10 nm Ni as deposited on undoped SOI, as well as c) 10 nm Ni with a 20 nm TiN cap on F-implanted SOI ($3 \cdot 10^{15}$ cm^{-2}) after a thermal ramp at 3 °C s^{-1} in purified He quenched at 380°C. d) CBED pattern acquired from the region labeled in c).

The samples used for the *in situ* XRD experiment were capped with TiN while those used for the stress measurement were not. The bending force curves must be analyzed with caution and any attempt to quantify the behavior would be risky. Still, we can clearly see that the peak near 300 °C shifts to higher temperatures and is gradually suppressed by an increasing F dose. In the undoped sample, this peak correlates with the return of δ-Ni_2Si and the simultaneous formation of NiSi. The stress evolution during the beginning of the reaction is unaffected by F implantation, indicating that the apparent delay in the formation of δ-Ni_2Si is an artifact of the XRD intensity scale.

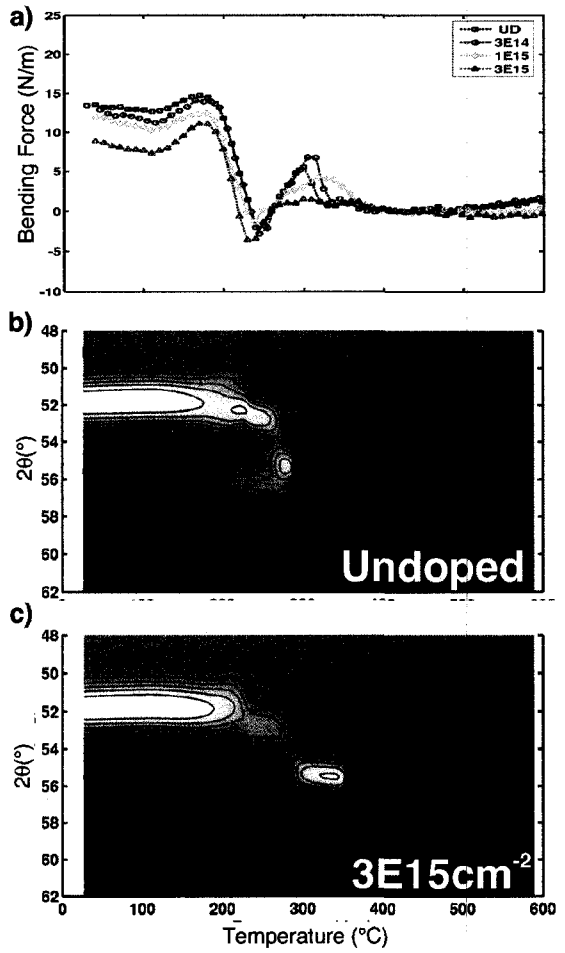

Figure 6.7: a) *in situ* bending force plotted as a function of annealing temperature T_a during thermal ramps at 0.3 °C s^{-1} in purified He for 10-nm-thick Ni layers deposited on c-Si(001) implanted with F doses ranging from $3{\bullet}10^{14}$ to $3{\bullet}10^{15}$ at cm^{-2} b) and c) corresponding *in situ* XRD intensity contour maps (λ = 0.1797 nm) for the un-implanted and $3{\bullet}10^{15}$ cm^{-2} F-dose cases.

SIMS depth profiles (Figure 6.8) were acquired from samples implanted with $3{\times}10^{15}$ F cm^{-2} at three different stages of the reaction: as-deposited, annealed and quenched at 330 °C (corresponding to the maximum intensity of in θ-Ni_2Si), as well as at 600 °C (fully grown NiSi). We show the profiles for both SiF^+ and F^+ species as they respectively yield the largest signal-to-noise ratio and represent the actual species we are interested in. Both species produce the same profiles, indicating that SiF^+ ions are good

markers of the F distribution. The peak in the as-deposited sample is located at ~10 nm from the sample surface, which is 5 nm less than values determined from TRIM calculations and XTEM measurements. We attribute this discrepancy to the difficulties in obtaining an accurate depth calibration in SIMS measurements, especially since the oxidized surface could have been etched at a different rate. Nevertheless, the increase in relative signal intensity between 2 and 8 nm for the sample annealed at 330 °C supports the hypothesis that a notable F redistribution occurs in the growing silicide layers. However, the peak around 15 nm in the same curve also indicates a significant plowing of F atoms and their accumulation at the silicide/Si interface. The SIMS data for the sample annealed at 600 °C is more uniform, indicating extensive fluorine redistribution across the sample's thickness.[1]

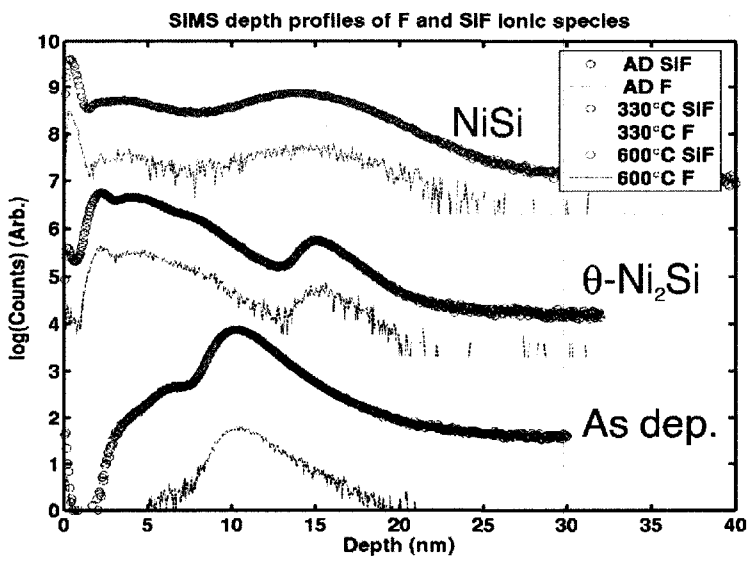

Figure 6.8: SIMS depth profiles of ionic species F^+ and SiF^+ in samples with 10nm Ni on c-Si(001) implanted with $3 \cdot 10^{15}$ F cm^{-2} after deposition - ● -, after thermal ramps at 3 °C s^{-1} in purified He quenched at 330 °C (θ-Ni_2Si) - ● - and 600 °C (NiSi) - ● - .

[1] It is not clear if the peak found at the very surface of the 600 °C sample indicates surface segregation and possible loss of F to the ambient as the signal from the surface regions of SIMS profiles are biased by the evolution of the sputtering yields.

While the behavior described above could be associated with the chemistry of F atoms, it is possible that some of the features could be related to the presence of the amorphous layer formed during the implantation. Samples were thus implanted with Si and N in order to verify if the resulting defects and partial amorphization could lead to similar signatures. Figure 6.9 and Figure 6.10 present the compound formation results for Si and N-implanted samples, respectively. Similarly to the case of fluorine discussed above, we note a stabilization of θ-Ni_2Si, albeit to a lesser extent with both Si and N.

Figure 6.9 (b) suggests that high-dose Si and F implantations have surprisingly similar effects. However, the resistance traces in Figure 6.9 (c) do not show the plateau that accompanied the presence of θ-Ni_2Si in F-implanted samples. Furthermore, a careful examination reveals that the increase in the θ-Ni_2Si (110) peak intensity between 310 and 380°C is not as gradual as for F-implanted sampled, which could explain the different resistance traces. Figure 6.10 also reveals that N-implantation slows down the reaction between Ni and Si, a result that is in agreement with the findings of Scott *et al.*[123,127] Still, even though the delay in Ni consumption increases with the implanted dose, the reaction is not suppressed and the low-resistivity NiSi forms, even for the largest dose of 5×10^{15} cm^{-2}. In contrast, in the sample with the largest dose, the formation of δ-Ni_2Si and θ-Ni_2Si appears to be totally suppressed. We also note for 1×10^{15} N cm^{-2} that despite a low diffracted intensity and a rather broad diffraction peak (indicating smaller/thinner grains), the temperature range over which the θ-Ni_2Si compound forms is extended with respect to the un-implanted case.

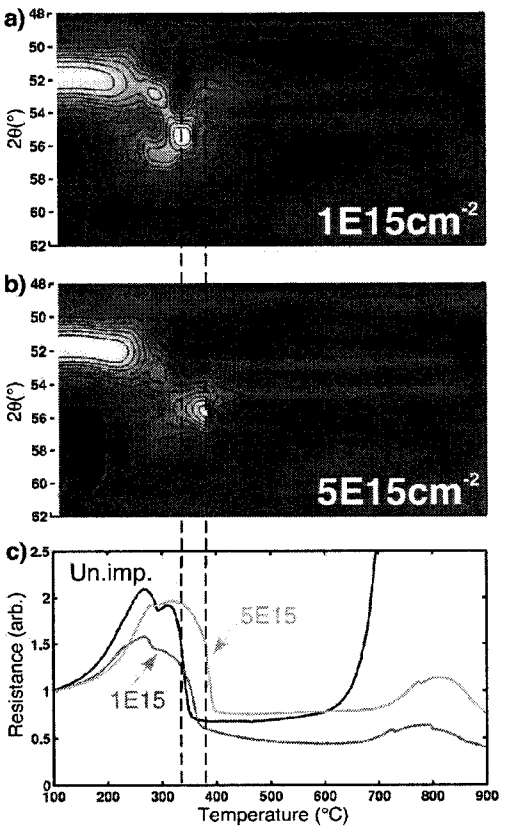

Figure 6.9: XRD intensity contour maps (λ = 0.1797 nm) plotted as a function of annealing temperature T_a during thermal ramps at 3 °C s^{-1} in purified He for 10-nm-thick Ni layers deposited on c-Si(001) implanted with Si at doses of $1 \cdot 10^{15}$ and $5 \cdot 10^{15}$ d) Corresponding *in situ* resistance data. Resistance is normalized to the value at the beginning of the reaction.

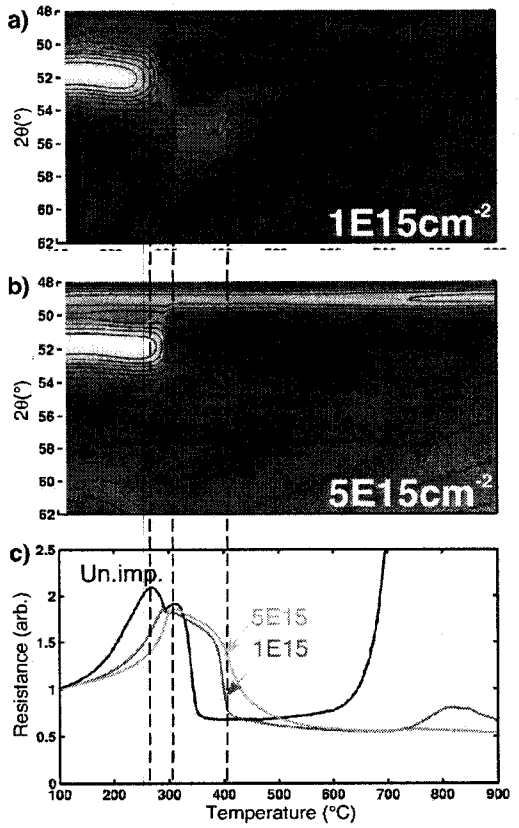

Figure 6.10: XRD intensity contour maps (λ = 0.1797 nm) plotted as a function of annealing temperature T_a during thermal ramps at 3 °C s^{-1} in purified He for 10-nm-thick Ni layers deposited on c-Si(001) implanted with N at doses of $1 \cdot 10^{15}$ and $5 \cdot 10^{15}$ d) Corresponding *in situ* resistance data. Resistance is normalized to the value at the beginning of the reaction.

6.3.4 Formation on amorphous Si substrates

As a final verification of the origin of the F-implantation effect, we have studied the reaction of a 10 nm Ni layer deposited on a-Si, which is presented in Figure 6.11. We again note the prevalence of the θ-Ni_2Si (110) peak in the low temperature part of the reaction. The resistance trace exhibits a slowly decreasing plateau similarly to the F-implanted case. Figure 6.11 (b) also suggests that the formation of $NiSi_2$ is accelerated, as evidenced by the emergence of the $NiSi_2$ (220) peak near 600 °C. Since the $NiSi_2$ and Si (220) reflections are just 0.1° apart, we cannot rule out that the intensity increase could be the result of metal-induced crystallization of the a-Si. Still, the first increase in diffracted intensity around $2\theta = 55°$ at 400 °C is most likely due to the formation of the NiSi.

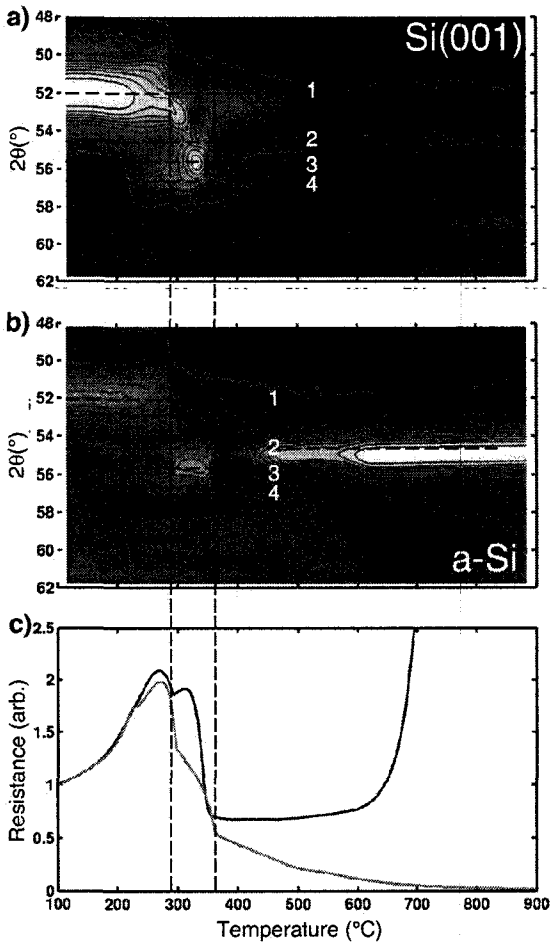

Figure 6.11: XRD intensity contour maps ($\lambda = 0.1797$ nm) plotted as a function of annealing temperature T_a during thermal ramps at 3 °C s^{-1} in purified He for 10-nm-thick Ni layers deposited on a) c-Si(001) and b) a-Si. c) Corresponding *in situ* resistance data. Resistance is normalized to the value at the beginning of the reaction.

6.4 Discussion

6.4.1 Effect of alloying impurities

We have shown in Chapter 5 that the formation of the metastable hexagonal θ-Ni_2Si compound is possible because little atomic motion is required for the transformation to occur from δ-Ni_2Si. In other words, we proposed that this transformation corresponds to a lower activation energy pathway compared to the formation of the thermodynamically stable compounds Ni_3Si_2 and NiSi, which are not yet able to nucleate possibly because of strong concentration gradients at the interface. This hypothesis is supported by the work of d'Heurle who estimated that the formation of NiSi from the reaction of δ-Ni_2Si and Si is at the limit of being limited by the nucleation.[11]

Studying the effect of Pt and Co enables us to verify whether the formation of θ-Ni_2Si would be suppressed (promoted) by impurities that could improve (worsen) the stability of NiSi with respect to Ni_2Si, should nucleation play a decisive role in the formation of NiSi. While the results with Pt suggest that stabilizing NiSi compromises the θ-Ni_2Si formation, our results with Co strongly suggest that impurity solubility also plays a key role in influencing θ-Ni_2Si formation. Co additions in excess of 10 at.% lead to a suppression of θ-Ni_2Si whereas its growth should be favored if NiSi nucleation were effectively compromised by the alloying. Also, the differences in lattice parameters between the completely miscible Co_2Si and Ni_2Si compounds being at less than 2%, the presence of Co should not prevent δ-Ni_2Si from promoting the nucleation of θ-Ni_2Si through the templating mechanism described in Chapter 5. We thus reach the conclusion that Co has little solubility in θ-Ni_2Si, which eventually leads to an increased nucleation barrier for its formation.

This result is particularly interesting because, based on the similarities between the crystal structures of Co_2Si, δ-Ni_2Si and θ-Ni_2Si[51], we were anticipating an extended Co solubility in the latter and potentially a stabilizing effect. Indeed, the Co-Si equilibrium phase diagram shows a β-Co_2Si phase that lies in a portion of the diagram that is qualitatively similar to that in the corresponding Ni-Si diagram (see Figure 1.4 and Figure 1.8 for the Co-Si and Ni-Si equlibrium phase diagrams). The main difference is that the eutectoid decomposition of θ-Ni_2Si results in δ-Ni_2Si and ε-Ni_3Si_2 while that of β-Co_2Si leads to Co_2Si and CoSi, the latter of which is structurally dissimilar from NiSi. Despite these similarities, our experimental results suggest that the crystal structure of β-Co_2Si is much different than that of θ-Ni_2Si (there is no report of the crystal structure of β-Co_2Si in the literature).

Since the Pt_2Si and δ-Ni_2Si structures are very different we expect the Pt solubility in δ-Ni_2Si and in θ-Ni_2Si to be limited.[117,182] This should limit the variations in the δ-Ni_2Si lattice parameters with Pt addition and thus the effect on the texture inheritance-driven transformation. Our experimental results therefore lead us to believe that the formation of θ-Ni_2Si is hindered by a combined effect of a low solubility of the alloying impurity in the compound and by an enhanced NiSi nucleation. Our results suggest that the formation pathway, and possibly the composition of the hexagonal θ-Ni_2Si as we observe it, differ from those reported by Föll *et al.*[50], d'Heurle *et al*[51]., and Dai *et al.*[121] In the latter cases, the hexagonal phase was forming as a simple deformation of the NiSi MnP structure which is stabilized by Pt in its epitaxial relationship with Si(111). We clearly see no stabilizing effect of Pt in our experiments.

6.4.2 Effect of CMOS doping impurities and microstructure

The addition of B or P results in an overall delay of the reaction scheme observed in undoped samples. The light scattering data exhibit a sharp peak near 400 °C which coincides with a rapid decrease in film resistance. It is not possible to conclude *a priori* from the light scattering data whether this peak corresponds to events occurring at the surface or at the interface of the layer stacks, since both changes in surface roughness and variations of the refractive index on a relatively flat surface can lead to an increased diffuse light scattering signal. Nonetheless, this peak is a definite signature of a two-dimensional transformation process. The correlation length of 5 μm seems incommensurate with the typical 10-30 nm grains we measured in XTEM. Yet, this light scattering feature clearly occurs at the temperature where the θ-Ni_2Si is consumed and where the concurrent re-growth of δ-Ni_2Si and growth of NiSi occur. It could arises from a late stage of the θ-Ni_2Si consumption where few remaining grains are scarcely distributed over the sample's surface with an average inter-grain distance much larger than the grain size itself, which in this case would be of the order of 5um.

6.4.3 Effect of F, Si and N implantations and stress

Comparing the results of F and Si implantation enables us to conclude that F has both chemical and physical effects. While TEM results show that no amorphous layer remains when the growth of θ-Ni_2Si is complete, its presence when θ-Ni_2Si nucleates cannot be excluded. Clevenger *et al.*[52] have shown that amorphous silicide growth could be thermodynamically favored between 350 and 650 K. We hypothesized that that the presence of impurities could increase the temperature below which this remains true. From the thermodynamic point of view, the nucleation of θ-Ni_2Si from an amorphous phase could indeed be favored.

Our results show that an amorphous or amorphized substrate, at least when present in the first stages of the reaction, stabilizes the θ-Ni_2Si.[1] The fact that θ-Ni_2Si forms on amorphous Si substrates confirms that epitaxy is not necessary to stabilize the formation of that compound and that it must form through a different pathway than previously reported.[50,51,121] Our hypothesis that the presence of δ-Ni_2Si promotes the formation of θ-Ni_2Si is supported by our N-implantation study since the intensity of the θ-Ni_2Si(110) peak decreases together with those of δ-Ni_2Si(013) and (020).

The chemical effects of fluorine could originate from changes in interface energies. Our SIMS data are compatible with the findings of Wong *et al.*[177] who suggested that F segregates at the silicide grain-boundaries where it forms strong Si-F and Ni-F bonds, which decrease the inter-grain interface energies. Furthermore, Donthu *et al.*[183] have shown that the grain size of NiSi was reduced when formed on BF_2^+-implanted samples. Assuming the same applies to δ-Ni_2Si with F implantations, a larger number of smaller grains would offer more nucleation sites for θ-Ni_2Si. Also, given the crystal structure of θ-Ni_2Si, which allows for a large number of vacancies, the solubility limit of F could be larger in that compound than in NiSi or δ-Ni_2Si. This, again, would favor its nucleation and growth with respect to the other silicides. While the increase in the F signal in the region closer to the surface in the SIMS profile for the samples annealed at 330 °C is consistent with a larger F solubility in θ-Ni_2Si than in δ-Ni_2Si, the extensive redistribution in NiSi suggests a larger solubility in the latter. Finally, the accumulation of F atoms at the silicide/Si interface could reduce the overall diffusion by sticking to defects, filling grain boundaries, or simply occupying vacancy sites in the hexagonal structure. This would delay the formation of NiSi, which we have shown in Chapter 5 and earlier in this chapter to be the most probable cause of θ-Ni_2Si consumption. All this being said, since F, Si and N were implanted without removing the

[1] We expect at least the grain size and the growth kinetics of the δ-Ni_2Si to be different, which must affect the conditions for the nucleation and growth of θ-Ni_2Si.

native oxide of the Si wafers, we cannot exclude the possibility that O impurities, knocked-in by the implantation, contribute to some extent to the various effects described here.

We reported in Chapter 5 that the maximum intensity of the θ-Ni_2Si(110) XRD peak coincides with a maximum compressive stress in 100 nm Ni samples. Figure 6.7 reveals that in 10 nm samples, θ-Ni_2Si grows after the beginning of stress relaxation. This suggest that the large compressive stress measured for the 100 nm Ni sample arises mostly from volume expansion during the formation of δ-Ni_2Si or from the thermal expansion of Ni. A reasonable explanation for the decreasing tensile peak near 300 °C with increasing F dose could be tied to the corresponding suppression of the δ-Ni_2Si regrowth upon consumption of θ-Ni_2Si. Regardless of the θ-Ni_2Si composition (that we do not know), regrowth of δ-Ni_2Si will result in volume shrinkage.[1] Assuming a θ-Ni_2Si composition at the eutectoid point (39 at.% Si), the formation of NiSi from θ-Ni_2Si involves little volume change. With a decreasing δ-Ni_2Si regrowth upon consumption of θ-Ni_2Si, less volume shrinkage occurs in the layer stack, therefore decreasing the tensile stress build up.

Regardless of the implanted impurity and of its activation state, the suppression of the δ-Ni_2Si regrowth correlates with the increasing temperature at which the consumption of the θ-Ni_2Si occurs. We conclude that higher temperatures most likely favor both the nucleation and rapid growth of NiSi, suppressing the return of δ-Ni_2Si upon consumption of θ-Ni_2Si.

---

[1] The volume per mole of atoms are: δ-Ni_2Si (6.57 cm^3), NiSi (7.26 cm^3), θ-Ni_2Si (ranges from 7.11 cm^3 @ 37.5 at.% Si to 7.59 cm^3 @ 41 at.% Si).

6.5 Conclusion

The formation of the θ-Ni_2Si is strongly influenced by the presence of impurities and by the crystallinity of the substrate, suggesting that nucleation plays a limiting role in the growth of that compound. While the possibility of epitaxy with the Si substrate is not a necessary condition to the nucleation of θ-Ni_2Si, the template provided by δ-Ni_2Si is crucial in promoting it. Activated CMOS dopants and alloying impurities delay the growth of all Ni-rich compounds and eventually suppress the formation of the θ-Ni_2Si possibly because of a limited solubility. Impurities implanted without subsequent re-crystallization anneals also stabilize the compound partly through the presence of an amorphous interface, at least at the beginning of the reaction. The stabilization effect is enhanced by segregation of F to grain boundaries, by its ability to form strong Si-F and Ni-F bonds, and by a possible large F solubility in θ-Ni_2Si in which the F atoms would most likely occupy the vacancy sites of its relatively open crystal structure. The consumption of θ-Ni_2Si is not triggered by the accumulation of stress, but rather by the nucleation of NiSi. Finally, the tensile stress build-up occurring upon consumption of the θ-Ni_2Si could be associated to the regrowth of δ-Ni_2Si as both events are gradually suppressed by increasing F-implantation doses.

Chapter 7 : Growth kinetics of θ-Ni_2Si on undoped and F-implanted Si (001) substrates

7.1 Introduction

In chapter 6 we have shown that the formation of θ-Ni_2Si is strongly influenced by the presence of impurities, suggesting that nucleation is a growth-limiting step. We have also shown that fluorine implantation without subsequent activation anneal stabilizes the compound, increasing the temperature window over which it is observed during constant temperature ramp rates experiments. The fluorine most likely influences the reaction by binding to the vacancies left on the Ni sub-lattice of the θ-Ni_2Si, blocking the consumption mechanism of the compound.

In the current chapter we investigate the growth and consumption kinetics of the θ-Ni_2Si during the reactions of 10 nm Ni layers with undoped and F-implanted c-Si (001) substrates. This particular Ni thickness was chosen for its pertinence with the current state of the CMOS technology. Using real-time *in situ* X-ray diffraction (XRD), we monitor the evolution of the transformed volumes of θ- and δ- Ni_2Si during both isothermal and ramped anneals. We show that the complex growth of the θ-Ni_2Si cannot be explained using classic nucleation-and-growth or diffusion-controlled growth models. The θ-Ni_2Si consumption data however, is successfully analyzed using the classic Johnson-Mehl-Avrami-Komolgorov model for nucleation and growth. The activation energies deduced from the analysis of the growth data in the isothermal regime using different kinetics models are correlated with values extracted using Kissinger's analyses of reaction data obtained during temperature ramp annealing experiments to identify the best model to describe the θ-Ni_2Si growth.

7.2 Experimental procedures

7.2.1 Sample preparation

Our experiments we carried out on Si (100) substrates, either undoped or implanted with Fluorine. Implantations were done at 2keV on 4-inch 250 μm thick bulk wafers using a commercial implanter, with the wafers normals tilted 7° away from the ion beam direction to avoid channeling. Doses of 3×10^{14}, 1×10^{15}, and 3×10^{15} at/cm^2 were implanted without activation annealing such that the subsequent Ni depositions took place on at partially amorphized Si(001) surfaces. The projected range of F atoms, calculated using TRIM,[180] is about 5nm, which is less than required to convert 10nm Ni layers into δ-Ni_2Si, even when taking into account the straggle value which is about half of the projected range. All the implanted Si is most likely consumed before the formation of the θ-Ni_2Si.

Prior to the Ni deposition, the undoped and F-implanted Si(001) wafers were etched for 55s in dilute HF (10%), blown dry with high-purity N_2 and immediately loaded in the deposition system. Magnetron sputter deposition from a 99.999% pure Ni target was carried out at room temperature in a MRC-643 tool under 10mTorr of high-purity Ar after reaching a base pressure of 2×10^{-7} Torr. As-deposited samples were cleaved into 0.5-1cm^2 dices for the *in situ* XRD experiments.

7.2.2 *In situ* XRD during annealing

In situ XRD measurements during annealing were performed at the National Synchrotron Light Source (Brookhaven National Laboratory), on beam line X-20C. The samples were introduced in a vacuum chamber with rapid thermal anneal capabilities. To minimize contamination from oxygen, the chamber was evacuated twice to 5×10^{-6} Torr

(7×10^{-4} Pa), back-filling each time with purified He. Anneals were performed under a steady flow of 1 L/min of purified He at 1 atm.

The annealing parameters we have used were selected so as to cover both the formation and subsequent consumption of the θ-Ni_2Si. Isothermal annealing dwell temperatures were reached with nominal 27°C/s ramps starting at 100°C. The current study covered target temperatures ranging between 240 and 300°C, all reached within 20 s. Table 7-1 summarizes the annealing parameters (duration of experiment and temperatures) used for the isothermal study of the various samples. Temperature ramp anneals for Kissinger's analyses were performed with nominal rates of 0.3,1, 3, 9 and 27°C between 100 and 600°C. The sample temperature was measured with a thermocouple calibrated for each ramp rate to ±3°C using the Si-Au, Si-Al, and Si-Ag eutectic melting points. All measurements were performed with the same thermocouple.

Table 7-1: Isothermal annealing parameters. Duration (min) and temperature of the reaction.

T°	Undoped Si	3E14 F+ cm^{-2}	1E15 F+ cm^{-2}	3E15 F+ cm^{-2}
240	90	150		
250	60	135	150	
260	45	90	75	
270	30	45	90	150
280	20	30	60	90
290		15	60	60
300				35

The diffraction experiment used a high-intensity monochromator built from a band pass W-Si multi-layer filter that provides an x-ray beam of 6.9 keV ($\lambda = 0.1797$ nm) with an energy resolution of 1.5% and a typical intensity at the sample of 1×10^{13}

photons s^{-1}. The incident x-rays irradiated a sample area of about 2×2 mm. Diffraction spectra were collected using a position sensitive detector (PSD) consisting of a linear diode array covering a 2θ window of 14 °.

All our experiments were performed with the detector centered at 55° (2θ). This corresponds to the position of the θ-Ni_2Si (110) diffraction peak, the only strong reflection we observe for this compound. In order to optimize the diffraction conditions, undoped and F-implanted test samples were annealed at 3°C/s and quenched at the maximum development of the θ-Ni_2Si. The ω-angle (the angle between the incident beam and the sample's surface) was then scanned to maximize the intensity of the peak. The ϕ-angle (rotation of the sample about its surface normal) was not varied since our pole-figure data indicate the (110) planes belong to a fiber texture (c.f. Chapter 5). All the samples were then introduced in the chamber with the same orientation, and the diffraction geometry was kept constant for all the experiments reported.

7.2.3 Kinetics analyses and extraction of the integrated diffracted intensities

The study of growth kinetics by x-ray diffraction uses the direct proportionality between the volume of a growing compound and the integrated intensity under its diffraction peak(s). This proportionality is expressed by:

$$I_I(\theta) = K_{hkl} \left\| F_{hkl} \right\|^2 v_{growth}$$

where $I_I(\theta)$ is the integrated intensity, v_{growth} the diffracting volume, F_{hkl}, the structure factor of the XRD reflection under consideration, and K_{hkl} a factor taking into account the effects of the diffraction geometry (including the diffraction angle), the x-ray

polarization, the distribution of grain orientations (i.e. texture), the temperature, and the x-ray absorption. We have shown in Chapter 4 that analytical expressions of K_{hkl} can be found for powder samples but that it is generally unknown for textured polycrystalline thin films. As long as this term can be assumed constant during the reactions, the fact that it is unknown does not affect one's ability to determine growth-limiting mechanisms and their activation energies. Indeed, as shown in Chapter 4, the variation of this term can be neglected during both isothermal and temperature ramp anneals since we assume that there are no changes in the texture of the films. F_{hkl} is also constant unless compositional changes occur. The effects of a varying composition on the results of a study of kinetics based on XRD will be addressed later in this chapter.

We have seen in Chapters 5 and 6 that the θ-Ni_2Si (110), the δ-Ni_2Si (013)/(211) and (020) peaks are so close to one another that they strongly overlap during the θ-Ni_2Si growth. In order to properly separate their respective integrated intensities in that portion of the reaction, they need to be fitted with appropriate functions. It is a common practice in the XRD field to use the pseudo-Voigt (PV) function to describe diffraction peaks.[184,185] It consists of a linear combination of Gaussian (G) and Lorentzian (L) functions, as an approximation of the actual Voigt function, which is a convolution of G and L. The PV function we have used is given by:[185]

Equation 7-1

$$f(\theta) = M\left[Ae^{-\left(\frac{(\theta-\theta_0)}{(FWHM/2\sqrt{\ln 2})}\right)^2}\right] + \frac{(1-M)}{\left[1+\left(\frac{2(\theta-\theta_0)}{(FWHM)}\right)^2\right]}$$

Peaks are thus fitted with four parameters, θ_0 the central position, A the amplitude, $FWHM$ the full width at half-maximum and M the G-L mixing factor, which varies between 0 and 1. The integrated intensities are computed for each peak using their respective fitted parameters as detailed in Figure 7.1. Figure 7.1 (a) shows the typical *in*

situ XRD measurement performed during the 60-minute isothermal anneal of a 10 nm Ni layer on c-Si(001) substrate at 250°C. The diffracted intensity is plotted as levels of grey (bright = high and dark = low intensities) versus diffraction angle 2θ (ordinate) and annealing time (abscissa). Figure 7.1 (b) shows the data points of a single spectrum taken along the dotted line in (a) along with the pseudo-Voigt fits of all peaks, the total fit and an example of the integrated intensity (hatched area), which will be referred to as I_i in the rest of this chapter. Clearly, the pseudo-Voigt functions result in very good fits to the data (black line)

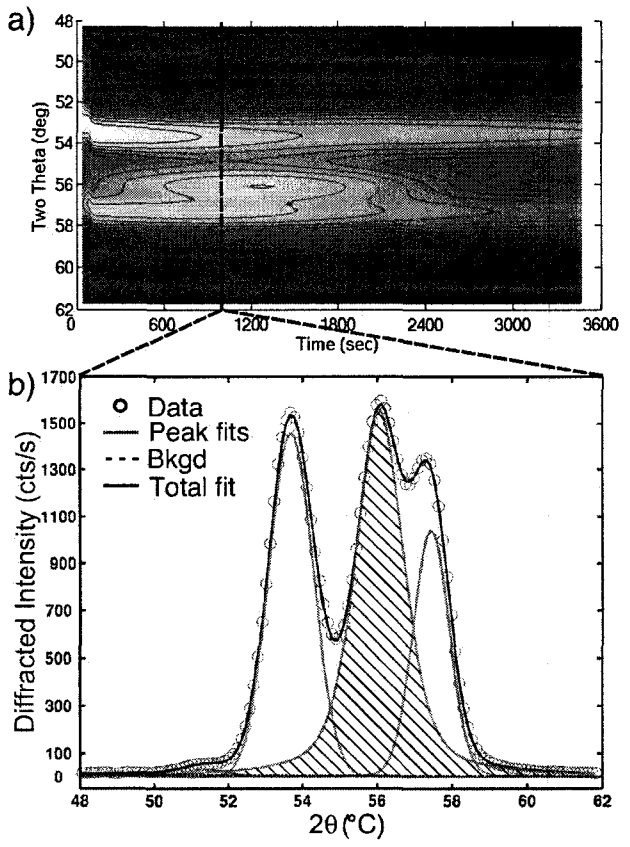

Figure 7.1: (a) XRD intensity contour map (λ = 0.1797 nm) plotted as a function of annealing time during the isothermal annealing at 250 °C in purified He of a 10-nm-thick Ni layer deposited on c-Si(001). (b) Single spectrum taken along the dotted line in (a) together with typical fitting results. Circles (o) represent data points, the different fitted peaks are plotted in light grey, and the resulting sum of all fitted peaks in plotted in solid black. The hatched area represents the integrated intensity.

In order to fit the data of a complete isothermal annealing experiment such as the one presented in Figure 7.1, we have an implemented automated MatLab routine that sweep through all the scans of the data set to fit them. The fitting procedure begins with a set of initial values chosen by the operator. If p peaks are fitted at the same time, $4p$ parameters are used; position, amplitude, FWHM, Gauss-to-Lorentz ratio for each peak. The routines then atomatically use the fit results of a scan as the initial values for the fit of the next scan. The operator can choose whether any of the $4p$ parameters may vary or not from one scan to the other. In many instances, we have tested up to seven different combinations of such constraints and of initial parameters to establish the uncertainty imparted by the fitting procedure on the kinetics analysis.

7.3 Results:

7.3.1 Undoped Si

Figure 7.2 presents the reaction of 10 nm Ni layers on undoped Si(001) as monitored by *in situ* XRD during isothermal anneals at temperatures between 240 and 280 °C. A log scale was used for the time axis to allow for comparing very different reaction rates on a same scale. As expected, the reaction accelerates as the temperature is increased, resulting in earlier *i)* consumption of δ-Ni_2Si and *ii)* concurrent formation of θ-Ni_2Si. For the highest temperature we investigated, the δ-Ni_2Si (013)/(211) peak clearly goes through a minimum as the θ-Ni_2Si (110) peak reaches its maximum, after what it re-increases upon the consumption of the θ-Ni_2Si. This is similar to what was observed during ramp-type annealing experiments for instance in Chapter 5.

Figure 7.3 shows the integrated diffracted intensities and positions of the θ-Ni_2Si (110) and δ-Ni_2Si (013)/(211) XRD peaks extracted by fitting the data of Figure 7.2 with pseudo-Voigt functions. We observe that the θ-Ni_2Si growth proceeds in two clearly observable steps, the second of which gains an increasing relative importance as the temperature increases. This result suggests that at least two mechanisms are controlling the growth, either in sequence or in competition, such that standard kinetics analysis procedures cannot be readily applied. Theθ-Ni_2Si growth will be carefully modeled later in this chapter.

The evolution of the δ-Ni_2Si (013)/(211) peak during the first stage of the θ-Ni_2Si growth is not plotted on Figure 7.3 (b) because it is obscured by an intense Ni (111) peak. The automated fitting routines therefore fail to successfully separate the contributions of both peaks in that 2θ-angle region so that the integrated intensity data is not reliable.

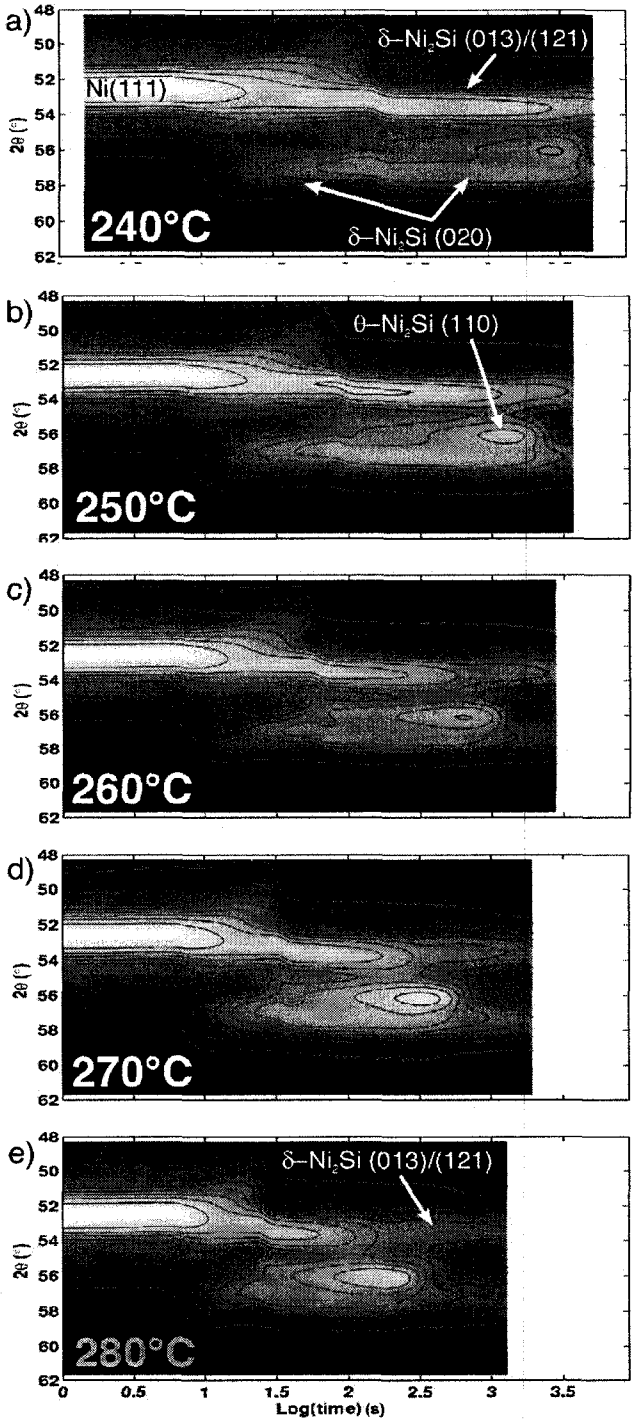

Figure 7.2: XRD intensity contour map ($\lambda = 0.1797$ nm) plotted as a function of annealing time during the isothermal annealing in purified He of 10-nm-thick Ni layer deposited on c-Si(001) at (a) 240, (b) 250, (c) 260, (d) 270 and (e) 280 °C.

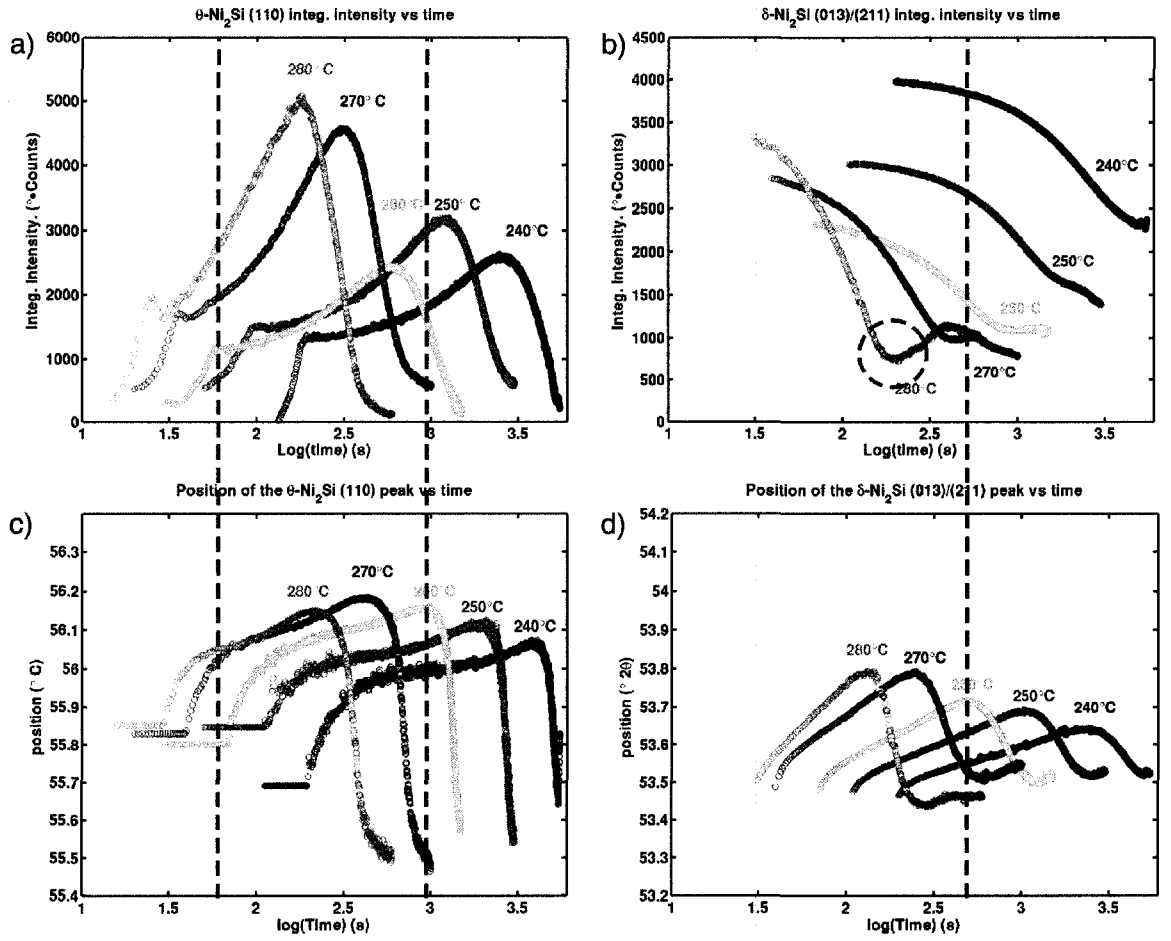

Figure 7.3: (a) and (b) Integrated diffracted intensity I_i along with (c) and (d) position of the θ-Ni_2Si (110) and δ-Ni_2Si (013)/(211) XRD peaks as a function of time during the growth of the θ-Ni_2Si and the concurrent consumption of δ-Ni_2Si during isothermal annealing of 10-nm-thick Ni layer deposited on c-Si(001) at temperatures between 240 and 280°C in purified He. The dashed lines indicate critical points for the 260 °C anneal. The dashed circle in (b) indicates the strong decrease of the δ-Ni_2Si (013)/(211) peak.

Figure 7.4 (a) presents the raw intensities summed under the δ-Ni_2Si (020) and the θ-Ni_2Si (110) peaks over the ranges identified by horizontal lines in the XRD contour map of Figure 7.4 (b). The figure shows qualitatively that the δ-Ni_2Si (020) peak gradually increases in intensity during the first growth stage. We may presume that the same holds true for the δ-Ni_2Si (013)/(211) peak. The figure also shows that even without

resorting to fits, we clearly observe two stages in the increase of the θ-Ni_2Si (110) peak, which indicates that the trends observed in Figure 7.3 do not result from an artefact of the fitting procedure.

The flat part of the signal in the early stages of the reaction in Figure 7.3 (c) is a consequence of forcing a constant position for the θ-Ni_2Si (110) peak in that region for fit convergence reasons. We have verified however that changing the fitting constraints in the analysis consistently leads to a two-staged growth as in Figure 7.3 (a). Figure 7.3 (c) and (d) also indicate that both the θ-Ni_2Si (110) and δ-Ni_2Si (013)/(211) XRD peaks shift in position following the same qualitative trend as the reaction unfolds. They first drift towards larger angle values then towards smaller values. Since θ-Ni_2Si is a non-stoichiometric compound, one may want to associate these shifts to possible compositional changes. However the stoichiometric nature of δ-Ni_2Si rather points to an evolution of stress. Indeed, even though the shift direction changes earlier for the δ-Ni_2Si (013)(211) peak, the peak shifts could simply be explained by the stress becoming tensile, then compressive, as observed in Chapter 6 during ramp-type anneals. This would cause the spacing of all of the crystallographic planes that are parallel to the surface of the film to respectively contract and expand. Nevertheless, a compositional change cannot be excluded at this point, and could be concurrent to the stress variations. The reason why the position of the δ-Ni_2Si (013)/(211) changes direction earlier than the θ-Ni_2Si (110) is not well understood, it could correspond to a point where the consumption of the δ-Ni_2Si is such that it becomes discontinuous, becoming free to relax.

Figure 7.3 (b) confirms the trend observed in Figure 7.2 whereby the δ-Ni_2Si (013)/(211) peak goes through a minimum while the θ-Ni_2Si (110) reaches its maximum value. The phenomenon is apparently accentuated by increased reaction rates. Indeed, higher reaction temperatures result in an increased δ-Ni_2Si consumption as the integrated

intensity of the (013)/(211) peak reaches lower minimum values with increasing temperature.

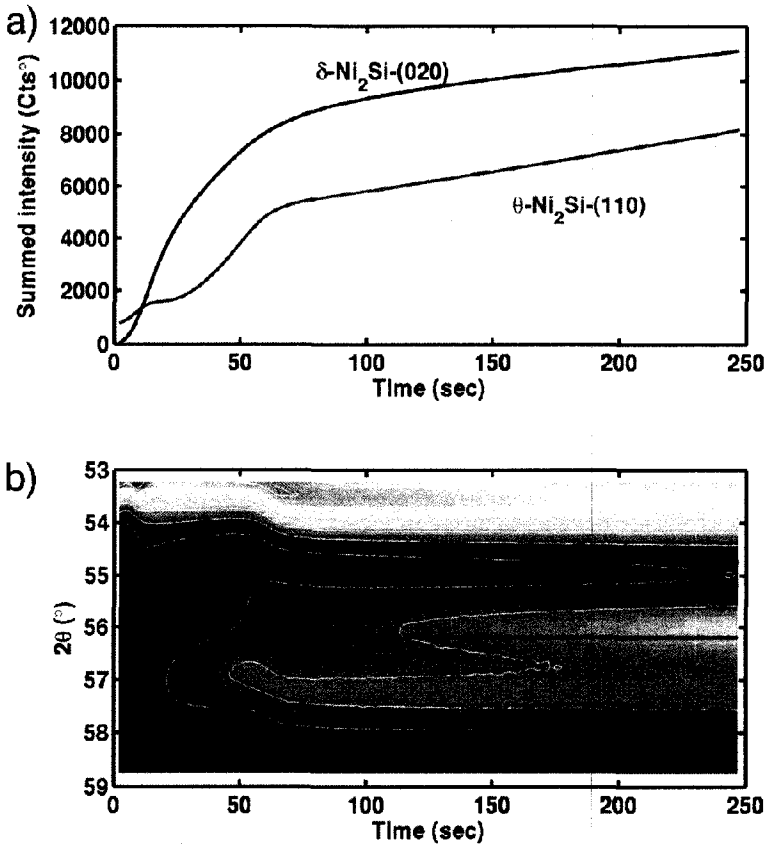

Figure 7.4: (a) Raw summed intensity under the θ-Ni_2Si (110) (red) and δ-Ni_2Si (002) (black) XRD peaks in the early stages of the growth during the reaction of a 10nm Ni layer on c-Si(001) at 260°C in purified He. (b) XRD intensity contour map (λ = 0.1797 nm) plotted as a function of annealing time with the angular ranges over which the summations are performed: from 54.75 to 56.25 (red) and from 56.25 to 58.00.

Figure 7.5 shows the reaction of 10nm Ni layers on c-Si(001) as monitored by *in situ* XRD during ramp anneals with heating rates ranging between 0.3 and 27 °C/s. As expected from thermally activated processes, an increase in heating rate delays the reaction to higher temperatures. These heating-rate-dependant temperature shifts are used

to determine activation energies through an analysis method proposed by Kissinger.[29] Mittemeier *et al.*[31,32] have shown that Kissinger's analysis could be applied to obtain the apparent activation energies of any given reaction process without the use of a specific kinetic model (e.g 1D diffusion-controlled growth, 2D or 3D nucleation-controlled growth etc.).

The procedure for determining the apparent activation energy for the formation and consumption of θ-Ni_2Si is presented in Figure 7.6. The XRD intensity summed over a range of 2 °(2θ) around the position of the θ-Ni_2Si (110) peak is shown in Figure 7.6 (a) together with its derivative as a function of temperature for the different ramp rates we investigated. The temperatures of maximum θ-Ni_2Si growth and consumption rates are readily observed in Figure 7.6 (b) in the form of sharp positive and negative peaks. The Kissinger plots for the growth and consumption of the θ-Ni_2Si compound, are presented in Figure 7.6 (c) and (d). The activation energies E_a were determined using the true (measured) ramp rates and we have assumed an uncertainty of 5 °C on the maximum rate temperatures. These two latter quantities are provided in Table 7-2.

We obtain from the Kissinger's analysis presented in Figure 7.6 activation energies of 2.05 ± 0.5 eV and 1.7 ± 0.4 eV respectively for the growth and consumption of θ-Ni_2Si. We note that the activation energy for the θ-Ni_2Si growth is larger than those usually reported for the growths of δ-Ni_2Si and NiSi (1.4-1.8eV),[2,44,51,59,64,81,82,83] although the range over which the values for NiSi are distributed overlaps with the range allowed by the uncertainty on our measured values.

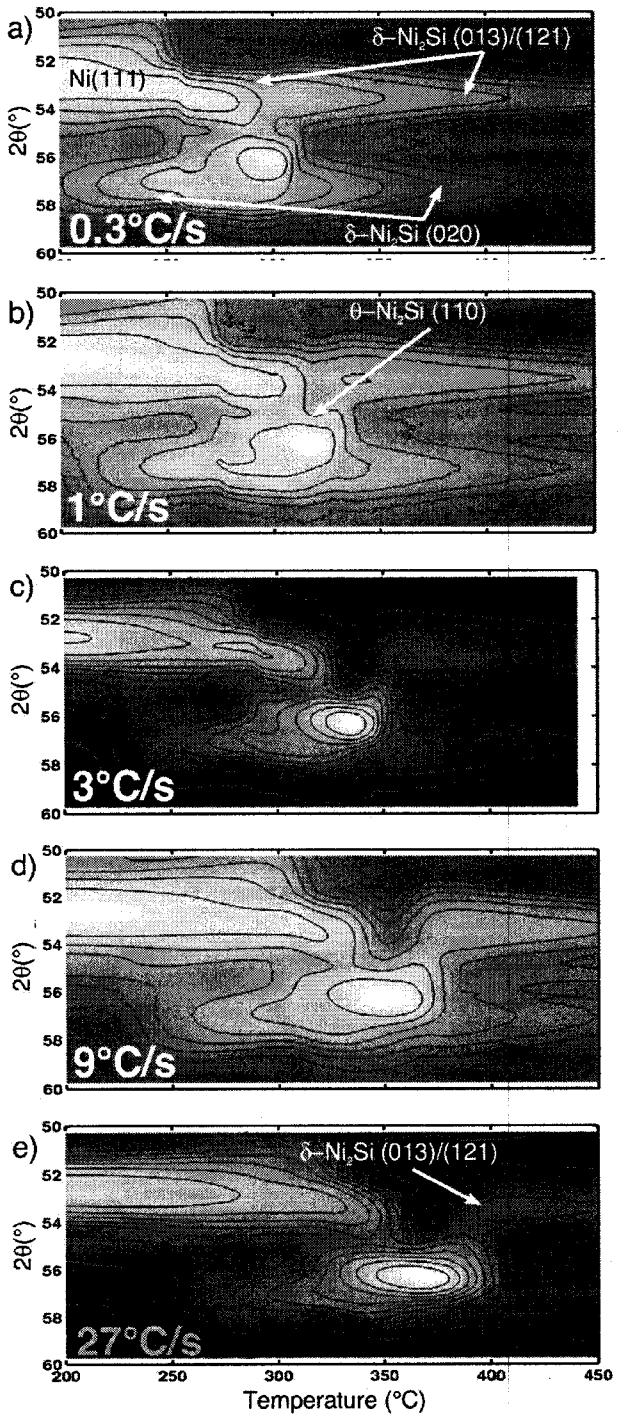

Figure 7.5: XRD intensity contour map ($\lambda = 0.1797$ nm) plotted as a function of annealing temperature T_a during thermal ramps in purified He of 10-nm-thick Ni layers deposited on c-Si(001) at (a) 0.3 °C/s, (b) 1 °C/s, (c) 3 °C/s, (d) 9 °C/s and (e) 27 °C/s from 100 °C to 450 °C.

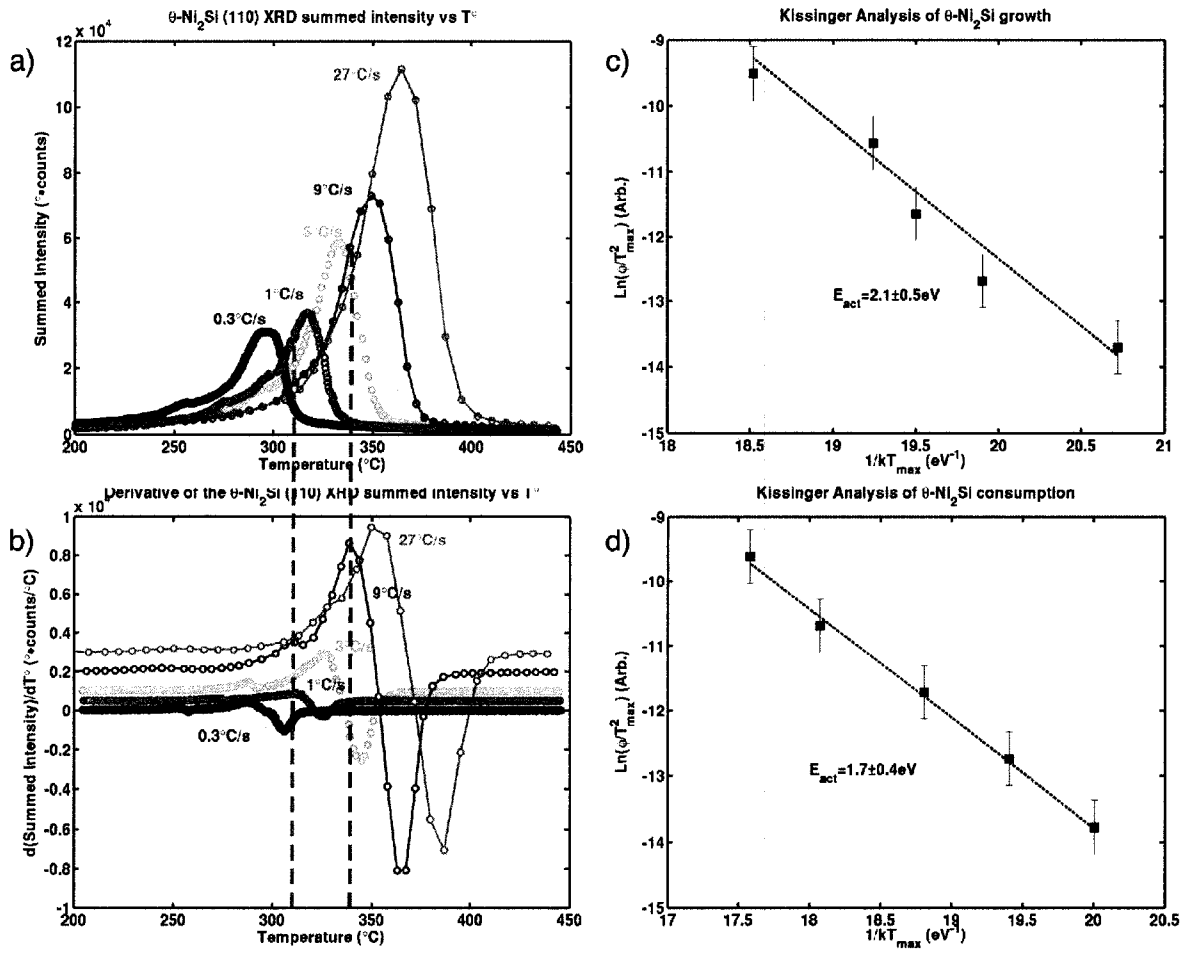

Figure 7.6: (a) XRD intensity summed over a range of 2° about the θ-Ni_2Si (110) peak (56.2°) during ramp anneals of Figure 7.5. (b) Derivative of the XRD summed intensity (a) (growth rate). (c) and (d) Kissinger's analysis for the growth and consumption of θ-Ni_2Si using the critical temperature values obtained from (b) and summarized in Table 7-2.

Table 7-2: Temperatures of maximum θ-Ni_2Si growth and consumption rates for the Kissinger's analysis of the reactions on undoped Si(001).

Nominal heating rate (°C/s)	Actual heating rate (°C/s)	T° @ max growth rate	T @ max consumption rate
0.3	0.35	287	307
1	1.05	309	325
3	3.1	321	344
9	9.4	326	370
27	29	350	387

We have established in Chapters 5 and 6 that the consumption of the θ-Ni_2Si is initiated by the nucleation of NiSi and that it most likely unfolds through a two-dimensional process. We have shown in Chapter 2 that nucleation and growth phenomena are usually described within the Avrami formalism whereby the transformed volume fraction follows a law of the form:

$$\xi = 1 - e^{-k(t-t_0)^n}$$

where k is the Avrami growth constant, t and t_0 the time and time offset for the onset of the growth and n the Avrami exponent, which is related to the dimensionality of the growth. In Chapter 2 we have shown that when a growth process is well described by the Avrami model, plotting the $\log(\ln(1/(1-\xi)))$ vs $\log(t-t_0)$ yields straight lines of slope n and y-intercept $\log(k)$. This procedure is usually referred to as the Avrami analysis.

Figure 7.7 (a) presents the Avrami analysis performed on the decreasing part of the θ-Ni_2Si (110) XRD peak. Since the neighboring δ-Ni_2Si peak have a relatively low intensity at that point of the reaction, fitting the data, which is a difficult and time consuming process, is not necessary so we rather used the raw intensity summed over a range of 2° (2θ) about the position of the peak. For the purpose of this analysis, the time scale was offset so that the maximum of the θ-Ni_2Si (110) peak corresponds to $(t-t_0) = 0$. The consumed volume fraction was established as $(I_{\theta\text{-}(110)\text{-}max} - I_{\theta\text{-}(110)}(t-t_0)) / (I_{\theta\text{-}(110)\text{-}max} - I_{\theta\text{-}(110)\text{-}min})$. Figure 7.7 (a) shows that the analysis yields exponents close to 2 for all annealing temperatures, which we correlate to a site-saturated two-dimensional nucleation-controlled consumption. We have observed in Chapters 5 and 6 that this consumption usually results in a simultaneous appearance of NiSi and δ-Ni_2Si, the link between these results will be discussed later.

Figure 7.7 (b) shows an Arrhenius plot of the Avrami growth constant k where the slope is –3.35±0.9 eV. This is precisely twice the value of the activation energy obtained with the Kissinger's analysis of Figure 7.6 (d), as expected from an Avrami-like growth process with an exponent of 2 (c.f. sections 2.2.1and 2.2.4.).

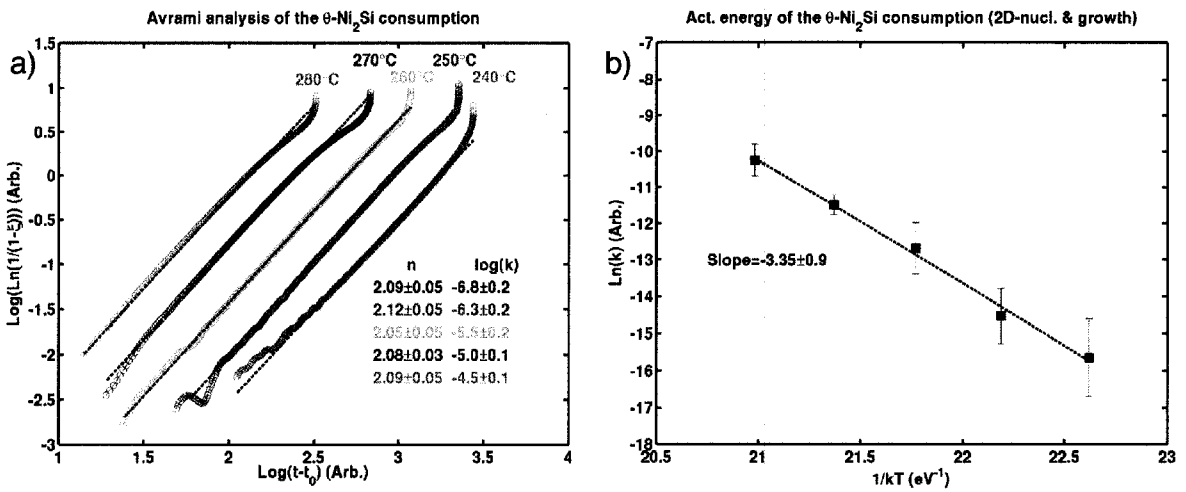

Figure 7.7: (a) Avrami plots of the θ-Ni_2Si (110) intensity summed (not fitted) over a range of 2° (2θ) about 56.2° for isothermal anneals in purified He of 10nm Ni layers on undoped c-Si (001) at temperatures between 240 and 280 °C and (b) Arrhenius plot of the Avrami constant.

7.3.2 F- implanted Si(001)

Figure 7.8 shows the *in situ* XRD data acquired during the reactions at 250°C and 280°C in samples with 10nm Ni on undoped and F-implanted c-Si(001) (doses of 3×10^{14}, 1×10^{15} and 3×10^{15} at. F cm^{-2}). We observe that the exhaustion of the Ni and the stress relaxation in δ-Ni_2Si occur at the same time regardless of the fluorine dose over most of the temperature range covered in our experiments. However, in contrast with our observations in the ramp-type annealing regime reported in Chapter 6, the formation of θ-Ni_2Si is clearly delayed by the fluorine implantation under isothermal treatments. It

follows that the exhaustion of the δ-Ni_2Si is also delayed, although this trend changes for the largest implantation dose at 280°C. A detailed analysis of XRD intensity ratios presented in Figure 7.9 reveals that the XRD peak intensities of the δ-Ni_2Si first increase with the F dose and then monotonically decrease for the higher doses. For the sample with 3×10^{15} at. F cm^{-2}, the intensity relative to the Ni (111) peak is 40-50% lower than in the undoped sample.[1] While the θ-Ni_2Si goes through a similar qualitative trend, the θ-Ni_2Si/δ-Ni_2Si proportion becomes significantly large for the 3×10^{15} at. F cm^{-2} dose. While this could result from an increasing θ-Ni_2Si formed volume, the earlier consumption of the δ-Ni_2Si in the sample with 3×10^{15} at. F cm^{-2} is certainly linked to an initially lower formed volume of δ-Ni_2Si; if less δ-Ni_2Si can form (presumably because of excessive amounts of F), complete consumption will occur earlier.

The local maxima in intensity ratios observed for the 3×10^{14} at. F cm^{-2} dose in all the traces of Figure 7.9 suggest a larger volume of metal-rich phases in this sample. It is interesting to note a correlation between these maxima and the results reported in Chapter 6 whereby the Ni-rich part of the resistance trace is lower for the 3×10^{14} at. F cm^{-2} dose (c.f.Figure 6.5).

[1] Black circles : 0.26 vs 0.42, black squares : 0.071 vs 0.145

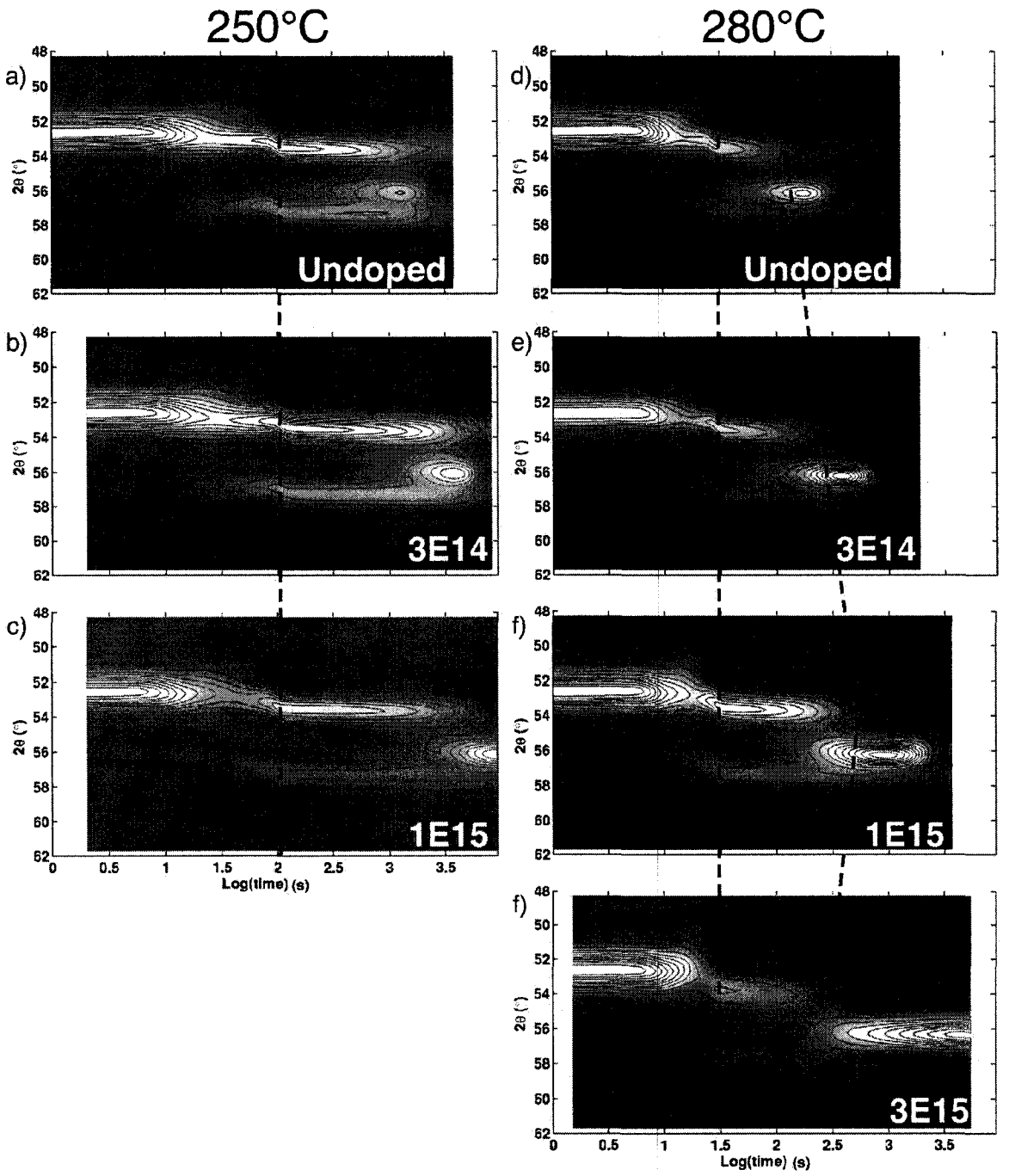

Figure 7.8: XRD intensity contour map ($\lambda = 0.1797$ nm) plotted as a function of annealing time during the isothermal annealing in purified He of 10-nm-thick Ni layer deposited on c-Si(001)) implanted with 0, 3×10^{14}, 1×10^{15} and 3×10^{15} F at. cm^{-2}. (a)-(c) 250 °C and (d)-(g) 280 °C isothermal annealing.

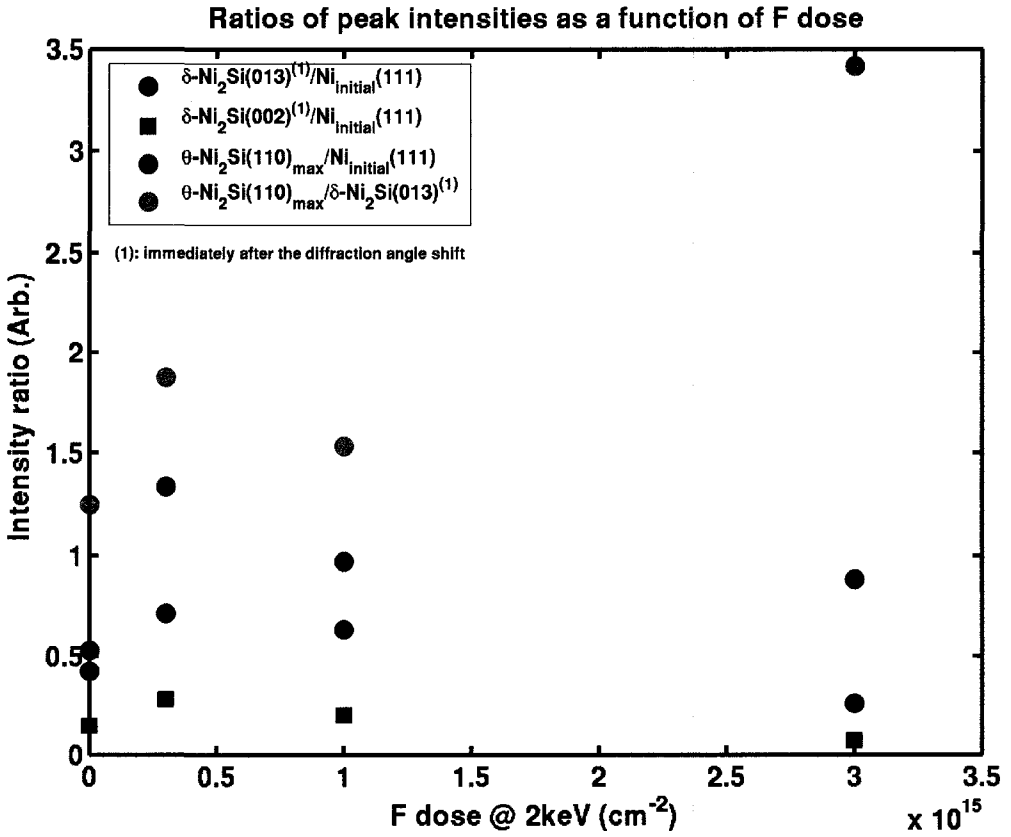

Figure 7.9: Ratio of XRD peak intensities (raw data, not fitted) during the isothermal annealing at 280 °C in purified He of 10-nm-thick Ni layer deposited on c-Si(001)) implanted with 0, 3×10^{14}, 1×10^{15} and 3×10^{15} at. F cm^{-2} (c.f. Figure 7.8 (d)-(g)). ■ δ-Ni_2Si (013) after its angle shift / initial Ni(111), ● δ-Ni_2Si (002) after its angle shift / initial Ni(111), ● θ-Ni_2Si (110) at the maximum of its development / initial Ni(111) and ● θ-Ni_2Si (110) at time of its maximum development / δ-Ni_2Si (013) after its angle shift..

Figure 7.10 shows the integrated intensity under the θ-Ni_2Si (110) peak during the isothermal reaction of 10 nm Ni layers on undoped and F-implanted c-Si(001) (a) at 280°C with variable F dose and (b) at different isothermal annealing temperatures with a constant F dose of 3×10^{15} at. cm^{-2}. In Figure 7.10 (a) we find that in addition to delaying the formation of the θ-Ni_2Si, F implantations seem to change the reaction pathway. The kink associated to the transition between the first and second growth regimes observed in the undoped sample, is gradually suppressed by the increasing implantation dose.

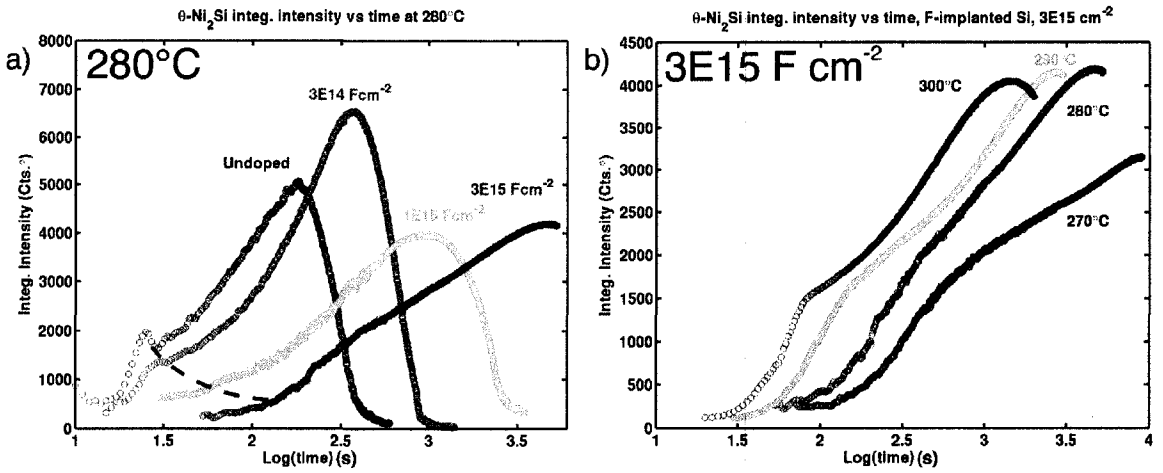

Figure 7.10: Integrated intensity of the θ-Ni_2Si (110) peak as a function of time during the isothermal annealing in purified He of 10 nm Ni layers on undoped and F-implanted Si(001). (a) Annealing at constant temperature of 280°C with doses of 0, 3×10^{14}, 1×10^{15} and 3×10^{15} F atoms cm^{-2}, and (b) between 270°C and 300°C with a constant F dose of 3×10^{15} at. cm^{-2}.

Focussing on the case of the largest fluorine dose, Figure 7.10 (b) shows that the reaction still proceeds in two stages. Transposing on Figure 7.8 (g) the time at which the kink occurs on the 280°C trace of Figure 7.10 ((a) or (b)), we find that this new transition point correlates with the disappearance of the δ-Ni_2Si peaks. We conclude that high-dose fluorine implantation causes the appearance of a third growth stage, which corresponds to an increase in XRD intensity of the θ-Ni_2Si (110) peak in the absence of δ-Ni_2Si (as well as Ni). While this increase can represent further growth of θ-Ni_2Si, as suggested by the slight decrease in resistance observed during the corresponding formation stage of 3°C/s ramps (c.f.Figure 6.5), it could also result from compositional or microstructural changes within that layer.

Figure 7.11 presents the effect of fluorine on the Kissinger's analysis of the θ-Ni_2Si growth using ramp anneals with heating rates varying from 0.3 to 27 °C/s. Figure 7.11 (a) shows the intensities summed over a range of 2°(2θ) centered about the position

of the θ-Ni_2Si along with (b) the corresponding derivatives, as a function of temperature for the reaction in samples with 3×10^{15} F at. cm^{-2}.

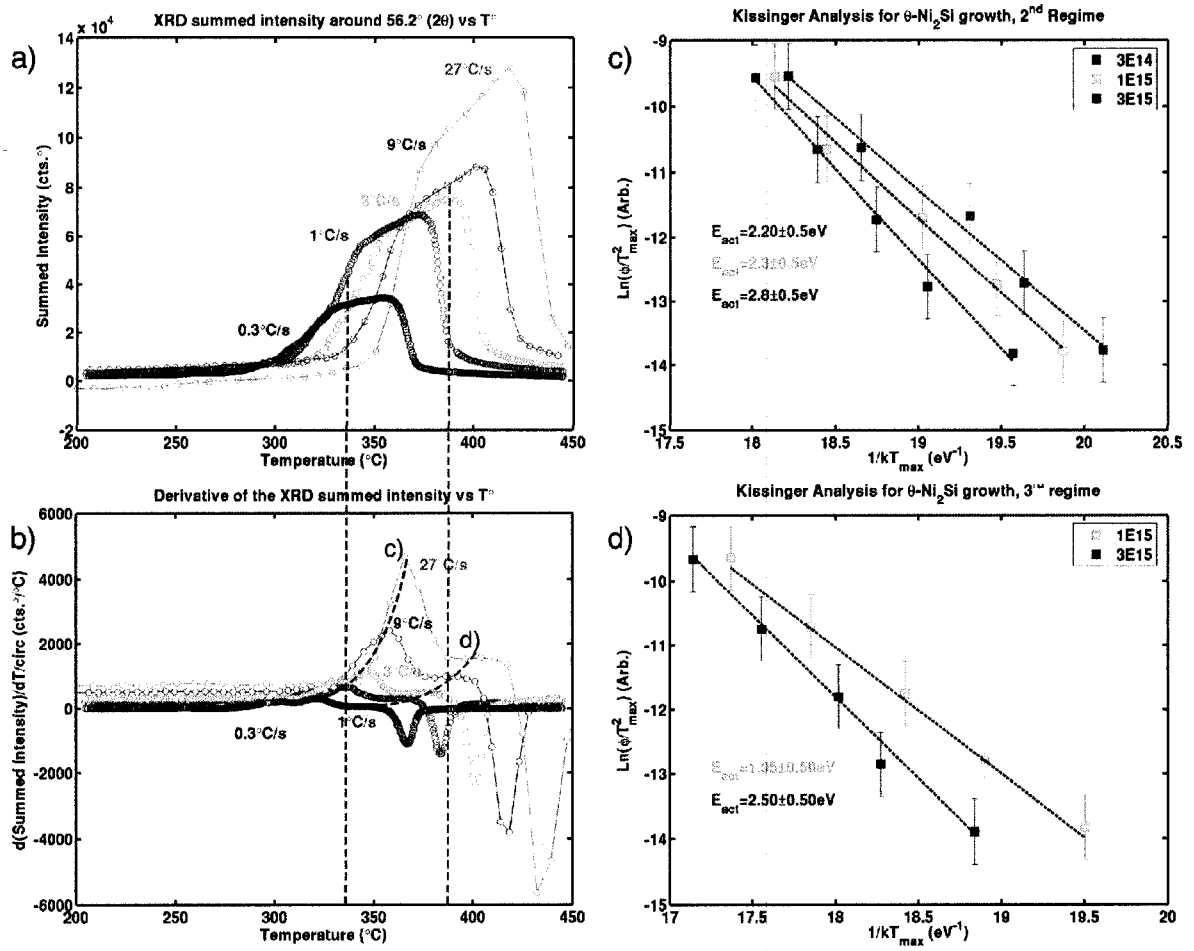

Figure 7.11: (a) XRD intensity summed over a range of 2° about the θ-Ni_2Si (110) peak (56.2°) during ramp anneals at 0.3, 1, 3, 9, and 27 °C/s in purified He of 10nm Ni layers deposited on c-Si(001) implanted with 3×10^{15} F at. cm^{-2} (b) Derivative of the XRD summed intensity in (a) (growth rate). (c) Kissinger analysis of the growth regime associated to the consumption of the δ-Ni_2Si (2nd regime). (d) Kissinger's analysis of the growth regime in absence of δ-Ni_2Si (3rd regime).

The second and third growth stages defined in Figure 7.10 and clearly observed in the ramp-type annealing regime results of Figure 7.11 (a), are associated to two corresponding peaks in the derivative signal of Figure 7.11 (b). The 0.3°C/s trace shows a

peak around 300°C that could correspond to the first growth stage observed on undoped Si, but its presence is not clear in the other traces. Figure 7.11 (c) and (d) show the Kissinger analysis of the second and third growth stages. Only two sets of data are presented in Figure 7.11 (d) because the third growth stage is not observed in the samples with 3×10^{14} F at. cm^{-2}.

As expected from the delay observed in the θ-Ni_2Si growth, F implantation increases the activation energy of the second growth regime from 2.05±0.5 eV (undoped) to 2.80±0.5 eV (3×10^{15} F at. cm^{-2}), which is beyond the uncertainty on the values. The same trend seems to apply to the activation energy of the third growth regime, which increases from 1.95±0.5 eV (1×10^{15} F at. cm^{-2}) to 2.5±0.5 eV (3×10^{15} F at. cm^{-2}). In Chapter 6 we have shown through the use of SIMS that there was some F redistribution in the growing Ni-rich silicides formation, although a clear plowing at the growth front is also observed. The results here support an incorporation of F atoms to the growing θ-Ni_2Si, which slows down the growth.

Figure 7.12 shows the effect of fluorine on the consumption kinetics of θ-Ni_2Si. Figure 7.12 (a) and (b) present Avrami plots of the summed intensity for samples with 3×10^{14} and 1×10^{15} F at. cm^{-2} respectively. Figure 7.12 (c) shows the Arrhenius plot of the Avrami constants of (a) and (b). Figure 7.12 (d) shows the Kissinger's analysis of the θ-Ni_2Si consumption built using the minima of the derivative traces (not shown for the 3×10^{14} and 1×10^{15} F at. cm^{-2} doses). The Avrami analysis data for the 3×10^{15} F at.cm^{-2} dose is not presented because the NiSi (103) peak appears upon the decrease of the θ-Ni_2Si(110) peak in these samples. Since their positions coincide almost exactly, even a careful fit fails to separate their respective contributions. The overlap is also present in samples with 1×10^{15} F cm^{-2} but to a lesser extent so that the analysis can still be carried out but may be less reliable.

Figure 7.12 (a) and (b) suggest that the θ-Ni_2Si consumption also proceeds with an Avrami exponent close to 2 in fluorine-implanted samples. The slight increase in the exponent for the 1×10^{15} F at.cm^{-2} dose could be linked to the presence of the NiSi (103) peak, which would also bias the value of the activation energy of the Avrami constant in Figure 7.12 (c).

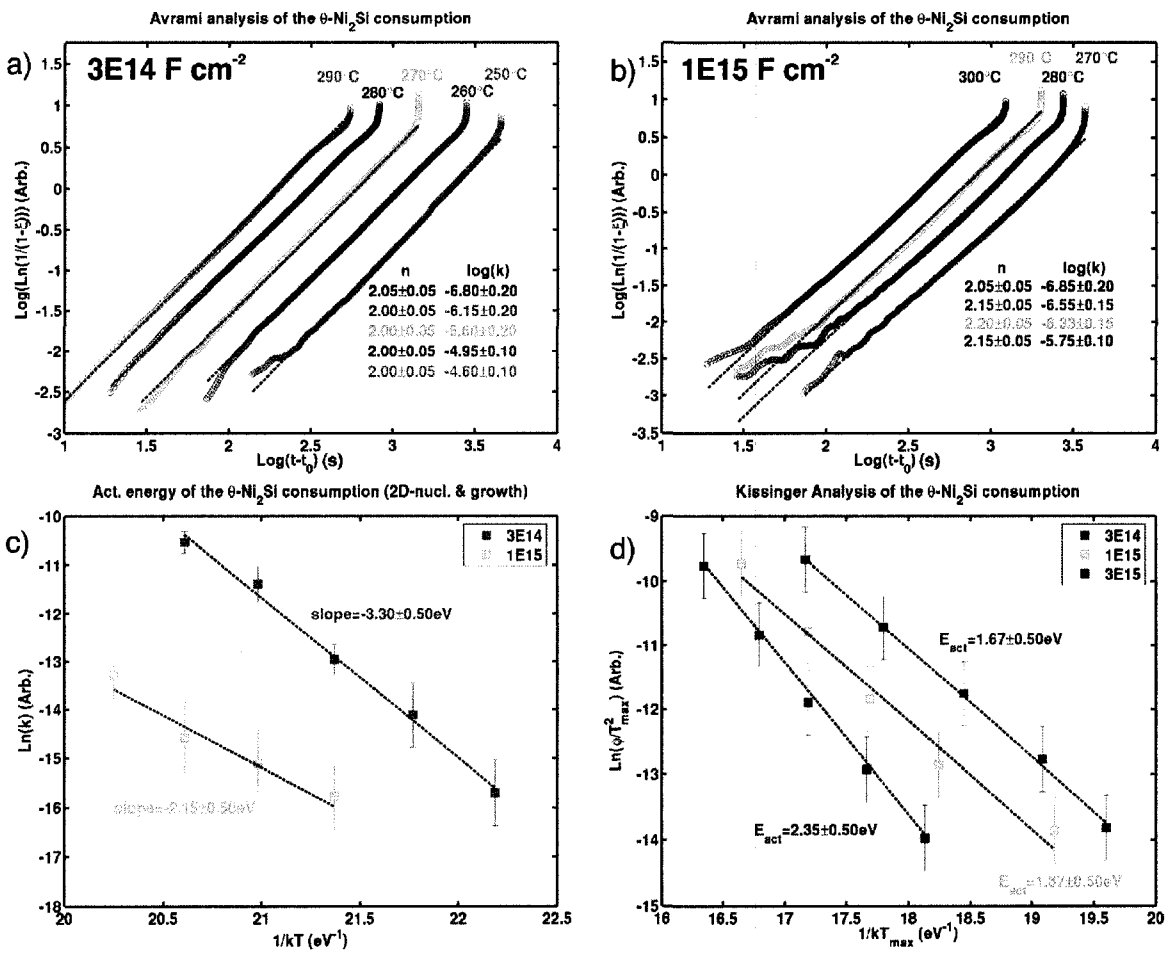

Figure 7.12: Avrami plots of the θ-Ni_2Si (110) intensity summed (not fitted) over a range of 2° (2θ) about 56.2° for isothermal anneals in purified He of 10nm Ni layers on c-Si (001) implanted with (a) 3×10^{14} and (b) 1×10^{15} F at. cm^{-2} at temperatures between 250 and 300 °C along with (c) the Arrhenius plot of the Avrami constants in (a) and (b). (d) Kissinger's analysis of the θ-Ni_2Si consumption during ramp anneals at 0.3, 1, 3, 9, and 27 °C/s in purified He of 10nm Ni layers deposited on c-Si(001) implanted with 3×10^{14}, 1×10^{15}, and 3×10^{15} F at. cm^{-2}.

Given the nature of the measurement, the Kissinger's analysis is more direct[1] and was applied for all F doses. Although the results of Figure 7.12 (c) and (d) must be interpreted with prudence given the possible bias from the Ni (103) peak, they indicates that the apparent activation energy of the consumption reaction increases with the F implantation. However, because of the lack of match between the activation energies of the Avrami constant and the ones obtained from the Kissinger's analysis for the 1×10^{15} F at.cm^{-2} dose, it is not clear if the Avrami model effectively gives an adequate description of the consumption kinetics in F implanted samples.

7.4 Analysis and discussion

7.4.1 Growth kinetics of θ-Ni_2Si on Undoped c-Si (001): *The Coffey-Clevenger-Barmak-Rudeman-Thompson model*

Our extensive TEM investigation did not lead to a clear depiction of the microstructure evolution during the θ-Ni_2Si growth. In the absence of such information, we rely on a detailed analysis of the growth kinetics to form holding hypothesis about the growth geometry and the controlling mechanisms. Since the volumes formed during each of the two stages of the θ-Ni_2Si growth contribute for significant portions of the total formed volume, any analysis of the growth kinetics must proceed from a model where both regimes are treated simultaneously in the formalism.

The large difference in growth rate between the two regimes bares an interesting resemblance with the formation of δ-Ni_2Si on amorphous Si, whereby a one-dimensional diffusion-controlled thickening of the product layer follows a two-dimensional

[1] While the superposition of two peaks may significantly alter the actual time dependance of the integrated diffracted intensity one may measure, the effect of the superposition on the position (on the temperature scale) of an extremum in the reaction rate may be smaller, especially if the extremum corresponds to a strong variation in rate.

nucleation-controlled growth stage. Coffey *et al.* have proposed a formalism that treats simultaneously both growth regimes in a single unified model.[54] The analyses we present in this chapter will be based on this formalism and on three modifications of the original model.

Figure 7.13 illustrates schematically the CCBRT model. The first stage consists of a site-saturated two-dimensional nucleation-and-growth regime governed by the following Avrami-like equation:

Equation 7-2 $$\chi_A = 1 - e^{-\eta \pi r^2}$$

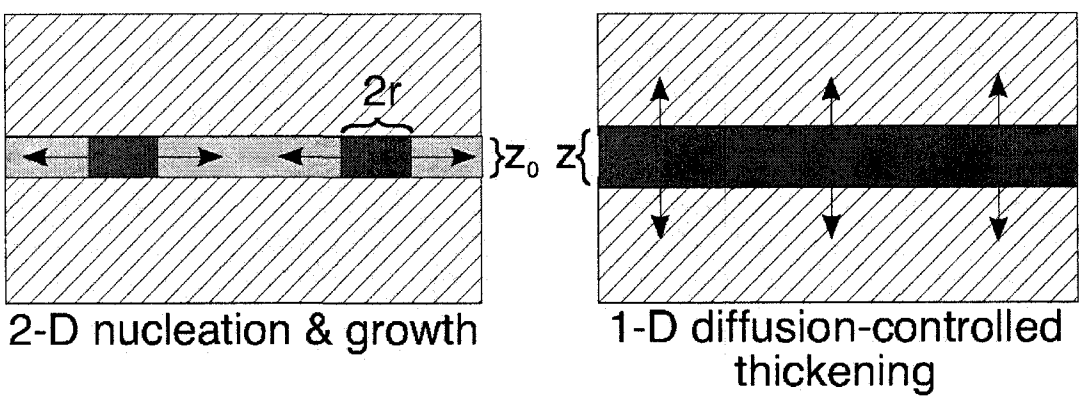

Figure 7.13: Illustration of the Coffey-Clevenger-Barmak-Rudman-Thompson (CCBRT) model.

χ_A is the <u>*areal*</u> transformed fraction, η is the nucleation site density and r is the average radius of the cylindrical nuclei. The latter are assumed to have a constant height z_0 throughout the entire first stage of the growth. The growth rate dr/dt of the radius is given by:

Equation 7-3 $$\frac{dr}{dt} = K_{i0}\, e^{-\frac{Q_i}{k_B T}}$$

where K_{i0} is the growth constant, Q_i is the activation energy for the growth, k_B and T are the Boltzmann's constant and temperature. At constant temperature this growth rate is constant.

The second stage consists of a classic one-dimensional diffusion-controlled thickening beginning once the nuclei have impinged and coalesced into a continuous layer of thickness z_0. The thickening rate dz/dt of this layer is given by:

Equation 7-4

$$\frac{dz}{dt} = \frac{K_{d0}}{z} e^{-\frac{Q_d}{k_B T}}$$

where z is the thickness, Q_d is the activation energy for diffusion, and K_{d0} is the diffusion-controlled growth constant. This constant depends on multiple factors such as the diffusion coefficient, some geometrical, driving force, and stoechiometry terms (c.f.sections 2.1.1 and 2.2.2). The two growth regimes are unified through the transformed <u>*volume*</u> fraction χ_V which is expressed as:

Equation 7-5

$$\chi_V = \chi_A \frac{z}{z_{\max}}$$

where z_{max} is the maximum thickness reached during the 1D diffusion-controlled growth stage. The overall volume growth rate $d\chi_V/dt$ is therefore given by:

Equation 7-6

$$\frac{d\chi_V}{dt} = \frac{d\chi_A}{dt}\frac{z}{z_{\max}} + \frac{\chi_A}{z_{\max}}\frac{dz}{dt}$$

Assuming an isothermal reaction, Equation 7-3 and Equation 7-4 can easily be integrated and combined to obtain an analytical expression for Equation 7-6:

Equation 7-7

$$\frac{d\chi_V}{dt} = \left[\left\{2\pi\eta K_{i0}^2 t e^{-\left(\frac{2Q_i}{kT}\right)} e^{-\left(\pi\eta K_{i0}^2 t^2 e^{-\left(\frac{2Q_i}{kT}\right)}\right)}\right\}\left\{z_0^2 + 2K_{d0} t e^{-\left(\frac{Q_d}{kT}\right)}\right\}^{\frac{1}{2}}\right]\left(\frac{1}{z_{\max}}\right) + \ldots$$

$$\ldots\left[\left\{1 - e^{-\left(\pi\eta K_{i0}^2 t^2 e^{-\left(\frac{2Q_i}{kT}\right)}\right)}\right\}\left\{\frac{K_{d0} e^{-\left(\frac{Q_d}{kT}\right)}}{\sqrt{z_0^2 + 2K_{d0} t e^{-\left(\frac{Q_d}{kT}\right)}}}\right\}\right]\left(\frac{1}{z_{\max}}\right)$$

For analysis purposes we explore two limits of this growth model : *i)* Before coalescence of the nuclei in the first stage, whereby $z \equiv z_0$ and $dz/dt \equiv 0$ and *ii)* after coalescence of the nuclei whereby $\chi_A \equiv 1$ and $d\chi_A/dt \equiv 0$.

i) Before coalescence

After setting $z \equiv z_0$ and $dz/dt \equiv 0$, Equation 7-7 can be rearranged as :

Equation 7-8

$$\frac{d\chi_V}{dt} = \frac{z_0}{z_{\max}}\left\{A t e^{-2At^2}\right\} \text{ where } A = \pi n K_{i0}^2 e^{-\left(\frac{2Q_i}{kT}\right)}$$

The position in time of the maximum reaction rate $d\chi_V/dt$ can then be determined by setting $d^2\chi_V/dt^2$ to zero, which yields :

Equation 7-9

$$t_{\max rate} = \sqrt{\frac{1}{2A}} = \sqrt{\frac{1}{2\pi\eta K_{io}^2 e^{-\left(\frac{2Q_i}{kT}\right)}}}$$

Inspecting Equation 7-9 reveals that plotting $\ln(t^2_{max\ rate})$ vs $(2/kT)$ should yield a straight line of slope Q_i and y-intercept $-\ln(2\pi\eta K_{i0}^2)$. Assuming that our experimental growth-vs-time data is well described by the CCBRT model, we can locate $t_{max\ rate}$ for the different temperatures we have investigated such that the activation energy Q_i and the combined term ηK_{i0}^2 for the growth during the first stage can be determined.

i) After coalescence

After setting $\chi_A=1$, Equation 7-7 can be rearranged to give :

Equation 7-10

$$\chi_V = \frac{z}{z_{\max}} = \frac{1}{z_{\max}}\left\{z_0^2 + 2K_{d0}te^{-\left(\frac{Q_d}{kT}\right)}\right\}^{\frac{1}{2}}$$

where t_0 is the time at which coalescence occurs, hence where the second regime starts. Inspecting Equation 7-10 reveals that plotting $(\chi_V^2-\chi_{V0}^2)$ vs t should produce straight lines of slope $(2/z^2_{max})K_{d0}e^{-(Q_d/k_BT)}$. Plotting $\ln[(2/z^2_{max})K_{d0}e^{-(Qd/k_BT)}]$ vs $1/kT$ for the different temperatures we investigated should produce straight lines of slope $-Q_d$ and y-intecept $\ln(2K_{d0}/z^2_{max})$ and therefore yield the activation energy for the diffusion-controlled growth in the second stage.

Note that since our data consists of diffracted intensity, we have no direct knowledge of z. We only assume a direct proportionality between the integrated diffracted intensity I_i and the transformed volume fraction χ_V (and in this very case z/z_{max}). Equation 7-10 needs to be modified to be expressed in terms of I_i, which is our measured data:

Equation 7-11

$$\frac{I_i}{I_{i\max}} = \frac{1}{I_{i\max}}\left\{I_{i0}^2 + 2K'_{d0}te^{-\left(\frac{Q_d}{kT}\right)}\right\}^{\frac{1}{2}} = \ldots$$

$$\ldots \frac{1}{C_{hkl} z_{\max}} \left\{ (C_{hkl} z_0)^2 + 2 C_{hkl}{}^2 K_{d0} t e^{-\left(\frac{Q_d}{kT}\right)} \right\}^{\frac{1}{2}}$$

where $C_{hkl} = K_{hkl} \| F_{hkl} \|^2$ is the proportionality constant between the interaction volume and the diffracted intensity (c.f. section 4.2.4). Plotting $(I_i^2 - I_{i0}^2)$ vs t should permit to determine Q_d and a combined term $2 C_{hkl}{}^2 K_{d0} / z^2_{max}$ instead of the diffusion-controlled growth constant.

7.4.2 Analysis of the θ-Ni_2Si growth kinetics using the CCBRT model

The rise in integrated intensity being very sharp and rapid in the first growth stage (c.f. Figure 7.3 (a)), the time to half rise was used instead of the time of maximum growth rate $d\chi_A/dt$ (c.f.Equation 7-9) to establish the activation energy Q_i and the combined term ηK_{i0}^2. Table 7-3 gives the time to half-rise values as measured on the traces presented in Figure 7.3 (a) for the different reaction temperatures we have investigated. An error of 10% on the measured time was arbitrarily selected.

Table 7-3: Time to half-rise during the 1st growth stage on undoped Si(001).

Reaction T°	Time to half rise
240	34 ± 3 s
250	21.5 ± 2 s
260	14 ± 1.5 s
270	7 ± 0.7 s
280	5 ± 0.5 s

Figure 7.14 presents the analysis of the θ-Ni_2Si growth based on the CCBRT model using the data from Figure 7.3 (a). In Figure 7.14 (a) the data of Table 7-3 was

plotted according to Equation 7-9 to analyze the first growth stage. Figure 7.14 (b) shows $\log(I_i^2-I_{i0}^2)$ vs $\log(t-t_0)$ plots, as derived from Equation 7-11, which should yield straight lines of slope equal to unity if the second growth stage is well described by the CCBRT model. Figure 7.14 (c) shows the plots of $(I_i^2-I_{i0}^2)$ vs $(t-t_0)$ derived from Equation 7-11, where I_{i0} is measured at t_0. Finally, Figure 7.14 (d) shows the Arrhenius plot of the slopes of Figure 7.14 (c).

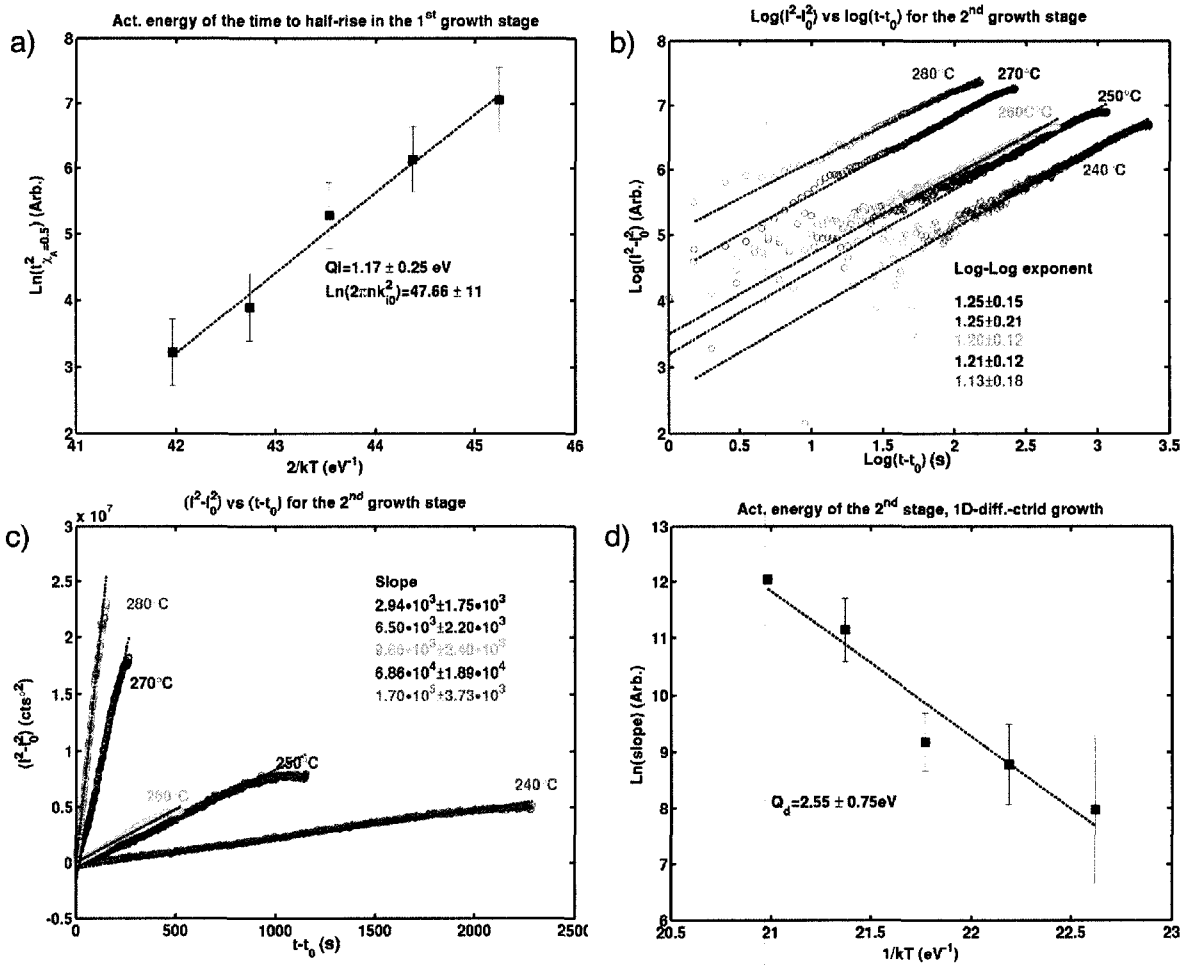

Figure 7.14: (a) Apparent activation energy for the site-saturated nucleation-controlled growth during the 1st stage of the reaction determined using the formalism of the CCBRT model, (b) $\mathrm{Log}(I_i^2-I_{i0}^2)$ vs $\mathrm{Log}(t-t_0)$ plot assuming diffusion-controlled thicknening during the 2nd growth stage using the formalism of the CCBRT model, (c) $(I_i^2-I_{i0}^2)$ vs $(t-t_0)$ assuming diffusion-controlled thicknening during the 2nd growth stage and d) apparent activation energy for the diffusion-controlled thicknening.

Figure 7.14 suggests overall that the two-stage CCBRT model describes relatively well the variation in diffracted intensities we measure. From the detailed analysis, we first see in Figure 7.14 (a) that the 2D nucleation-and-growth stage would have an activation energy of 1.17 ± 0.25eV. We find however that the slopes of Figure 7.14 (b) exceed 1 beyond the uncertainty in most of the cases. The uncertainties correspond to the standard deviation of the different values obtained when using different sets of constraints on the fit parameters as explained in the experimental section. For the diffusion-controlled growth stage, we find an apparent activation energy of 2.55 ± 0.75eV from the Arrhenius plot of Figure 7.14 (d). This value is relatively large compared to the activation energies commonly reported for the diffusion-controlled growth of δ-Ni_2Si and NiSi (1.4 to1.8eV), but also, and mostly, larger than the value obtained above with the Kissinger's analysis of the θ-Ni_2Si growth (2.05eV). However, the uncertainty we have determined on the values is large enough to cover the mentioned differences. Note that the numerical value of the slope for the 260 °C anneal is about 50% larger than for the 250 °C while the actual data curves are almost parallel. This is explained by the fact that *(i)* the numerical value is the average of 7 values obtained from fits using different constraints on the fit parameters (c.f. Equation 7-1) while the green curve is the data obtained from one single set of fit constraints. Also, as can be seen on Figure 7.14 (d) the 260 °C data point is slightly outlying.

The parameters derived in Figure 7.14 were inserted back into Equation 7-7, which was then used to generate simulated growth data. The complete list of parameters used for the simulations is provided in Table 7-4 and the resulting simulated growth data are presented in Figure 7.15, where they are overlaid on the experiment data for comparison.

The parameter t_{offset} accounts for the reaction steps prior to the formation of θ-Ni_2Si, i.e. the consumption of the Ni and the formation of δ-Ni_2Si. All other parameters

have been defined in Equation 7-7. The diffusion-controlled growth constant obtained from the y-intercept of the line in Figure 7.14 (d) is the combined term $2K_{hkl}^2K_{d0}/z^2_{max}$. However, the CCBRT model requires the use of K_{d0}. Since our data does not allow for separating both terms, K_{d0} was determined by optimizing the fit of the model to the growth data at 260°C using z_{max}=16 nm as it is the value expected with the complete conversion of a 10 nm Ni layer into θ-Ni_2Si (assuming a 60:40 Ni:Si ratio). The value of z_0 was then adjusted to get the appropriate height of the initial intensity increase. Q_i, ηK_{io}^2, Q_d, K_{d0} and z_0 were then kept fixed for all temperatures leaving z_{max} and t_{offset} as the only adjustment parameters. The necessity of adjusting z_{max} comes from the variation of the relative importance of the two growth stages identified in Figure 7.2 and Figure 7.3.

Table 7-4: List of parameters for the fits of the CCBRT model to the experimental growth data.

T° (°C)	Q_i (eV)	ηK_{io}^2 (s^{-2})	Q_d (eV)	K_{d0}(cm^2s^{-1})	z_0 (nm)	z_{max} (nm)	t_{offset} (s)
240	1.175	3.5×10^{19}	2.5	1×10^9	7	14	140
250	1.175	3.5×10^{19}	2.5	1×10^9	7	15	55
260	1.175	3.5×10^{19}	2.5	1×10^9	7	16	36
270	1.175	3.5×10^{19}	2.5	1×10^9	7	20	22
280	1.175	3.5×10^{19}	2.5	1×10^9	7	23	15

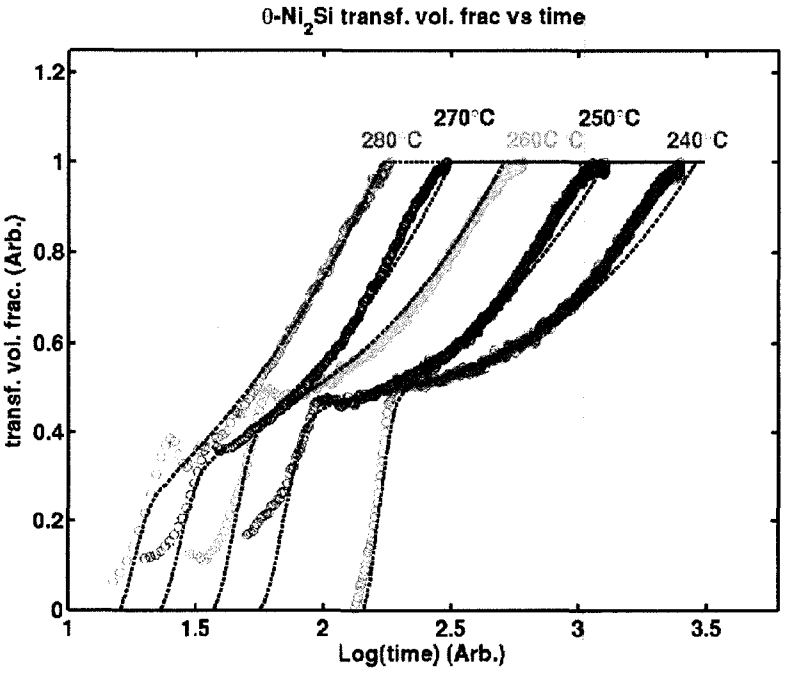

Figure 7.15: Transformed θ-Ni_2Si volume fraction as a function of time during the isothermal annealing of 10 nm Ni layers on c-Si (001) at different temperatures. Comparison of the CCBRT model with the experimental data. Dashed curves represent simulations and colored data markers represent experimental data.

Figure 7.15 shows that with the current assumptions on t_0 and z_{max}, the CCBRT model yields a reasonable fit to the data. Unless K_{d0} is adjusted, the goodness of the fit decreases slightly towards the end of the reaction for all temperatures aside from 260°C, where the initial parameter optimization was performed. The z_{max} values for 270°C and 280°C are clearly too large considering the initial Ni thickness of 10nm. However, one must not give too much meaning to the absolute values of z_0 and z_{max}, since the value of K_{d0} we used was determined from a hypothetical value of z_{max}. One must rather interpret the increase in z_{max} as an indication that θ-Ni_2Si most likely forms in increasing quantities with the reaction temperature. This is consistent with the more pronounced decrease in the δ-Ni_2Si (013)/(211) peak intensity (c.f. Figure 7.3 (b)) at higher reaction temperatures.

The growth microstructure we expect from a diffusion-controlled thickening in the second growth stage is a planar reaction front such that the growing and the consumed compounds co-exist as superimposed continuous layers as illustrated in Figure 7.13. The second growth stage as proposed in the CCBRT model therefore precludes *a priori* the lateral coexistence of θ-Ni_2Si and δ-Ni_2Si in the same layer, unless the growth rates *dr/dt* (Equation 7-3) and *dz/dt* (Equation 7-4) are similar at the growth temperature. In such a case, the growth would appear as a 3D process, which would then be compatible with the laterally non-uniform microstructure we have reported in Chapter 5.

Figure 7.16 compares the growth rates *dr/dt* and *dz/dt* using an Arrhenius plot. The K_{i0} term was separated from the combined ηK^2_{i0} by using two hypothetical η values of 1×10^{14} cm^{-2} and 2.5×10^{9} cm^{-2}, which correspond to 1 nucleation site per square of 1×1 nm and of 200×200 nm respectively. The *dz/dt* rate was evaluated using a z_{max} value of 15nm. Inspecting Figure 7.16 reveals that using the activation energies and *K* parameters defined above, the growth rates associated the two regimes could be equal between 290 and 430 °C depending on the value of the nucleation site density. From the TEM investigations presented in Chapter 5 the grain size of the θ-Ni_2Si is of the order of 10-20 nm, which would point to η values around 5×10^{11}, and to equal rates at temperatures around 360°C. On one hand, this result does not rule out that a growth described by the CCBRD model could result in laterally non-uniform reaction fronts. On the other hand, should *dr/dt* and *dz/dt* be equal during isothermal anneals at the temperatures we investigated, the growth would most likely not proceed in two clearly distinct stages as we observed in Figure 7.3.

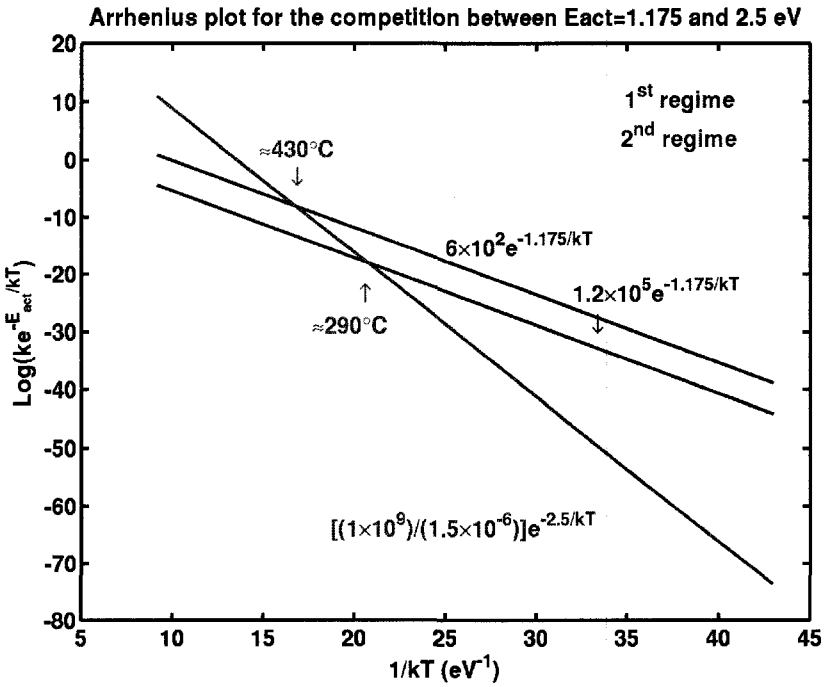

Figure 7.16: Arrhenius plot of the growth rates *dr/dt* (blue lines) and *dz/dt* (red lines). Growth rates *dr/dt* are evaluated for nucleation site density η values of 1×10^{14} cm^{-2} (top blue curve) and 2.5×10^{9} cm^{-2} (bottom blue curve). Growth rate *dz/dt* evaluated for a thickness of 15 nm.

7.4.3 Analysis of the θ-Ni_2Si growth kinetics using a modified CCBRT model

Even though we have not established a clear growth microstructure and we have obtained a reasonable description of the experimental data with the CCBRT model, we certainly have not excluded the lateral coexistence of δ- and θ- Ni_2Si. Since it is not clear that the CCBRT model as presented does readily allow for it, we propose in what follows a modification of the CCBRT model that allows for a lateral co-existence of θ-Ni_2Si and δ-Ni_2Si. As will be seen, this modified model seems to offer an even better fit to our *in situ* XRD data.

Our modified model finds its roots in our TEM results and in the results of Barmak *et al.* who have reported a peculiar formation microstructure of Nb_2Al during Nb-Al reactions.[186] The growth of Nb_2Al consumes $NbAl_3$ by penetrating down its grain boundaries, resulting in a non-planar growth front and, mostly, a lateral co-existence of Nb_2Al and $NbAl_3$. The microstructure they reported is reproduced schematically in Figure 7.17.

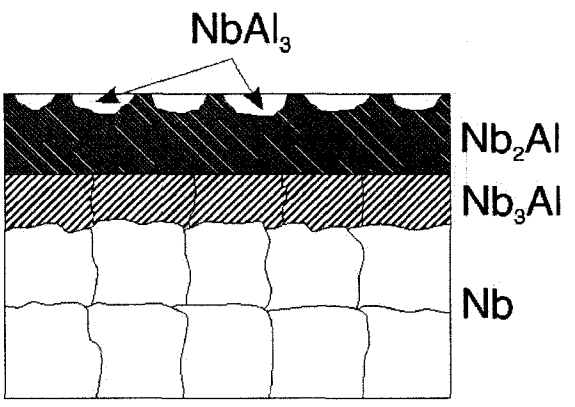

Figure 7.17: non-planar growth microstructure of Nb_2Al

Barmak *et al.* have stressed that this growth geometry would require a non-planar model to describe the growth kinetics. Correlating this microstructure with the one we observed in our samples in Chapter 5, we propose a modification to the CCBRT model whereby the 1D diffusion-controlled thickening of the second stage is replaced by a non-planar diffusion-controlled penetration of the θ-Ni_2Si into the grains of the overlying δ-Ni_2Si. This model is illustrated in Figure 7.18. In the modification we propose, the first stage of the growth is the same than presented previously and the penetration of the θ-Ni_2Si into the overlying δ-Ni_2Si during the second stage is modeled by growing hemispheres. The growth rate of their radius r_s is assumed to be described by a diffusion-like expression given by :

Equation 7-12

$$\frac{dr_s}{dt} = \frac{k_d}{r_s} e^{-\frac{Q_d}{kT}}$$

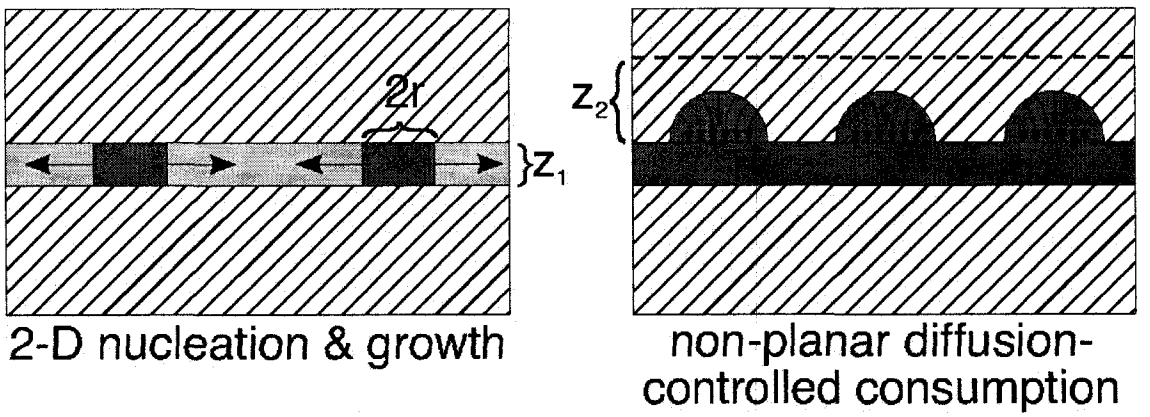

Figure 7.18: Modified CCBRT model with a second stage consisting of the non-planar diffusion-controlled penetration of θ-Ni_2Si into the grains of the overlying δ-Ni_2Si.

The volume fraction transformed during the second stage is then expressed using an Avrami-like formulation to account for the impingement of the spheres as they grow:

Equation 7-13

$$\chi_{v2} = 1 - e^{\frac{2\pi}{3} N_0 r_s^3}$$

where N_0 is a fixed number of "entry points", i.e. locations where hemispheres enter the grains boundaries of the overlying layers. We obtain r_s by integrating Equation 7-12:

Equation 7-14

$$r_s = \left\{ r_{s0}^2 + 2k_d(t - t_0)e^{-\frac{Q_d}{kT}} \right\}^{\frac{1}{2}}$$

where r_0 is the initial radius of the hemispheres that we assume to be zero. The limits of this assumption and of the model itself will be discussed later. The transformed volume fraction in the second growth stage is therefore expressed by:

Equation 7-15 $$\chi_{v2} = 1 - e^{-\frac{2\pi}{3}N_0\left\{2k_d(t-t_0)e^{-\frac{Q_d}{kT}}\right\}^{\frac{3}{2}}} = 1 - e^{-\left\{k_2(t-t_0)e^{-\frac{Q_d}{kT}}\right\}^{\frac{3}{2}}}$$

The two growth stages are unified through the thicknesses z_1 and z_2 such that:

Equation 7-16 $$\chi_{vtot} = \left(\frac{\chi_A \cancel{A} z_1}{\cancel{A} z_1}\right)\left(\frac{\cancel{A} z_1}{\cancel{A}(z_1+z_2)}\right) + \chi_{v2}\left(\frac{\cancel{A} z_2}{\cancel{A}(z_1+z_2)}\right)\ldots$$
$$= \frac{\chi_A z_1}{(z_1+z_2)} + \frac{\chi_{v2} z_2}{z_1+z_2}$$

where A is an arbitrary growth front surface area. The growth rate $d\chi_{vtot}/dt$ is then given by:

Equation 7-17 $$\frac{d\chi_{vtot}}{dt} = \frac{d\chi_A}{dt}\frac{z_1}{(z_1+z_2)} + \frac{d\chi_{v2}}{dt}\frac{z_2}{z_1+z_2}$$

After differentiating Equation 7-15 and substituting in Equation 7-17 along with the expression established earlier for $d\chi_A/dt$, we obtain an analytical expression for the growth rate of the total transformed volume fraction:

Equation 7-18 $$\frac{d\chi_V}{dt} = \left\{2\pi\eta K_{i0}^2 t e^{-\left(\frac{2Qi}{kT}\right)} e^{-\left(\pi\eta K_{i0}^2 t^2 e^{-\left(\frac{2Qi}{kT}\right)}\right)}\right\}\left(\frac{z_1}{z_1+z_2}\right)\ldots$$
$$\ldots + \left\{\frac{3}{2}k_2^{\left(\frac{3}{2}\right)}(t-t_0)^{\left(\frac{1}{2}\right)} e^{-\left(\frac{3Qd}{2kT}\right)} e^{-\left(K_2^{\frac{3}{2}}(t-t_0)^{\left(\frac{3}{2}\right)} e^{-\left(\frac{3Qd}{2kT}\right)}\right)}\right\}\left(\frac{z_2}{z_1+z_2}\right)$$

As we propose it, our model has thee limitations worth discussing. First, assuming that r_{s0} is zero and expressing the total transformed volume fraction as a weighted sum of the fractions evolved during each of the growth stages involve the implicit assumption that the diffusion in the second growth stage is independent of the result of the growth in the first stage; The two stages are thus not intrinsically coupled as they were in the original CCBRT model. While this is not completely rigorous, treating explicitly the influence of the layer formed during the first stage on the magnitude of the diffusion flux, hence dr_s/dt, in the second stage would greatly increase the mathematical complexity of the model given the differences in the geometries of the growing volumes from one stage to the other. Secondly, Equation 7-12 involves that the diffusion of atoms in the growing hemispheres is radial such that dr_s/dt should be infinite at the beginning of the second stage and at any later time at the center of the hemispheres. Such is certainly not the case, in fact the diffusion most likely occurs following the arrows drawn in the hemispheres of Figure 7.18 such that the diffusion flux is never infinite at any point of the space. Clearly the hemispherical shape is an oversimplification of the growth geometry, yet is it easily treated mathematically. Finally, if the Avrami formulation used to express χ_{v2} corrects the transformed fraction for the impingement between growing nuclei, our model does not consider the impingement with the top free surface of the film. This will delay slightly the saturation of the simulated growth with respect to the experimental data and underestimate the transformed volume fraction towards the end of the reaction. Bearing in mind these limitations, we will see later the model as we propose it gives a very good description of the experimental data.

The assumptions we have made allow for easily determining χ_{V2} from our experimental diffraction data :

Equation 7-19

$$\chi_{v2} = \frac{I(t)\big|_{t>t_0} - I(t_0)}{I_{max} - I(t_0)}$$

where t_0 is the time at which the first growth stage ends and the second one starts. Should the growth model we have defined above effectively prevail, performing an Avrami analysis on the data corresponding to the second growth stage would yield an exponent of 3/2.

Figure 7.19 shows (a) the Avrami analysis of the second stage of the θ-Ni_2Si growth and (b) an Arrhenius plot of the Avrami constant. The Avrami plot yields straight lines and the exponents we deduce from the lines slopes are close to 1.5 for all the reaction temperatures. The Arrhenius plot of the corresponding Avrami constants has a slope around 3.15eV, which translates to an activation energy Q_d of 2.05eV if considering the Avrami exponent value of 1.5 (c.f. section 2.2.1). This is almost exactly the value obtained with the Kissinger's analysis (2.05eV). From the y-intercept we deduce a growth constant K_2 of 3.51×10^{17}.

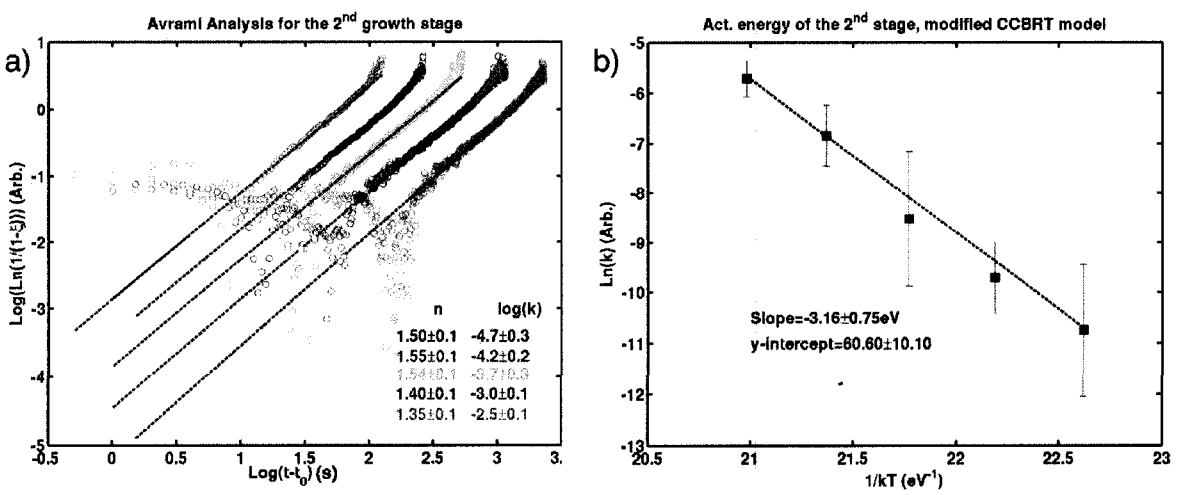

Figure 7.19: (a) Avrami analysis of the second stage of the θ-Ni_2Si growth according to the modified CCBRT model and (b) Arrhenius plot of the Avrami constant obtained in (a).

It is interesting to note that with the modified CCBRT model we find an activation energy closer to that obtained with the Kissinger's analysis than with the

original CCBRT model, although the larger difference observed in the latter case remains within the uncertainty. Nevertheless, the Avrami exponent of 3/2 and the match of the activation energies suggest that the modified CCBRT model gives a very good description of the experimental data.

Similarly to what was done for the original CCBRT model, the parameters obtained from the above analysis were inserted in Equation 7-18, which was then used to generate simulated growth data. The complete list of parameters is provided in Table 7-5 and the result of the simulations are presented in Figure 7.20 where they are overlaid on the experimental data. Note that the value of K_2 was slightly optimized to fit the growth data and is 3.5 times smaller than what obtained on Figure 7.19 (b). This optimization, which kept the value of K_2 well within the boundaries allowed by its uncertainty, was done at 260°C using a value of z_1=7nm. We adjusted z_2 and K_2 to get the appropriate height of the initial intensity increase and time to complete reaction. Q_i, ηK_{io}^2, Q_d, and z_0 were then kept fixed for all temperatures leaving z_2 and t_{offset} as the adjustment parameters. Exceptionally, K_2 had to be slightly re-adjusted, still within its uncertainty, to get a good fit to the data at 270 and 280°C.

Table 7-5: List of parameters for the fits of the modified CCBRT model to the experimental growth data.

T° (°C)	Q_i (eV)	ηK_{i0}^2 (s^{-2})	Q_d (eV)	K_2(cm^2s^{-1})	z_1 (nm)	z_2 (nm)	t_{offset} (s)
240	1.175	3.5×10^{19}	2.05	1×10^{17}	7	7	140
250	1.175	3.5×10^{19}	2.05	1×10^{17}	7	8	55
260	1.175	3.5×10^{19}	2.05	1×10^{17}	7	8	36
270	1.175	3.5×10^{19}	2.05	8×10^{16}	7	12	22
280	1.175	3.5×10^{19}	2.05	6.5×10^{16}	7	13	15

Figure 7.20 indicates that the modified CCBRT model yields a fit to the experimental data that is at least as good as with the original model in Figure 7.15. Figure 7.20 (b) shows the comparison of both the original and modified CCBRT models with the data

obtained at 260°C on a linear time scale. We see that both models fail to describe accurately the transformed volume fraction towards the end of the growth. Indeed the underestimation of the transformed volume fraction by the modified CCBRT model (due to the lack of correction for the impingement of nuclei with the surface) is obvious between 500 and 600 s.

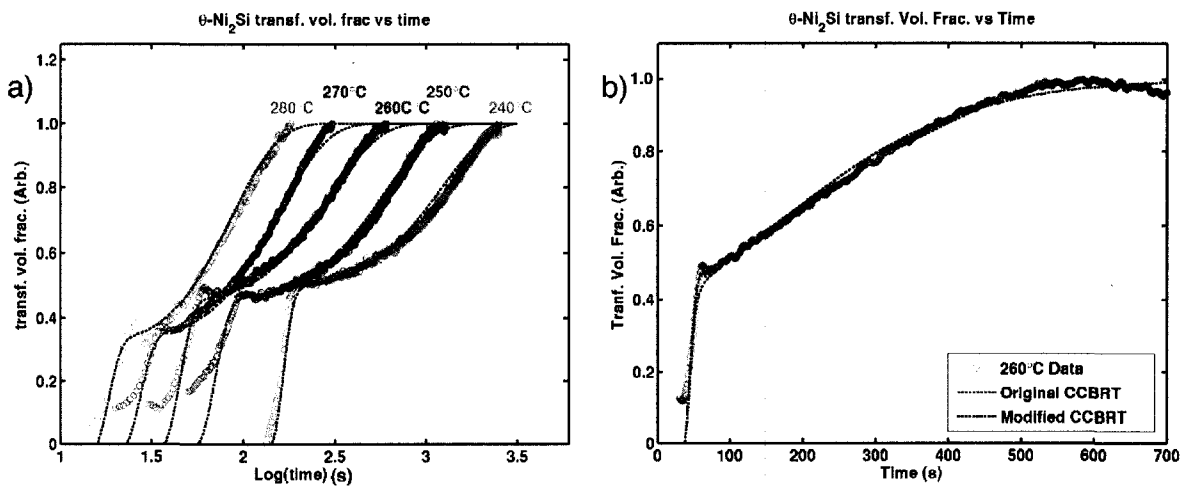

Figure 7.20: (a)Comparison of the modified CCBRT model with the experimental data on a logarithmic time scale for all the investigated temperatures (240 – 280 °C). (b) Comparison of the original and modified CCBRT models with the 260°C experimental data on a linear time scale.

In order to compare the validity of the original and the modified models, we have respectively applied the Avrami and the $\log(\chi_v^2-\chi_{v0}^2)$ vs $\log(t)$ analyses to the data simulated with each of them. The results are presented in Figure 7.21. The Avrami exponent obtained with the original model is 1 instead of 3/2, while the diffusion-controlled growth analysis applied to the data simulated using the modified model produces the same exponent than we have measured on the experimental data in Figure 7.14, i.e. 1.2. The modified CCBRT model therefore appears to give a more complete description of the experimental data.

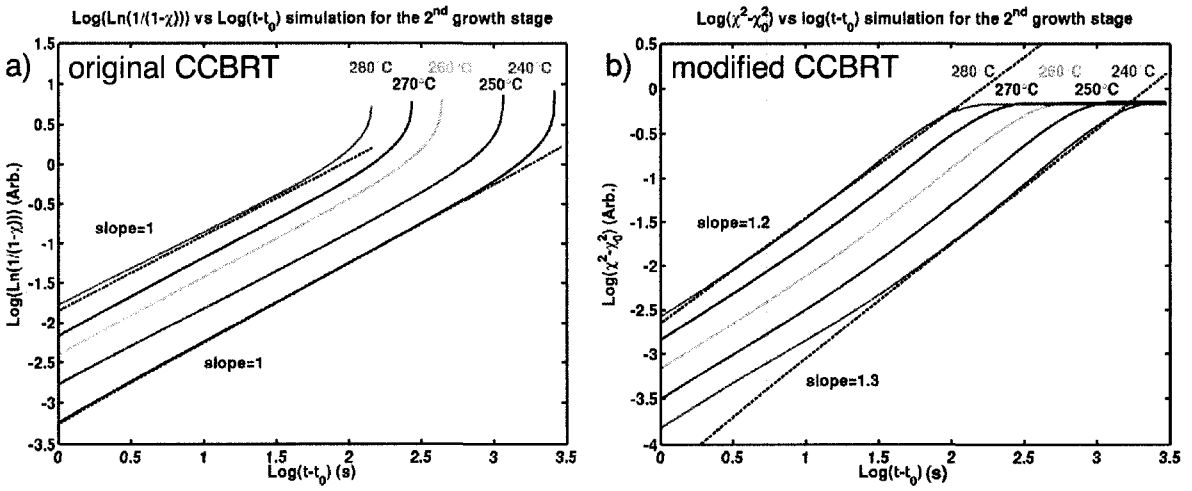

Figure 7.21: a) Avrami analysis of the growth data simulated using the original CCBRT model. b) Diffusion-controlled growth analysis [Log(χ_v^2-χ_{v0}^2) vs Log(t-t_0)] for the growth data simulated using the modified CCBRT model.

An important remark should be made concerning the compatibility of the modified CCBRT model with the growth microstructure. In our simulations, we have allowed the transformed volume fraction in the second stage χ_{v2} to vary up to 1. This means that all the growing hemispheres have coalesced into a continuous layer by the end of the simulation. In fact, the lateral co-existence of the two compounds could only be observed if the θ-Ni_2Si growth were interrupted before χ_{v2} reaches unity. This could be caused by the sudden nucleation of NiSi, which should interrupt the θ-Ni_2Si growth by destabilizing it. The consequence of an incomplete transformation on the signature of the growth in the kinetics analysis therefore needs to be addressed. Figure 7.22 (a) presents the simulation of an arbitrary Avrami-like growth process with an exponent of 1.5 using the following general expression :

Equation 7-20 $$\chi = 1 - e^{-kt^{\frac{3}{2}}}$$

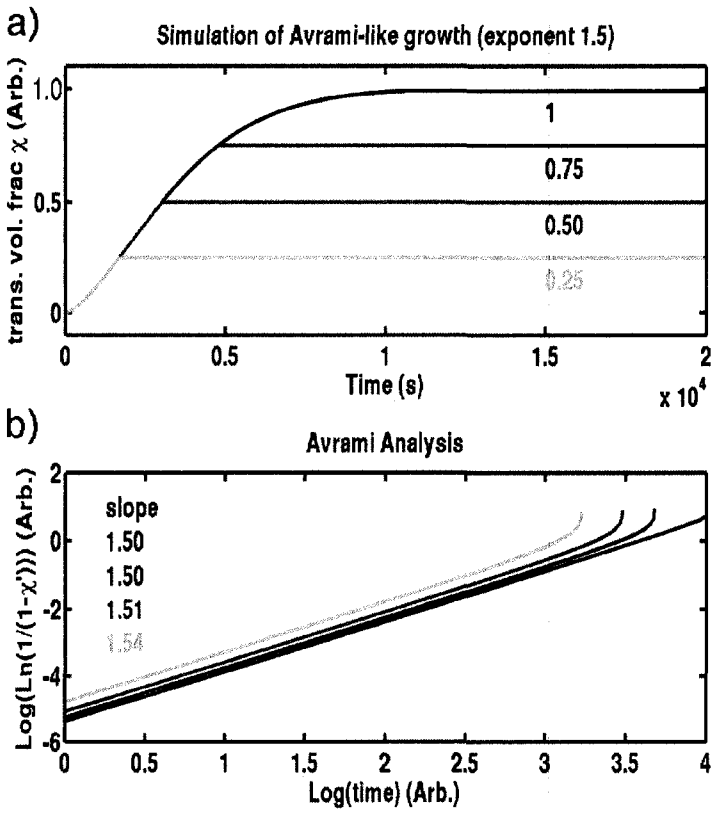

Figure 7.22: a) Simulation of Avrami-like growth with an exponent of 1.5. The different colors indicate different values of the transformed fraction at which the growth is interrupted. b) Avrami analysis of the data in a).

The simulated growth presented in Figure 7.22 (a) was stopped at different values of χ to simulate an early interruption of the reaction. Figure 7.22 (b) presents the Avrami analysis of each case, using a transformed fraction χ', which is computed as χ renormalized to its value at the moment of the interruption. Figure 7.22 shows that regardless the growth stage at which the interruption occurs, the Avrami analysis yields the same exponent to within the measurement accuracy. Consequently, despite our modified CCBRT model simulates a complete transformation, a growth process described by this model and interrupted at an intermediate stage will produce the same

signature in the kinetics analysis. The modified CCBRT model is therefore compatible with a lateral co-existence of δ-Ni_2Si and θ-Ni_2Si and with our experimental data.

As a last test of the validity of the modified CCBRT model, an Avrami analysis of the δ-Ni_2Si consumption was performed using the integrated intensity under the (013)/(211) XRD peak of the compound in the time range corresponding to the second growth stage of θ-Ni_2Si. Figure 7.23 shows that the data is well fitted with straight lines, except in the very early stages. The straight lines have slopes around 1.5 and the Arrhenius plot of the Avrami constant yields an activation energy of 2.1±0.45eV, which is the same than the one obtained in Figure 7.19. Our results therefore suggest that the growth of θ-Ni_2Si clearly consumes the δ-Ni_2Si and that it is better described using a non-planar growth model.

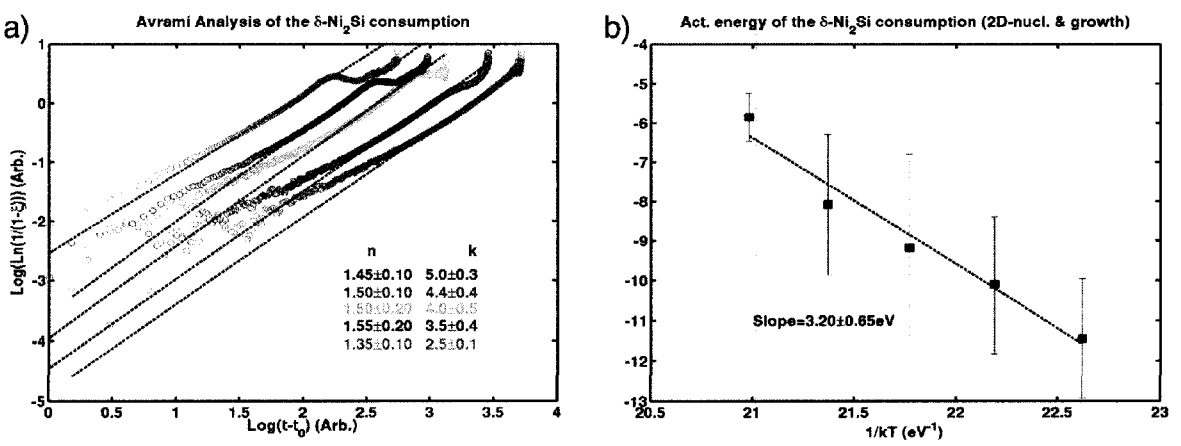

Figure 7.23: a) Avrami plot of the δ-Ni_2Si consumption using the integrated intensity under the (013)/(211) XRD peak. b) Arrhenius plot of the Avrami constant.

7.4.4 1D-diffusion-controlled growth with non-constant diffusion coefficient.

The growth kinetics of a non-stoichiometric compound like θ-Ni_2Si cannot be investigated without considering the possibility of a varying composition during the reaction. As a consequence of compositional changes, the diffusion coefficient is expected to vary during the growth, a problem which was addressed by d'Heurle and Ghez.[187] They have studied more particularly the solid-state formation of the non-stoichiometric compound AlNi, which has an homogeneity range of about 10%, extending on either sides of the 50:50 Al:Ni composition. They have found that the growing AlNi layers consist of two regions of almost constant, yet different, compositions C_m, each corresponding to a local maximum of the diffusion coefficient $D(C_m)$. These two C_m compositions are located almost symmetrically about the 50:50 value and the two maxima $D(C_m)$ correspond in fact to a maximum in Ni diffusion and in Al diffusion respectively. d'Heurle and Ghez have shown that the growth of each region can be described mathematically using a single combined and constant diffusion coefficient expressed as a function of the maximum and minimum values $D(C_m)$ as well as the composition values C_m at which they occur.

AlNi is a fairly well characterized compound with a known dependence of the integrated diffusion coefficient on composition. θ-Ni_2Si is not as well characterized, and we can only speculate about its diffusion properties. We can certainly expect the diffusion coefficient to be maximal at some given composition but it is not clear whether only one or several of such compositions can exist over its homogeneity range. Moreover, θ-Ni_2Si is a Ni-rich compound that changes composition by varying the occupancy of sites on a Ni sublattice. It is therefore not likely to observe a maximum in Si diffusion. We consequently expect a single composition where the diffusion coefficient will be maximal, such that we would expect the composition of θ-Ni_2Si, and

hence the diffusion of Ni, not to change much during the growth. If the composition and diffusion coefficient did change, d'Heurle has shown that the growth could still be described using a single and constant diffusion coefficient value and that we should still observe the typical square-root of time dependence for the thickness of the product layer. However, the exponent of 1.2 we obtain from the log-log analysis of the second growth stage suggests that the diffusion coefficient and the composition could be varying slightly.

In order to address the problem of growth with varying diffusion coefficient, we have simulated the θ-Ni_2Si growth using the original CCBRT model where k_{d0} is given a hypothetical time variability. Such simulations come however with an additional difficulty since we use x-ray diffraction to monitor the transformed volume. If we admit a compositional variation, we must take into account its effect on diffraction. This is typically achieved by modifying the structure factor F_{hkl} that enters the calculation of the diffracted intensity. Figure 7.24 presents the θ-Ni_2Si unit cell where the atoms composing the motif are emphasized by hatched and crosshatched patterns. The corresponding atomic positions in the unit cell are summarized in Table 7-6.

The general form of the structure factor for the hexagonal θ-Ni_2Si is given by:

Equation 7-21
$$F_{hkl} = f_{Ni}\left[e^{-2\pi i(0h+0k+0l)} + e^{-2\pi i(0h+0k+\frac{1}{2}l)} + e^{-2\pi i(\frac{2}{3}h+\frac{1}{3}k+\frac{3}{4}l)} + e^{-2\pi i(\frac{1}{3}h+\frac{2}{3}k+\frac{3}{4}l)}\right] + f_{Si}\left[e^{-2\pi i(\frac{1}{3}h+\frac{2}{3}k+\frac{3}{4}l)} + e^{-2\pi i(\frac{2}{3}h+\frac{1}{3}k+\frac{1}{4}l)}\right]$$

where f_{Ni} and f_{Si}, the atomic scattering factors of Ni and Si, are respectively 19.982 and 8.6945 as calculated using the procedure detailed in reference 188. If all the internal,

cross-hatched Ni atom sites are occupied, i.e. if the composition is precisely Ni_2Si, the structure factor for the θ-Ni_2Si (110) reflection is:

Equation 7-22 $$F_{110} = 4f_{Ni} + 2f_{Si}$$

For a Ni-deficient θ-Ni_2Si it becomes :

Equation 7-23 $$F_{110} = 2f_{Ni}(1+\chi_{Ni}) + 2f_{Si}$$

where χ_{Ni} is the occupancy fraction of the internal Ni sites. It is 1 for the composition of Ni_2Si (33% Si) and would be 0 for the composition of NiSi (50% Si). Note however, that based on the Ni-Si phase diagram, the hexagonal structure is not stable beyond 41% Si.

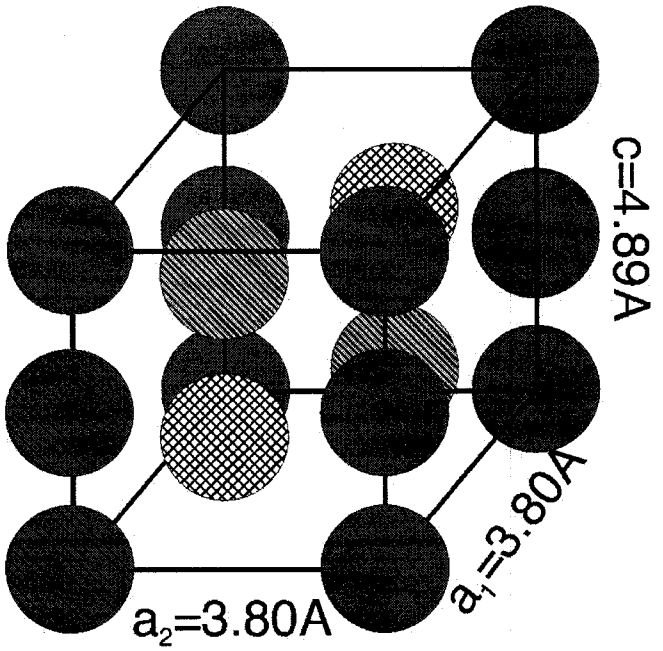

Figure 7.24: Unit cell of θ-Ni_2Si. The hatched and cross-hatched atoms build the motif which serves for the calculation of the structure factor.

Table 7-6: Atomic positions in the θ-Ni_2Si unit cell for the calculation of the structure factor F_{hkl}

Atom	Position
Ni	(0 , 0 , 0)
Ni	(0 , 0 , 1/2)
Ni	(2/3 , 1/3 , 3/4)
Ni	(1/3 , 2/3 , 1/4)
Si	(1/3 , 2/3 , 3/4)
Si	(2/3 , 1/3 , 1/4)

Figure 7.25 (a) shows the dependence of F_{110} on the occupancy fraction (bottom abscissa) and on the composition in Si (top abscissa). The relationship is almost linear between the compositions 0.33 and 0.41. Figure 7.25 (b) shows that the effect of composition on the θ-Ni_2Si (110) XRD peak's position is also quite linear. In Figure 7.3 (c), we have shown that the position of the θ-Ni_2Si (110) changes by about 0.4° during the second stage of its formation. If we assume that the shift in position is solely caused by a compositional change, as opposed to stress, its magnitude would be estimated to about 4%.

While we can readily estimate that the structure factor will vary by about 15%-25% (~1500 compared to about 7000) upon such a compositional change, we cannot predict the magnitude of the variation in the diffusion constant. It is known that small changes in composition can cause variations in the diffusion by orders of magnitude. For the purpose of our simulations, we have assumed a variation by a factor of 10. Bearing in mind that Ni is the main moving species in all Ni silicides, we have assumed this variation to be such that Ni diffusion increases as the internal Ni sites are emptied. F_{110} and k_{d0} therefore vary in opposite directions; F_{110} decreases as k_{d0} increases.

Figure 7.26 shows the results of the simulations done with the original CCBRT model including the corrections for variable K_{d0} (increasing) and F_{110} (decreasing). We

present two sets of simulations in which K_{d0} and F_{110} vary respectively with the square root of time - $\sqrt{t}$ - (a-d) and linearly with time - ct - (e-g).

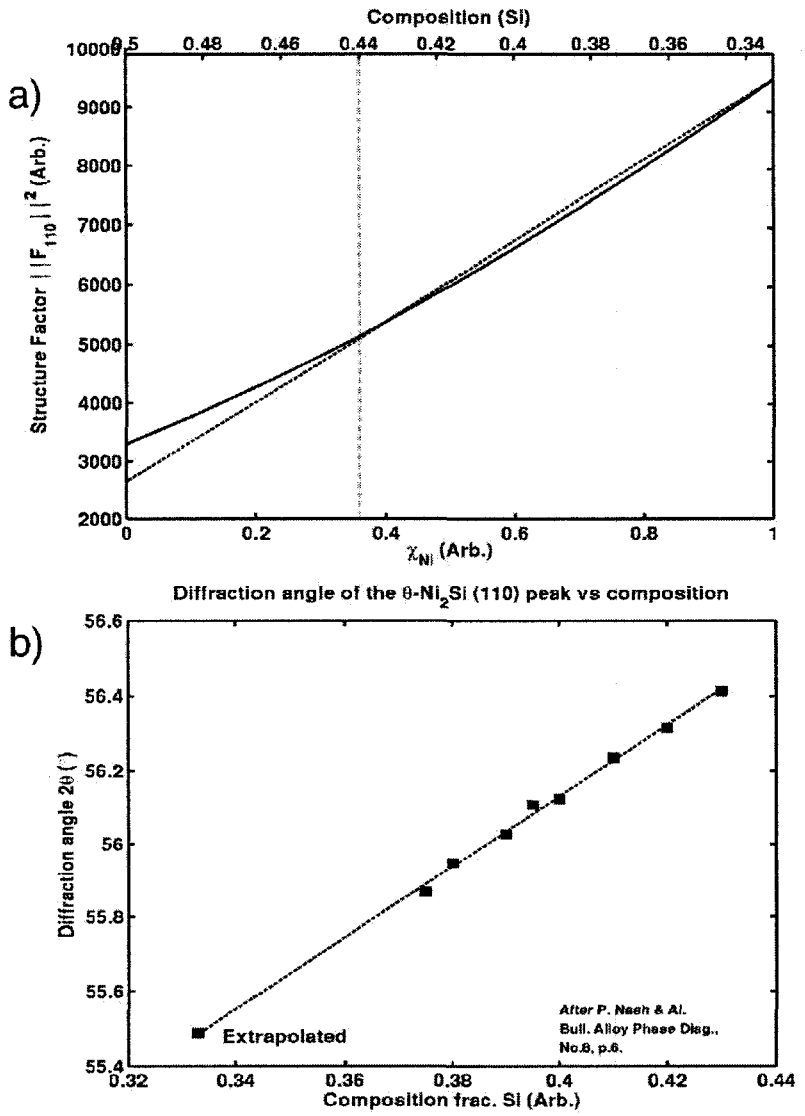

Figure 7.25: a) Structure factor of the θ-Ni_2Si (110) reflection as a function of the occupancy of the Ni sites (crosshatched atomes in Figure 7.24) and composition (top x-axis). b) Position of the θ-Ni_2Si (110) XRD peak as a function of composition.

For the purpose of the modeling, we have arbitrarily assumed the composition to be constant at $Ni_{61}Si_{39}$ and $Ni_{62}Si_{38}$ during the first growth stage of the $\sqrt{t}$ and ct cases

respectively. The transformed volume fraction $\chi_v(t)$ is calculated, incorporating the variation of k_{d0} for the whole duration of the experiment, and is then corrected for the variation of F_{110}. For this correction, a new transformed fraction $\chi_v'(t)$, weighted by the structure factor, is established as $\chi_v'(t)= F_{110}(t)\chi_v(t)$ and $\chi_v'(t)$ is then renormalized so that its maximum is 1. In all cases, the variations in K_{d0} and F_{110} correspond to about 3-4% changes in composition. Both the $\sqrt{t}$ and the ct variation schemes yield reasonable fits to the data. However, while the diffusion-controlled analysis produce exponents similar, within the measurement accuracy, to those observed with the experimental data (Figure 7.26 (d) and (h)), the Avrami exponents are slightly lower in these simulations than in the experimental results (Figure 7.26 (c) and (g)). Simulations done with decreasing K_{d0} (and increasing F_{110}) resulted in even poorer fits to the data (not shown). The Avrami exponents were 1 and 1.05, respectively for the $\sqrt{t}$ and ct variation schemes, while the log-log exponents were around 1.1 in both cases. Since the time variations of K_{d0} and F_{110} are forced and arbitrary, we cannot validate the simulations using the activation energies.

Beyond the two easy choices of time dependence we have investigated, one could most likely find other suitable combinations of K_{d0} and F_{110} time dependences that would produce exactly the expected kinetics signatures. However, as long as they remain hypothetical and user-set, it is difficult or probably impossible to validate the choices using activation energies. We therefore conclude that the simulations of Figure 7.26 are not sufficient to confirm nor exclude the possibility that θ-Ni_2Si changes composition as it grows.

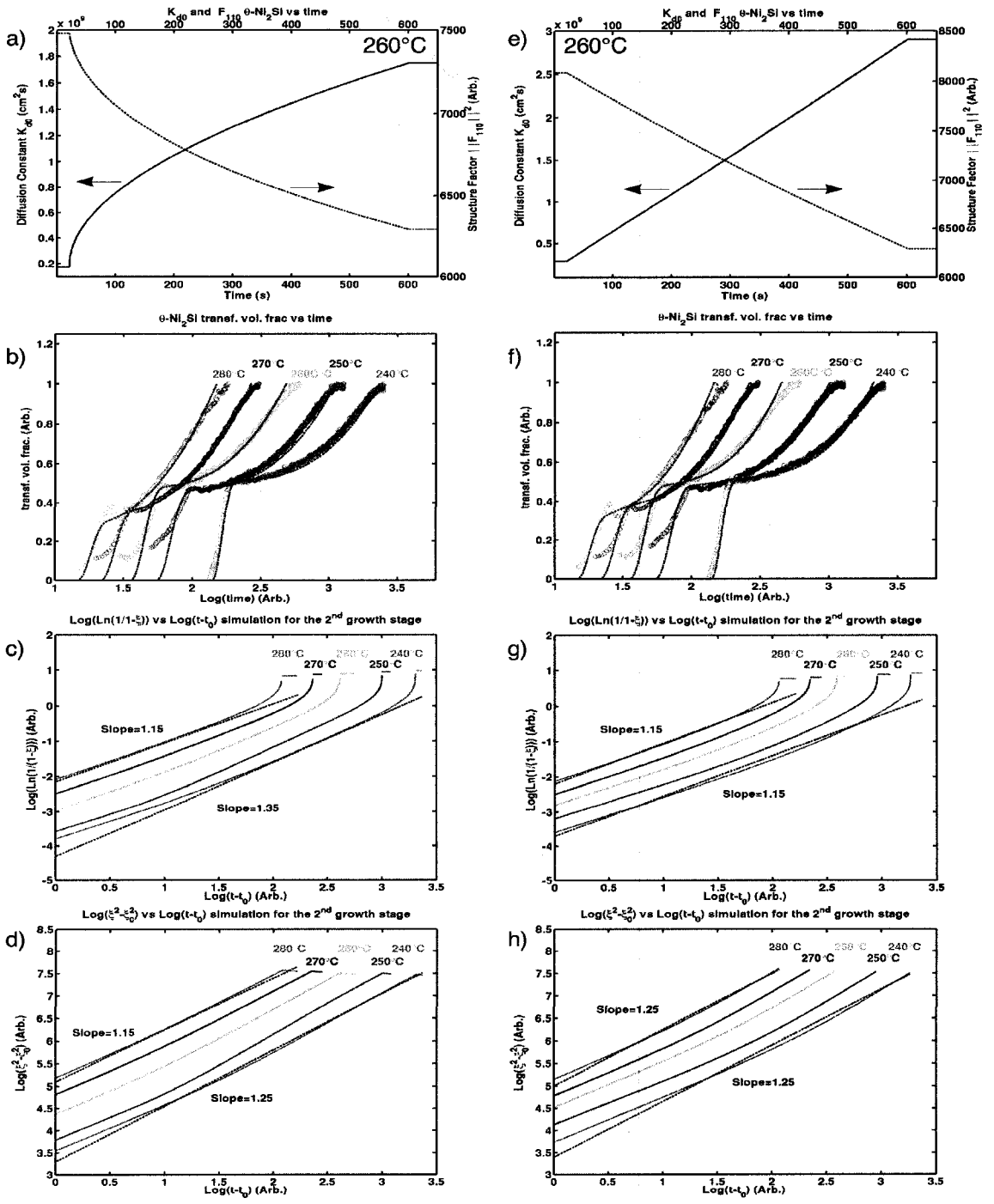

Figure 7.26: Simulations of growth using the CCBRT model incorporating a compositional variation. The diffusion constant K_{d0} and structure factor F_{hkl} vary as √time on the left and as time on the right. a),e) K_{d0} and F_{hkl} vs time, b),f) comparison of the simulations with the experimental data, c),d) Avrami Analysis and d),h) diffusion-controlled growth analysis.

7.4.5 Effect of fluorine on the θ-Ni_2Si growth kinetics

Our results on fluorine-implanted c-Si (001) indicate that the first stage of the reaction consisting of the 2D nucleation-controlled growth is suppressed in samples with the largest F dose. However, a third stage appears in which the intensity of the θ-Ni_2Si (110) peak increases in the absence of δ-Ni_2Si until θ-Ni_2Si becomes the only compound revealed by the XRD. From the TEM investigation presented in Chapter 6, we know that θ-Ni_2Si forms a continuous layer at the end of its growth in F-implanted samples. In the modified model we propose, the growth starts with the 3D diffusion-controlled scheme presented above (the modified part of the CCBRT model) and ends with a 1D-diffusion-controlled growth occurring when the θ-Ni_2Si has consumed all the δ-Ni_2Si layer an coalesced into a continuous layer.

Figure 7.27 compares the results of the simulated growth with the experimental data at 280°C on a linear time scale. It is now very clear that simple 1D diffusion-controlled growth in the third stage fails to describe accurately the experimental data. The actual reaction slows down more rapidly than the simulations. From the SIMS data presented in Chapter 6, we know that some fluorine redistributes in the growing θ-Ni_2Si, possibly slowing down the diffusion either within the grains, in grain boundaries or in both. We have also shown that the largest part of what we assume to be θ-Ni_2Si growth in F-implanted samples occurs in the absence of δ-Ni_2Si, while we do not know exactly what is consumed to provide the Ni atoms required to convert into θ-Ni_2Si the Si or an eventual amorphous Ni-poor silicide present at the interface. The non-stoechiometric compound could very well serve as its own source of Ni atoms, therefore growing with a decreasing content in Ni.

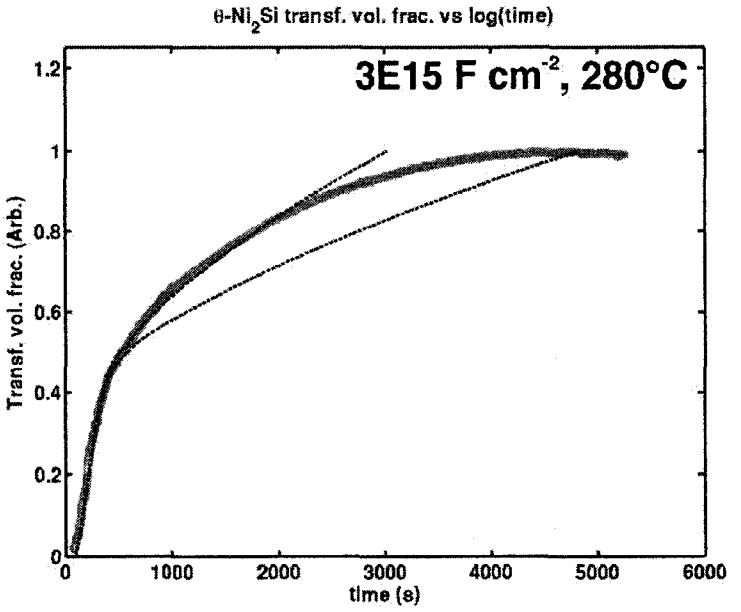

Figure 7.27: Comparison on a linear time scale of the growth data at 280°C with a modified CCBRT model where the third growth stage consists of 1D diffusion-controlled growth.

Figure 7.28 shows the comparison of two additional modifications of the CCBRT model with the experimental data obtained on samples with 3×10^{15} F cm^{-2}. The data is presented on both logarithmic and linear time scales to help appreciate the fit in both the early and late stages of the reaction. In all cases, the growth starts by the 3D diffusion-controlled growth of θ-Ni_2Si at the expense of δ-Ni_2Si with the activation energy and the diffusion constant found in Table 7-5. In Figure 7.28 (a) and (b) the diffusion constant K_2 of the subsequent 1D diffusion-controlled growth decreases linearly with time by one order of magnitude to simulate the simple case where the incorporation of fluorine into the growing θ-Ni_2Si slows down the diffusion. In Figure 7.28 (c) and (d) K_2 increases while the structure factor F_{hkl} decreases (both linearly with time) to simulate the case where θ-Ni_2Si serves as its own source of Ni atoms. In such a case, the volume increases as the compound grows but its concentration in Ni atoms decreases, damping the increase in diffracted intensity. While not explicitly treated, there could still be an effect of

fluorine on both the diffusion and the structure factor, competing with the decrease in Ni content.

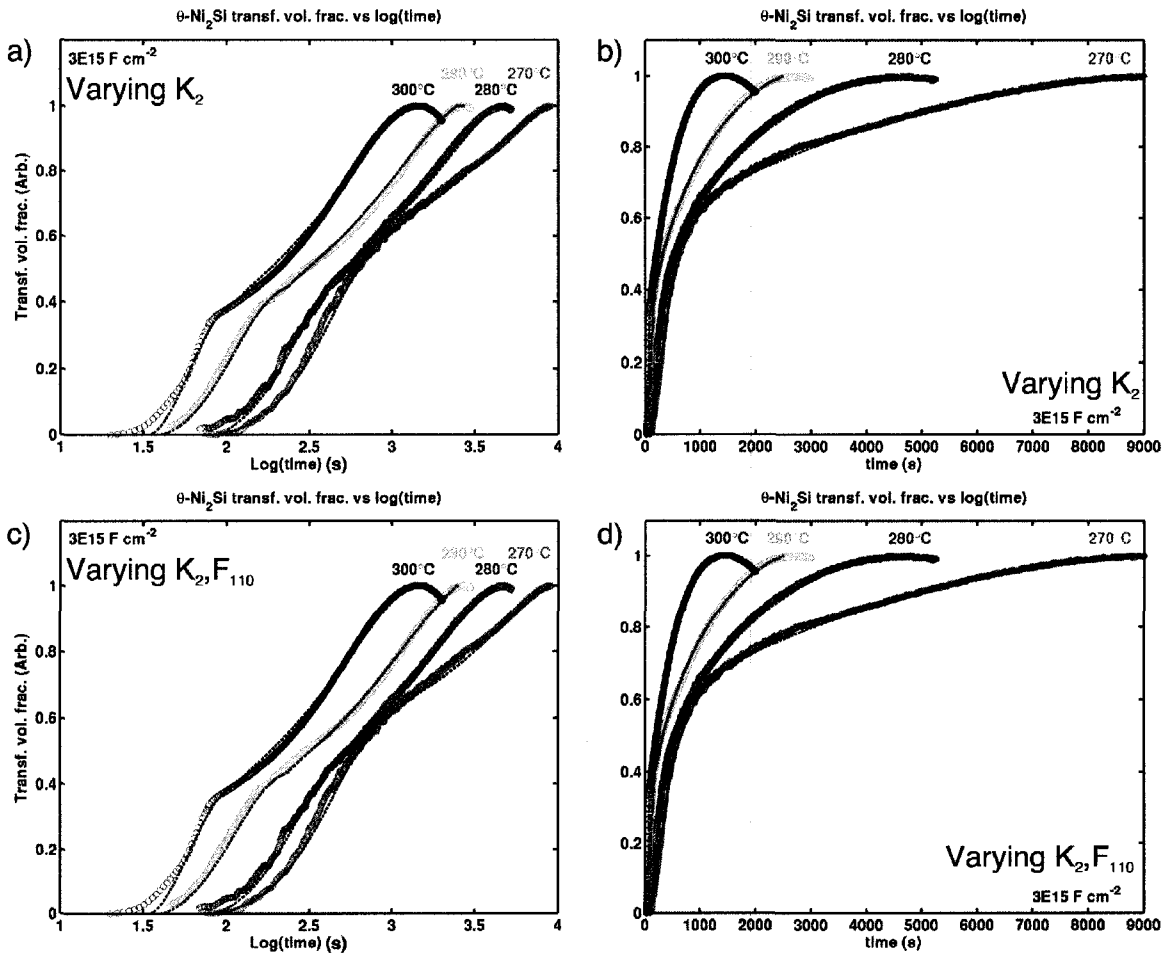

Figure 7.28: Comparison of two modifications of the CCBRT model with the experimental data on samples with 3E15 F cm^2. Data plotted on logarithmic (left) and linear (right) time scales. (a)-(b) Varying diffusion coefficient and (c)-(d) Varying diffusion coefficient and composition.

In both cases (varying K_2, varying K_2 and F_{hkl}) we find a reasonable fit to the data. It is not possible to establish from Figure 7.28 which model best describes the data. Figure 7.29 shows the comparison of the signatures of the two kinetics analyses we have used throughout this chapter.

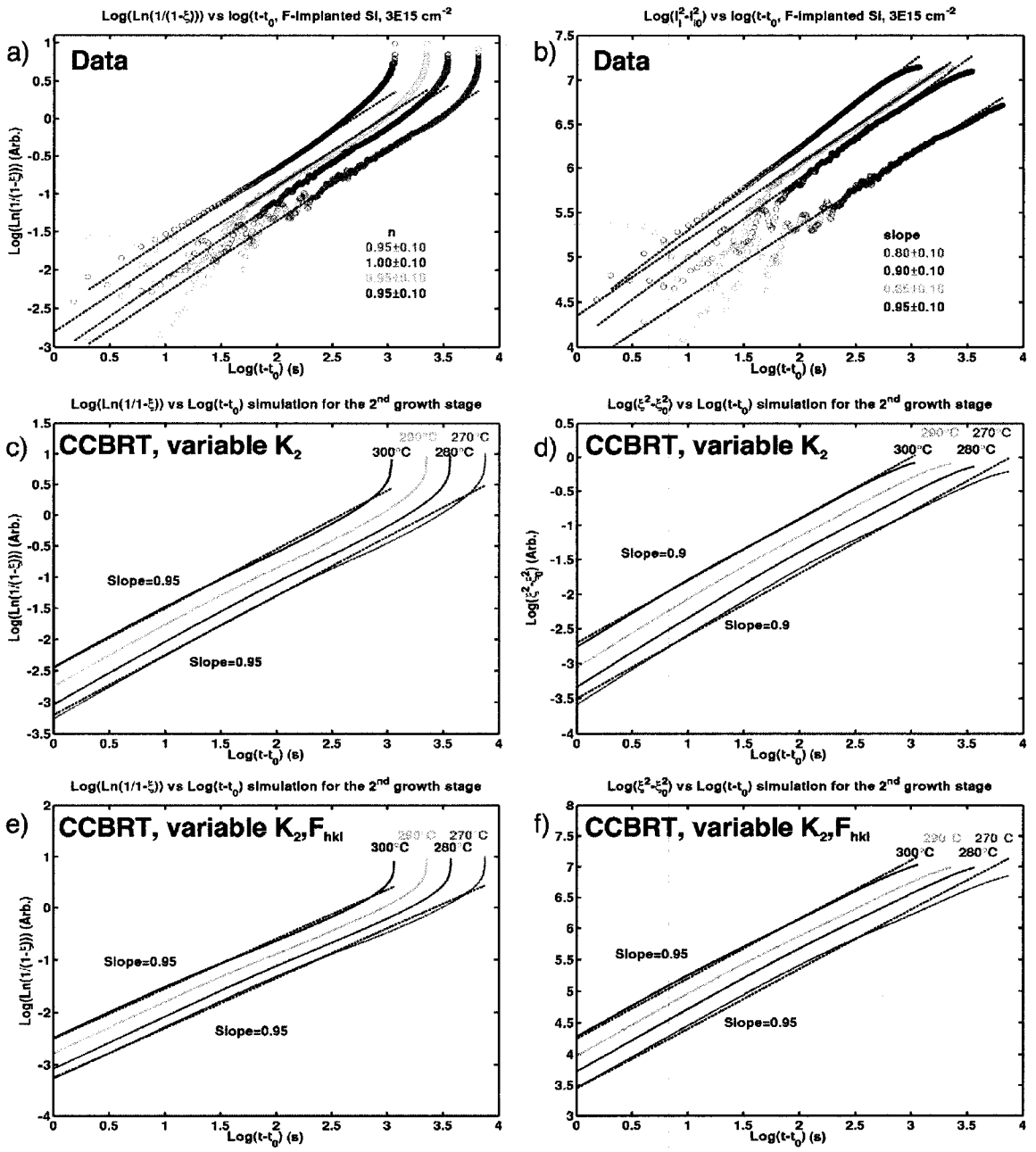

Figure 7.29: Kinetics analyses of the experimental and simulated growth data. (a),(c) and (e) Avrami Analysis, (b),(d) and (f) Diffusion-controlled growth analysis. Growth data simulated using the modified CCBRT model with (c), (d) varying K_2, and (e), (f) varying K_2 and F_{hkl}.

The Avrami analysis is presented in Figure 7.29 for (a) experimental data and for the growth data simulated with (c) varying K_2 and (e) varying K_2 and F_{hkl}. Figure 7.29 (b),

(d), and (f) presents the diffusion-controlled growth analysis for the same sets of data. In all cases, the simulated signatures are sufficiently close to the experimental signatures so that it is not possible to discriminate which model give the best description of the data. While we cannot determine from the above analysis whether the θ-Ni_2Si changes composition during the growth on F-implanted Si(001) substrates, it appears clear that the diffusion coefficient is not constant.

7.4.6 Consumption of θ-Ni_2Si

Our results on both undoped and F-implanted Si(001) indicate that the consumption of the θ-Ni_2Si is well described by an Avrami-like growth with an exponent of 2, suggesting that the process occurs in two dimensions. This claim finds support in the match between the activation energy obtained through the Avrami and the Kissinger's analyses. The results we have presented in the preceding chapters point at the formation of NiSi as the trigger of the θ-Ni_2Si consumption. However, we have also shown that the consumption of θ-Ni_2Si is accompanied by a return of δ-Ni_2Si. In Chapter 5 we have explained that this return is consistent with the structure of the Ni-Si phase diagram and that the simultaneous formation of NiSi and δ-Ni_2Si is a normal consequence of the consumption of the metastable θ-Ni_2Si. The re-growth of Ni_2Si must therefore occur at the expense of the θ-Ni_2Si, contributing to the decrease of its measured volume.

On one hand it cannot be excluded that both NiSi and Ni_2Si form in the same plane through a process which can globally be described by an Avrami-like model. Figure 5.11 clearly gives evidence of the lateral co-existence of θ-Ni_2Si, δ-Ni_2Si and NiSi in samples with 100nm starting Ni thickness. On the other hand, all the TEM micrographs taken on samples with 10nm Ni quenched at the maximum development of the θ-Ni_2Si during isothermal experiments showed a dominant, large-grained NiSi layer

at the interface with the Si, while θ-Ni_2Si, δ-Ni_2Si co-exist laterally in the top layer. This microstructure is consistent with a 2D nucleation-controlled growth of NiSi in samples that might have undergone un-controlled reaction during the TEM specimen preparation. One must therefore be careful in attributing the exponent of 2 to the growth of either NiSi or δ-Ni_2Si alone.

θ-Ni_2Si, δ-Ni_2Si and NiSi having different compositions, there should be mass transport during the θ-Ni_2Si consumption process while nucleation-and-growth processes are usually expected to occur in compositionally homogeneous regions. It is interesting to note that the activation energy we find for the consumption process is very close to that obtained for the diffusion-controlled growth of NiSi. However, log-log plots of the consumption data similar to those of Figure 7.14 (b) (not shown) yield exponents around 1.5 suggesting that it is not well described by a 1D diffusion-controlled growth model.

Assuming that the Avrami model applies, the exponent of 2 means that the activation energy of 1.7eV is the sum of the activation energy for nucleation (E_{nuc}) and twice that for the growth (E_{growth}) (c.f. section 2.2.3). E_{nuc} is therefore very small and E_{growth} is below 1. A low nucleation barrier for the consumption process is consistent with the metastable nature of θ-Ni_2Si, because the drive for its disappearance should be large; however it is surprising to observe a nucleation-controlled growth scheme for a reaction that should have a large driving force.

In Chapters 5 and 6, we have shown that the vacancies the θ-Ni_2Si can sustain play an important role in its consumption. Vacancy diffusion is known to be rapid and characterized by low activation energies: an activation energy of 0.44eV was reported for the diffusion of vacancies in Si,[189] and a value of 0.67eV was reported for the diffusion of Si vacancies in $ErSi_2$[190]. The simultaneous formation of δ-Ni_2Si and NiSi could therefore be the consequence of vacancy motion within the θ-Ni_2Si. Vacancy

accumulation would result in the formation of NiSi while depletion would result in the formation of δ-Ni_2Si. Since the crystal structures of θ-Ni_2Si, δ-Ni_2Si and NiSi are similar, δ-Ni_2Si and NiSi can nucleate at very low interface energy cost, and subsequently grow very fast through further vacancy motion. We have proposed in Chapter 5 that the θ-Ni_2Si consumption could proceed in two steps; nucleation and growth of NiSi until sufficient vacancy depletion favors the return towards the more stable δ-Ni_2Si. The results we present in this chapter suggest that both events may not be as separated in time as the Avrami exponent we obtain for the consumption remains the same over a range of temperature where the extent of the θ-Ni_2Si growth as well as that of the δ-Ni_2Si consumption and re-growth change significantly.

Vacancy-mediated consumption is also consistent with the gradual suppression of the δ-Ni_2Si re-growth by fluorine implantations and by addition of impurities in general. Foreign atoms with an affinity for vacancies will occupy them, suppressing a fast kinetic path for the consumption of the θ-Ni_2Si and mostly for the re-growth of δ-Ni_2Si. On one hand the impurity solubility stabilizes the metastable compound, delaying its consumption, and the other hand, it hinders the formation of δ-Ni_2Si once the consumption occurs.

7.4.7 Activation energies

Beyond the growth geometry assumed in the original and modified forms of the CCBRT model, an important result of this chapter is that θ-Ni_2Si grows in two distinct stages with different activation energies. The major part of the growth occurs in the second stage, where the diffusion is the limiting mechanism. This stage, whereby the δ-Ni_2Si is consumed, is characterized by a larger activation energy than both the nucleation-controlled initial growth stage and the consumption stage. In Chapters 5 and 6

as well as in Figure 7.2 and Figure 7.3, we have shown that the annealing temperature and mode (isothermal or ramp-type) had an impact on the extent to which the δ-Ni_2Si is consumed by the growth of θ-Ni_2Si. Indeed, for reactions occurring on undoped c-Si (001), the δ-Ni_2Si (013)/(211) peak decreases significantly more during isothermal anneals above 260 °C and ramped-type anneals, where the formation of θ-Ni_2Si is completed around 330 °C, than during isothermal annealings at temperatures below 270 °C. The larger activation energy of the second growth regime compared to the two other processes is consistent with a faster increase in its reaction rate as the temperature increases, while a slower increase in rate is expected in the lower activation processes.

7.5 Conclusion

In this chapter we have shown that the growth of θ-Ni_2Si is a complex two-staged process that cannot be readily described using standard growth kinetics models. We have proposed a modification of the Coffey-Clevenger-Barmak-Rudeman-Thompson model whereby the first growth stage consists of a 2-D nucleation-controlled growth with an activation energy of 1.17eV and the second stage consists of a 3D diffusion-controlled penetration of θ-Ni_2Si in the grain boundaries of the overlying δ-Ni_2Si. The process is characterized by an activation energy of about 2.05±0.5 eV which increases to 2.8±0.5 eV with F-implantation. We have shown that θ-Ni_2Si grows most-likely with a constant composition and diffusion coefficient on undoped Si(001) while both quantities seem to vary in reactions on F-implanted Si(001). We have shown that the consumption of θ-Ni_2Si is well described by a Johnson-Mehl-Avrami model with an exponent of 2, indicating a two-dimensional planar process with an overall activation energy of about 1.7eV. This value, which is the sum of the activation energy for nucleation and twice that for growth, is consistent with a consumption process where δ-Ni_2Si and NiSi form possibly at the same time through vacancy motion.

Chapter :8 Conclusion, general discussion, and perspectives

8.1 Summary of the results

The objective we set out to accomplish at the beginning of this thesis was to develop a fundamental understanding of the thermally induced solid-state reactions that lead to the formation of NiSi. Accordingly, we have revisited the Ni-Si reactions through the means of *in situ* XRD and wafer curvature measurements, in combination with *ex situ* transmission electron microscopy, Rutherford backscattering spectroscopy as well as secondary ions mass spectroscopy. Using these techniques, we have investigated the compound formation sequence, and the microstructure of the reacted samples in addition to studying the effects of alloying and doping elements on the reaction pathways and growth kinetics.

Our results have revealed that Ni-Si reactions are much more complex than initially thought and reported in the vast literature pertaining to the subject. While δ-Ni_2Si was traditionally the only compound reported to form before NiSi upon annealing, we have found evidence for the formation of up to three additional Ni-rich compounds, θ-Ni_2Si, $Ni_{31}Si_{12}$, and Ni_3Si_2, before the formation of the monosilicide. In apparent contradiction with the common understanding of thin film reactions, these additional compounds co-exist laterally (within the same layer) with δ-Ni_2Si, which they consume upon growing, and subsequently redeem in part upon being consumed.

The nucleation of the metastable θ-Ni_2Si is promoted by a complex combination of *i)* the low driving force for the growth of NiSi and Ni_3Si_2 (which are further hindered

by concentration gradients at the silicide/Si interface), *ii)* a simple crystal structure, *iii)* a low interface energy offered by the δ-Ni_2Si grain boundaries, *iv)* the ability of the compound to sustain vacancies, which permits fast growth, and, finally, *v)* a wide homogeneity range which allows for easier nucleation in an interfacial layer with a very sharp composition gradient. The low interface energy offered by the δ-Ni_2Si grain boundaries is a consequence of the similarity between the crystal structures of θ-Ni_2Si and δ-Ni_2Si. Furthermore, the compound forms systematically at the same time/temperature regardless of the initial Ni film thickness (4-500 nm), an indication that nucleation mostly plays a limiting role in the growth of θ-Ni_2Si. Its disappearance is correlated with both the growth of NiSi and with a surprising return of orthorhombic δ-Ni_2Si. Indeed, θ-Ni_2Si is most likely consumed by the growing NiSi as it absorbs fast moving vacancies until a return towards a richer Ni content in the remaining unconsumed θ-Ni_2Si becomes favorable. The regrowth of δ-Ni_2Si then simply follows from a polymorphic transformation of a Ni-rich θ-Ni_2Si facilitated by the structural similarity between both compounds.

The formation of $Ni_{31}Si_{12}$, observed in samples with 100 nm Ni and more, is initiated in the grain boundaries of the δ-Ni_2Si, when a combination of appropriate Ni atoms flux and temperature (~ 375 °C) is reached. The extent of its formation depends strongly on the Ni supply, and its disappearance is also correlated with the simultaneous formation of NiSi and δ-Ni_2Si. The mechanism is, however, different than for θ-Ni_2Si, as both events now occur at different interfaces. Indeed, upon the shortage in Ni supply, NiSi can nucleate at the δ-Ni_2Si/Si interface and Si diffusion in the δ-Ni_2Si grain boundaries brings enough reactant towards the top part of the layer stack to convert the $Ni_{31}Si_{12}$ back into δ-Ni_2Si. In samples with large initial Ni layers (500 nm), $Ni_{31}Si_{12}$ takes over δ-Ni_2Si, presumably growing through a diffusion-controlled growth, after it was able to nucleate, as long as Ni is available.

The formation of Ni_3Si_2 is only observed in samples where δ-Ni_2Si and NiSi are simultaneously present at temperatures above 600 °C. It is not clear whether the nucleation of the compound occurs because of an instability of δ-Ni_2Si as it becomes so thin that surface energies become too important or because the combination of the temperature and Ni supply allows for the nucleation of its complex crystal structure.

An investigation of the effect of alloying elements and impurities on the Ni-Si reactions confirms that nucleation plays a limiting role in the growth of metastable θ-Ni_2Si and that the template provided by δ-Ni_2Si is crucial in promoting the nucleation. Activated CMOS dopants and alloying impurities delay the growth of all Ni-rich compounds and eventually suppress the formation of θ-Ni_2Si presumably because of limited solubility. The suppression of the formation by Pt results most probably from favored NiSi nucleation and growth. Conversely, impurities implanted without subsequent re-crystallization anneals stabilize θ-Ni_2Si partly through the presence of an amorphous interface, at least at the beginning of the reaction. The stabilization effect is enhanced by the segregation of F to grain boundaries, where it forms strong Si-F and Ni-F bonds, and by a possibly large solubility in θ-Ni_2Si in which the F atoms would occupy the vacancy sites of this relatively open structure. In doing so, they would reduce both the diffusion of the vacancies and of the Ni atoms.

The study of stress in F-implanted c-Si(001), where the re-growth δ-Ni_2Si is suppressed, indicates that the disappearance of θ-Ni_2Si is not triggered by the accumulation of compressive stress. The nucleation of NiSi is thus the most likely cause of this behavior. Furthermore, reactions with amorphized and amorphous substrates indicate that the possibility of epitaxy with the Si substrate is not a necessary condition for the formation of that compound.

A quantitative investigation of the θ-Ni_2Si growth kinetics on undoped Si(001) reveals two distinct stages which are well described by a model incorporating 2D nucleation-controlled growth at the silicide/Si interface followed by the non-planar diffusion-controlled penetration of θ-Ni_2Si in the overlying δ-Ni_2Si grains. Despite the very good fit of the non-planar model to our data, we cannot completely rule out the possibility that the second stage consists of a 1D diffusion-controlled planar growth during which the composition of the non-stoichiometric θ-Ni_2Si changes.

We also observed two stages during the raction in F-doped samples. In this case, however, the second stage is clearly consistent with a 1D diffusion-controlled growth in the absence of δ-Ni_2Si and Ni, which suggests a possible compositional change during growth. The hypothesis that vacancies play a crucial role in the θ-Ni_2Si consumption finds support in the low activation energy value we obtain from the Avrami analysis of this process. The same study suggests that the formation of δ-Ni_2Si and NiSi, occurring upon the consumption of θ-Ni_2Si, are not necessarily separated events, at least at the time and space scales we probe with our *in situ* XRD technique.

8.2 Current understanding of solid state reactions

Our results on the formation of the metastable θ-Ni_2Si phase underline several interesting characteristics of the Ni-Si system, one of which being a difficult nucleation of NiSi. This result is surprising since most, if not all, earlier studies of the NiSi growth kinetics on Si (001) have reported a diffusion-controlled growth. As indicated by d'Heurle,[11] the transformation from δ-Ni_2Si to NiSi is at the limit of being nucleation-controlled given the small difference in Gibbs free energies of formation between these two compounds. Also, as pointed out by Hodaj and Gusak, NiSi nucleation is further hindered by the existence of concentration gradients at the δ-Ni_2Si/Si interface.[46]

Combined with a fast diffusion of Ni in δ-Ni_2Si grain boundaries, these phenomena prevent the formation of NiSi at the δ-Ni_2Si/Si interface as long as unreacted Ni remains available. Following similar arguments, it is easy to understand how a complex crystal structure and a heat of formation close to those of δ-Ni_2Si and NiSi, renders the nucleation of Ni_3Si_2 at the δ-Ni_2Si/Si even more difficult than for NiSi. This explains the absence of the compound from the reaction sequence.

In these conditions – where the nucleation of stable compounds is difficult – the observation of the metastable θ-Ni_2Si is striking since we expect a higher nucleation barrier for this compound than for Ni_3Si_2 and NiSi. Indeed, while the results of Chapters 6 and 7 support the hypothesis that the nucleation of θ-Ni_2Si is rate-limiting at least initially, the low formation temperature and the systematic appearance of the compound over a large range of initial Ni thicknesses are signs that its nucleation is favored over Ni_3Si_2 and NiSi. Our extensive experimental work has allowed for pinpointing as much as five phenomena, which in combination explain this favored nucleation. Of these five phenomena, one appears to be paramount and a distinct characteristic of the Ni-Si system: the similarity between the crystal structures of δ-Ni_2Si, θ-Ni_2Si and NiSi. Nonetheless, should the nucleation of NiSi be easier, the formation of θ-Ni_2Si would not have been observed.

Also, whereas the formation of θ-Ni_2Si instead of Ni_3Si_2 and NiSi is surprising, the return of the δ-Ni_2Si phase upon the consumption of θ-Ni_2Si, and to some extent upon that of $Ni_{31}Si_{12}$, along with the co-existence of several compounds in the same layer, is perhaps our most striking result as far as solid-state thin-film reactions are concerned. This is in stark contrast with the widely accepted concept that *thin-film* solid-state reactions should result in the successive appearance of continuous layers of compounds with monotonically varying compositions. Nonetheless, beyond merely observing such peculiar behaviors, we were able to identify the thermodynamic (metastability and

similarity between crystal structures) and kinetic (diffusion of vacancies, non-planar growth fronts, sensitivity to the Ni supply) phenomena that explain them. Again, the structural similarity mentioned together with the abundance of the Ni supply (in the case of the $Ni_{31}Si_{12}$ consumption) appear to be the most important factors.

In summary, the results presented in this thesis clearly demonstrate that even though the literature on Ni-Si and solid-state thin-film reactions in general is abundant, much was left, and still remains, to be understood. They also show that *in situ* x-ray diffraction is a powerful tool for revealing unsuspected, or not yet unobserved, behaviors. Indeed, beyond all the peculiarities we have reported, the unprecedented time resolution provided by *in situ* synchrotron X-ray diffraction enabled us to observe in real time the kinetic competition between the different compounds that can nucleate at the silicide/Si interface and that δ-Ni_2Si wins most of the time. This competition was predicted by many models of solid-state reactions before, but was never observed directly to our knowledge.

8.3 Technological impact of θ-Ni_2Si

As explained in the introductory chapter, our work was in part motivated by the technological importance of the Ni-Si system for advanced microelectronic circuits. During the course of this thesis, NiSi has been successfully implemented as a contact material in CMOS circuits by IBM as well as by several other integrated-circuit manufacturers such as AMD, Intel, and Sony.

The integration of the NiSi SALICIDE process has been fraught with a number of issues, concerning among others the thermal stability of NiSi. We have mentioned in Chapter 3 that alloying Ni with Pt allows for significantly increasing the temperature range over which the NiSi is morphologically stable. However, other problems related to the heat-induced silicidation reaction, and presumably to the formation of Ni-rich

compounds before the appearance of NiSi, have been encountered. While we cannot expose the details of these problems here because of confidentiality issues, an interesting correlation can be discussed. To the candidate's knowledge, no clear link has been made between the problems mentioned above and the presence of θ-Ni_2Si in the reaction sequence. However it is worth pointing out that in addition to stabilizing NiSi towards agglomeration and transformation to $NiSi_2$, we have shown in Chapter 6 that Pt also suppresses the formation of θ-Ni_2Si. Bearing in mind the formation mechanisms of this compound (non-planar growth, diffusion of vacancies), the microstructure of the layer stacks where it is present (interface roughness, lateral co-existence with δ-Ni_2Si) as well as the sensitivity of the reaction to processing parameters, the formation of θ-Ni_2Si could very well result in peculiar effects when occurring in finely patterned CMOS contacts and lines. Surfaces and interfaces provided by the various dielectric structures can influence the energetics of the reactions, serve as fast diffusion paths, or impart particular stress loading conditions. All these factors can result in an increasingly difficult control of the silicidation reaction. It is therefore the candidate's opinion that Pt alloying has been instrumental to the successful integration of the Ni-Si contact metallurgy by solving more than the thermal stability issues with NiSi.

8.4 Perspectives

Many avenues could be envisioned for the continuation of this work. The use of differential scanning calorimetry (DSC) as a complementary tool for investigating the reaction kinetics immediately comes to mind as this technique can provide a direct measurement of the heat involved at each stage of the reaction. Although earlier DSC studies of Ni-Si reactions have failed to reveal the formation of θ-Ni_2Si or have perhaps mistaken it with some other phenomenon such as grain growth, we believe that the new knowledge provided by our work could guide future DSC studies. This would provide

valuable information about the energetics of the reactions and could be instrumental in confirming the driving force behind the formation and the consumption of θ-Ni_2Si.

Pursuing the investigation of texture evolution during the reaction is another area worthy of further efforts. In particular, we mentioned in Chapters 5 and 6 the existence of a highly textured layer (close to epitaxial) most likely located at the silicide/Si interface in samples where the reaction was stopped at the maximum development of θ-Ni_2Si. According to pole figure experiments (not reported in this thesis), the signal corresponding to this layer is stronger in samples implanted with high F doses. To this date, the crystal structure, the composition, and the microstructure of the layer as well as the driving force behind its formation remain unknown. The possibility that it consists of some metastable compound (not indicated in the equilibrium phase diagram) cannot be excluded since the diffraction patterns could not be fitted with any of the known Ni silicides. Further studies aiming at understanding the force driving the formation of this layer should involve samples with fluorine implants and with amorphous Si, two types of substrates that were shown to yield similar Ni-Si reactions schemes. It would be very interesting, among other things, to determine whether the highly textured layer is also present on amorphous Si and if so, if it plays a role in the formation of θ-Ni_2Si.

In order to further elucidate the role of δ-Ni_2Si in the formation of θ-Ni_2Si it would be interesting to investigate the effects of a change in δ-Ni_2Si texture or grain size on the reaction. Low-rate deposition of Ni layers on cryogenically cooled substrates would avoid the formation of the initial intermixed layer, possibly changing the texture of the first compound to form. Also, long, low-temperature (≤ 200 °C) anneals followed by 3 °C s^{-1} ramps or higher temperature isothermal anneals would allow to study Ni-Si reactions starting from larger-grained δ-Ni_2Si layers.

Finally, in a more general perspective, an increasing amount of research is being done on meta-materials and nano-composite materials where several different elements (including Si) are combined toghether to build complex heterogeneous structures with tailored properties. The multiple interfaces one finds in such heterogenous structures, e.g. in systems comprised of nano-particles embeded in a solid matrix, can host solid-state reactions which lead to the production of compounds (including silicides) that may play a key role in setting the properties of the overall meta-material. The *in situ* x-ray diffraction technique we have presented in this thesis could be used to study the formation and the characteristics of these interfaces and to develop strategies to optimize their properties.

REFERENCES

1 M.A. Nicolet and S.S. Lau (1983), Formation and Characterization of transition-Metal Silicides, in *VLSI Electronics, Microstructure Science, **Vol. 6**,* (Academic Press, NY), p.330.

2 J.P. Gambino, E.G. Colgan (1998), Silicides and Ohmic contacts, Materials Chemistry and Physics, **52** ,p. 99.

3 C. Detavernier, T.R.L. Van Meirhaeghe, F. Cardon, K. Maex (2001), $CoSi_2$ nucleation in the presence of Ge, Thin Solid Films, **384**, p.243.

4 F.M. d'Heurle, (1988), Nucleation of new solid phases from chemical interactions at an interface, Journal of Materials Research, **3**, p.167.

5 C. Lavoie, F.M. d'Heurle, C. Detavernier, C. Cabral Jr. (2003), Towards implementation of a Ni silicide process for CMOS technologies, Microelectronic Engineering, **70** , p.144.

6 F.M. d'Heurle, S.-L. Zhang (1996), Comment on "Dominant diffusing species during cobalt silicide formation [J. Appl. Phys., **79**, 153 (1996)], Journal of Applied Physics, **87**, p.8216.

7 W. Xia, C.A. Hewett, M. Fernandes, S.S. Lau, D.D. Poker (1989), On the thermodynamical driving force during ion mixing of the Co-Si system, Journal of Applied Physics, **65** , p.2300.

8 C. Lavoie, B. Purtell, C.Coia, C. Detavernier, P. Desjardins, J. Jordan-Sweet, C. Cabral Jr., F.M. d'Heurle, J.M.E. Harper (2002), Electrochem. Soc. Symp. Proc., **2002-11**, p.455.

9 C. Coia, C. Lavoie, K.J. Kellock, F.M. d'Heurle, C. Detavernier, P. Desjardins (2005), Proceedings of The 1st International Conference on Diffusion in Solids and Liquids DSL-2005, July 6-8, 2005, University of Aveiro, Aveiro, Portugal

10 L.S. Darken (1949), Journal of metals, American institute of mining and metallurgical engineers, No. 5, Sec. 3, p.304.

11 d'Heurle (1983), Nucleation phenomena in transitions from two to three phases, diffusion couples, phase stability, the thin film formation of some silicides, IBM Research Reports, **RC10422** p.37 & p.14.

12 Walser, R.M., Bené R.W. (1976), First phase nucleation in silicon-transition-metal planar interfaces, Applied Physics Letters, **28** , p.624.

13 Pretorius, R. (1996), Prediction of silicide formation and stability using heats of formation, Thin Solid Films, **290-291**, p.477

14 Pretorius, R., Vredenberg, A.M., Saris, F.W., de Reus, R. (1991), Prediction of phase formation sequence and phase stability in binary metal-aluminium thin-film systems using the effective heat of formation rule., Journal of Applied Physics, **70**, p.3636.

15 d'Heurle F.M., Gas,P . (1986), Kinetics of formation of silicides : a review, Journal of materials research, **1**, p.205.

16 d'Heurle F.M., Gas, P., Philibert, J. (1995), Diffusion-reaction: The ordered Cu_3Au rule and its corollaries, Solid state phenomena, **41**, p.93.

17 d'Heurle, F.M., Ghez, R. (1992), Reactive diffusion in a prototype system : Nickel-Aluminium. II : The ordered Cu_3Au rule and the sequence of phase formation, nucleation, Thin Solid Films, **215** , p.26.

18 C. Canali, F. Catellani, G. Ottaviani, M. Prudenziati (1978), On the formation of Ni and Pt silicide firt phase: the dominant role of kinetics, Applied Physics Letters, **33**, p.187.

19 K.N. Tu (1975), Selective growth of metal-rich silicide of near-noble metals, Applied Physics Letters, **27**, p.221.

20 Thompson, C. (1992), On the role of diffusion in phase selection during reaction at interfaces, Journal of materials research, **7**, p.367.

21 Christian J.W. (1975), The theory of transformations in metals and alloys: An advanced textbook in physical metallurgy, 2nd edition, Pergamon press, New York, pp.15-20.

22 M. Avrami (1939), Kinetics of phase change I*, Journal of Chemical Physics, **7**, p.1103.

23 M. Avrami (1940), Kinetics of phase change II*, Journal of Chemical Physics, **8**, p.212.

24 M. Avrami (1940), Kinetics of phase change III*, Journal of chemical physics, **9**, p.177.

25 U. Gösele, K.N. Tu (1982), Growth kinetics of planar binary diffusion couples: "Thin-film case" versus "bulk cases", Journal of Applied Physics, **53**, p.3252.

26 S.L. Zhang, F.M. d'Heurle (1994), Modelization of the growth of three intermediate phases, Materials Science Forum, **155-5**, p.59.

27 V.I. Dybkov (1986), Reaction diffusion in heterogeneous binary systems part 2 Growth of the chemical compound layers at the interface between to elementary substances: two compound layers, Journal of Materials Science, **21**, p.3085.

28 V.I. Dybkov (1992), Growth kinetics of silicide layres: a physicochemical viewpoint, Journal of Physical Chemistry of Solids, **53**, p.703.

29 H.E. Kissinger (1957), Reaction kinetics in differential thermal analysis, Analytical Chemistry, **29**, p.1702.

30 E.G. Colgan, F.M. d'Heurle (1996), Kinetics of Silicide formation measured by *in situ* ramped resistance measurements, Journal of Applied Physics, **79**, p.4087.

31 E.J. Mittemeier, A. Van Gent, P.J. van der Schaaf, (1986), Analysis of transformation kinetics by nonisothermal dilatometry, Metallurgical Transactions A, **17**, p.1441.

32 E.J. Mittemeier, L. Cheng, P.J. van der Schaaf, C.M. Barkman, B.M. Korevaar, (1987), Analysis of nonisothermal transformation kinetics; tempering of iron-carbon and iron-nitrogen martensites, Metallurgical Transactions A, **19**, p.925.

33 P. Nash, A. Nash (1987), Bulletin of Alloy Phase Diagrams, **8**, p.6.

34 JCPDS-International Center for Diffraction Data- datasheet #06-0690.

35 JCPDS-International Center for Diffraction Data- datasheet #71-0638.

36 JCPDS-International Center for Diffraction Data- datasheet #73-2092.

37 JCPDS-International Center for Diffraction Data- datasheet #73-2093

38 JCPDS-International Center for Diffraction Data- datasheet #17-0881.

39 JCPDS-International Center for Diffraction Data- datasheet #38-0844.

40 K.N. Tu, J.W. Mayer, Silicide formation. *In*: Poate JM, Tu KN, Mayer JW, editors (1978). Thin films – inter-diffusion and reactions. John Wiley; [Chapter 10],

41 A. Lauwers, A. Steegen, M. de Potter, R. Lindsay, A. Satta, H. Bender, K. Maex (2001), Materials aspects, electrical performance and scalability of Ni silicide towards sub-0.13μm technologies, Journal of Vacuum Science and Technology, **B 19**, p.2026.

42 M. Tinani, A. Mueller, Y. Gao, E.A. Irene, Y.Z. Hu, S.P. Tay (2001), *In Situ* real-time studies of nickel silicide phase formation, Journal of Vacuum Science and Technology. **B 19**, p.376.

43 G. Ottaviani (1986), Metallurgical aspects of the formation of silicides, Thin Solid Films, **140**, p.3.

44 K.N. Tu, W.K. Chu and J.W. Mayer (1975), Structure and growth of Ni_2Si on silicon, Thin Solid Films, **25**, p.403.

45 E.G. Colgan, J.P. Gambino, Q.Z. Hong (1996), Formation and stability of silicides on polycrystalline silicon, Materials Science and Engineering, **R. 16**, p.43.

46 F. Hodaj, A.M. Gusak (2004), Suppression of intermediate phase formation inf binary couples with metastable solubility, Acta Materialia, **52**, p.4305

47 J.P. Sullivan, R.T. Tung, F. Schrey (1991), Control of interfacial morphology: $NiSi_2$/Si(100), Journal of Applied Physics, **72**, p.478.

48 K.N.Tu, E.I. Alessandrini, W.K. Chu, H. Krautle, J.W. Mayer (1974), Epitaxial growth of silicide $NiSi_2$ on Silicon, Japanese Journal of Applied Physics, **suppl. 2**, pt. 1, p.669.

49 M.A. Nicolet, S.S. Lau, in N.G. Einspurch and G.b. Larrabee editors (1983), VLSI Electronics, Microstructure Science, **6**, Academic press, New York, [Chap 6].

50 H. Foll, P.S. Ho, K.N. Tu (1982), Transmission electron microscopy of the formation of nickel silicides, Philosophical Magazine, **45**, p.31.

51 F.M. d'Heurle, C.S. Petersson, J.E.E. Baglin, S.J. La Placa, C.Y. Wong (1983), Formation of thin films of NiSi: Metastable structure, diffusion mechanisms in intermetallic compounds, Journal of Applied Physics, **55**, p.4208.

52 L.A. Clevenger, C.V. Thompson (1990), Nucleation-limited phase selection during reactions in nickel/amorphous-silicon multilayer thin films, Journal of Applied Physics, **67**, p.1325.

53 M.O. Aboelfotoh, H.M Tawancy, F.M. d'Heurle (1987), Transmission electron microscope study of the formation of Ni_2Si and NiSi on amorphous silicon, Applied Physics Letters, **50**, p.1453.

54 K.R. Coffey, L.A. Clevenger, K. Barmak, D.A. Rudman, C.V. Thompson (1989), Experimental evidence for nucleation during thin-film reactions, Applied Physics Letters, **55**, p.852.

55 E. Ma, W.J. Meng, W.L. Johnson, M.-A. Nicolet, M. Nathan (1988), Simultaneous planar growth of amorphous and cristalline Ni silicides, Applied Physics Letters, **53**, p. 2033.

56 K. Holloway, R. Sinclair, M. Nathan (1989), Amorphous silicide formation by thermal reaction: A comparison of several metal-silicon systems, Journal of Vacuum Science and Technology, **A7**, p.1479.

57 C.D. Lien, M.A. Nicolet, S.S. Lau (1984), Low Temperature formation of $NiSi_2$ from evaporated silicon, Physica Status Solidi, **A81**, p.123.

58 C.D. Lien, M.A. Nicolet, S.S. Lau (1986), Kinetics of silicides on Si<100> and evaporated silicon substrates, Thin Solid Films, **143**, p.63.

59 J.O. Olowolafe, M.A. Nicolet, J.W. Mayer (1976), Influence of the nature of the Si substrate on nickel silicide formed from thin Ni films, Thin Solid Films, **38**, p.143.

60 G. Majni, M. Costato, F. Panini (1985),The growth process of thin film silicides in Si/Ni planar systems, Thin Solid Films, **125**, p.71.

61 G. Ottaviani (1979), Review of binary alloy formation by thin-film interactions, Journal of Vacuum Science and Technology, **16**, p.1112.

62 C. Canali, G. Majni, G. Ottaviani, G. Celotti (1979), Phase diagrams and metal-rich silicide formation, Journal of Applied Physics, **50**, p.255.

63 K.N. Tu, G. Ottaviani, U. Gösele, H. Föll (1982), Intermetallic compound formation in thin-film and in bulk samples of the Ni-Si binary system, Journal of applied physics, **54**, p.758.

64 L.R. Zheng, L.S. Hung, J.W. Mayer, G.Majini, G. Oattaviani (1982), lateral diffusion of Ni and Si through Ni_2Si in Ni/Si couples, Applied Physics Letters, **41**, No.7, p646.

65 L.R. Zheng, L.S. Hung, J.W. Mayer (1983), Silicide formation in lateral diffusion couples, Journal of Vacuum Science and Technology, **A1**, p.758.

66 J.H. Gülpen, A.A. Kodentsov, F.J.J. Van Loo (1995), Growth of silicides in Ni-Si and Ni-SiC bulk diffusion couples, Zietschrift für Metallkunde, **86**, p.530.

67 S.H. Chen, C.B. Carter, Z. Elgat, L.R. Zheng, J.W. mayer (1987), Journal of Applied Physics, **62**, p.1189.

68 A.D. Smigelskas, E.O. Kirkendall (1947), Transaction of the American Institute of Mining and Metallurgical Engineers, **171**, p.130.

69 A. Paul, M.J.H. van Dal, A.A. Kodentsov, F.J.J. van Loo (2004), The Kirkendall effect in multiphase diffusion, Acta Materialia, **52**, p.623.

70 S.H. Chen, L.R. Zheng, C.B. Carter, J.W. Mayer (1985), Structure analysis of Ni-siilicides formed in lateral diffusion couples, Journal of Applied Physics, **57**, p.260.

71 P. Gas, F.M. d'Heurle, F.K. LeGoues, S.J. LaPlaca (1986), Formation of intermediate phases, Ni_3Si_2 and Pt_6Si_5: Nucleation identification and resistivity, Journal of Appplied Physics, **59**, p.3458.

72 P.Gas (1989), Diffusion mechanism in bulk silicides: relation with thin film behaviour (case of Ni_2Si formation), Applied Surface Science, **38**, p.178.

73 W.K. Chu, H. Krautle, J.W. Mayer, H. Muller, M.A. Nicolet, K.N.Tu (1974), Identification of the dominant diffusing species in silicide formation, Applied Physics Letters, **25**, p.454.

74 K.n.Tu (1977), Analysis of marker motion in thin-film silicide formation, Journal of Applied Physics, **48**, p.3379.

75 H. Takai, K.N. Tu (1988), Dopant effect on intrinsic diffusivity in nickel silicide, Physical Review B, **38**, p.8121.

76 R. Pretorius, C.L. Ramiller, S.S. Lau, M.-A. Nicolet (1977), Radioactive Si as a marker in thin-film silicide formation, Applied Physics Letters, **30**, p.501.

77 J.E.E. Baglin, H.A. Atwater, D. Gupta, F.M. d'Heurle (1982), Radioactive Ni* tracer study of the nickel silicide growth mechanism. Thin Solid Films, **93**, p.255.

78 J.C. Ciccariello, S. Poize, P.Gas (1990), Lattice and grain-boundary self-diffusion in Ni_2Si: Comparison with thin film formation, Journal of Applied Physics, **67**, p.3315.

79 F.M. d'Heurle, S. Petersson, L. Stolt, B. Strizker (1982), Diffusion in intermetallic compounds with the CaF_2 structure: A marker study of the formation of $NiSi_2$ thin films, Journal of Applied Physics, **53**, p.5678.

80 F.M. dHeurle, D. Gupta, P. Gas, J. Philibert (2000), On diffusion in intermetallic compounds, P. Vincensini & V. Buscaglia editors, Mass and Charge Transport in Inorganic Materials, Advances in Science and Technology, **29**, p.173.

81 E.G. Colgan (1996), Activation energy for Ni_2Si and NiSi formation measured over a wide rage of ramp rates, Thin Solid Films, **279**, p.193.

82 E.G. Colgan, F.M. d'Heurle (1996), Kinetics of silicide formation measured by *in siu* ramped resistance measurements, Journal of Applied Physics, **79**, No. 8, 4087.

83 E. Ma, B.S. Lim, M.A. Nicolet, M.Natan (1987), Growth of Ni_2Si by rapid thermal annealing: Kinetics and moving species, Applied Physics A, **44**, p.157.

84 C.D. Lien, M.A. Nicolet, S.S. Lau (1984), Low temperature formation of $NiSi_2$ on evaporated Silicon, Physica Status Solidi, **81**, p.123.

85 T.G. Finstad (1981), A Xe marker study of the transformation of Ni_2Si to NiSi in thin films, Physica Status Solidi, **A63**, p.223.

86 C.D. Lien, M.A. Nicolet, S.S. Lau (1986), Kinetics of silicides on Si <100> and evaporated silicon substrates, Thin Solid Films, **143**, p.63.

87 J.A. Kittl, M.A. Pawlak, C. Torreginai, A. Lauwers, C. Demeurisse, C. Vranken *et al.* (2007), Kinetics of Ni_3Si_2 in the Ni_2Si-NiSi thin-film reaction from in-situ measurements, Applied Physics Letters, **91**, p. 232102-1.

88 J.H. Gülpen (1995), PhD thesis, Eindhoven University of Technology, Eindhoven, The Netherlands.

89 L.A. Clevenger, C.V. Thompson, R.C. Cammarata, K.N. Tu (1988), Reaction kinetics of nickel/silicon multilayer films, Applied Physics Letters, **52**, p.795.

90 C.D. Lien, M.A. Nicolet (1984), Impurity effects in transition metal silicides, Journal of Vacuum Science and Technology, **B2**, p.738.

91 A. Severino, A. Lamagna, R. Anzalone, C. Bongiorno, E. Rimini, F. La Via, (2007), Effect of Mo interlayer on thermal stability of polycrystlaline NiSi thin films, Journal of Applied Physics, **101**, p.063544-1.

92 R.N .Wang, J.Y. Fen (2003), Comparison of the thermal stabilities of NiSi films in Ni/Si, Ni/Pd/Si and Ni/Pt/Si systems, Journal of Physics: Condensed Matter, **15**, p.1935.

93 X.P. Qu, Y.L. Jiang, G.P. Ru, F. Lu, B.Z. Li, C. Detavernier, R.L. Van Meirhaeghe (2004), Thermal stability, phase and interface uniformity of Ni-silicide formed by Ni-Si solid-state reaction, Thin Solid Films, **462-463**, p.462.

94 J.F. Liu, H.B. Chen, J.Y. Feng, J. Zhu (2000), Improvement of the thermal stability of NiSi films by using a thin Pt interlayer, Applied Physics Letter, **77**, p.2177.

95 W.L. Tan, K.L. Pey, S.Y.M. Chooi, J.H. Ye, T. Ozipowicz (2002), Effect of a titanium cap in reducing interfacial oxides in the formation of nickel silicide, Journal of Applied Physics, **91**, p.2901.

96 W. Huang, L.Zhang, Y.Gao, H. Jin (2007), Effect of a thin W, Pt, Mo and Zr interlayer on the thermal stability and electrical characteristics of NiSi, Microelectronic Engineering, **84**, p.678.

97 W. Huang, L.C. Zhang, Y.Z. Gao, H.Y. Jin (2006), The improvement of thermal stability of nickel silicide by adding a thin Zr interlayer, Microelectronic Engineering, **83**, p.245.

98 J.S. Maa, Y.O. Ono, D.J. Tweet, F. Zhang, S.T. Hsu (2001), effect of interlayer on thermal stability of nickel silicide, Journal of Vacuum Science and Technology, **A19**, p.1596.

99 S.L. Chiu, Y.C. Chu, C.j. Tsai, H.Y. Lee (2004), Effects of Ti interlayer of Ni/Si reaction systems, Journal of the Electrochemical Society, **151**, p.G452.

100 O. Nakatsuka, K. Okubo, Y. Tsuchiya, A. Sakai, S. Zaima, Y. Yasuda (2005), Low-temperature formation of epitaxial $NiSi_2$ layers with solid-phase reaction in Ni/Ti/Si(001) systems, Japanese Journal of Applied Physics, **55**, p.2945.

101 O. Chamirian, A. Lauwers, J.A. Kittl, M. Van Dal, M. De Potter, R. Lindsay, K. Maex (2004), Reaction of Ni and $Si_{0.8}Ge_{0.2}$: Phase formation and thermal stability, Microelectronic Engineering, **76**, p.297.

102 C.J. Choi, S.Y. Chang, S.J. Lee, Y.W. Ok, T.Y. Seong (2007), Thickness effect of a Ge interlayer on the formation of Nickel Silicides Journal of the Electrochemical Society, **154**, p. H759.

103 Y. He, L. Liu, J.Y. Feng, Q.L. Wu (2004), Effect of a Ge interlayer on the high-temperature behavior of NiSi films, Journal of Applied Physics, **96**, p. 6928.

104 F.M. d'Heurle, D.D. Anfiteatro, V.R. Deline, T.G. Finstad (1985), Reaction of silicon with films of Co-Ni alloys: Phase separation of the monosilicides and nucleation of the disilicides, Thin Solid Films, **128**, p.107.

105 C. Detavernier, R.L. Van Meirhaeghe, F. Cardon, K. Maex (2000), Influence of mixing entropy on the nucleation of $CoSi_2$, Physical Review B, **62**, p.12045.

106 A. Ishizaka, Y. Shiraki (1986), Low temperature cleaning of silicon and its application to silicon MBE, Journal of the Electrochemical Society, **133**, p.666.

107 V. Teodorescu, L. Nistor, H. Bender, A. Steegen, A. Lauwers, K. Maex, J. Van Landuyt (2001), *In situ* transmission electron microscopy study of Ni silicide phases formed on (001) Si active lines, Applied Physics Letter, **90**, p.167.

108 R.T. Tung (1996), Oxide mediated epitaxy of $CoSi_2$ on silicon, Applied Physics Letters, **68**, p.3461.

109 R.T. Tung, S. Ohmi (2000), Epitaxial silicide interfaces in microelectronics, Thin Solid films, **369**, p233.

110 C. Lavoie, C. Detavernier, C. Cabral Jr., F.M. d'Heurle, A.J. Kellock, J. Jordan-Sweet, J.M.E. harper (2006), Effect of additive elements on the phase formation and morphological stability of nickel monosilicide films, Microelectronics Engineering, **83**, p.2042.

111 A. Lauwers, J.A. Kittl, M.J.H. Van Dal, O. Chamirian, M.A. Pawlak, M. De Poter, *et al.*, (2004), Ni-based silicides for 45nm CMOS and beyond, Materials Science and Engineering, **B114-115**, p.29.

112 F. Corni, B. Grignaffini Gregorio, G. Ottaviani, G. Queirolo, J.p. Follegot (1993) Dilute NiPt alloy interactions with Si, Applied Surface Science, **73**, p.1997.

113 F. Corni ,C. Nobili, G. Ottaviani, R. Tonini, B. Grignaffini Gregorio, G. Queirolo (1995), Metallurgical and electrical investigations of Pt_5Ni_{95}/silicon interactions, Applied Surface Science, **91**, p.107.

114 H. Zimmermann, H. Ryssel (1992), Gold and platinium diffusion: The Key to understanding of intrinsic point defects behavior in silicon Applied Physics, **A55**, p.121.

115 S.P. Murarka, D.S. Williams (1987), Dopant redistribution in silicide-silicon and silicide-polycrystalline silicon bilayered structures, Journal of Vacuum Science and Technology, **B5**, p.1674.

116 D. Mangelinck, P. Gas, J.M. Gay, B. Pichaud, O. Thomas (1998), Effect of Co, Pt and Au additions on the stability and epitaxy of $NiSi_2$ films on (111)Si, Journal of Applied Physics, **84**, p.2583.

117 D. Mangelinck, J.Y. Dai, J.S. Pan, S.k. Lahiri (1999), Enhancement of thermal stability of NiSi films on (100) Si and (111) Si by Pt addition, Applied Physics Letters, **75**, p.1736.

118 O. Cojocaru-Mirédin, D. Mangelinck, K. Hoummada, E. Cadel, D. Blavette, B. Deconihout, C. Perrin-Pellegrino (2007), Snowplow effect and reactive diffusion in the Pt doped Ni-Si system, Scripta Materialia, **57**, p. 373.

119 C. Detavernier, C. Lavoie (2003), Influence of Pt addition on the texture of NiSi on Si (001), Applied Physics Letters, **84**, p. 3549.

120 T.G. Finstad (1978), Silicide formation with Nickel and Platinum double layers on silicon, Thin Solid Films, **51**, p.411.

121 J.Y. Dai, D. Mangelinck, S.K. Lahiri (1999), Coexistence of hexagonal and orthorhombic structures in NiSi films containing Pt, Applied Physics Letters, **75**, p. 2214.

122 T.G. Finstad, D.D. Anfiteatro,W.R. Deline, F.M. d'Heurle, P. Gas, V.l. Moruzzi, K. Schwartz, J. Tersoff (1986), The formation of disilicides from bilayers of Ni/Co and Co/Ni on silicon: Phase separation and solid solution, Thin Solid Films, **135**, p.229.

123 D.M. Scott (1982), The effects of oxygen on the formation of nickel, palladium, and platinum silicides, PhD thesis, California Institute of Technology.

124 D.M. Scott, M.-A. Nicolet (1981), Modification of nickel silicide formation by oxygen implantation, Nuclear Instruments and Methods, **182/183**, p.655.

125 P.J. Grunthaner, F.J. Grunthaner, D.M. Scott, M.A. Nicolet, J.W. Mayer (1981) Oxygen impurity effects at metal/silicide interfaces: formation of silicon oxide and suboxides in the Ni/Si system, Journal of Vacuum Science and technology, **19**, p.641.

126 C.S. Pai, F.A. Baiocchi, D.S. Williams (1990), Arsenic redistribution during Cobalt silicide formation, Journal of Applied Physics, **67**, p.1340.

127 D.M. Scott, L. Wielunski, H. Von Seefeld, M.A. Nicolet (1981), Retardation and suppression of nickel silicide formation by N^+ implantation, Nuclear Instruments and Methods, **182/183**, p.661.

128 S.P. Murarka, D.S. Williams (1987), Dopant redistribution in silicide-silicon and silicide-polycrystalline silicon bilayered structures, Journal of Vacuum Science and Technology, **B5**, p.1674.

129 R. Madar (1995), Phase diagrams and crystallographic data for TM-Si-Dopant systems, *in* Properties of Metal Silicides, Edited by K. Maex and M. Van Rossum, Short Run Press, Exeter, Chapter 3.4, P. 109.

130 F.M. d'Heurle (1986), Material properties of silicides for VLSI technology, *in* solid state devices 1985, P.Balk and O.G. Folberth Eds., Elsevier Science Publishers, p. 213-241.

131 L.R. Zheng, L.S. Hung, J.W. mayer (1985), Redistribution of dopant arsenic during silicide formation, Journal of Applied Physics, **58**, p.1505.

132 O. Thomas, P. Gas, F.M. d'Heurle, F.K. LeGoues, A. Michel, G. Scilla (1988), Diffusion of boron, phosphorous and arsenic implanted in thin films of cobalt disilicide, Journal of Vacuum Science and Technology, **A6**, p.1736.

133 I. Ohdomari, M. Akiyama, T. Maeda, M. Hori, C. Takebayashi, A. Ogura, T. Chikyo, I. Kimura, K. Yoneda, K.N. Tu,(1984), Low-Temperature redistribution of As in Si during Ni silicide formation, Journal of applied physics, **56**, p.2725.

134 A. Witzmann, A. Dittmar, K .Gärtner, G.Götz (1985), Formation of Ni-silicides on As-doped silicon, Physica Status Solidi, **A91**, p.439.

135 M.A. Pawlak, J.A. Kittl, O. Chamirian, A. Vedoso, A. Lauwers, T.Schram, K. Maex, A. Vantomme (2004), Investigation of Ni fully silicided gates for sub-45nm CMOS technologies, Microelectronic Engineering, **76**, p.349.

136 J.A. Kittl, A. Lauwers, O. Chamirian, M. Van Dal, A. Akheyar, M. De Potter, R. Lindsay, K. Maex (2003), Ni- and Co- based silicides for advanced CMOS applications, Microelectronic Engineering, **70**, p.158.

137 M. Wittmer (1988), Dopant diffusion in self-aligned silicide/silicon structures, Journal of the electrochemical society, **135**, p.2049.

138 J. Rinderknecht, H. Prinz, T. Kammler, N. Schell, E. Zschech, K. Wetzig, T. Gessner (2003), In situ high temperature synchrotron-radiation diffraction studies of silicidation processes in nanoscale Ni layers, Microelectronic Engineering, **70**, p.226.

139 C. Zaring, H. Jiang, B.G. Svensson, M. Ostling (1991), Boron redistribution during formation of nickel silicides, Applied Surface Science, **52**, p.147.

140 S.W. Lu, C.W. Nieh, L.J. Chen (1986), Epitaxial growth of $NiSi_2$ on ion-implanted silicon at 250-280°C, Applied Physics Letter, **49**, p.1770.

141 L.J. Chen, C.M. Doland, I.W. Wu, J.J. Chu, S.W. Lu (1987), Effect of implantation impurities and substrate crystallinity on the formation of $NiSi_2$ on silicon at 200-280°C, Journal of Applied Physics, **62**, p.2789.

142 L.J. Chen, C.M .Doland, I.W. Wu, A. Chiang, C.C. Tsai, J.J. Chu, S.W. Lu, C.W. Nieh (1988), The effects of doping impurities and substrate crystallinity on the formation of Nickel Silicides on Silion, Journal of Electronic Materials, **17**, p.75.

143 A. Mokhberi, R. Kasnavi, P.B. Grifin, J.D. Plummer (2002), Fluorine interaction with point defects, boron and arsenic in ion-implanted Si, Applied Physics Letters, **80**, p.3530.

144 M.S. Bae, H.H. Ji, H.J. Lee, S.Y. Oh, B.F. Huang, J.H. Yun (2004), Characterization of nickel-silicide dependance on the substrate dopants for nanoscale complementary metal oxide semiconductor technology , Japanese Journal of Applied Physics, **43**, p.91.

145 M. Tsuchiaki, K. Ohuchi, A. Nishiyama (2005), Suppression of thermally induced leakage of NiSi-silicided shallow junctions by pre-silicide fluorine implantation, Japanese journal of Applied Physics, **44**, p.1673.

146 W.J. Chen, L.J. Chen (1991), Interfacial reactions of nickel thin films on BF_2^+-implanted (001)Si, Journal of Applied Physcis, **70**, p.2628.

147 J.M. Bennett and L.M. Mattson (1989), Introduction to Surface Roughness and Scattering, Optical Society of America, Washington.

148 B.D. Cullity, Elements of x-ray diffraction, 2nd edition, Addison-Wesley publishing compagny, p. 408, (1978).

149 D.J. Barber (1970), Thin foils of non-metals made for electron microscopy by sputter-etching, Journal of Materials Science, **5**, p. 1.

150 M.J. Kim, R.W. Carpenter (1987), TEM specimen heating during ion beam thinning: microstructural instability, Ultramicroscopy, **21**, p.327.

151 Y.M. Park, D.S. Ko, K.W. Yi, I. Petrov, Y.W. Kim (2007), Measurement and estimation of temperature rise in TEM samples during ion milling, Ultramicroscopy, **107**, p.663.

152 C. Detavernier, C. Lavoie, F.M. d'Heurle, H. Bender, R.L. Van Meirhaeghe (2004), Low-Temperature formation of $CoSi_2$ in the presence of Au, Journal of Applied Physics, **95**, p.5340.

153 J.Rinderknecht, H.Prinz, T. Kammler, F.Berberich, E.Zschech (2002), *In situ* high-temperature synchrotron-radiation diffraction studies of Ni and Co-Ni silicidation processes, Microelectronic Engineering, **64**, p.143.

154 C. Lavoie, C. Cabral, F. M. d'Heurle, J. M. E. Harper (2001), Exploring thin film reactions by means of simultaneous x-rays, surface roughness and resistance measurements, Defect and Diffusion Forum, **194-199**, p.1477.

155 C. Rivero, P. Gergaud, M. Gailhanou, O. Thomas, B. Froment, H. Jaouen, V. Carron (2005), Combined synchrotron X-ray diffraction and wafer curvature measurements during Ni-Si reactive film formation, Applied Physics Letters, **87**, p.041904.

156 C. Lavoie, C. Coia, F.M. D'Heurle, C. Detavernier ,C. Cabral, Jr., P. Desjardins, A.J. Kellock (2005), Reactive diffusion in the Ni-Si system: phase sequence and

formation of metal-rich phases, Proceedings of the Defect and Diffusion Forum, vols. 237-240, p.825.

157 C. Coia, C. Lavoie, F.M. D'Heurle, C. Detavernier, P. Desjardins, A.J. Kellock (2005), Electrochemical Society Proceedings on Advanced Gate Stack, Source/Drain, and Channel Engineering for Si-Based CMOS: New Materials, Processes, and Equipment, Vol. 2005-05, p.585.

158 L.R. Doolitle (1985), Algorithms for the rapid simulation of Rutherford backscattering spectra, Nuclear Instrucments & Methods in Physics Research, **B9**, p.344.

159 M. Ohring (1992), *The Materials Science of Thin Films*, Academic Press, London, p.416.

160 G. Pilström (1961), Acta Chem. Scand. 15,4, 893 (1961).

161 C. Detavernier, C. Lavoie, F.M. d'Heurle (2002), Thermal expansion of the isostructural PtSi and NiSi: Negative expansion coefficient in NiSi and stress effects in thin films, Journal of Applied Physics, **92**, p.2510.

162 C. Detavernier, A.S. Ozcan, J.Jordan-Sweet, E.A. Stach, J. Tersoff, F.M. Ross, C. Lavoie (2003), An off-normal fibre-like texture in thin films on single-crystal substrates, Nature, **426**, p.641.

163 C. Detavernier, C. Lavoie (2004), Influence of Pt addition on the texture of NiSi on Si (001), Applied Physics Letters, **84**, p. 3549.

164 S. Gaudet, C. Coia, P. Desjardins, C. Lavoie (2008), Metastable phase formation driven by texture inheritence during the reaction of thin Ni films with Si(001), Applied Physics Letters, *in press*.

165 F.M. D'Heurle, P. Gas, J. Mater. Res, V. 1, 1, 205 (1986).

166 J.P. Gambino, E.G. Colgan, Mat. Chem. & Phys., 52, 99 (1998).

167 K.R. Coffey, K. Barmak (1994),A new model for grain boundary diffusion and nucleation in thin film reactions , Acta Metallurgica et.Materialia,**42**,p. 2905.

168 R. de Ridder, G. Van Tendeloo, S. Amelinckx (1977), The ordering of vacancies in $Ni_{1-x}Al$. Study of the transition state by electron diffraction, Physica Status Solidi, **43**, p.133.

169 D. Colaitis, D. Van Dyck, P. Delavignette, S. Amelinckx (1979), On the diffraction features of two-layer systems. Application to $Ni_{3\pm x}Te_2$, Physica Status. Solidi A, **53**, p.105.

170 D. Colaitis, D. Van Dyck, P. Delavignette, S. Amelinckx (1980), High-resolution electron microscopic and electron diffraction study of non-stoichiometric phases in $Cu_{3-x}Te_2$, Physica Status Solidi, **58**, p.271.

171 K.S. Bartwal, O.N. Srivastava (1992), Superlattices in non-stoiciometric ZrS_2 single crystals, Materials Science & Engineering, **B14**, p.L20.

172 P.J. Desré, A.r. Yavari (1990), Suppression of crystal nucleation in amorphous layers with sharp concentration gradients, Physical Review Letters, **64**, p.1533.

173 A.M. Gusak, F. Hodaj, A.O. Bogatyrev (2001), Kinetics of nucleation in the concentration gradient, Journal of Physics: Condensed Matter, **13**, p.2767.

174 H. Von Känel, C. Schwartz, S. Goncalves-Conto, E. Müller, L. Miglio, F. Tavazza, G. Malegori (1995), New epitaxially stabilized CoSi phase with the CsCl structure, Physical Review Letters, **74**, p.1163.

175 L. Miglio, F. Tavazza, G. Malegori (1995), Stability hierarchy of the pseudomorphic $FeSi_2$ phases: α, γ, and defected CsCl, Applied Physics Letters, **67**, p.2293.

176 T. Tokunaga, K. Nishio, H.Ohtani, M. Hasebe (2003), Thermodynamic assessment of the Ni–Si system by incorporating ab initio energetic calculations into the CALPHAD approach, CALPHAD, **27**, p.161.

177 A.S.W. Wong, D.Z. Chi, M. Loomans, D.Ma, M.Y. Lai, W.C. Tjiu, S.J. Chua, C.W. Lim, J.E. Greene, F-enchanced morphological and thermal stability of NiSi films on BF_2^+-implanted Si(001), Applied Physics Letters, **81**, p.5138.

178 L.W. Cheng, S.L. Cheng, J.Y. Chen, L.J. Chen, B.Y. Tsui (1999), Effects of nitrogen ion implantation on the formation of nickel silicide contacts on shallow junctions, Thin Solid Films, **355-356**, p. 412.

179 P.S. Lee, D.Mangelinck, K.L. Pey, J. Ding, D.Z. Chi, J.Y. Dai, A. See (2001), Nickel Silicide formation on Si(100) and poly-Si with presilicide N_2^+ implantation, Journal of Electronic Materials, **30**, p.1554.

180 J.F. Ziegler, J.P. Biersack, U. Littmark (1985), *The Stopping and range of ions in matter*, vol. 1 (Pergamon, New York).

181 M.S Bae, H.H. Ji, H.J. Lee, S.Y. Oh, B.F. Huang, J.G. Yun,J.S. Wang, S.H. Park, H.D. Lee (2004), Characterization of nickel-silicide dependance on the substrate dopants for nanoscale complementary metal oxide semiconductor technology, Japanese Journal of Applied Physics, **43**, p.91.

182 F.M. d'Heurle, P. Gas, J. Philibert (1994), Investigating the role of grain boundaries in interface reactions, Materials Research Society Symposium proceedings, **343**, p.181.

183 S.K. Donthu,D.Z. Chi, S. Tripathy, A.S.W. Wong, S.J. Shua, (2004), Micro-Raman spectroscopic investigation of NiSi films formed on BF_2^+, B^+ and non-implanted (100) Si substrates, Applied Physics A, **79**, p.637.

184 D. Balzar, Voigt-Function model in diffraction line-broadening analysis, *in*

185 G.K.Wertheim, M.A. Butler, K.W. West, D.N.E. Buchanan, Review of Scientific Instruments, **45**, p.1369, (1974).

186 K. Barmak, K.R. Coffey, D.A. Rudman, S. Foner (1990), Phase formation sequence for the reaction of multilayer thin films of Nb/Al, Journal of Applied Physics, **67**,

187 F.M. D'Heurle, D. Ghez (1992), Reactive diffusion in a prototype system: nickel-aluminium. I. Non-constant diffusion coefficient, Thin Solid Films, **215**, p. 19....

188 E.N. Malsen, A.G. Fox, M.A. O'keefe, X-ray Scattering,in : International Tables for Crystallography Volume C : Mathematical, Physical and Chemical Tables,

Part 6 : Interpretation of diffracted intensity, E.Prince Editor, (Springer, New York).

189 K. Saravanan, B.K. Panigrahim S. Amirthapandian, K.G.M .Nair (2008), Resonant Rutherford backscattering spectrometry for carbon diffusion in silicon, Nuclear Instruments and Methods in Physics Research, **B266**, p.1502.

190 G.W. Peng, Y.P. Feng, M. Bouville, D.Z. Chi, A.C.H. Huan, D.J. Srolovitz (2007), First-principles simulations of Si vacancy diffusion in erbium silicide, Physical Review B, **76**, p.033303.